Modelling Of An Automotive Natural Gas Engine For A/F Control Investigations.

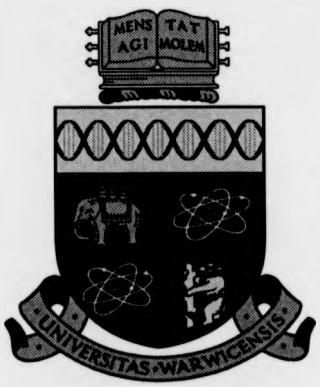

Alister Julian Thomas.
Department of Engineering,
University of Warwick.

Thesis submitted to the University of Warwick for the degree of Doctor of Philosophy

October 1995

Contents

List of Figures

List of Tables

Acknowledgements

I would like to acknowledge the help and advice of friends and colleagues in the work described in this thesis. I would firstly like to thank my academic supervisor Dr. Peter Jones, of the Department of Engineering, at the University of Warwick, for his expert guidance and extensive knowledge in many areas of vehicle simulation and control.

I would also like to thank my academic supervisors at the British Gas Research Centre, Loughborough, namely Dr. Kay Kerbyson and Dr. Sean Goodhart, for their continued support of the project. Also at British Gas, I would like to acknowledge Mr. Medhi Daragheh and Mr. Richard Heath for their assistance during engine testing. I would also like to thank Mr. Paul Weall for supplying valued information.

In respect of the Department of Engineering computer services, I would like to thank Mr. Alan Hulme for his continued hard work in maintaining reliable operation. I would also like to thank Martin Rouse for his expertise in Unix programming and general computer knowledge and John Outram for his valued opinions and discussions.

I would further like to express my deep gratitude for the patience and support shown by my close family and friends during the production of this thesis, especially to Natalie.

Declaration

This thesis is the original work by the author, parts of which are to be presented at an I. Mech. E Seminar.

Summary

In this thesis, the problem of A/F ratio control in a natural gas, internal combustion engine is addressed, with the global objective of reducing exhaust emission pollutants. A review of some mechanical approaches to exhaust pollutant reduction are assessed. It is found that many techniques aid the reduction of exhaust pollutants, but the most effective is the 3-way catalytic converter. To maintain conversion efficiency, the A/F ratio must be strictly controlled within the catalyst window limits around the stoichiometric operating point.

In order to investigate possible control techniques, a mathematical model is developed to simulate the physical behaviour of the engine processes. This approach allows a quick turn-around in terms of cost and time, for control investigations. The model demonstrates close trend-wise approximation of the engine states with previous modelling studies, however, a full validation study was not possible.

The model is then used to conduct investigations into A/F ratio control through the process of simulation. Conventional PI-closed-loop control is assessed for steady-state and transient engine conditions, and for varying microprocessor sampling rates. It is found that PI-control effectively removes state estimation errors, but is unable to remove A/F ratio excursions under transient operation.

An open-loop compensation control structure is then developed as an extension to the PI-controller action. Simulation results show this approach to drastically reduce A/F ratio excursions for a number of typical driving scenarios. Potential problems that could well be encountered in the "real" engine environment are then investigated, and the practicality of the new controller assessed.

A new approach to control is simulated that affords the most appropriate state estimation for the modelled system. This is shown to improve A/F ratio control upon that of the conventional approach but cannot match the compensation controller ability.

Chapter 1

Introduction

1.1 Vehicle Emissions

1.1.1 Environmental Factors and Legislation

The modern internal combustion engine plays a significant role in the way in which we live and run our lives. From its inception, dating back only to the turn of the 20^{th} century, the four-stroke cycle engine has become so successful in its development that it now powers millions of cars around the world. The motor vehicle is accountable for providing an apparent 'shrinking' of the globe enabling the transportation of people and cargo across large distances to be conducted with rapid ease and without much concern. In 1987 the number of motor vehicles in worldwide use was placed at 516 million and it is estimated that, by the year 2000, the total number of passenger cars and commercial vehicles on the roads will be approaching 700 million [1].

The popularity of motor travel is due to a variety of factors but perhaps the most noteworthy is that of the convenience and practical utility provided. The owner of a passenger car has been given the privilege of having a form of transport at their disposal which is readily available, close at hand, comfortable, reliable and enjoyable. Such vehicles were deemed to be luxurious items afforded only by the wealthy. In recent times this perception no longer exists and statistics state that,

in 1987, in the UK alone, passenger cars were as common as 1 for every 3 persons. In the USA these figures were even more extreme being 1 car for every 2 persons in 1980 [1].

The environmental penalties associated with the use of these vehicles are numerous. The sheer number of vehicles in use means that the current level of exhaust emission pollutants being dispensed into the atmosphere is required to be reduced dramatically. California has suffered heavily from the effects of vehicle emissions for many years due to a combination of the high number of cars, geographical location and climatic conditions. It was largely from the problems in the 1940's, when large amounts of photochemical smog were encountered, that Civic Councils were formed to take action in reducing emissions.

The Civic Councils established that motor vehicles were a major contributor to the high levels of atmospheric hydrocarbon in conjunction with those emissions from stationary sources. Due to the severity of the problem, California lead the way in implementing reductions of vehicle exhaust emissions via the creation of the Californian Motor Vehicle Pollution Control Board in 1960 [2]. The board set specifications on emissions and ensured that future vehicles to be sold in the State were meeting the designated certification. Figure 1.1 displays the exhaust emission limits that have been imposed in the U.S.A. for new production petrol-powered cars since 1960. These lowering limits have helped reduce U.S. levels of harmful exhaust emissions by as much as 96% [3]. California continues to enforce ever tightening legislation on vehicle emissions and these standards influence regulations on a global scale, not just in the USA.

The State actually has a directive that, by the year 2003, a proportion of 10% of the total number of cars sold in the state must be zero emission [4]. These vehicles are expected to be electrically powered in some form, either by harnessed solar power or by the more likely method of on-board batteries.

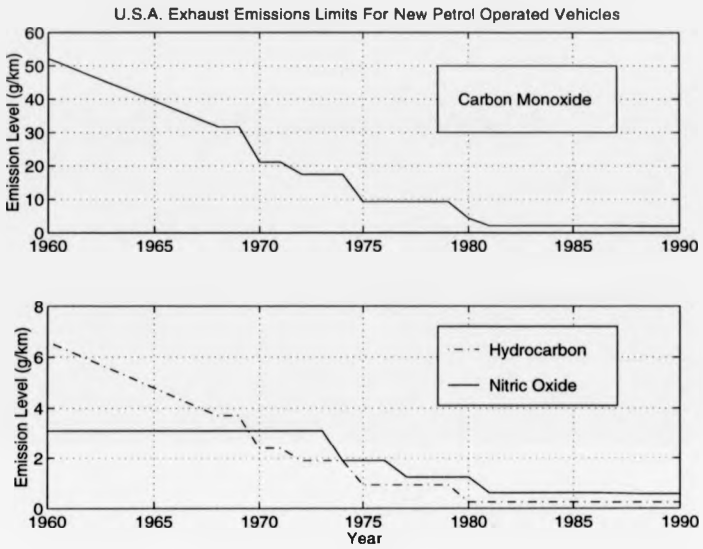

Figure 1.1: U.S.A exhaust emission reductions legislation since 1960. Limits applied to newly manufactured, petrol powered, passenger cars. [1, 3]

Recently, in Europe, new EC directives have come into effect requiring significant reductions in the emission levels of new production cars. This has lead to the extensive introduction of the 3-way catalytic converter. Further mandates are being implemented to decrease the levels of diesel derived emissions from trucks and buses along with off-road vehicles. These directives are having significant beneficial effects on the level of air pollution reduction. In 1994 the Department for the Environment released figures exhibiting a decline in the levels of major urban pollutants. The reduced levels of carbon monoxide and oxides of nitrogen reached a peak between 1990/92 and forecasts predict a definite continuation of their reduction that is expected to continue for another ten years [5]. This demonstrates the significant advances that have been made in controlling and minimising vehicle exhaust pollutants and bodes well for further reduction.

In the U.K., the 1987 emission levels of the greenhouse gas CO_2 from automobiles were placed at 16%, and for other European countries the levels were estimated as high as 21%. The European Commission has proposed a 40% reduction in this pollutant by 2005 [6]. But as the rate of vehicle production continues to grow, these technological advances will be outweighed. At this juncture the only forseeable strategy for reducing atmospheric pollution from road transport would be to reduce the number of vehicles in use or switch to a high number of low, ultra-low and zero emissions vehicles, as outlined by the Californian directive in the previous section.

The EC currently enforces a directive that all new cars sold within Europe must be equipped with a three way catalyst. The "Stage 3" proposals, as discussed by Hadded et al. [7], projects the requirement of ultra-low-emissions vehicles (ULEV) to meet the proposed emissions levels that are presented in table 1.1 and vehicle manufacturers are working hard to bring these vehicles to the market place.

Directive and Year of Intr.	Fuel Type	Pollutant	
		CO (g/km)	HC + NO (g/km)
91/441/EEC	Gasoline	2.72	0.97
	Diesel	2.72	0.97
EC Stage 2 1995/96	Gasoline	2.2	0.5
	Diesel	1.0	0.7
EC Stage 3 1999/2000	Gasoline	1.5	0.2
	Diesel	0.5	0.2-0.5

Table 1.1: European emissions legislation for light duty vehicles.

1.1.2 Pollutants

The two dominating vehicle fuels, currently in use, are petrol and diesel - powering spark-ignition (S.I.) and compression-ignition (C.I.) engines respectively. Both these fuels are in liquid form, comprising a whole variety of complex hydrocarbon combinations from the paraffins, olefins, napthenes and aromatics. They are

derived from the fractional distillation of crude oil where the most volatile hydrocarbons forming petrol (known as gasoline in the USA), are vapourised first and the lesser volatile hydrocarbons form diesel and other heavy fuels [8].

The dominant exhaust emissions from vehicles operating on hydrocarbon fuels consist of carbon monoxide (CO), carbon dioxide (CO_2), oxides of nitrogen (NO_x) and unburned hydrocarbons (HC). Other lesser pollutants include sulphur dioxide, lead compounds and hydrogen chloride. Diesel engines also produce a large quantity of particulate emissions composed of soot and adsorbed hydrocarbon substrate but are not a significant producer of carbon monoxide. For both these fuels, NO_x emissions are of comparative levels although hydrocarbon emissions are slightly higher for petrol engines

Carbon Monoxide

For a fuel to burn, it must have an adequate supply of air to ensure thorough oxidation. The products of complete combustion are carbon dioxide and water, as shown in equation 1.1, where n denotes the number of carbon atoms and m denotes the number of hydrogen atoms,

$$C_nH_m + (\frac{m}{4} + n)O_2 \rightarrow \frac{m}{2}H_2O + nCO_2. \tag{1.1}$$

A deficiency in the amount of free oxygen available to the reaction will produce higher levels of the poisonous gas carbon monoxide (CO). Conversely, the presence of excess oxygen will result in a minimum level of CO pollutant being reached, the level of which is somewhat dependent upon the combustion chamber design facilitating comprehensive combustion. Heywood [9, 10] presents a thorough discussion of CO formation. It is important to note that the air-fuel ratio (A/F ratio) level is a presiding factor over the levels of CO emissions and places great importance for maintaining charge mixture between stoichiometric and lean settings to reduce high levels of CO.

Oxides of Nitrogen

The presence of nitrogen in the atmosphere contributes to an undesirable pollutant by-product from internal combustion engines, that of nitric oxide, NO. At normal combustion temperatures, for open combustion reactions, nitrogen behaves as an inert gas, unreactive to other chemical elements but having a significant effect on the thermodynamic characteristics by absorbing large amounts of the heat energy generated. Under the extreme temperature and pressure conditions, exerted by the internal combustion process, nitrogen reacts with the disassociated oxygen atoms to form the endothermic molecule NO. Nitrogen oxide is much more stable at high temperatures and is the main oxide of nitrogen product formed in the combustion chamber. The Zeldovich chain, shown by the sequence of equations 1.2 - 1.5 [11], describes the process of NO formation, initiated by the high temperatures and pressures of internal combustion.

The duration of combustion is important in determining an equilibrium state of NO concentration. NO forms in the two regions of the high temperature burned gases and the actual flame front of the combustion sphere. The life of the flame is actually very short in the combustion chamber and the majority of NO is produced in the burned gases as the pressures and temperatures continue to increase due to piston rise compression. The formation of NO is a very fast reaction, in comparison to the slow process of fuel burning, and as such the two phenomena can be regarded separately. Bernhardt [12] describes a model for predicting NO formation in S.I. engines based on this assumption and realises that the post-flame gas temperature is the major governing parameter over the predictions. Figure 1.2 displays the regions of NO formation within the combustion chamber and the large volume that the burned hot gases occupy, aiding their development.

The separation of oxygen, O_2, into free oxygen atoms is required to initiate the Zeldovich chain and the first event occurs within the temperature range of

between 2000-5000K [9]. The formation of nitrogen dioxide can establish itself at lower temperatures (300K - 5000K) and largely occurs while the hot exhaust gas resides in the exhaust pipe.

$$O + N_2 \rightarrow NO + N, \tag{1.2}$$

$$N + NO \rightarrow N_2 + O, \tag{1.3}$$

$$O + NO \rightarrow O_2 + N, \tag{1.4}$$

$$N + O_2 \rightarrow NO + O. \tag{1.5}$$

Dry air is composed of 20.9% oxygen, 78.1% nitrogen and 0.9% argon based on mole fractions. The remainder is accounted for by traces of helium, neon, hydrogen and carbon dioxide. In the process of combustion, the argon is treated as nitrogen and the trace elements are neglected giving an approximation of 21% O_2 and 79% N_2. The structure of the combustion reaction shown in equation 1.1 now takes the form of equation 1.6, where the atmospheric oxygen is accompanied by the nitrogen. This is the complete combustion process with no free oxygen or unburned hydrocarbons contributing to the exhaust products and is known as the theoretical combustion reaction.

$$C_nH_m + (\frac{m}{4} + n)(O_2 + 3.76N_2) \rightarrow \frac{m}{2}H_2O + nCO_2 + (\frac{m}{4} + n)3.76N_2. \tag{1.6}$$

The rate of NO formation is highly dependent upon the temperature of the burned gases within the chamber and the balance between the hydrocarbon fuel and oxygen. As with CO formation, it is apparent that NO_x formation is heavily influenced by the A/F ratio entering the combustion chamber. The engine design is also instrumental in determining NO_x levels and can modify the concentrations by as much as 10% [11]. The compression ratio and combustion chamber shape determine the flame speed and length as does engine speed and spark timing.

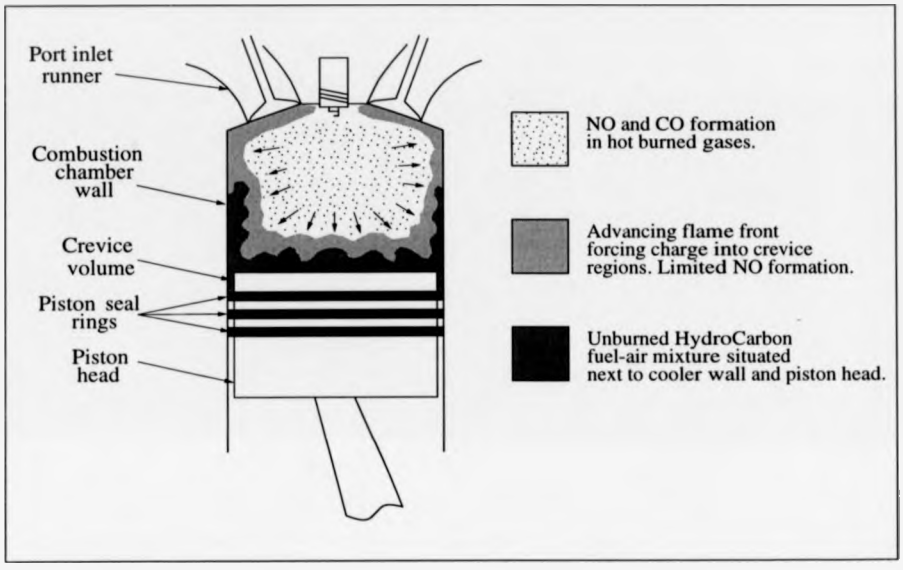

Figure 1.2: Formation zones of CO, NO and HC pollutant as the flame front travels though the combustion chamber.

Unburned Hydrocarbons (HC)

A large constituent of combustion exhaust gases is the unburned hydrocarbons (HC's). Maximum levels of HC emissions are seen at fuel settings just rich of stoichiometry and at extremely lean fuel settings, with a minimum level being observed at just lean of stoichiometry. The proportions of exhaust pollutant formation can be seen as a variation of the A/F ratio in figure 1.3.

HC's occur due to incomplete combustion of the fuel-air mixture. In the case of S.I. engines, it may not be possible to ignite extremely *fuel-lean* mixtures if the spark generated does not have sufficient energy. Operation is said to be outside of the flammability limits and total misfire will occur. When the spark does ignite the fuel, it may be the case that the flame front does not have adequate time to propogate through the entire charge before the engine crankshaft moves the

piston into the expansion stroke reducing the gas temperatures and pressures. Under these conditions, the flame is suppressed and the exhaust stroke emits a high level of HC compounds.

Further reasons for HC's are due to the crevices and quench layers established in the chamber. The term *crevices* denotes the spatial volume between the piston head, piston rings and cylinder walls, and other volumes (as seen in figure 1.2), where the flame front may encounter difficulties igniting the fuel. The combination of a narrow crevice entrance and the cool temperature of the fuel as it is resides against a cooler surface, promotes a high inability of the flame to actually burn residing fuel. The result is that a significant proportion of hydrocarbon compounds are scraped off the cylinder wall and ejected during the exhaust stroke.

Quenching is the process whereby the advancing hot flame front approaches the as yet unburned fuel situated at the cylinder walls and piston head. The heat transfer from the flame front through the unburned fuel to the cooler surfaces raises the temperature of the fuel but does not ignite it. The effect is a quenching of the flame front by thermodynamic equilibrium before it can burn the entire charge, leaving a chemically transformed HC compound mixture at the cylinder walls. Again these are ejected during the exhaust stroke and the larger the surface-to-volume ratio the higher the levels of HC exhaust discharge.

The underlying influential factor on the levels of hydrocarbon emissions is, like those of CO and NO_x, the ratio of air and fuel entering the combustion chamber. Figure 1.3 displays the characteristics of all three pollutants with the variation in A/F ratio, the λ value. This figure is well known as the characteristic emissions trends from 'spark ignition' engines. This figure can be directly compared to figure 3.5, which displays the equivalent emissions for actual natural gas operation.

The value λ is defined as the ratio of the actual A/F ratio to the theoretical (stoichiometric) A/F ratio:

$$\lambda = \frac{(AFR)_{actual}}{(AFR)_{stoich}}. \tag{1.7}$$

For petrol, the stoichiometric AFR value is placed at 14.7. If the actual AFR value is greater than this value, then λ shall be greater than 1 and the mixture is fuel *lean* whereas if the actual AFR is less than stoichiometric, the mixture is fuel *rich* and λ shall be less than 1.

$$\lambda > 1 \rightarrow \text{Lean} \quad , \quad \lambda < 1 \rightarrow \text{Rich}.$$

This is a very useful method of determining the composition of a charge mixture entering an engine and allows for a comparison of engine performance and behaviour characteristics over a given range of λ.

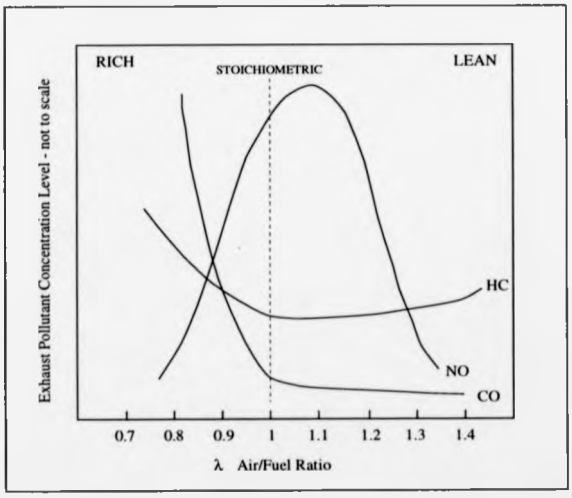

Figure 1.3: Characteristic exhaust emission pollutants from spark ignition engines dependent upon λ A/F ratio value.

Particulates

Compression ignition engines, more commonly known as *Diesel* engines, suffer from a severe problem of particulate emissions. These pollutants are clusters of carbon atoms which are relatively large in size (approximately 30 nm) arising from incomplete combustion and traces of lubricating oil. As the temperature of these clusters cools below 500°C, the adsorption of heavy hydrocarbon compounds (such as oxygenated, unburned and polynuclear aromatic hydrocarbons) increases the size and weight of the particulates [9]. Particulate emissions present major problems in cities and municipal areas where their removal is hampered by their density and high quantity production from buses and trucks. They are noticeable for their "blackening" effects on buildings and can cause breathing difficulties under badly aerated conditions. Much concern arises over these pollutants being carcinogenic in nature, increasing the risk of respiratory diseases.

1.2 Exhaust Emission Reduction Strategies

The aim of this section is to present some of the common methods that are employed in combating high levels of exhaust pollutants and to express the variation in engine designs and mechanical techniques that are currently used on production vehicles.

Many methods exist for reducing the level of exhaust emissions. Principally, these strategies may be catergorised as to their application area on the engine and fall into three divisions:

- intake (pre-combustion),
- in-cylinder (combustion),
- exhaust (post-combustion).

1.2.1 Intake Area and Pre-combustion

The action of air intake is of far greater importance for S.I. engines than it is for the C.I. engine. This is because the fuel in an S.I. engine is introduced into the air stream to allow adequate time to enable charge mixing and fuel evaporation before entering the combustion chamber. The purpose of the intake manifold is to feed the individual cylinders as well as promoting an homogeneous mixture. Whereas in a C.I. engine, the fuel is injected directly into the combustion chamber requiring the action of the manifold to simply feed air to the cylinders and have no concern with the fuel behaviour. For this reason, this section is intended to demonstrate the emphasis placed on intake system designs for S.I. engines.

Fuel Administration

The air flow rate entering the intake manifold is regulated by the driver's demand on the throttle plate. The amount of fuel that is metered to the air flow is carried out either by a fuel carburettor or by a fuel injection system. Carburettors have been used for many years and have evolved far from the basic venturi principle in order to meet the demand of increased metering precision. As emissions legislation grows tighter, carburettors have become largely superseded in this task by the fuel injector. These systems have much greater control in administering the desired amount of fuel and have the advantage of placing the fuel at precise locations. Both these systems, however, must be able to provide a thorough mixing of the air and fuel to promote adequate homogeneity once inside the combustion chamber. The carburettor is placed some distance upstream of the inlet ports and relies on the manifold volume to allow charge mixing - and fuel vaporisation in the case of liquid fuels.

The configuration of fuel injector systems allows for a variability in fuel placement and two notable designs are *throttle body injection* (TBI) and *inlet port* in-

jection. The throttle body injection system simply replaces the carburettor with one or two fuel injectors at the same location upstream of the throttle valve. A small reduction in emissions levels is seen with this system but, more importantly, tighter control on the amount of fuel injected has aided in the increase of vehicle fuel economy, especially during *overrun* conditions where the fuel is cutoff during vehicle deceleration [13]. Mixing is enhanced by the use of throttle body injectors as the fuel emanates as a fine spray over a wide radial area and the fuel spray droplets have a large surface-to-volume ratio, aiding in their vaporisation.

Inlet port fuel injection systems require a fuel injector to be placed in each port runner leading to the individual cylinders. Fuel is sprayed onto the backs of the inlet valves and each injector is actuated once every 2 crankshaft revolutions [13]. Improvements in thermal efficiency are achievable with this approach due to the removal of cylinder-to-cylinder variations and the resultant increase in volumetric efficiency leads to uprated power and torque outputs.

In general, the use of electronic fuel injectors has helped reduce the levels of all types of exhaust pollutants from vehicles since their introduction in the early 1960's and has greatly improved fuel economy. With the increased complexity of fuel injectors, over that of mechanical carburettors, came the need for a more comprehensive approach to controlling these systems and the development of the electronic control units (ECU) became the cornerstone for further improvements to fuel management (see section 1.4).

Exhaust Gas Recirculation

The recirculation of exhaust gases (EGR) is a method well known for reducing NO_x emissions in both S.I. and C.I. engines [14, 15]. A proportion of the exhaust gas is transported back to the intake system to mix with the fresh air-fuel charge. The effect is to dilute the mass of unburned gas mixture with the high content of

CO_2 and H_2O in the exhaust gas. The high specific heat values of these two exhaust constituents reduce the peak temperature reached after combustion thereby reducing the level of NO_x formation. Unfortunately, the level of other emissions tends to increase, limiting the fraction of EGR to a practical maximum of around 5 - 10% [16]. Maintaining combustion stability can also be a problem at high fraction EGR's, due to reduced burn rates, and maximum achievable fractions will depend on combustion chamber design, speed and load. Another side effect of EGR is increased wear on valve train mechanics. Kano et al [17] discuss the nature of higher levels of sulphuric acid that have accelerated this condition since the introduction of the Japanese 10 mode emissions regulations in 1986.

Many light-duty, and the vast majority of heavy goods vehicles, use C.I. engines. Because NO_x emissions are a particular problem for these engines, EGR techniques are commonly employed in this sector. EGR rates are typically set according to the expected engine behaviour without considering the actual composition of the exhaust gases. Strict control of EGR rates (%EGR) is necessary as high levels of %EGR leads to high levels of HC's, CO and soot emissions. Limitations on %EGR are set to eliminate this consequence. Recent work by Amstutz and Del Re has shown the potential for controlling EGR in passenger cars using the already-popular exhaust gas oxygen (EGO) sensor as an indicator of the combustion state [18].

Intake Manifold Design

The action of the intake manifold is to ensure thorough mixing of the air and fuel and distribute the subsequent charge to the individual combustion chambers. The structure of the manifold takes the form of a plenum, into which the incoming air enters, and a series of runners branching off, through which the air is delivered to the chambers. Manifold design criteria rest largely on the type of fuel system

being used and may differ considerably when implementing port fuel injection or a carburettor. For the latter systems, the fuel is introduced upstream of the throttle plate and is carried in the air throughout the entire manifold until reaching the chambers. It is important that the manifold has a low flow resistance ensuring a high volumetric efficiency and equal distribution of the charge to each cylinder to reduce cylinder-to-cylinder variations.

To aid mixing homogeneity, and reduce the effects of transport delay, heating of the manifold can be used to increase the rate of fuel vapourisation, especially during cold engine operation (particularly at start-up) when large fractions of the fuel impinge on the side walls condensing to form substantial films of liquid fuel. Due to the nature of fuel film development, extra fuel is introduced during cold operation, known as choking, to ensure adequate driving performance of the vehicle by prevention of misfire.

Port fuel injection and diesel systems place less demands on the design of the inlet manifold. As the fuel is not carried through its entire volume, its role is one of managing the air only, and in some cases EGR, and manifold heating need not be used.

Swirl

To improve air-fuel mixing inside the combustion chamber, helical manifold port areas can be designed to promote the action of *swirl*. The port entry runner sets the air rotating about the valve axis before entering the chamber. As the air enters the chamber it has an angular momentum which continues to force the charge to swirl around inside the chamber speeding the mixing process. The air velocity moves swiftly downwards and sideways in a circular motion within the cylinder. An excellent discussion of swirl phenomena is given by Arcoumanis and Whitelaw [19] with details of further engine flow mechanics including valve influences.

Swirl is mainly used in C.I. engines where mixing occurs in the chamber with the directly injected fuel. Because of the finite amount of time available for mixing, the desirable effect of swirl is an important method of mixing optimisation for these engines. For S.I. engines, the effect is to speed up the combustion process thereby inciting complete combustion and reduction of HC exhausts [20].

1.2.2 In-cylinder

Research efforts aimed at reducing emissions by consideration of the combustion process itself have produced a variety of imaginative techniques for both S.I. and C.I. engines. The majority of these imaginative strategies have remained in the laboratories where they were born, but some attempt is made here to introduce the more common methods used in production vehicles.

Chamber and Piston Head Design

The effect of swirl, as discussed in section 1.2.1, is used for continued mixing of fuel and air to achieve optimal homogeneity. This action can be prolonged once inside the chamber. By consideration of the piston head and chamber roof geometry, turbulence can be enhanced to increase the velocity of motion and thereby increase flame velocity. HC emissions are reduced through the combustion of higher fractions of the charge.

Chapman et. al. [21] review a series of combustion chamber proposals that contrast in their geometry and effects on charge action. A "pent roof" 4-valve design produced a reduction in all three emissions and exceptionally good operation under lean-burn conditions where charge mixing is of prime concern. This design has since been adopted by Rover and is incorporated in their current production of K-series engines [21].

A family of chamber designs that act to draw the charge into two distinctly

different mixture strengths are known as *stratified charge* engines. A fuel rich mixture is placed close to the spark plug to ensure ignition and the flame front spreads rapidly through the leaner mixture that is distributed throughout the remaining chamber volume. There are many methods of achieving stratification but essentially they all rely on either of two principles - open chamber or pre-chamber.

Open Chamber Stratification

Open chambers generally make use of a piston head that has a sunken volume called a bowl - which itself generates large amounts of swirl. The fuel is injected directly into the chamber close to the spark plug location late into the compression stroke. The projected flame jet that arises from ignition spreads violently through the remaining charge as fuel injection continues. The attribute of this active flame front aids in the combustion of increased fractions of the fuel quantity thus reducing the necessity for an overall homogenous charge mixture. A large proportion of the combustion process is completed during the expansion stroke due to the ability to delay the spark timing by late introduction of the fuel into the compression stroke. Under all engine operating conditions, the total quantity of fuel injected is lean of stoichiometry and the overall mixture ratio within the chamber is lean [22].

The benefits of lean burn operation on emissions is shown in figure 1.3, but careful chamber design is required to ensure ignition when operation is close to the misfire limits.

Pre-Chamber Stratification

The second type of stratification is much more costly in terms of hardware production and requires the physical division of the chamber into two combustion areas,

the pre and main combustion volumes, which are connected by a narrow opening. The spark plug is located in the pre-chamber which constitutes about 5-15% of the total volume [22]. During the induction stroke, a small fuel-rich quantity of charge is admitted into the pre-chamber via a separate inlet valve whilst the main chamber is filled with an extremely lean charge. The spark plug easily ignites the pre-chamber charge and a high energy flame jet is projected through the narrow orifice igniting the lean main chamber charge during the compression stroke. One notable production engine using lean burn stratified charge technology is that of the Honda Civic CVCC engine [16, 23]. The effect of overall lean mixtures (19.5:1 for petrol) reduces both CO and HC's emissions and lower peak temperatures significantly inhibit NO_x emissions.

Lean-Burn

Lean-burn operation refers to running the engine with more air than is necessary. This is said to be lean of stoichiometry ($\lambda > 1$ in equation 1.7). A reduction in all exhaust pollutants is achieved with reduced fuel consumption and with reference to figure 1.3, NO_x is seen to drop by significant amounts at values of λ=1.3 and above. Problems can arise if the lean-burn limit is exceeded for a particular combination of fuel type, engine speed and chamber design. Ensuing misfire will cause the entire ejection of the charge during the exhaust stroke, reducing fuel economy and efficiency, increasing HC emissions and impairing the smooth operation of the engine.

To ensure misfire does not occur, the timing of the spark has to be brought forward - in terms of degrees of crank angle before top dead centre (BTDC) - to enable ignition of the charge and allow sufficient burn time for flame travel. A study by Andrews and Salih [24] showed that an advance in spark timing from 6° to 12° BTDC was able to reduce the three main pollutants for a fuel mixture

of 30% ethanol gasoline. Combustion stability can be improved by increasing the energy of the ignition system and establishing the optimum fuel injection timing according to a swirl ratio [25] such that the fuel rich mixture is positioned at the spark location at the event of sparking.

Swirl techniques must be used on lean burn engines to increase the velocity charge turbulence. Combustion chamber shapes, with centred spark positioning, are effective in reducing flame propogation distance and it has been shown, by Sakurai et. al. [26], that lean-burn technology requires the use of carefully designed combustion chambers to reduce emissions. Some combustion systems, such as that reported in [27], attempt to control burnrate by spatially varying A/F ratio over the speed and load range.

Lean-burn technology has also proved to reduce engine knock for a variety of hydrocarbon fuels, without pushing the A/F ratio's too close to their respective misfire limits. A study by Ronney et al. [28] determined that engine knock is largely dependent on fuel type. The term knock is used to explain an undesirable tapping sound that arises due to autoignition of the fuel before the flame front actually reaches it. The cause and effects of engine knock are not to be detailed here but further reading may be obtained from [29].

1.2.3 Exhaust Aftertreatment - Catalytic Conversion

The dominant method of reducing exhaust emissions directly from the exhaust gas is by the use of a 3-way catalytic converter (3-WCC). The device is a canister volume placed in the exhaust pipe. An aluminium support frame, usually of a honeycomb structure, sits inside the canister to form a thermally stable base providing a large surface area upon which a layer of active material is deposited. Typically a platinum/rhodium (Pt/Rh) combination of noble materials with a ratio of 11:1 is favoured over base metals due to their higher resistance to poisoning [30] . Poi-

soning occurs through prolonged exposure to elements that either physically block the activation cells or chemically interact with the active layer [9].

As the hot exhaust gases are forced through the converter, the catalyst oxidises the carbon monoxide and hydrocarbon gases to form carbon dioxide and water, simultaneously fragmenting the nitrogen oxides to inert nitrogen and free oxygen. Hence the name *3-way catalytic converter*, by its action on the three main exhaust emission pollutants.

Their use as a viable method of reduction became apparent in the mid 1970's and much research was undertaken to characterise their performance. Optimum efficiency is realised when the A/F ratio is set at the stoichiometric value for the fuel in use. Figure 1.4 displays the catalyst conversion efficiency of all three pollutants as a variation in A/F ratio [31]. HC and CO are most effectively oxidised at lean mixture settings where there is excess oxygen but NO_x removal is very poor. Conversely, when the mixture is fuel rich oxidation of HC and CO is virtually eliminated but NO_x removal is abundant.

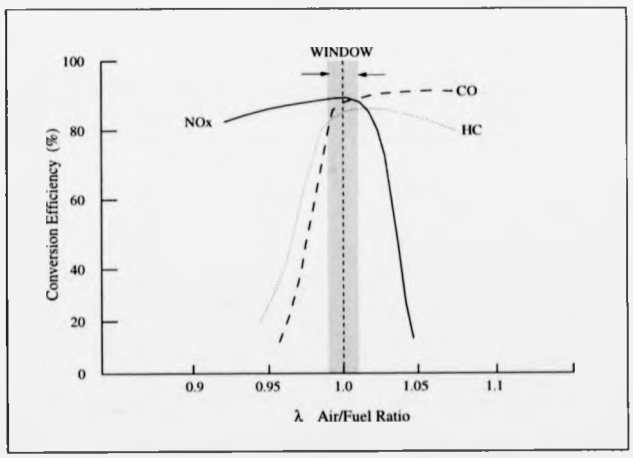

Figure 1.4: 3-way catalytic converter, exhaust pollutant conversion efficiency.

A narrow "window" of optimum conversion efficiency exists around the stoichiometry point of approximately ±0.3 A/F ratio. Within this operating region, optimum conversion of around 80-90% of all three pollutants is achieved. It is found that, if the A/F ratio is modulated within this window, the averaging effects of the catalyst can be exploited as the gases flow through its volume. Falk and Mooney [30] discovered that as the amplitude of the modulation increased outside these limits, the gradients of all three slopes decrease due to the large swings between rich and lean, ultimately reducing the overall efficiency rating. They conclude that if the modulation amplitude is increased to the window limits of ±0.3 A/F ratio about stoichiometry, optimum exhaust pollutant reduction is achieved.

An increase in the frequency of the modulation raises the amount of all three pollutants converted and it is found that frequencies of approximately 1.5 Hz produce significant improvements in operation [30].

The temperature of the catalyst is significant in its effectiveness. The catalyst must be heated to approximately 550K [10] before substantial reduction is achieved and is relied upon by direct contact with the exhaust gases. From a cold start, it is estimated that 90% [32] of total hydrocarbon emissions result due to a combination of the cold operation of the catalyst (until it reaches its "light-off" temperature) and the enriched fueling strategy (choking) to overcome fuel film development, as mentioned in section 1.2.1. To combat cold-start effects, electrically heated catalysts are being developed to reduce the time required to reach the light-off temperature [32].

The Zirconia Sensor

It is obvious then, that for correct use of the 3-way catalyst, the A/F ratio must be strictly controlled within the defined limits. The development of the zirconia

sensor has been instrumental in performing this task and has become the standard AFR sensor for use on production vehicles employing a 3-WCC.

The sensor is small and compact in size (about the size of a standard spark plug), located in the exhaust pipe just upstream of the catalytic converter. The device is constructed from a gas-tight sintered zirconia ($ZrO_2 - Y_2O_3$) tube with both sides coated with porous platinum which form the electrodes [33]. One electrode is in contact with the hot exhaust gases whilst the other is exposed to the reference atmospheric air. A penetrable metal jacket surrounds the inner electrode to protect the device from poisoning elements such as lead, sulphur and phosphorus. Figure 1.5 portrays a typical zirconia sensor used on commercial vehicles [34].

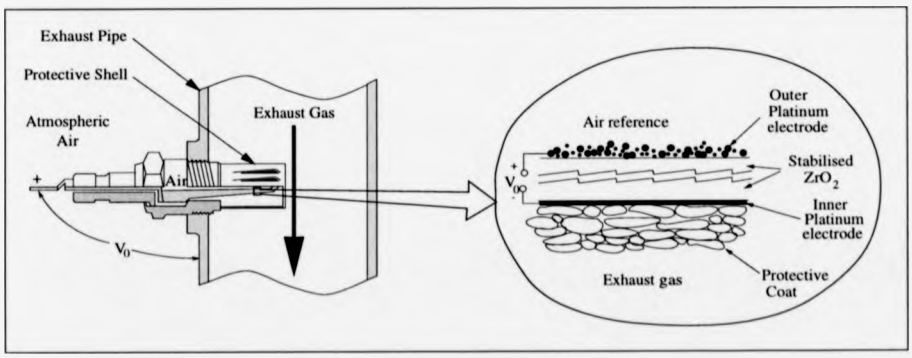

Figure 1.5: λ-Zirconia exhaust gas oxygen sensor.

A partial pressure, between the exhaust and atmospheric oxygen, is established and a change in the output voltage of the inner electrode, with respect to the outer reference electrode, results from an imbalance of the two oxygen sources. The thermodynamic Nernst equation (which can be found in [33]) describes the output voltage as a function of partial pressure, temperature and resistance.

The characteristic response of the sensor is highly non-linear, producing about

100mV for lean mixtures and approximately 850-900mV for rich mixtures. The device is essentially a 'switch' between these two voltages about the stoichiometric point. Therefore, the zirconia sensor is considered to be well suited for use as a feedback sensor in the control of engine A/F ratio, as it quickly informs the ECU of the condition of the exhaust A/F ratio, i.e. rich or lean.

Like the catalytic converter, the zirconia sensor is sensitive to temperature. At approximately 600K the sensor becomes "activated" and, for increasing temperature, the response changes marginally - giving a slightly higher output voltage for rich mixtures as the temperature increases [35]. Improvements in the control of A/F ratio for exhaust emission reduction can again be obtained through heating the sensor independently of the exhaust gases. This reduces the time for which the sensor, and hence control unit, remains idle after the engine has started from cold. Wiedenmann et al. [36] provide a comprehensive report on a study of electrically heated sensors, based upon the common unheated zirconia sensor, with conclusive proof that "warm-up time" can be significantly reduced with the added advantage of increased positioning flexibility.

1.2.4 Alternative Fuels

The vast majority of vehicles in service in the U.K. and abroad operate on either petrol or diesel and, as explained in section 1.1.2, these are derived from crude oil. But in recent decades, growing research has demonstrated that many other forms of hydrocarbon fuels can be used to power internal combustion engines.

These fuels exhibit environmentally attractive qualities by way of substantial reductions in exhaust pollutants. The dependency of a society's transportation sector upon any one source is also eliminated by using alternative fuels. This is viewed as an increasingly important issue as the depletion of world petroleum stocks accelerates. The matter of crude oil costs has also been highlighted, during

times of war, when many nations are dependent upon foreign oil production for power and transportation. During such instances, massive price increases in world stocks ensue, leading to what is termed as a "fuel crisis".

There are four predominant fuels that show potential to compete realistically for a stake in the transport industry. These are :

- Ethanol,
- Methanol,
- Compressed natural gas (CNG),
- Liquefied petroleum gas (LPG),

and shall be referred to as the *alternative fuels.*

Electrically powered vehicles also show promise as an alternative method of transport but their development and widespread introduction rests largely on improved battery technology and reduced costs. However, long term use of electric vehicles may go some way to offsetting their initial cost disadvantage as the low maintenance expense incurred is reflected in their reduced complexity [37].

Ethanol

Ethanol fuel is derived from fermentation of bio-mass sources such as corn, sugarcane and grains. It is a high-octane alcohol and is considered to produce no net increase in atmospheric CO_2, since it is derived from non-fossil renewable material which make use of the exhaust CO_2 within the carbon-cycle upon re-implantment [38]. Ethanol feedstocks have the potential to reduce greenhouse gases from automotive emissions and have a marked reduction in CO, NO_x and HC. However, cold start problems are more acute due to high vaporisation temperatures and are likely to hinder the spread of ethanol vehicles globally.

Methanol

The other alcohol-based alternative fuel is methanol. Methanol can be derived from wood and coal but its principle origin is from natural gas. In the United States, 43% of all methanol produced is actually used for transport purposes [38]. In 1983, the state of California enrolled 500 methanol vehicles for government use demonstrating the confidence and expectations placed in alternative fuels [39]. Like ethanol, methanol has high knock resistance resulting from a high octane rating, allowing greater compression ratios to capitalise on fuel efficiency.

CNG and LPG

Natural gas is found to be contiguous with underground oil reserves, either directly in the upper regions of the oil well or in porous rock strata some distance away. Natural gas composition is dependent upon the region of origin but in the main contains 85-99% methane (CH_4). The remaining portion is typically made up of equal increments of ethane, butane, propane and trace elements of nitrogen, helium and carbon dioxide [40]. Because minimal refining is required, the final composition is largely untouched.

Natural gas can be cryogenically refrigerated to produce liquefied petroleum gas (LPG). Liquefaction takes place just below the boiling point of methane (111.48K) necessitating the use of vacuum storage vessels for refuelling stations and on-board vehicle storage.

Octane ratings are much higher than petrol - typically 26% higher [41] - giving improved knock resistance and cold start operation. This permits the use of natural gas in current gasoline engines without undermining its performance in terms of anti-knock characteristics. Both these fuels have been proved to reduce automotive emissions of HC, CO, and CO_2 by substantial amounts. The levels of NO_x have, in some cases [39], shown to be equivalent to petrol and diesel whereas

other reports [42] have shown as much as 80% reductions. Virtual elimination of particulate emissions over C.I. engines establish natural gas as the most popular and viable alternative fuel for commercial fleet and private vehicles alike. LPG is gaining in popularity, attributable in part to its higher energy density than natural gas.

The four alternative fuels presented here all display excellent potential for reduction of the three main exhaust pollutants with virtual elimination of NO_x. Table 1.2 provides a summary of statistics from a catalogue of recent publications [37, 38, 39, 41, 43, 44] presenting estimated achievable reductions through dedicated use of these fuels.

Alternative Fuel Type	Estimated Reduction Of Pollutant Over Petrol And Diesel Vehicles					Fuel Economy Improvement %
	HC %	CO %	CO_2 %	NO_x %	Particulate %	
Ethanol	10	15	100 (NET)	20	100	5
Methanol	20	20	10	20	100	15
CNG	40	50	30	0	100	5 - 30
LPG	40	50	30	0	100	5 - 30

Table 1.2: Estimated pollutant reductions and fuel economy improvements of alternative fuels over current petrol and diesel vehicles.

Emissions reduction is the overwhelming motivator for alternative fuels and natural gas is deemed to be the most cost effective approach.

1.3 Natural Gas Vehicles

Natural gas vehicles (NGV's) are becoming a popular choice of fleet vehicle providing environmental and cost benefits. Globally, NGV's have been in use for many years, spanning from Russia which has approximately 350,000 NGV's, Italy with 260,000, USA with 30,000 to Canada with 25,000 - with world total NGV's esti-

mated at 800,000 [45]. But in Britain, attitudes towards NGV has been apathetic and the current in-service figure stands at only 350 [46]. With the total number of vehicles in service in Britain standing at 25.5 million in September 1995, the number of NGV's amounts to only 0.0013% of the total British vehicle population. This compares to America, where approximately 0.02% of all on-road vehicles are NGV's - since the figure for American on-road vehicles stood at 151,677,900 in December 1993 [47].

The vast majority of NGV's are bi-fuel conversions where a standardised conversion kit enables the vehicle to operate on either natural gas or petrol. Due to the current lack of an adequate refuelling infrastructure, bi-fuel operation is likely to be dominant over dedicated use for the near future. But NGV's are attractive for fleet vehicles where refuelling can take place at a central depot. However, with many homes having gas supply installations in place, long term prospects for the personal vehicle market with the possibility of home refuelling are encouraging.

Natural gas has a 75% lower volumetric energy content than petrol and must be stored under high pressures, typically 3000psi [48], to achieve acceptable storage capacities. Consequently, the cylindrical storage tanks can be quite heavy but prove to be safer than liquid fuel tanks. Safety regulations require the vessels to withstand pressure levels up to 2.5 times that of service pressures and in the event of fuel leakage, natural gas is rapidly dispersed reducing the risk of accidental ignition, making it somewhat safer than liquid fuels.

NGV's do not suffer from cold start conditions unlike liquid fuels (as mentioned in section 1.2.1) since the fuel is already in a gaseous state and does not condense on the manifold surfaces at ambient temperatures. As a result, fuel enrichment is not necessary, cold operation emissions are reduced and, coupled with the fact the 80% of all car journeys are less than ten miles in duration, NGV environmental benefits are amplified.

Power output from bi-fuel NGV's is approximated to be 10% lower than when operated on petrol. This is due to the lower density of the fuel supplying approximately 10% less energy per litre of combustion chamber volume. Dedicated NGV's however, can take full advantage of the higher compression ratios attainable, offsetting this power reduction by vastly improved efficiency [49]. NGV operation is much smoother and quieter running than diesel engines and is considered more attractive for city applications where light duty trucks and public buses are high in numbers.

1.4 Engine Control

The requirement for vehicles of all types to operate safely, optimise on fuel economy and drastically reduce emissions has given great emphasis to the importance of control. Application areas that benefit from control implementation are varied and, in recent years, a growth in this field has lead to significant levels of electronic control hardware and vehicle complexity. This section is intended to present the applications and benefits of control implementation on production vehicles, and to establish the necessity for engine management through strict A/F ratio control.

In the last decade, the introduction of numerous safety features has been built upon the increased ability of control systems and, more directly, microcomputer technology. The most notable of controlled vehicle conditions is the anti-lock braking system (ABS) which has become increasingly common in production vehicles. ABS is capable of eliminating wheel lock during braking by constantly monitoring all four wheels independently and reducing brake pressure if the condition of rapid wheel deceleration is encountered. Other controlled areas that have improved driveability and general safety include suspension control, traction control and automatic transmission control, but these tend to be found in production

vehicles of higher performance and specification. In general, the addition of these systems has improved vehicle capabilities whilst giving the driver increased traffic awareness.

Increased driver and passenger comfort has come about through cabin climate control and cruise control which make use of conventional control techniques to maintain desired in-vehicle temperatures and vehicle speeds, respectively. Such systems have been in use for many years and are appreciated most during long journeys reducing the amount of driver work load and providing relief.

The most widespread application of control on vehicles is the engine control unit (ECU). Current ECU's are complex electronic devices, born out of the necessity to take account of many engine conditions in order to maintain a host of operating requirements. The first significant engine improvement from electronic control was through programmed spark ignition systems [50]. By precise timing of the spark occurrence within the engine cycle, misfires were reduced and a more complete combustion of the fuel increased power output and fuel economy. Early spark control systems made use of engine maps that relate the optimum choice of ignition timing to a set of measurable engine variables. The process of 'table lookup' is then used to obtain the required timing for the measured conditions [13]. These systems were inherently *open-loop* in design and could not compensate for changes in engine performance due to wear, ageing effects and significant changes in atmospheric conditions.

In a similar fashion to the open-loop lookup-table procedure for spark control, %-EGR is metered to the operating conditions of the engine by monitoring a few measurable states, such as engine speed and fuel flow. The EGR valve is actuated to allow the correct amount of exhaust gas to enter the intake system as read from an experimentally determined engine map [18]. However, performance maps that are derived by steady-state test procedures, cannot be expected to perform

perfectly well under typical dynamic operating conditions.

The introduction of the "automatic choke" improved cold start operation of carburettor systems by controlling mixture strength. An actuator placed on the choke valve is used to restrict the air flow rate. Dependent upon temperature and speed conditions, the choke valve is typically reduced whilst the engine is running cold to provide an enriched mixture compensating for fuel film development. This same technique is used when the vehicle is undergoing rapid acceleration and the enriched charge provides reliable dynamic performance. These early control systems tended to be relatively simple and did not utilise electronic control to any great extent to reduce exhaust emissions but aided in the driveability of the vehicle upon cold starting.

With the advent of *closed-loop control*, carburettors became more electronically advanced. By the use of a controlled throttle by-pass valve the engine idle speed could at last be maintained as close to a set value as possible [13]. When the vehicle is stationary there are no large demands for mechanical power but peripheral demands, such as air conditioning, power steering and other electrical loads, need to be supported. Without closed loop control, when these electrical drains are switched on, the engine speed would vary greatly becoming unstable and even stalling. The control procedure is one of continually comparing the actual engine speed to the desired value. The resulting difference provides an error signal that is fed to the controller and acted upon to actuate the by-pass valve and hence regulate the charge flow rate and subsequent idle speed. The desired value is closely maintained, enabling a low value to be chosen improving engine fuel economy.

Although controlled carburettor systems much improved the driving quality of a vehicle, the greatest step in precise engine management came about with electronic fuel injection (EFI). Stimulated by the fuel crisis in the 1970's, fuel

economy become a highly important issue in the performance of automotive vehicles and the need for EFI systems to affect the necessary reduction in fuel usage encouraged the development and application of microprocessor engine control. The 1970's saw a continued growth in the use of electronic control systems [51] and the benefits have become so apparent that they are becoming standard in the vast majority of production vehicles. EFI systems are even replacing carburettors in vehicles that could be perceived as low performance.

In more recent years, ever-more-stringent exhaust emission legislation has required the continual improvement of electronic fuel control which, in turn, has required more advanced electronic and microprocessor technology. These much improved ECU's are generally known as engine management systems as they control many aspects of engine performance. A primary role of the engine management system is to maintain the engine A/F ratio as accurately as possible to a desired setting - either at stoichiometry or lean burn. These systems are vital for the successful implementation of 3-way catalytic converters discussed in section 1.2.3, as the air-fuel charge mixture needs to be controlled within precise window limits around stoichiometry (see figure 1.4). The closed-loop control of A/F ratio is an extremely arduous task, given the rapid variations in air flow in response to throttle input changes. Fuel film development/evaporation, manifold filling dynamics and sensor lag further complicate the control task. Under static conditions, the control of a desired A/F ratio is relatively simple and could be completed by standard closed-loop techniques. However, driving conditions are rarely in steady state for any length of time (particularly during urban driving) and excursions from the set point are encountered due to the dynamic behaviour of the engine air flows. It is the role of the ECU to rectify these excursions as quickly as possible to maintain strict A/F ratio levels for effective exhaust emission reduction and to minimise catalyst degradation.

Current production ratio control systems use conventional PI control in conjunction with feedback from the zirconia sensor. The control of A/F ratio is the largest influence on emissions levels, as demonstrated in figure 1.3, which is relevant for both petrol and natural gas operation, and constitutes the motivation for much of the work reported in this thesis.

1.5 Engine Modelling

Many different forms of mathematical, and hence computational, models exist to describe the processes of an internal combustion engine .

Extremely complex models have been built which breakdown the 4-stroke process to very fine detail in an attempt to simulate the internal chemical and thermodynamic reactions occuring in the closed chamber environment. These models tend to be concerned mainly with the working fluids, their composition, transport and combustion properties. Such models make use of the conservation laws of both mass and energy, encompassing the rates of fuel and heat transfer by describing the system internal enthalpy. These models are usually referred to as thermodynamic models [9], and can be tailored to suit S.I. or C.I. engines as well as the combustion chamber design.

Another group of models are concerned with the physical flow of the air/fuel mixture into and out of the combustion chamber. These models are known as *intake and exhaust* models. Three underlying frameworks exist on which to base such models [9]:

- Quasi-steady models,
- Filling and emptying models,
- Gas dynamical models.

All three share a commonality found in the concerns of the manifold design - particularly its volume, layout, structure, crevices and any components that will influence the flow. Tabaczynski [52], in 1982, detailed the effects of manifold design upon engine performance. Currently, much effort is being expended on these model types. They tend to be extremely computationally intensive, but as the cost for higher computer power is rapidly coming down, the practicality (with particular reference to timescales) of these *fluid dynamical* models is becoming more realistic.

Many of these models make use of 'computer meshs', which allows a multi-dimensional computation of the flow characteristics in precisely defined locations within the manifold. Gosman [53, 54] presents the discretisation methods used in transforming the differential equations of each mesh 'cell', describing the turbulent flow rate and pressure, into algebraic equations. However, these models still require much computer power and time to run even small simulations.

Another form of model aims to simulate an engine on a much wider, and less microscopic level. These popular models, known as mean value models, do not attempt to simulate the fluid properties at precise locations within the engine volume, but model the 'gross' internal states, such as the pressure and mass flow rate of the fluid, and the external states of engine speed and torque [55, 56].

These dynamic models describe the engine states using non-linear differential equations that operate on time scales slightly longer than an engine event (one full engine revolution). The important aspects of these models is their ability to encompass simulation of the entire engine - from intake to combustion and exhaust - with inclusion of the relevant system time delays. An additional benefit of these models is their compactness and, hence, computational efficiency. This is one of the main reasons for deciding to use this approach to model the natural

gas engine featured in this thesis.

The main purpose of the thesis is two fold: 1) to model the operation of a natural gas engine, and 2) to use the model to investigate possible air/fuel ratio control algorithms. To this end, the entire engine process, not just the air flow (i.e. throttle body and manifold) should be modelled. This is because it is not just the throttle valve which controls air flow, but also the engine speed influences the rate of air intake, eg. during acceleration and deceleration. Hence, consideration must be given to the engine external loads that determine engine speed. This is another strong reason for choosing a mean value model approach.

The controlled input to the model is the natural gas fuel flow rate, the system disturbance is that which causes a disturbance to the air flow (i.e. the throttle valve and the engine speed) and the model output is the air/fuel ratio λ value. Because the natural gas engine being modelled is converted from a conventional petrol engine, the sole difference between them is the fuel administration system. The original petrol engine was of a throttle body injector type, where the petrol was injected just prior to the throttle valve. Upon conversion, the natural gas is injected still at the same location - upstream of the throttle valve. This means that no modification of the down-stream apparatus, i.e. the intake manifold, is required. This is because, for both systems, the air and fuel commence mixing in the throttle body, and continue on their way through the manifold.

The model reflects this via the consideration of the gas administration unit. The delivery pipe connecting the injector unit to the air intake hose, gives rise to a delay in the delivery of gas. This is fully described in more detail in section 2.10. Although this is the sole difference between the petrol and the gas systems, the same inherent control problem remains the same for natural gas as it does for petrol: that of maintaining the operational air/fuel ratio within the bounds of the catalyst air/fuel ratio limits (stoichiometry ± 0.3 air/fuel ratio). This must be

achieved during transient and steady-state operating conditions.

1.6 Aims Of The Thesis

Chapter 1 has provided an introduction to the problems faced by vehicle manufacturers in bringing about necessary pollutant level reductions, with a discussion of the numerous 'mechanical' methods developed to reduce overall exhaust emissions. It has been illustrated that optimal homogeneity and fuel vapourisation are desired to promote thorough combustion, thereby reducing unburned HC levels. Many production engines employ these techniques to enhance charge mixing.

It has been established that the most effective method of reducing emissions is during the post-combustion stage. Specifically, under strictly controlled conditions, the 3-WCC is extremely effective at reducing the three main exhaust pollutants. The high performance of these systems has lead to their widespread usage and hence they are fast becoming standard equipment on many vehicles.

Alternative fuels have also been discussed, and show promise for further pollutant reduction. Research and development in this field is increasing with a good number of vehicles operating daily on 'cleaner' HC-based fuels.

The work reported in this thesis is, therefore, motivated by the three criteria established above and a concatenation of all three. 1) By using natural gas as an alternative fuel, enhanced air/fuel mixing is achieved over that of liquid fuels, since the fuel is already in a gaseous state and manifold wall wetting does not occur. 2) Natural gas has displayed substantial reductions in emissions and current stocks exist to provide sufficient motivation to research into its performance in a passenger vehicle engine. 3) The use of a 3-WCC on the engine to further reduce emissions. This requires the air/natural gas ratio to be controlled closer about the stoichiometric point, in the same manner as petrol vehicles, as demonstrated in figure 3.5.

The aims of the thesis are to construct a non-linear model of a natural gas automotive engine to run in a continuous simulation computer language. The purpose of the model is to simulate engine operation under transient operation covering a wide range of engine conditions that could well be expected under normal driving scenarios. The theory of the dynamic model is fully developed that encompasses both dynamic and static engine behaviour, as well as the natural gas fuelling dynamics. A set of practical engine experiments is necessary to finalise the theory of the engine model, and allow empirical relationships to be characterised.

The model is then to be used to investigate different methods of fuel control with the intention of maintaining A/F ratios close to the stoichiometry point, and within the catalyst window limits. The investigations will take the form of simulations where the engine is subject to varying driving conditions.

The aim of the designed controller is to demonstrate improved A/F ratio control upon that of current production controllers, through a practical approach utilising currently sensed engine states. To this end, the engine model is required to estimate mean states that are used as inputs to the controller.

The controller shall then be subject to investigative procedures aimed at assessing the practical implications of the controller. Such problems as signal noise corruption and injector limitations shall be considered to determine the worthiness of the control algorithm.

The structure of the thesis can be seen in figure 1.6, where the stages of model theory, experiments, model characterisation, control and simulation can be seen to develop in a sequential manner.

The contributions of the thesis are towards the fields of modelling and control, as laid out below

- A natural gas engine is modelled using a mean value approach, with a consideration of the fuel delivery dynamics.

- The manifold A/F ratio computation is made by considering the manifold dynamics, as opposed to an instantaneous ratio of the separate air and fuel flow rates, found in many other modelling approaches.
- An investigation is made into the consequences of microprocessor sampling rates by describing the fuel control algorithm in the discrete environment.
- A control algorithm is designed to reduce A/F ratio drifts attributable to transient engine operation, and is termed Open-loop Transient Compensation Control (OTCC).
- Two steady-state map control approaches have been investigated demonstrating the versatility of the engine model to enable the investigation of various fuel control approaches.

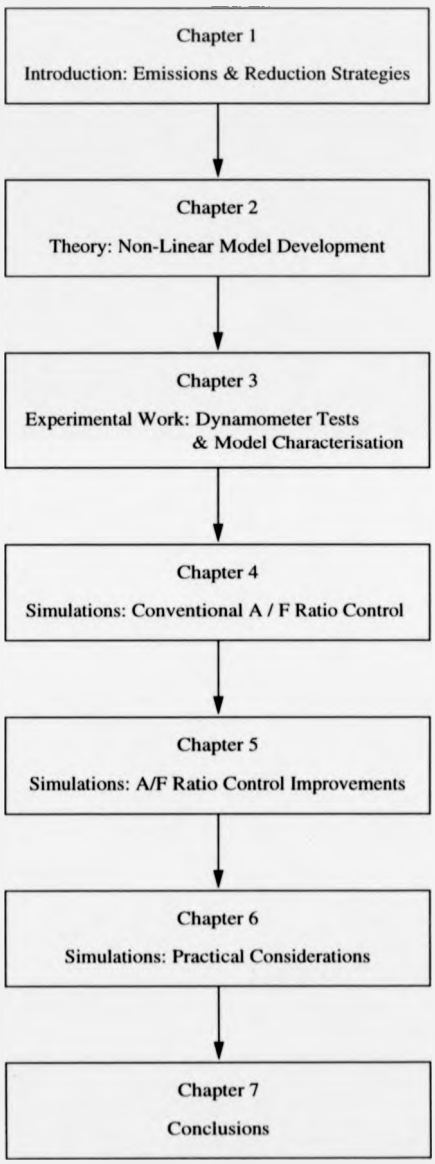

Figure 1.6: Thesis structure.

Chapter 2

Non-Linear Engine Model Development

An internal combustion engine is a highly non-linear system which presents many problems in respect of control. Engine models have become a popular method of aiding controller design and are now becoming essential in their application to allow I.C. engines to achieve stipulated emissions levels.

The engine modelled in this thesis is a 1.4 litre, natural gas operated 4-stroke cycle, I.C. engine. A Gaseous Fuel Injection (G.F.I.) system is fitted to a standard production petrol engine mounted on a test bed configuration running solely on compressed natural gas. In a production vehicle there is the possibility of interchange between petrol and gas operation. Details of the engine and test-bed dynamometer can be found in Appendices A and B.

The nonlinear engine model developed here is based upon a characterisation of the engine subsystems as represented by a set of non-linear differential equations derived from consideration of the engine's physical processes. The model incorporates all relevant delays and lags, that are inherent in 4-stroke cycle engines, which present particular problems to the design of effective control algorithms.

The modelling intention was to be able to predict the mean values of the engine states, under steady-state and transient behaviour, by consideration of the

dynamic behaviour of the spatial volumes and rotational moments of inertia and the characteristics of the natural gas fuelling dynamics. The model facilitates the application of control algorithms for A/F ratio control investigations.

2.1 Engine Submodel Classification

The engine is theoretically divided into a set of submodels that, when "fitted" together, produce the overall, continuous, time-domain engine model. There are essentially 7 submodel classes which depict the characteristics of operation. Figure 2.1 presents the submodel regions in relation to the engine areas. The figure displays one cylinder of a multi-cylinder engine (the engine modelled in the project had four cylinders) and represents a simplified understanding of the compartments. There are four dynamic elements which describe the action of the engine under transient conditions. These are:

- manifold filling and emptying dynamics to determine manifold pressure, air mass quantity and manifold A/F ratio, ②,
- rotational dynamics of the crankshaft and related resistance torques to determine engine speed, ⑤,
- engine transport delays and dynamics associated with the λ-sensor, ⑥,
- dynamical behaviour of the fuel delivery pipe to model fuel delivery delay, ⑦

The remaining submodels are considered on an instantaneous basis and are determined from static test bed experimentation.

2.2 Throttle Body

The first compartment to be determined is the throttle body. This device is an elliptical flat plate (known as the throttle valve) placed in the intake pipe housing,

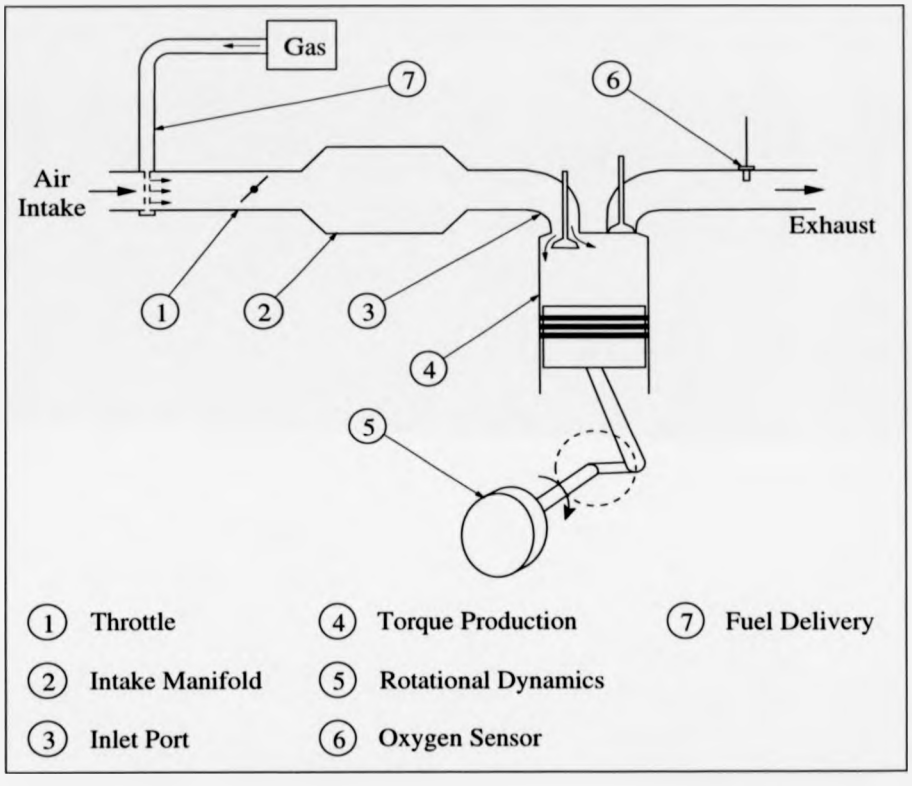

Figure 2.1: Schematic of the I.C. engine with natural gas fuelling.

which rotates on a spindle perpendicularly to the flow of incoming air. The basis of the throttle body model is the assumption that it is an instantaneous device responding rapidly to changes in throttle angle and pressure ratio. The flow is considered to be a steady, compressible flow of ideal air through a choked area. An approximation is made in common with other research efforts [57, 58] in assuming that the air has uniform velocity, temperature and pressure across the flow at the throttle valve. This assumption is valid given that the minimum cross-sectional bore of the intake system occurs at the throttle valve and is measured to be 68mm

in diameter at maximum 90° opening with no appreciable gradients in temperature or velocity. It is also assumed that the flow is adiabatic, resulting in no heat losses to the pipe walls.

A drivers demand on the accelerator pedal controls the amount of rotation of the throttle valve, thereby opening and closing the intake area by varying amounts. The flow rate of air entering the intake manifold is governed by both the angle of the throttle valve and the pressure ratio across the device. The dependency of air flow rate on these two variables is highly non-linear and is described as :

$$\dot{m}_{ai} = f(\theta, Pr_m), \tag{2.1}$$

where $\dot{m}_{ai}$ is the mass flow rate of incoming air, θ is the throttle angle and Pr_m is the pressure ratio. The pressure ratio is defined as the ratio of downstream pressure to the upstream pressure. In the case of an engine intake system, these conditions are readily taken to be the manifold pressure, P_m, and atmospheric pressure, P_a, resulting in

$$Pr_m = \frac{P_m}{P_a}. \tag{2.2}$$

The pressure ratio term is more commonly expressed as an *influence* factor that is exerted on the flow rate. For a given open area, the maximum flow rate that can be achieved is dependent upon this *pressure ratio influence*, Φ_m, which occurs when the velocity of air reaches the ambient sonic velocity (mach no. =1). This condition is known as the *critical flow*, and for any further increase in the pressure ratio above that of the *critical pressure ratio*, P_{crit}, no further increase in mass flow rate can be achieved. The value of P_{crit} is dependent upon the ratio of specific heats, γ_a, and for atmospheric air,

$$\gamma_a = \frac{C_p}{C_v} = 1.4, \tag{2.3}$$

where C_p and C_v are the specific heats at constant pressure and volume, respectively. The critical pressure ratio for air is then defined as

$$Pr_{crit} = \left(\frac{2}{\gamma_a + 1}\right)^{\gamma_a/(\gamma_a - 1)} = 0.528. \tag{2.4}$$

The equation describing the mass flow rate at the throttle, 2.1, can now be written in terms of Φ_m,

$$\dot{m}_{ai} = f_\theta(\theta, \Phi_m). \tag{2.5}$$

The pressure ratio influence function, Φ_m, is dependent upon the value of Pr_m and is described by the equation for a compressible flow [59, 60] :

$$\Phi_m = \begin{cases} \sqrt{\left(\frac{2}{\gamma_a - 1}\right) \cdot \left[(Pr_m)^{\frac{2}{\gamma_a}} - (Pr_m)^{\frac{\gamma_a + 1}{\gamma_a}}\right]} & \text{, for } Pr_m > Pr_{crit} \\ \sqrt{\left(\frac{2}{\gamma_a + 1}\right)^{(\gamma_a + 1)/(\gamma_a - 1)}} & \text{, for } Pr_m \leq Pr_{crit} \end{cases} \tag{2.6}$$

The dependency of air mass flow rate upon the throttle angle is, by some researchers, expressed as function of the throttle open area, A_{th}. Purdy et al. [61] describe the cross-sectional area as a simple *cos* function of the throttle angle with inclusion of the closure angle, θ_c, as:

$$A_{th} = \pi r^2 \left(1 - \frac{\cos\theta}{\cos\theta_c}\right). \tag{2.7}$$

The closure angle is not necessarily at 0°, as one might expect, but for an elliptical throttle plate the area shall be fully closed at some positive inclination. This is to ensure complete sealing of the air passage when the driver releases the accelerator pedal and the engine is required to idle under the control of the bypass valve.

The open area may be seen in figure 2.2, for the Purdy equation, for a throttle radius of 68mm, which is the size used on the gas engine being modelled.

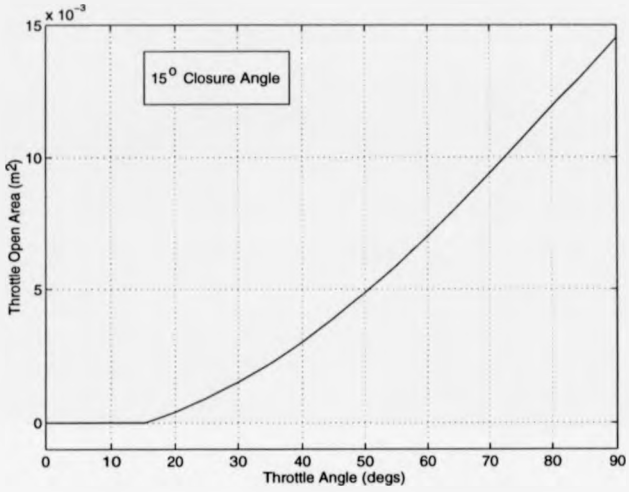

Figure 2.2: Throttle open inlet area, described by the Purdy equation [61], for the throttle used on the natural gas engine.

Other equations to describe the throttle area are given by Harrington and Bolt [62] and Moskwa [57], but which are much more complex in their structure and include the effect of the spindle diameter. It was impossible to validate the estimation of the area from these equations, with that of the true area, and the favoured approach was therefore to use the throttle angle itself in the throttle model, without explicitly defining the area. By using this approach, the dependency of air flow rate upon throttle angle would have to be determined from steady-state engine tests. This method has been used by other researchers, [63, 64], and is viewed by many to be the standard procedure of obtaining the throttling characteristic. The throttle model is thus defined by equations 2.5 and 2.6 where the dependency on θ is determined from steady-state experimental data in the next chapter.

2.3 Intake Manifold

The purpose of the manifold is to serve the engine cylinders with an equal amount of charge mixture and promote the mixing of fuel and air. As such, the manifold is generally regarded as being one of the most important influences in the dynamical behaviour of an engine, and is accountable for the delay in torque production as a response to changes in the throttle angle. Manifold model complexities may vary, but generally the principle of mass conservation and continuity is upheld.

The objective of the manifold model described in this section is to consider the plenum and runners as a single control volume and thereby predict the pressure. The model proposed here is described as a filling-and-emptying model, with the assumption that, at any instant, the pressure and temperature within the manifold are uniform. By assuming the fuel to be of negligible volume at a stoichiometric A/F ratio, the amount of air flowing into the manifold is dictated by the throttle, as described in the previous section. The mass flow rate out of the manifold is dependent upon the engine speed and manifold pressure and shall be discussed in the following section.

The contents of the manifold are regarded as obeying the ideal gas law. By consideration of mass conservation, the manifold mass is obtained from the integration of the difference between the incoming air mass rate, $\dot{m}_{ai}$, and outgoing air mass rate, $\dot{m}_{ao}$, as:

$$\dot{m}_m = \dot{m}_{ai} - \dot{m}_{ao}, \tag{2.8}$$

$$m_m = \int (\dot{m}_{ai} - \dot{m}_{ao})\, dt, \tag{2.9}$$

where m_m is the mass of air within the manifold. This approach is similar to that of Thompson and Duan [65], where a single cylinder engine manifold model is considered as the flow rate in at the throttle and out at the single port runner.

A simplified schematic of the manifold is shown in figure 2.3, where the indi-

vidual port runners guide the air flow out of the manifold to the separate engine cylinders.

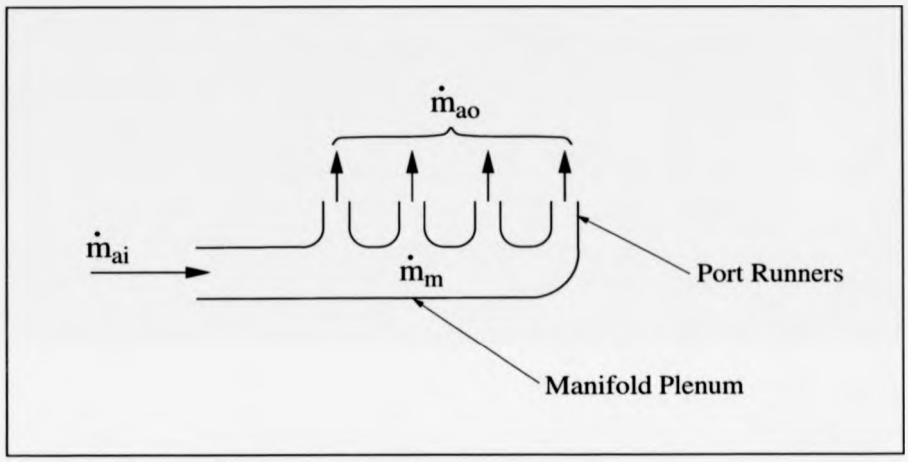

Figure 2.3: Schematic of intake manifold, displaying filling and emptying process.

The equation of state for a unit mass of an ideal gas is given in terms of the temperature (T), pressure (P), and volume (V), as:

$$PV = \frac{RT}{\bar{M}}, \tag{2.10}$$

where R is the universal molar gas constant and $\bar{M}$ is the molar mass of gas. For any mass of gas, m, the equation of state is thus

$$PV = \frac{mRT}{\bar{M}}. \tag{2.11}$$

By rearrangement of equation 2.11 and substitution into the mass conservation equation 2.9, the manifold pressure can be expressed as

$$\frac{P_m V_m \bar{M}}{RT_m} = \int (\dot{m}_{ai} - \dot{m}_{ao})\, dt, \tag{2.12}$$

$$P_m = \frac{RT_m}{V_m \tilde{M}} \int (\dot{m}_{ai} - \dot{m}_{ao})\, dt, \tag{2.13}$$

where subscript m denotes manifold variables.

The manifold volume for the engine being modelled is 2.5 litres and the universal molar gas constant is $R = 8.31441 J mol^{-1} K^{-1}$. Atmospheric air is considered to be 79% N_2 and 21% O_2, as described in section 1.1.2, giving the molar mass of air to be $\tilde{M} = 28.48 kg \cdot kmol^{-1}$ [66]. The temperature inside the manifold is taken to be that of standard temperature 25° (298K). A *manifold constant*, K_m, can therefore be defined as:

$$K_m = \frac{RT_m}{V_m \tilde{M}} = \frac{8.31441(kJ \cdot kmol^{-1} \cdot K^{-1})\ 298(K)}{0.0025(m^3)\ 28.48(kg \cdot kmol^{-1})}, \tag{2.14}$$

$$K_m = 34.799 \times 10^3 (kJ \cdot m^{-3} \cdot kg^{-1}), \tag{2.15}$$

to result in the final manifold pressure model equation as:

$$P_m = K_m \int (\dot{m}_{ai} - \dot{m}_{ao})\, dt. \tag{2.16}$$

Manifold models that are constructed to simulate petrol engine operation, may incorporate the dynamics of wall wetting and fuel film development as discussed in section 1.2.1. The amount of fuel that condenses on the internal surfaces is dependent upon the temperature of both the manifold air and the side-wall surfaces. Port fuel injection systems go some way to minimising the delay caused by wall wetting but still a significant quantity of fuel develops on the runner side walls and the back of the inlet valve.

This phenomenon is regarded as one of the most important influences on transient AFR excursions and its inclusion in manifold models is being adopted by many researchers, variations of which may be seen in [67, 68, 69]. Under steady-state conditions, the amount of fuel being deposited on the walls equals that of

the evaporation rate back into the air stream. Thus, the quantity of fuel injected into the manifold is actually that amount which enters the combustion chamber.

As liquid fuel enters the air stream, the fuel transport process is usually divided into a fast flow and a slow flow. The fast flow is that proportion that has sufficiently small, and adequately vapourised, fuel droplets to be supported and carried with the air stream directly into the combustion chamber. The slow flow is the remainder that feeds the fuel film by impingement on the side-walls. In comparison to the air flow and evaporated fuel, the liquid film moves slowly down the manifold wall as the air rushes passed towards the chambers. With eventual evaporation of the liquid fuel back into the air stream, a finite time delay is encountered before all the injected fuel enters the combustion chamber. Under very cold conditions, the film may actually reach the inlet port before it is vapourised, causing unstable and unpredictable driving behaviour. Wu et al. [70] found that a single time constant was inadequate for close prediction of transient AFR excursions and proposed a two-puddle model. The first puddle was designed to capture the initial rise and peak amplitude of the excursion, whereas the second puddle model simulated the decay portion back to the desired value. This approach lead to a much improved determination of the fuel film effects and hence better approximations of the AFR excursions.

When using natural gas, it is clear that the fuel is already in a vapourised state and will be held in the air stream immediately upon its introduction. The fuel does not condense on the manifold surfaces, even under the most extremely cold conditions, since the boiling point of methane is $-161^{o}C$ at atmospheric pressure [13]. For this reason, the model of the manifold being used for natural gas operation need not encompass the dynamics of fuel lag due to fuel film development.

It has been suggested by Aquino [71] that transient AFR's do not occur when using gaseous fuel. Whilst this is true of the fuel condensation phenomenon, this

statement is slightly optimistic since AFR excursions are seen due to manifold filling and backflow phenomena. A technique known as air ramming, requires the timing of closure of the intake valve to be set just after BDC to capitalise on the momentum of the incoming charge, thereby increasing volumetric efficiency. At high engine speeds, this technique is effective, but at low engine speeds where the charge inertia is low, backflow of induced charge through the inlet port can occur as the piston begins the upward stroke of compression. AFR excursions are subsequently produced due to the difference of the backflow AFR and that of the charge held within the chamber. Chang et al. [67] support this effect by observation of AFR excursions when using methane. No liquid-film development was encountered but transient excursions where attributable to fuel injection timing being too close to the intake valve closing event. The following section (2.4) describes a model for estimating the A/F ratio value within the manifold, under gaseous fuel operation.

To summarise the manifold model under gaseous operation, equation 2.16 is accepted as an adequate representation of the filling and emptying dynamics by inclusion of the manifold volume.

2.4 Manifold A/F Ratio Computation

The air and gaseous fuel entering the intake system begin to mix the instant that gas is injected into the air stream. Under ambient conditions, natural gas mixes readily with air in any proportion, without the need to vaporise [49]. Since natural gas is lighter than air, it quickly disperses [48]. The *mean drift path* of the gas in still atmospheric air can be found by the use of Fick's first law of diffusion [72], as

$$\bar{x} = (2Dt)^{1/2} \tag{2.17}$$

where $\bar{x}$ is the mean drift path, D is the diffusion coefficient, and t is time.

The mean speed of methane (CH_4) molecules in ambient air (T = 298 K, $M = 16 \times 10^{-3}$ kgmol^{-1}, $R = 8.314$JK^{-1}mol^{-1}) is given as [73]

$$\bar{c} = \left(\frac{8RT}{\pi M}\right)^{1/2} \tag{2.18}$$

$$\bar{c} \approx 628\ ms^{-1}. \tag{2.19}$$

The mean *free* path, λ_{fp}, of CH_4 at ambient pressure ($P = 1 \times 10^5$Pa) is also defined as [73]

$$\lambda_{fp} = \frac{kT}{\sqrt{2}\sigma P} \tag{2.20}$$

$$\lambda_{fp} \approx 63\ nm, \tag{2.21}$$

where the collision cross-sectional area for methane is $\sigma = 0.46 \times 10^{-18}$ m^2, and Boltzmann's constant $k = 1.38 \times 10^{-23}$ [73].

The diffusion coefficient for CH_4, is then defined as [73]

$$D = \frac{1}{3}\lambda_{fp}\bar{c}, \tag{2.22}$$

$$D \approx 0.013 \times 10^{-3}\ m^2s^{-1}, \tag{2.23}$$

or

$$D \approx 0.13cm^2s^{-1}. \tag{2.24}$$

Thus, the mean free path of CH_4 in still air is approximately 1.612 cm for a period of 10 s, which is approximately 8% faster than nitrogen, N_2. Therefore, within the confines of the air intake system, the turbulent air flow caused by the throttle valve will act to enhance the mixing of gas and air.

Since there is no manifold wall wetting, *all* the gas is considered to begin mixing with the air and it is assumed that homogeneity is reached once the air and fuel reside in the main inlet manifold plenum. Figure 2.4 displays the mass flow rates in and out of the manifold and the manifold mass constituents that induce manifold pressure.

The A/F ratio at the throttle body could quite simply be approximated as the ratio of the two throttle flows, but at this stage full charge mixing would not have taken place and hence this approximation would not be the true A/F ratio entering the combustion chambers.

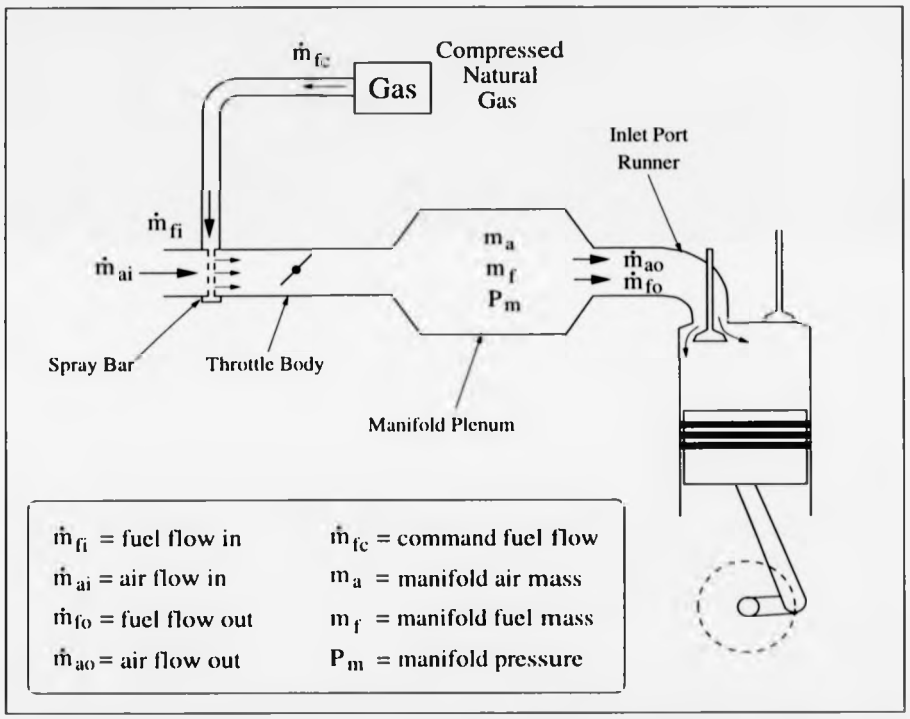

Figure 2.4: Manifold in/out mass flow rates. Full charge mixing takes place within the manifold volume.

It was considered that, by approximating the A/F ratio downstream of the throttle body and actually in the manifold plenum, a closer estimate of the cylinder A/F ratio would be achieved. The A/F ratio within the manifold plenum may be

determined as the ratio of the contained masses m_a and m_f as

$$AFR_m = \frac{m_a}{m_f}. \tag{2.25}$$

The exact values of m_a and m_f are not measurable however, and equation 2.25 is differentiated to obtain A/F in terms of the manifold mass rates of change :

$$\dot{AFR}_m = \frac{m_f \cdot \dot{m}_a - m_a \cdot \dot{m}_f}{m_f^2}, \tag{2.26}$$

$$= \frac{1}{m_f}\left\{\dot{m}_a - \frac{m_a}{m_f} \cdot \dot{m}_f\right\}. \tag{2.27}$$

Equation 2.25, for the mixed manifold A/F ratio, may substituted back into equation 2.27 to give

$$\dot{AFR}_m = \frac{AFR_m}{m_a}\left\{\dot{m}_a - AFR_m \cdot \dot{m}_f\right\}. \tag{2.28}$$

The mass of air, m_a, and fuel, m_f, held within the manifold can theoretically be expressed, as the mass balance equations, in terms of the flows in and out of the manifold, as:

$$\dot{m}_a = \dot{m}_{ai} - \dot{m}_{ao}, \tag{2.29}$$

and

$$\dot{m}_f = \dot{m}_{fi} - \dot{m}_{fo}. \tag{2.30}$$

Substituting equations 2.29 and 2.30 into equation 2.28 gives

$$\dot{AFR}_m = \frac{AFR_m}{m_a}\left\{\dot{m}_{ai} - \dot{m}_{ao} - AFR_m \cdot (\dot{m}_{fi} - \dot{m}_{fo})\right\}. \tag{2.31}$$

This expression contains the terms for the port flow rates of air and fuel which are not measurable quantities. Assuming homogeneity to be reached in the manifold plenum (as mentioned previously), the charge mixture leaving the plenum through the port runners shall take the A/F ratio of the manifold charge by considering

the A/F value to be quasi-static at the cylinder port. Thus, the port flow A/F ratio, AFR_p, is given to be

$$AFR_p = \frac{\dot{m}_{ao}}{\dot{m}_{fo}} = AFR_m, \tag{2.32}$$

$$\dot{m}_{fo} = \frac{\dot{m}_{ao}}{AFR_m}, \tag{2.33}$$

which can be substituted into equation 2.31 to give

$$\dot{AFR}_m = \frac{AFR_m}{m_a}\left\{\dot{m}_{ai} - \dot{m}_{ao} - AFR_m \cdot \dot{m}_{fi} + \dot{m}_{ao}\right\}, \tag{2.34}$$

$$= \frac{AFR_m}{m_a}\left\{\dot{m}_{ai} - AFR_m \cdot \dot{m}_{fi}\right\}. \tag{2.35}$$

Equation 2.35 may indicate a possible solution to resolving the air/fuel ratio control problem. If AFR_m is maintained exactly at the stoichiometry point for all conditions, then $\dot{AFR}_m = 0$, and the equation reduces to

$$\dot{m}_{ai} = AFR_m \cdot \dot{m}_{fi}. \tag{2.36}$$

thus,

$$\dot{m}_{fi} = \frac{\dot{m}_{ai}}{AFR_m} \tag{2.37}$$

This is in fact the minimum control law embodied in all air/fuel ratio controllers, and is called the *nominal* fuel control. In Chapter 4, section 4.3, it is revealed that the nominal control algorithm requires the air flow rate to be measured (or estimated via a map) in order to meter the correct amount of fuel.

A series of simulations, also shown in section 4.3 (figures 4.3, 4.5 and 4.7), demonstrate the characteristics of engine control solely under the action of nominal control. In these simulations, it is seen that the air/fuel ratio is accurately maintained during steady-state conditions only if the air flow measurement (or map estimation) is correct. During such times as sensor drift (or incorrect estimation), the fuel flow rate is incorrectly metered and the ratio is off set-point. It

is also seen from the transient simulations, that if the measured (or estimated) air flow differs from the air flow at the location of the fuel injector, then sharp air/fuel ratio transients will occur. Thus, $\dot{AFR}_m \neq 0$, and equation 2.37 must be compensated in some way. This is the reason for further investigation into air/fuel ratio control - such as the open-loop compensation controller developed in this thesis.

It can be seen that equation 2.35 now contains only flow rates that are measurable and estimated variables in the engine model. The throttle mass flow rate, $\dot{m}_{ai}$, is determined from the throttle model, governed by the driver-input, throttle angle command, whereas the fuel flow rate, $\dot{m}_{fi}$, is to be controlled by the electronic control unit (ECU) containing the A/F ratio control algorithm and so shall be exactly known from the fuel computation.

The term m_a in equation 2.35 is the mass of air held in the manifold. Although this value is not strictly measurable, it is approximated from the manifold pressure estimation in the ideal equation of state (2.11) where the assumption is made that the contribution of natural gas to the overall pressure is regarded as negligible for a stoichiometric ratio of 17:1. This allows the final manifold A/F ratio estimation to be given as:

$$\dot{AFR}_m = \frac{AFR_m}{m_m} \left\{ \dot{m}_{ai} - AFR_m \cdot \dot{m}_{fi} \right\}, \tag{2.38}$$

$$= \frac{AFR_m \cdot K_m}{P_m} \left\{ \dot{m}_{ai} - AFR_m \cdot \dot{m}_{fi} \right\}. \tag{2.39}$$

where P_m is the manifold pressure and K_m is the manifold constant, computed in equation 2.14.

The initial value of AFR is set at λ=1 (stoichiometry) to reflect steady-state operation at the commencement of simulation. All other initial values of the model states are computed using a *back-propogation* method. Having decided upon the desired operating conditions of engine speed and load for the simulation,

an **INITIAL** section (see the ACSL model code in appendix D), calculates the corresponding values of engine torque (Tq_e), manifold pressure (P_m), air flow ($\dot{m}_{ai}$ & $\dot{m}_{ao}$) and fuel flow ($\dot{m}_{fi}$) that are required to meet the desired operating conditions. The INITIAL section is essentially a rearrangement of the engine submodel equations.

The **INITIAL** section is necessary to ensure that the correct values are established for the initial states at commencement of the simulation, prior to the **DYNAMIC** section of the model. Therefore, the initial conditions of P_m, $\dot{m}_{ai}$, and $\dot{m}_{fi}$ in equation 2.39 are selected for steady-state operation at the start of all simulations.

2.5 Inlet Port Flow

The mass flow rate of air entering the combustion chambers is related to the manifold pressure, engine speed and engine displacement. The behaviour of the combustion chamber is discontinuous in nature, with discrete modes of operation described by the four discrete strokes as a function of crank angle rotation. For a multi-cylinder engine, the flow of air is continuously maintained due to the timing of the strokes and inlet valve overlaps. Considering one cylinder only, the amount of air contained within the chamber, m_{cyl}, can be described in terms of the equation of state, 2.11, as:

$$m_{cyl} = \frac{P_{cyl} V_{cyl} \bar{M}}{R T_{cyl}}, \tag{2.40}$$

where P_{cyl} and T_{cyl} denote the pressure and temperature within the cylinder and V_{cyl} is the volumetric displacement of one cylinder. Under normal circumstances, it is not possible to measure P_{cyl} and T_{cyl} directly, and it is assumed that, at BDC (maximum cylinder volume) these values do not deviate to any great degree from the measurable manifold pressure and temperature quantities. This is

a valid assumption if one considers that more appreciable temperature and pressure rises occur only after inlet valve closure when the engine process enters the compression stroke.

The flow rate of air into the cylinder is dependent upon the number of induction strokes per unit of time which is defined by the speed of rotation of the crank angle. A four-stroke-cycle engine must complete two crank angle revolutions for every induction stroke, allowing the mass flow rate for one cylinder to be expressed as

$$\dot{m}_{cyl} = \eta_v \frac{P_m V_{cyl} \bar{M} N_e}{2RT_m}, \tag{2.41}$$

where η_v is the volumetric efficiency and N_e is the engine speed.

The volumetric efficiency is a measure of an engine's capability to draw air. All the surfaces and barriers that make up the intake system, such as the air filter, throttle valve and intake valves, constitute a significant resistance to air flow. The volumetric efficiency is a unitless value and, for a four-stroke-cycle engine, may be expressed as [74]:

$$\eta_v = \frac{2\dot{m}_{cyl}}{N_e V_{cyl} \rho_i}, \tag{2.42}$$

where ρ_i is the air density at the inlet port. The value of ρ_i is usually not measurable so an idealisation is made by measuring the atmospheric air density at the point of entry to the intake system and defining η_v to be the overall efficiency of the intake system from air entry point to the cylinder.

For the entire engine, a quasi-steady state approximation of the mass flow rate of air induction can be expressed as the sum of all cylinder intake flow rates (as seen in figure 2.3) and is known as the *speed density* model [75], given by:

$$\dot{m}_{ao} \Rightarrow \sum \dot{m}_{cyl} = \eta_v \frac{P_m V_d \bar{M} N_e}{2RT_m}, \tag{2.43}$$

where $\dot{m}_{ao}$ is now the total mass flow rate of air leaving the manifold defined by the total engine volumetric displacement V_d.

The port flow rate is not usually measured from an engine since placing flow measurement devices close to the inlet valves causes major flow restrictions. Therefore $\dot{m}_{ao}$ is computed from the expression above using the measured values of the volumetric efficiency.

For the engine experiments conducted on the natural gas engine, the values of η_v were not available and, as such, equation 2.43 could not be explicitly employed as the port flow model. The derivation that port flow is dependent on manifold pressure and engine speed gave sufficient impetus to determine an empirical, port flow model based on a first approximation model equation

$$\dot{m}_{ao} = f_p(P_m, N_e). \tag{2.44}$$

Both the manifold P_m and engine N_e are readily measured from the engine tests allowing for the model to be determined analytically.

2.6 Engine Torque Production

Engine combustion torque is a useful output variable used to define an engine's capacity to do rotational work and allows for comparisons to be made between engine varieties. The chemical energy stored in the charge mixture is converted to mechanical energy during the combustion stroke of the engine cycle, when the piston is forced downwards acting on the crankshaft.

Over the years, the internal combustion process has been the subject of much research and to varying degrees of complexity. The actual process of charge ignition and subsequent expansion in a pre-chamber, lean-burn engine has been studied by Snyder et al. [76] using rapid photography techniques. Small windows placed in both chamber side-walls allow the fast jet and turbulent flame front processes to be analysed with a high-speed movie camera at a frequency of 14 kHz sampling rate. It is found that, for increasingly lean mixtures, the flame-

front speed rapidly diminishes, requiring larger crank angle intervals to burn all the charge, reflecting the loss in torque due to a reduction in chemical energy available.

Other research work has focused on cylinder pressure development [77, 78] and its effects on the mass-burned fraction. It is found that peak pressure magnitude and location is highly dependent on the spark timing. The earlier the spark occurs - up to as much as 50° BTDC - the chamber pressure is seen to rise much more rapidly and peak close to TDC with the effect of burning more than 20% of the total mass before the piston begins the expansion stroke of the combustion process. Maximum torque values are seen for spark timing which induces maximum pressure a few degrees after TDC.

The majority of research has concentrated on characterising the dependent variables of engine operation, and it transpires that the amount of torque produced is governed by 4 engine variables:

- mass of charge drawn into the cylinders,
- A/F ratio of charge mixture,
- engine crank angle speed,
- spark timing,

summarised by the relation:

$$Tq_e = f(m_{cyl}, AFR, N_e, \delta_s), \tag{2.45}$$

where Tq_e is the net production torque, AFR is the A/F ratio and δ_s is the spark-timing influence.

The maximum torque an engine can generate is dependent upon the maximum amount of charge that can be ingested for a given operating speed. If this quantity

is restricted, for example by a low volumetric efficiency, the amount of chemical energy available for combustion is heavily restricted, limiting the working ability of the engine below the maximum achievable. This reflects the importance of designing an induction system with the precedence of reducing friction flow and increasing the effectiveness of induction techniques.

It is common to construct a *torque map* of an engine which conveniently relates engine output torque to the throttle angle and engine speed as these are easily measured variables. It was considered in this model that, by defining torque explicitly in terms of the mass air flow out of the manifold, the throttle non-linearities would be eliminated from the torque model allowing charge mass dependency to be fully realised.

As engine speed increases from an initial low value, the torque produced is seen to increase steadily until a maximum is reached. Further increase in speed beyond this point results in a notable reduction in engine torque. This effect is due to the piston velocity increasing above that of the flame front propagation speed. Under these conditions, the flame does not have sufficient time to ignite the entire charge volume as the piston travels downward, subsequently moving into the exhaust stroke. The flame is extinguished as the exhaust valve is opened and the remaining unburned fuel is ejected. This phenomenon has been shown by many authors and is characterised in figure 2.5, reproduced from [79], for a variety of steady-state throttle angle settings. This phenomenon is the cause of high levels of unburned HC emissions, as described in section 1.1.2.

The discrete nature of the four stroke cycle introduces time delays to the system and accounts for the *induction-to-torque* delay encountered. If torque generation is considered to occur instantaneously at the point of BDC, and initial air induction, inlet valve closure and spark timing take place at 0°, 180°, and 360° ATDC respectively, then the induction-to-torque delay is a function of the

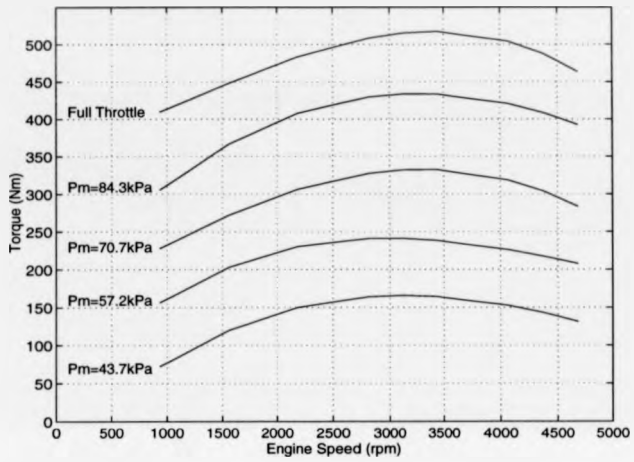

Figure 2.5: Steady-state engine model torque-speed curves from a 7.0L V8 spark ignition engine [79]

reciprocal of engine speed, 540° later. For a typical engine, operating between 600 rpm (idle) and 6000 rpm, this delay is calculated to be:

$$t_d(s) = 540^\circ \frac{60(s/m)}{N_e(r/m) \cdot 360(^\circ/r)}, \tag{2.46}$$

$$N_e = 600rpm, \quad t_d = 150ms, \tag{2.47}$$

$$N_e = 6000rpm, \quad t_d = 15ms. \tag{2.48}$$

By comparison, Dobner [64] accounts for this finite time delay by employing a fixed crank angle delay of 270°. However, there is no detailed explanation of why this crank angle interval is applied, which only leads to the assumption that the intake stroke is considered to be complete at BDC and the value of mean torque is expected to take place at 90° ATDC - midway through the combustion stroke. It is clear that this approach will result in half the delay time as calculated above for the same engine speeds.

The dynamics of torque production, however, do not occur at a single instant in time but develop over the entire combustion stroke crank angle interval. Combustion process dynamics are much faster than the rotational and manifold dynamics of the system and, for an engine operating at 6000 rpm, the combustion period lasts for only 5ms. Detailing the combustion dynamics is not the objective of this torque model and restriction will be made to using the induction-to-torque delay as detailed above. The prediction of the mean value of torque, dependent upon the gross engine variables, is considered appropriate for aiding controller design and developing insight into operating behaviour, therefore, the inclusion of the induction-to-torque delay is deemed adequate for the torque-modelling strategy.

Moskwa and Hedrick [57] incorporate a similar approach to modelling the torque delay by only considering delays which are justified in terms of the real-time control strategies. Their method reflects the non-coincidental timing of intake, spark and torque production by dividing the delay into two elements :

1. inlet valve closure-to-spark timing delay,

2. spark-to-torque production delay.

The delay computed by this method is much faster than the air, fuel and EGR transport dynamics of the modelled induction system relinquishing the need for torque dynamics.

It is widely known that AFR is significant in determining the level of combustion torque. An optimum value of AFR can be found to give maximum torque largely independent of the engine speed, and deviations from this setting prove to reduce the torque output. Boam et al. [80] characterised the AFR dependency of torque for a multipoint injection engine by leaning the mixture by as much as 24 parts air to 1 part fuel by mass. This can be seen in comparison to the normalised A/F ratio influence determined by Cho and Hedrick [63] in figure 2.6.

Both relationships are for petrol operated engines where the stoichiometric AFR is 14.7.

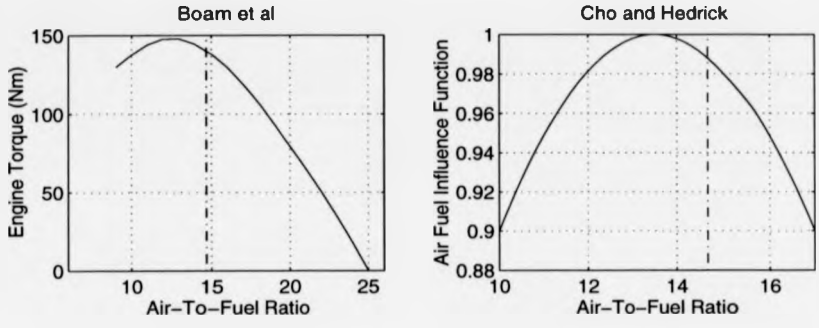

Figure 2.6: A/F ratio torque dependency and normalised influence function. (Reproduced from [80, 63])

The inclusion of AFR influence is not a well defined parameter in terms of physical variables. The torque response to AFR excursions is particular to each individual engine, being reliant on the processes of combustion, and may vary considerably between combustion chamber designs through the promotion of thorough mixing. What is clear from the graphs of figure 2.6 is that maximum torque occurs for mixtures just rich of stoichiometry, approximately 14.7 A/F ratio for petrol and denoted by the dotted line in figure 2.6. This is because there is sufficient fuel to react with the entire mass of oxygen available producing maximum power for the given volume. If the mixture becomes richer, the output torque begins to drop as the volume of oxygen ingested is replaced by larger quantities of fuel, reducing the oxidation concentration of the volume. Conversely, as the mixture becomes lean, the volume of chemical energy available from the fuel volume is replaced by higher volumes of oxygen. The entire fuel will (given sufficient combustion time) oxidise but leave high levels of exhaust oxygen and lower levels of torque production.

Characterisation of the AFR function must be realised through the capture of engine data and subsequent analysis and "curve fitting" techniques as recognised by Cho and Hedrick. It was decided, based on this evidence, that this should be the approach used in the torque model of the natural gas engine.

The effect of spark-timing on torque production has been well known for many years and its control lead to one of the first major steps towards engine management. For a given quantity of charge contained within the combustion chamber, there exists an optimum spark-timing position to reward maximum torque. This setting is known as the maximum brake torque (MBT) timing and is found using empirical test procedures by varying the timing whilst maintaining steady engine speed. Any drift away from MBT, either earlier or later, reduces the level of output torque and can alter emission pollutants by significant amounts. MBT timings are tabulated in the form of ignition maps, two examples of which can be seen in Bosch [13] page 406, for electronically and mechanically controlled systems. The map is embedded in the microcomputer of the engine control unit which reads off the required MBT upon receiving the speed and load signals measured from the engine.

In a similar vein to the approach adopted to characterise the AFR influence described above, Cho and Hedrick [63] normalise the effect of spark-timing between $\pm 30^{o}$ from MBT. The spark timing for the engine tests, and subsequent model described in this thesis, was always set at MBT, so as such the spark-timing event need not be explicitly defined within the torque combustion model.

To summarise, the torque model developed in this thesis is a variation of that given in equation 2.45 and has taken the form of :

$$Tq_e = f_{tq}(\dot{m}_{ao}, AFR, N_e), \tag{2.49}$$

where f_{tq} is to be determined from engine test data.

2.7 Rotational Dynamics

The third dynamic element of the engine model is the rotational dynamics of the crank shaft and engine flywheel. The crankshaft is assumed to be rigid and defined in terms of the engine polar moment of inertia and the angular acceleration. The purpose of modelling the rotational motion is to predict the engine speed under transient operation as the combustion torque and load torque vary. The angular acceleration of the crankshaft (a_e) is defined in terms of the combustion torque (Tq_e) and the external load torque (Tq_l) placed on the crankshaft as:

$$a_e = \frac{1}{J_{tot}} \cdot (Tq_e - Tq_l), \tag{2.50}$$

where J_{tot} is the total rotational inertia of the transmission system, comprised of the flywheel, driveshaft, gear box, final drive and wheels. Engine speed is derived from the simple integration of the engine acceleration as:

$$N_e = \int \left(\frac{1}{J_{tot}} \cdot (Tq_e - Tq_l) \right) dt. \tag{2.51}$$

This approach to modelling the rotational dynamics, and hence estimating engine speed, is widely used and is made in common with Powell [81], Cook and Powell [82] and Yuen and Servati [83].

External Load Calculation

The external load torque is considered to be composed of the sum of four elements of resistive force that occur due to vehicle operation, known as the *total driving resistance*. As these resistances act upon the vehicle wheels, their sum is transmitted up the driveshaft to exert a resistive load on the crankshaft. The engine is required to match the resistive load in order to maintain current vehicle speed or vary accordingly to allow acceleration or deceleration. A fifth resistive force is

that of the engine friction of the mechanical parts of the engine. Firstly, the four longitudinal resistive elements acting at the wheels are described below.

- **Rolling resistance,** F_{roll}. As the tyre constantly deforms, work is done in order to overcome the tractive resistances and rotate the wheel along the road's surface. This deformation translates to a resistive force to the vehicle's direction of motion, defined in terms of the vehicle mass (m_v) acting through all wheels and the acceleration due to gravity (g) as:

$$F_{roll} = f_{roll} \cdot m_v \cdot g, \tag{2.52}$$

  where f_{roll} is the coefficient of rolling resistance. The value of f_{roll} is dependent upon the composition of the tyre and the type of surface being driven on. Typical values range between 0.015 for low resistance conditions up to as much as 0.07 for off-road conditions [13].

- **Acceleration Resistance,** F_{accel}. As a vehicle accelerates, a resistive force is generated in proportion to the rate of change of vehicle speed (a_v) and the mass of the vehicle described by:

$$F_{accel} = e \cdot m_v \cdot a_v, \tag{2.53}$$

  where the rotational inertia coefficient, e, is a unitless parameter relating the mass moment of inertia of the complete vehicle driveline to the vehicle mass and wheel radius. The greater the desired vehicle acceleration, then the greater the required combustion torque has to be in order to provide the requested vehicle performance.

- **Climbing Resistance,** F_{cl}. As a vehicle ascends or descends undulating conditions, the resistive load increases or decreases, respectively, according to the expression

$$F_{cl} = m_v \cdot g \cdot sin\alpha, \tag{2.54}$$

where α is the degree of inclination above or below the horizon.

- **Aerodynamic Drag** F_{drag}. The frontal area of a vehicle presents a large cross-sectional surface area facing the oncoming air and generates large amounts of resistive force. The aerodynamics of a vehicle body are designed to reduce this drag force by allowing unbroken and smooth air motion over the surface panels. An index which quantifies the aerodynamics is the coefficient of drag c_d which is usually determined by the use of wind tunnel experiments. The total aerodynamic drag resistance is also dependent upon the air density (ρ_{air}), cross-sectional area (A_x) and the vehicle speed (v_v) as:

$$F_{drag} = c_d \cdot \frac{A_x \cdot \rho_{air} \cdot v_v^2}{2}. \tag{2.55}$$

The total resistive force (F_{res}) at the wheels is therefore defined to be the sum total of all four longitudinal resistances:

$$F_{res} = F_{roll} + F_{accel} + F_{cl} + F_{drag}. \tag{2.56}$$

F_{res} works against the direction of vehicle motion and acts to slow the vehicle down (with the exception of negative gradients for F_{cl}). F_{res} is translated into a rotational load torque at the crankshaft from the wheels via the driveshaft, gear box and final drive. Figure 2.7 displays a schematic of a typical transmission assembly for a manually-operated power train. The gear box allows for different operating conditions to be adopted by allowing the ratio of engine speed to driveshaft speed to be selected through a set of predefined transmission ratios. The ratio of a chosen gear is defined as:

$$gear\ ratio = \frac{engine\ speed}{driveshaft\ speed}. \tag{2.57}$$

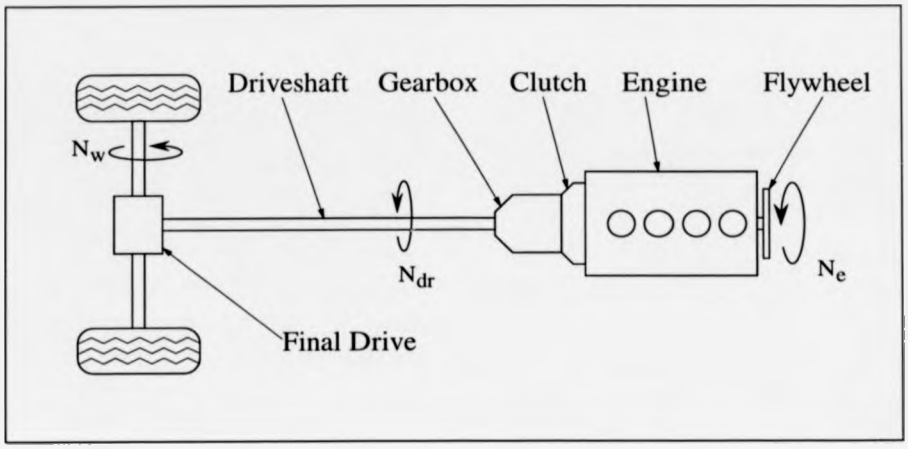

Figure 2.7: Manually-operated transmission assembly.

For a low gear selection, i.e. first gear, the gear ratio value is designed to be high to provide sufficient levels of engine torque to allow drive away from "stand still". The total transmission ratio, R_{tr}, is the product of the final drive ratio, which is constant for a given vehicle design, and the gear box ratio as:

$$R_{tr} = \frac{engine\ speed}{driveshaft\ speed} \cdot \frac{driveshaft\ speed}{wheel\ speed} \Rightarrow \frac{engine\ speed}{wheel\ speed}. \tag{2.58}$$

This allows the load torque due to the action of the driveshaft, $Tq_{l_{dr}}$, to be defined in terms of F_{res} as:

$$Tq_{l_{dr}} = \eta_{tr} \cdot \frac{r_{wh}}{R_{tr}} \cdot F_{res}, \tag{2.59}$$

where r_{wh} is the dynamic tyre radius and η_{tr} is the transmission efficiency.

The action of a typical manual transmission allows for energy losses to develop through gear teeth friction, oil churning and seal drag [84]. These effects decrease the overall transmission efficiency, reducing the gross torque available for vehicle

motion. The action of the transmission is not to be considered as a comprehensive modelling aspect in this thesis but is considered here to enable realistic driving scenarios to be devised and accurate determination of load torque to be computed. Therefore, transmission efficiency will be considered to be 100% and the wheel radius will be maintained at a constant value without incorporation of the dynamic behaviour of the tyres. The driveline compliance effects are ignored by assuming the driveshaft stiffness to be 100% stiff. Details of the wheel radius, engine inertia, gear and final drive ratios applicable to the modelled engine used in this study can be found in Appendix A.2.

The fifth element of resistance that acts upon the engine, even during idle conditions, is due to the internal work. Some portion of the mechanical work produced is dissipated through frictional losses of the internal moving parts of the engine such as the camshaft bearings, piston seal rings (see figure 1.2), valves trains and other working arrangements. Further losses are apparent in the heating of the system coolant and lubricant which are subsequently transmitted to the atmosphere via the action of the radiator and oil cooler, respectively. Internal work varies acutely with engine operation but is significant enough to match combustion torque exactly under idle conditions, thus maintaining constant speed.

The total internal friction work, W_{fr}, completed by the engine is defined in terms of the *mean effective pressure* (mep_{fr}), which is a measure of the work done per unit cylinder displacement volume [9] and allows for comparisons of varying engine capacity. Thus,

$$W_{fr} = mep_{fr} \cdot V_d. \tag{2.60}$$

The work per cycle is defined in terms of power, (P_w), per cylinder stroke for a four stroke engine as

$$W_{fr} = \frac{P_w}{(N_e/2)}. \tag{2.61}$$

This enables mep_{fr} to be defined as the power developed per cycle per cylinder volume as

$$mep_{fr}(Pa) = \frac{P_w(W)}{V_d(m^3) \cdot (N_e/2(s^{-1}))}, \tag{2.62}$$

and the unit of mep_{fr} is Pascals. Power is expressed in terms of the engine torque and speed as

$$P_w = 2\pi N_e T q_e, \tag{2.63}$$

which further allows the engine frictional work to be given by the equation

$$mep_{fr} = \frac{4\pi T q_e}{V_d}. \tag{2.64}$$

Mechanical inefficiencies become more apparent at high engine speeds, and for the comprehensive data shown by Heywood [9] (page 723), an algebraic equation of the form

$$mep_{fr}(kPa) = \left[0.97 + 0.15 \cdot \left(\frac{N_e}{1000}\right) + 0.05 \cdot \left(\frac{N_e}{1000}\right)^2\right] \times 100, \tag{2.65}$$

was found to successfully correlate a number of different capacity engines from 0.9 litre to 2.0 litres. On this basis, it was decided that internal engine friction of the 1.4 litre gas engine would be adequately represented using the above approach, enabling the load torque generated from engine friction to be given as

$$Tq_{l_{fr}} = \frac{mep_{fr} \cdot V_d}{4\pi}. \tag{2.66}$$

Total engine resistive load is therefore the sum of both the longitudinal resistive torque that acts up the driveshaft and the engine internal friction torque as

$$Tq_l = Tq_{l_{dr}} + Tq_{l_{fr}}. \tag{2.67}$$

2.8 Engine Time Delay Estimation

The action of the gas flows through the engine will cause some finite and time-varying delay between the occurrence of fuel injection at throttle body, and the

time at which the zirconia sensor measures a corresponding change in the oxygen content in the exhaust stream. These system dynamics are estimated as a time delay comprising three factors:

1. Inlet-manifold-filling and emptying dynamics. The gas and air enter the manifold at the throttle body and travel through the manifold before reaching the inlet valves.

2. Two engine crank rotations for one full stroke of the combustion process,

3. Exhaust manifold transportation time, from the exhaust valves to the zirconia sensor in the exhaust pipe,

The sum of all three factors gives an approximation to the system time delay and is found to be entirely dependent upon engine operating conditions.

Inlet Manifold Dynamics

Natural gas is admitted to the air stream, just prior to the throttle position. It is expected that there shall be some residence time for a new charge mixture to travel from the injector spray-bar to the inlet valves. Some researchers ([85, 86, 87]) have modelled the travel time, from injector to inlet valve, as a pure time delay, which is defined by the manifold length, mass flow rate and charge density.

The computation of the A/F ratio in this thesis, described in section 2.4, encompasses the dynamics of the manifold filling through the differential equation 2.39, incorporating the manifold pressure, and the air and fuel flow rates entering at the throttle. This affords an estimation of the A/F ratio further downstream of the throttle, that is considered to be *exiting* the inlet manifold. Hence, this approach envelops the manifold residence time as a dynamic time lag and does not call for a pure time delay to be explicitly defined.

The use of a pure time delay is valid for systems where the filling and emptying dynamics are considered negligible such as a constant radius pipe. Then, the transportation of the gas can be considered simply as the time required to travel from entry to exit, as defined by its velocity.

Crank Rotation Delay

When the charge mixture enters the combustion chamber, it is essentially maintained within a closed environment for approximately two crank rotations. When the inlet valves close, the charge is held until the exhaust valves open to commence the exhaust stroke. The crank rotation delay term is then wholly dependent upon the speed of the engine, the inlet valve open angle and exhaust valve closure angle which define the duration of one unit of charge 'capture'. Details of valve open and closure angles are contained in appendix A.

The exact crank angle duration for charge capture is calculated to be $\theta_d = 740^\circ$ (2 crank rotations + 20°). Given the engine speed, N_e (rpm), the approximate time delay, t_p, due to the piston strokes is defined as:

$$t_p = \frac{60}{N_e} \cdot \frac{\theta_d}{360} \approx \frac{123.3}{N_e}. \tag{2.68}$$

Exhaust Manifold Time Delay

The moment the exhaust valves open, the combustion pollutants will be expelled from the chamber and forced into the exhaust manifold. There exists a finite time for these hot gases to travel down its length and be ejected into the atmosphere. The zirconia sensor is placed within the exhaust system at a location just after the point at which all exhaust port runners meet. This is to allow the individual cylinder gases to mix and thereby obtain the overall measurement of the oxygen content. For the test bed engine, the sensor was located 37cm downstream of the exhaust valves.

The computation of the exhaust delay, may then be expressed as the transportation time, defined as

$$t_{ex} = \frac{\rho_{ex} V_{ex}}{\dot{m}_{ch}}, \tag{2.69}$$

where V_{ex} is the exhaust manifold volume from exhaust valve to sensor position ($V_{ex} = \pi \cdot r_{ex}^2 \cdot l_{ex} \approx 0.47m^3$). The exhaust gas density, ρ_{ex}, is not normally measured on production vehicles. Therefore, two approximations are required in order to estimate t_{ex}.

Firstly, the temperature of the exhaust gas is estimated to be that required to activate the zirconia sensor, as

$$T_{ex} = 600K.$$

This assumption is valid, as under normal operation, it can be expected that the exhaust temperature will vary considerably above this figure. Typical temperatures range from $500K$ during idle, to $900K$ at high-power operation [9]. The activation temperature, therefore, is considered an acceptable figure, as it facilitates the sensor and is a reasonable estimate of typical non-extreme conditions, for which the model range is constructed.

Secondly, the exhaust manifold pressure, P_{ex}, was not logged during testing. It was then approximated, in common with Kaidaintzis et. al. [87], that P_{ex} is equal to the inlet manifold pressure,

$$P_{ex} = P_m.$$

From the ideal equation of state (2.11), assuming no leakage or loss of the charge, the exhaust manifold density may be expressed as

$$\rho_{ex} \approx \rho_m \cdot \frac{P_{ex}}{P_m} \cdot \frac{T_m}{T_{ex}} \tag{2.70}$$

where subscripts m denote inlet manifold states. This value is finally substituted into the exhaust time delay equation 2.69, to estimate t_{ex}.

Thus, the total transport time delay is given as

$$t_d = t_p + t_{ex}. \tag{2.71}$$

From this approximation, the total time delay is seen to be dependent upon the states' air flow rate and engine speed. Both these engine states are obtained as outputs from the engine model. Typical values for t_d have been estimated in the region of 225 ms for low engine speeds and as short as 35 ms for high engine speeds [87].

2.9 λ-Sensor Dynamics

The principle of the Zirconia sensor modelled in this thesis is described in section 1.2.3. The performance of the exhaust gas oxygen sensor (EGO) exhibits a very sharp rise in output voltage gradient as the A/F ratio traverses the stoichiometric value. During a transition from lean to rich, a typical output voltage will change from approximately 100mV to 800mV due to the change in partial pressure established between the atmospheric reference air and the exhaust oxygen. This highly nonlinear characteristic makes the sensor inadequate for measuring precise levels of the A/F ratio since the output voltage changes minimally for changes in the rich or lean region. The window that exists between these two regions is extremely narrow and so short lived that the sensor is generally regarded as a *switching sensor* - stepping between the aforementioned voltage levels. Voltage output is dependent upon the temperature of the exhaust gas and may vary as pollutant material deposits on the surface build up and ageing becomes apparent. The sensor is therefore ideally suited to giving information on whether the mixture is actually lean or rich. The sensor characteristic used on the natural gas engine is shown in figure 2.8 where the narrow linear switching window is centred around the stoichiometry point.

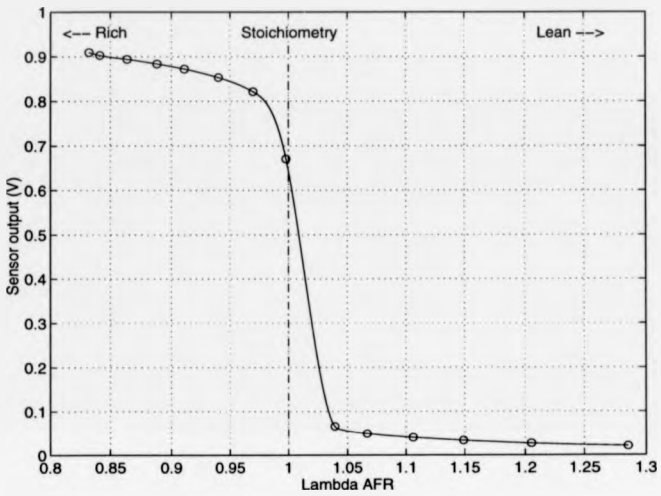

Figure 2.8: Zirconia EGO sensor characteristic used on the natural gas engine.

It is recognised that the sensor does have a finite switching time which, again, is dependent upon the temperature of the exhaust gas and describes the response time of the output voltage. Ageing effects are the most crucial cause for the variation in response time and it was shown by Wiedenmann et al. [36] that an unheated sensor can become as much as 53% slower after just 500 hours of operation. The cause was found to be due to the reduction of possible catalytic surface activity on the electrode in contact with the exhaust gas. Typical values of response times were found to lie between 85ms and 120ms for a moderately-aged sensor. It was therefore chosen, as a reasonable approximation, to model the sensor dynamics as a first-order system with a time constant τ_s of 100ms, being in common with other researchers, [87]. The first-order lag model equation for the sensor response is given as

$$\frac{\lambda_s(s)}{\lambda_e(s)} = \frac{1}{\tau_s \cdot s + 1}, \tag{2.72}$$

where λ_s is the sensor λ-value and λ_e is the exhaust λ A/F ratio value.

Early work by Hamburg and Shulman [88] considered the sensor to be comprised of a combination of a pure switching time delay, a first-order attenuation function and a switching function. The switching function was determined to be the overriding characteristic and allowed for the delay and attenuation effects to be ignored. The transfer function of the sensor was given as a '*sgn*' function whose output is either +1 or -1 depending on whether the exhaust A/F ratio is rich or lean of stoichiometry.

Most production A/F ratio control systems employing EGO sensors use the output voltage of the sensor as the voltage input of a *comparator* circuit to shape the sensor signal before it is used as the input signal to the AFR controller algorithm. The comparator reflects the practical implementation of the *sgn* function model by Hamburg and Shulman.

The zirconia sensor model to be used in the overall gas engine model, takes the form as shown in figure 2.9. The exhaust λ A/F estimation (as computed from equation 2.39) is passed through sensor time constant to represent the action of the response time. The non-linearity (shown in figure 2.8) then follows to produce the sensor output in volts. It is then this voltage signal that is fed to the controller of an ECU in the closed-loop, λ-feedback control approach.

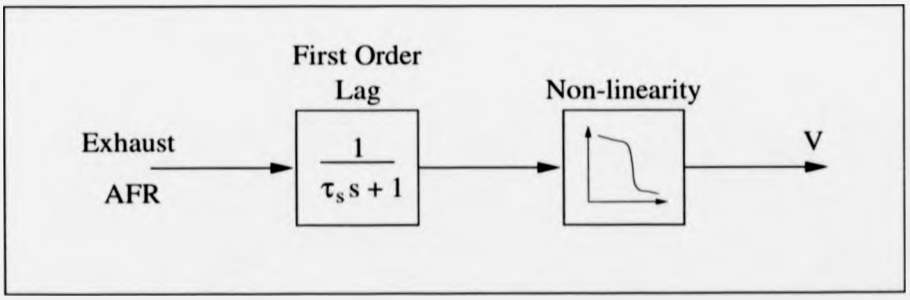

Figure 2.9: λ-zirconia sensor model structure.

2.10 Natural Gas Fuel Delivery

The administration of compressed natural gas is said to be fuel injected but differs from that of petrol fuel injection. Liquid fuel injectors actuate a needle valve in the fuel line by the use of an electromagnetic solenoid and closing spring arrangement. The valve is made to rapidly open and close the spray orifice, and for port fuel injection, this motion is sequenced once with every two crankshaft rotations. By maintaining a constant fuel-delivery pressure, the proviso is given that the injector open time defines the quantity of fuel delivered. The G.F.I. system also uses solenoidal valves but restricts the fuel perpendicularly to its flow. Unlike the petrol injector though, the valves may be held open for any length of time placing fuel metering dependency upon the orifice open area.

The gaseous fuel is admitted by the use of a cylindrical spray bar which is fitted up-stream of the throttle plate. The bar is constructed from an injection-molded plastic sheath which has four rows of holes running along its length. These holes are reduced in size to ensure that there is minimal pressure difference during high mass flow rates to maintain an equal flow of gas from each hole.

The spray bar is placed perpendicularly across the column of the air intake duct. Careful consideration of the direction in which the holes are facing is given to guarantee that all holes are discharging gas and not suffering from adverse pressure from incoming air flow. The gas is fed to the spray bar from an injector unit via a fuel delivery hose. This unit comprises two sets of metering valves. The first set comprises five injector valves which are employed to control the high velocity gas flow entering directly from the high pressure regulator. A second pair of injector valves is used to meter the low flow gas that enters the fuel delivery hose. This method of gas administration ensures the reduction of gas pressure from the high pressure (2500 psi) storage tank to an acceptable pressure upon entry into the air stream to provide optimum distribution.

A schematic for the injector unit supplied by GFI Systems is shown in figure 2.10 with the delivery pipe and spray bar arrangement.

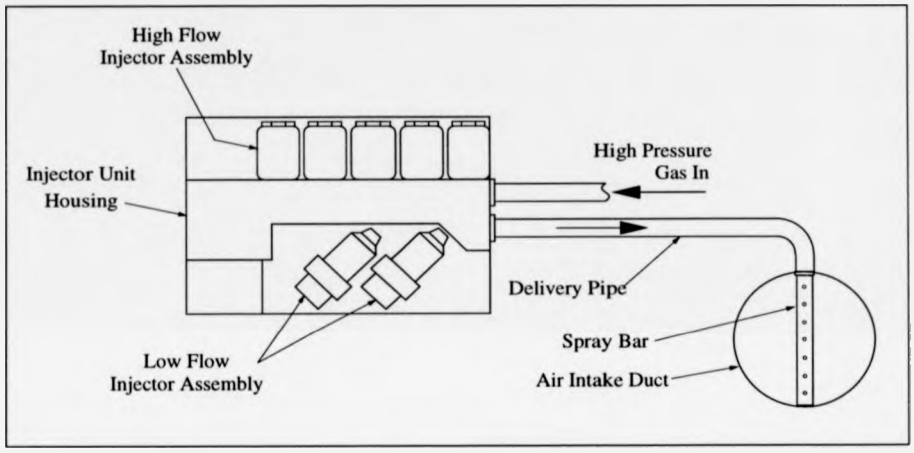

Figure 2.10: GFI system injector unit and fuel delivery spray bar arrangement.

Upon conversion of a vehicle to natural gas operation, the injector unit must be fixed to a structurally strong base within the engine compartment - which is usually the cross member of the chassis. The delivery pipe is then cut to length to reach between the injector unit and the position of the spray bar in the air intake pipe upstream of the throttle. Given the variation in vehicle designs the delivery hose is not a standard length and can vary from 30 cm to 1 m, but every attempt is made to combine safe injector mounting with the minimum of hose length.

The effect of the pipe on fuel delivery acts as a fuel delay or hold up due to its volume inducing transportation durations. Under steady-state conditions, the pipe has no net effect on the AFR as the inflow and outflow fuel rates of the pipe are equal. Under transient conditions the pipe acts as a single spatial volume allowing the gas flows in and out to be modelled independently under given parameters.

The flow rate of fuel entering the pipe, $\dot{m}_{fc}$, is determined by the injector unit which is, in turn, governed by the control algorithm to inject the commanded mass of gas. The mass flow rate leaving the pipe is a function of the spray bar orifice size, A_{sb} and the pressure ratio influence of the pipe (in a similar manner to the throttle model in equation 2.5) and is described as:

$$\dot{m}_{fi} = K_{sb}(\cdot A_{sb} \cdot \Phi_p), \tag{2.73}$$

where K_{sb} is the spray bar constant. The spray bar orifice size is given by the sum of the 12 holes that run along its length. Each hole has a radius of 1.488mm resulting in a total orifice area of $A_{sb} = 2.064 \times 10^{-5} m^2$. The maximum mass flow of gas was measured to be 3.86 g/s at wide open throttle (WOT) for the engine operating at 5500 rpm and the pipe pressure at the injector was measured as 120 kPa, just above atmospheric. Using equation 2.6, the value of Φ_p is calculated to be 0.5853 maximum influence, allowing a constant for equation 2.73 to be defined as

$$K_{sb} = \frac{\dot{m}_{fi}^{max}}{A_{sb}\Phi_p^{max}} = 3.1952 \times 10^5 (gs^{-1}m^{-2}). \tag{2.74}$$

The value of Φ_p is determined by equation 2.6 where the value of the specific heat ratio is now given to be that for methane, $\gamma_m = 1.299$ [89], and the manifold pressure ratio Pr_m is substituted for the delivery pipe pressure ratio Pr_p which is defined as:

$$Pr_p = \frac{P_a}{P_p}. \tag{2.75}$$

Use of the subscript p denotes variables and constants that refer to the fuel delivery pipe. The delivery pipe pressure is calculated using the mass flow equivalence expression, as was used for the intake manifold, as:

$$m_p = \int (\dot{m}_{fc} - \dot{m}_{fi})\, dt, \tag{2.76}$$

where m_p is the mass of gas in the pipe. The pipe pressure is therefore defined as:

$$P_p = K_p \int (\dot{m}_{fc} - \dot{m}_{fi})\, dt, \tag{2.77}$$

where the fuel pipe constant K_p is derived from the equation of state defined in terms the natural gas molar properties and the pipe volume (V_p) and temperature (T_p) as:

$$K_p = \frac{RT_p}{V_p M_f}. \tag{2.78}$$

As stated above, the pipe length may vary considerably between vehicles but the pipe bore remains constant at 1.27 cm. It was the intention of the fuel delivery model to investigate the effects of varying lengths of fuel pipe on the AFR under transient conditions. A typical value of 0.5 m shall be used for the pipe length here to obtain a typical value for the pipe constant, calculated as

$$K_p = \frac{8.31441 \cdot 298}{6.33e^{-5} \cdot 16} = 2.446 \times 10^6 (kJm^{-3}kg^{-1}) \tag{2.79}$$

for the same temperature conditions as for equation 2.14.

The delivery pipe model is therefore described by equations 2.73 and 2.77 with the appropriate constants.

2.11 Summary

It is a convenient location now to summarise the underlying model equations that have been introduced and to express the compact nature of the model.

State Equations

There are four state differential equations which define the dynamic behaviour of the gas processes and rotational dynamics. These are not to be determined from engine experiments but describe the physical nature of the gas dynamics and crankshaft rotational motion. They are:

1. Manifold pressure - (equation 2.16):

$$\dot{P}_m = K_m (\dot{m}_{ai} - \dot{m}_{ao})$$

2. Manifold A/F ratio - (equation 2.39):

$$\dot{AFR}_m = \frac{AFR_m \cdot K_m}{P_m} \{\dot{m}_{ai} - AFR_m \cdot \dot{m}_{fi}\}$$

3. Rotational dynamics - (equation 2.51):

$$\dot{N}_e = \frac{1}{J_{tot}} \cdot (Tq_e - Tq_l)$$

4. Fuel delivery pipe pressure - (equation 2.77):

$$\dot{P}_p = K_p (\dot{m}_{fc} - \dot{m}_{fi})$$

Empirical Functions

The engine model encompasses a number of characteristic equations that must be obtained from steady-state engine tests. These are known as the model "non-linear empirical equations" that relate the relevant engine variables of each model subsystem. There are essentially three non-linear functions that must be determined and these are summarised as:

- Throttle function - (equation 2.5):

$$\dot{m}_{ai} = f_\theta(\theta, \Phi_m)$$

  where f_θ is the throttle function to be determined.

- Port function - (equation 2.44):

$$\dot{m}_{ao} = f_p(P_m, N_e)$$

  where f_p is the inlet port function to be determined.

- Torque function - (equation 2.49):

$$Tq_e = f_{tq}(\dot{m}_{ao}, AFR, N_e)$$

where f_{tq} is the engine combustion torque function to be determined.

It is important, therefore, that the nature of the engine tests be structured to enable the functions f_θ, f_p and f_{tq} to be thoroughly established from a comprehensive set of measured engine variables.

Parameter Constants

Through the process of building the model, a number of parameter constants have emerged that are required to complete the state and empirical equations given above. These values pertain to the actual dimensions of the engine being modelled as well as establishing constants related to the atmospheric conditions. They are summarised in table 2.1.

Parameter Constant			Unit
V_m	=	Manifold volume	(m^3)
K_m	=	Manifold constant	$(kJm^{-3}kg^{-1})$
R	=	Universal gas constant	$(kJkmol^{-1}K^{-1})$
K_{sb}	=	Spray bar constant	(gs^{-1})
A_{sb}	=	Spray bar orifice area	(m^2)
K_p	=	Fuel delivery pipe constant	$(kJm^{-3}kg^{-1})$
J_{tot}	=	Total rotational inertia	(kgm^2)

Table 2.1: Engine model parameter constants

The engine model may be visualised in block representation as shown in figure 2.11. The flow of information is represented by the arrows connecting the sub-model blocks. The input to the model is the throttle valve angle (θ_{th}) which can be set to simulate any desired operating conditions. Reverse flow signals are necessary

to enable each block to be computed and thereby expresses the non-linear characteristics of the model as many variables are inter-related. The dynamic equation numbers, as listed above, are shown in their corresponding location to depict the interconnection between the dynamical aspects and the steady-state empirically-derived elements, which are also represented in their appropriate submodel block. The parameter constants are not shown explicitly but are encompassed within the appropriate blocks for clarity.

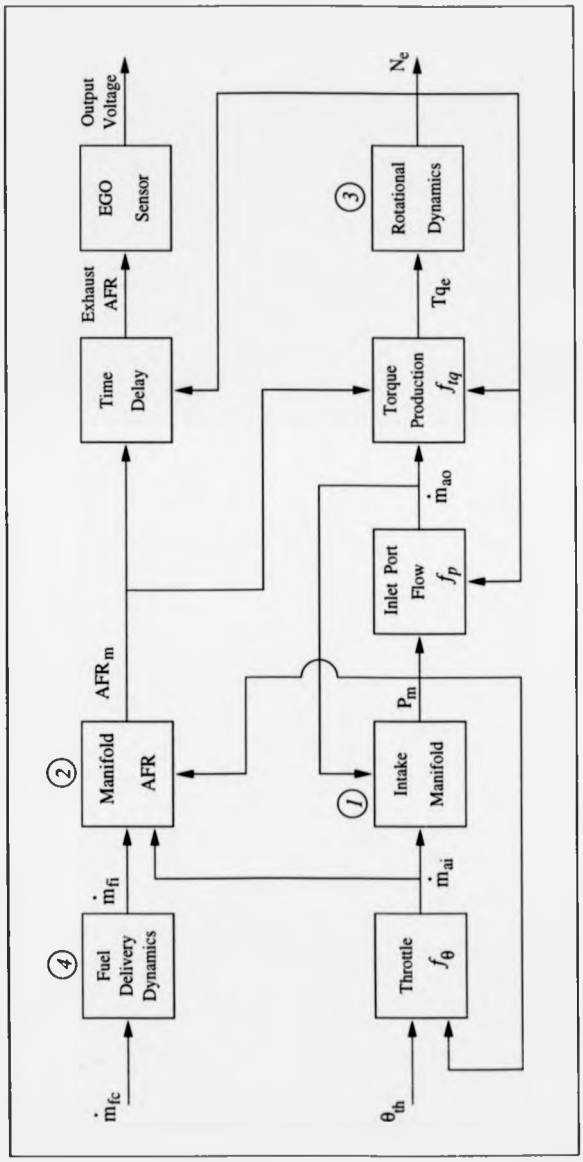

Figure 2.11: Engine model block representation.

Chapter 3

Engine Experiments

3.1 Aims

For the non-linear differential model equations defined in the previous chapter, a set of engine experiments is required to allow the three empirical functions to be determined. This chapter is aimed at presenting the experimental facilities available, and the test procedure that was carried out, to capture the required data.

Characterisation of each non-linear function, and resulting submodel descriptions, shall then be derived through the extensive use of regression analysis techniques. The choice of model orders is discussed and the accuracy of each empirical function is illustrated.

An investigation into the dynamics of the zirconia sensor is then conducted, using a set of input-output data that enables a "black-box" modelling approach to be adopted. The purpose of this work is to demonstrate the characteristic sensor non-linearity, which shall then support the approach adopted in utilising this sensor for control in chapter 4.

3.2 Dynamometer Testing

From the structure of the model developed in the previous chapter, a set of static tests were required to establish a set of data measurements to allow the determination of the functions f_θ, f_p and f_{tq} (see section 2.11). The engine variables required are:

- engine speed,
- engine torque,
- throttle angle ,
- manifold pressure,
- air flow rate,
- fuel flow rate,
- λ-exhaust A/F ratio.

A comprehensive array of engine variables measured from the test-bed and dynamometer may be seen in Appendix B.3.

The engine available for testing was a 1.4 litre automotive engine which is currently in production, and was adapted to operate on compressed natural gas. It was desirable to capture data for as large an operating range as possible to establish a model that was accurate for engine operation under all conditions and a test matrix procedure was designed to complete this task.

The engine speed range was set to cover from near idle conditions to high engine speeds. In practice, the lowest engine speed achievable was only as low as 2000 rpm due to restrictions of the air flow meter device. The device was designed for much larger capacity engines (8-12 litre) and difficulties arose at low speeds of

around 1750 rpm as flows became unstable and fluctuations in engine speed were encountered. Therefore, the speed range was restricted to a minimum of 2000 rpm and steps of 500 rpm intervals were selected up until 5000 rpm.

Under steady-state conditions, the combustion torque of the engine is equaled by the load torque placed on the crankshaft. The speed of the engine is adjusted by increasing or decreasing the load torque of the dynamometer allowing the indicated combustion torque to be easily measured from the dynamometer load torque. At each speed setting, the throttle angle was adjusted to allow the full range of combustion torque to be realised from 100% torque down in steps of 10%. This enabled the entire torque range to be covered. However, it was observed that maximum torque production could actually occur at less than 90° throttle angle. In order to ensure the full range of throttle angle was being achieved, the throttle was increased by steps of 15° from when maximum torque was encountered until wide open throttle (WOT). This emphasises the first encounter with the non-linear behaviour of the throttle action and expresses the care that must be taken to ensure that 'regions' of operating range are not left unaccounted for.

For each speed and load setting, a further requisite of the engine model was to vary the A/F ratio and allow the torque model to be completed. The A/F ratio could be adjusted manually by restricting the flow of gas in the fuel pipe by a simple metering valve. The value of A/F ratio was monitored using an electronic Horiba Lambda Monitor in conjunction with a Zirconia EGO-sensor. This allowed the λ-value to be accurately adjusted between 0.9 and 1.5 in steps of 0.1. Problems of misfire occurred when operating at lean mixtures of 1.5 λ at high speeds of 5000 rpm and therefore certain operating points were not obtainable. This does however verify the importance that λ has on engine drivability and effects on torque production - further emphasising the need for strict A/F ratio control for smooth engine operation.

The engine and dynamometer arrangement may be seen in Appendix B.2 where, although not to exact scale, the air-filter attached to the flow device can be seen to be overly large in capacity for the particular engine being tested. The fuel flow metering valve can be seen up stream of the injector assembly which is operated manually. The restriction is made by observing the Horiba λ-sensor output and adjusting the 'screw valve' until the desired setting is met.

The engine crankshaft is fixed to a rigid driveshaft without any intervening gear ratio, thus, the speed of the driveshaft equals that of the crankshaft. The driveshaft compliance is considered to be 100% rigid as mentioned in section 2.7. The driveshaft enters the input of an 'Eddy current dynamometer' which exerts the desired external load on the engine. Effectively, the dynamometer electromagnetically varies the work load required of the engine to allow a variation in the engine speeds as desired for the given throttle angle. The magnitude of the desired combustion torque is met through the positioning of the throttle angle to admit more or less air as appropriate. Absent from figure B.1 are the water cooling systems of both the engine and dynamometer for reasons of clarity and significance.

3.2.1 Test Bed Arrangement

The test sequence of the desired engine speed and load was programmed in an Archimedes personal computer (P.C.) running the commercially available Taskmaster software. The P.C. was in two way communication with a Talisman control system interface to control the engine torque (via the throttle angle) and the engine speed (via the dynamometer load). Figure 3.1 displays the engine test bed architecture with surrounding hardware and the direction of communication flows.

A host of sensors were placed on and around the engine as tabulated in Appendix B, and were automatically logged by the P.C.. A number of other engine

variables were manually recorded and are represented by the 'dotted' information flow lines in the diagram. The pollutant exhaust emissions were measured on-line over a sampling period of 1 minute to obtain an average. Details of the Horiba MEXA exhaust gas analyser can be found in Appendix B.

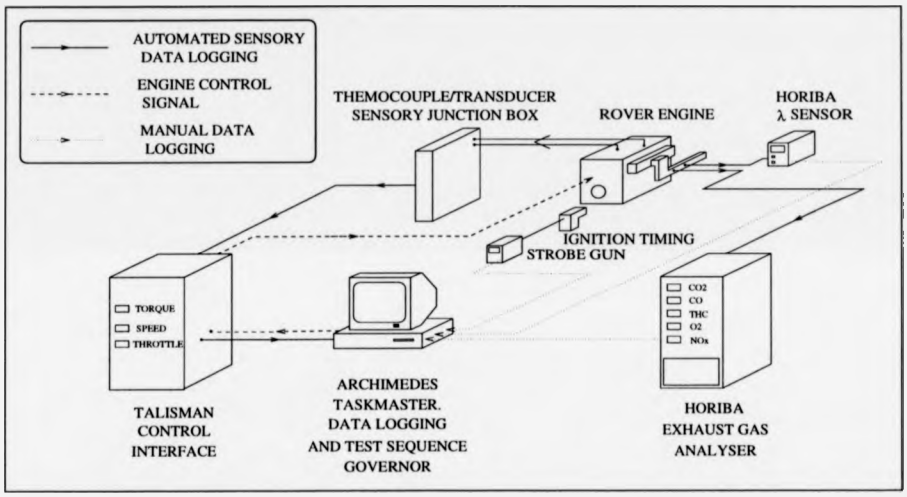

Figure 3.1: Engine test bed arrangement and system architecture.

At each operating point and A/F ratio setting, the engine was permitted to stabilise for a period of up to 3 minutes, to ensure steady-state operation was apparent before commencing data acquisition. After this period, all monitored signals were logged twelve times, with 5 second intervals. This produced a vast array of data consisting of 4366 data logs for each engine variable measured over the range of engine operation conducted.

All the engine data was downloaded from the Archimedes P.C. onto floppy disks in 'Lotus-123' spreadsheet format. The data was then loaded into the Lotus spreadsheet environment at the British Gas research centre. Subsequent conversion to ASCII format and again downloading onto portable floppy disks allowed

the final destination of the data to be loaded into the 'Matlab' mathematical environment for analysis. Matlab was then the tool used for all further model and parameter characterisation reported in this chapter.

3.2.2 Results

The torque map for the acquired engine data can be seen in figure 3.2, where the A/F ratio is set to stoichiometry. The engine output torque is expressed in terms of the throttle angle and can be seen to increase rapidly at low throttle angles, due to the nonlinear behaviour of the throttle valve governing the air mass flow entering the intake manifold. Output torque reaches a plateau at approximately 55° throttle, above which, any further increase in throttle angle produces only small increases in torque.

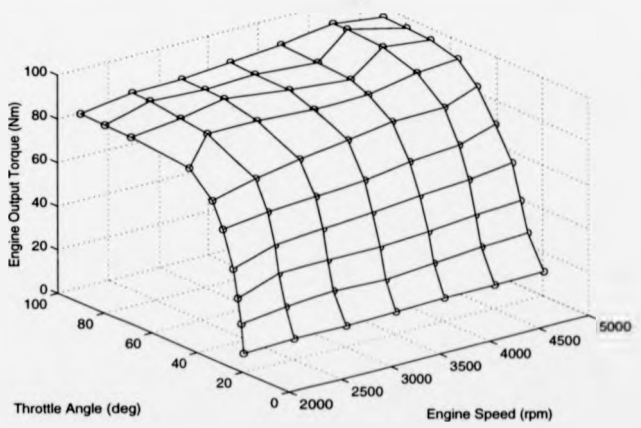

Figure 3.2: Engine torque map for Rover K-series 1.4 litre engine operating on natural gas. Dependency is placed on throttle angle and engine speed.

This type of torque map is generally regarded as the most useful approach to displaying torque production, since it relates the easily measured physical variables of the engine. A more conventional way of expressing engine torque is by

manifold pressure, since it decouples the dependency of the throttle body and places importance on the mass of air in the system. Many engine management units use the manifold pressure as an input variable to estimate load conditions and thereby interpolate the required spark timing for maximum brake torque (MBT) from the torque map.

The manifold pressure is a function of both the engine speed and throttle angle and, as such, is not a controlled variable. A more useful representation of the engine load is the mass flow rate of air entering the combustion chambers, as expressed in equation 2.49. This quantity is not usually available (as explained in section 2.5) from an engine, but under the steady-state conditions maintained by the dynamometer, the mass flow rate entering the chambers is equal to the flow rate at the throttle valve. The torque can then by represented as shown in figure 3.3, where the torque is seen to be a generally linear function of both the air flow rate and engine speed. Again, this torque map is shown for operation at the stoichiometric A/F ratio.

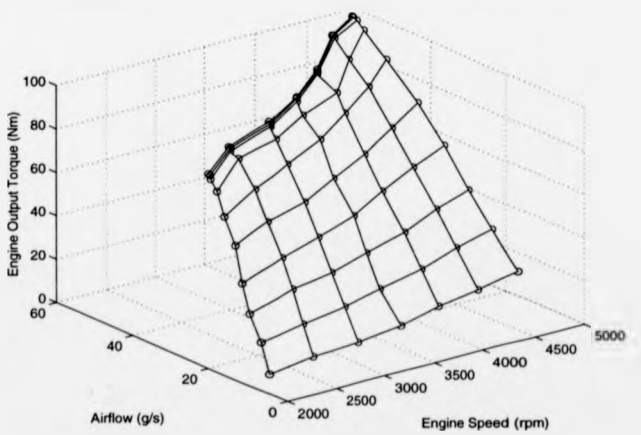

Figure 3.3: Engine torque map dependent on air flow rate for Rover K-series 1.4 litre engine operating on natural gas.

A gathering of data is seen at the top of the plot which corresponds to the aforementioned plateau region, where air flow rate remains at a maximum for increasing throttle angle above, approximately, 55°.

The amount of fuel metered to the incoming air was not governed by an engine controller, but, for the purpose of testing, was set manually to obtain a comprehensive sweep of A/F ratio. The fuel map can be seen in figure 3.4 for stoichiometric operation and reflects the nonlinear behaviour of the air flow as a function of throttle angle. Initial inspection of this map suggests that the fuel flow, and hence air flow, are almost linearly related to the engine speed. This gives confidence to the port flow model theory given in section 2.5.

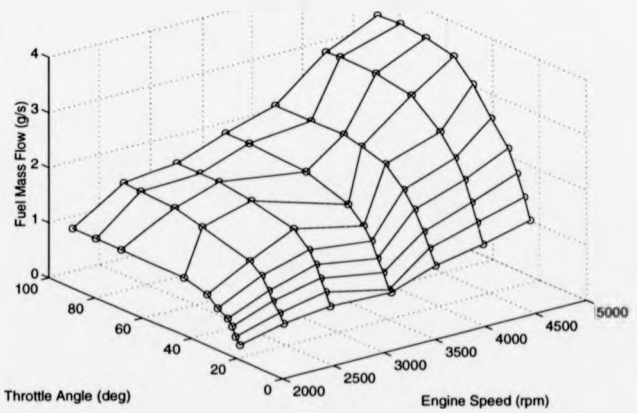

Figure 3.4: Engine fuel map for Rover K-series 1.4 litre engine operating on natural gas.

Figure 3.4, and to a greater extent figure 3.14, demonstrate typical maps that would be used in an engine control unit (ECU) to control the flow rate of fuel. This approach to metering fuel has been widely used for many years and by many manufacturers [13]. However, due to the fact that these maps are derived from steady-state conditions, their performance is only truely valid under steady-state

conditions. During fast dynamic conditions it must be expected that these maps will become less effective at maintaining the air/fuel ratio at the set-point.

The main exhaust pollutants, as described in section 1.1.2, may be seen in figure 3.5 for the natural gas engine operating at WOT. The emission concentration levels are displayed as functions of both the engine speed and λ A/F ratio value. It is immediately obvious that the most influential variable on determining emission levels is the A/F ratio, and engine speed has very little noticeable effect. By comparing the acquired emission maps with figure 1.3, the behaviour the natural gas combustion by-products matches those of expected I.C. operation.

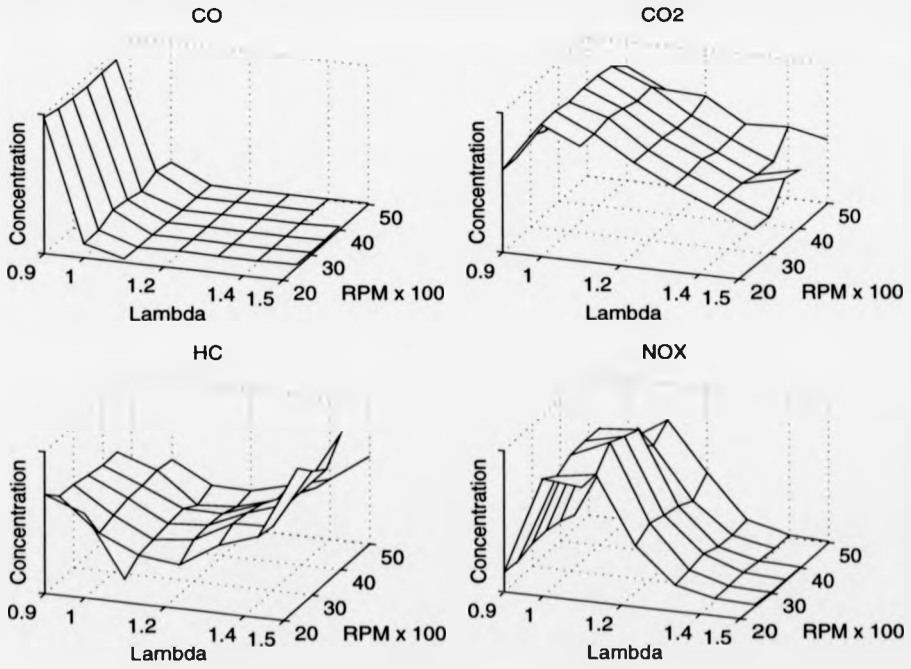

Figure 3.5: Emission concentration maps.

During cold engine operation, the requirement for petrol operated engines to

run on a fuel-rich mixture ($\lambda < 1$) and thereby ensure a combustible charge, allows CO and HC emissions to escalate, until the engine is sufficiently warmed up that fuel vaporisation takes place much more readily. Natural gas operation requires no such choking procedure and can operate at the desired λ-setting from start-up. The levels of NO_x are seen to peak at $\lambda = 1$ for the tests conducted and are in agreement with the peak limit which is seen just lean of stoichiometry in figure 1.3. Either side of this condition, NO_x levels drop dramatically - which gives major incentive behind lean-burn operation to moderate these emissions up until the "flammability limit" is approached.

The purpose of displaying the emission results is not one of comparing exact levels between those of petrol and natural gas, but to demonstrate the overpowering dominance that A/F ratio posses over these by-products. Modern production vehicles strive to maintain exhaust A/F ratios at settings that enhance the particular method of emissions management (aftertreatment or pre-chamber combustion). In the light of continuing reductions of permissible government levels, motivation behind improving engine control, and in particular A/F ratio control, to reduce not only emissions but fuel consumption, also continues to grow.

3.3 Analysis of Results

3.3.1 Throttle Characterisation

In common with carburettor engines, the fuel of the natural gas engine was admitted upstream of the throttle valve. Unlike liquid fuel systems, however, the density of the fuel cannot be ignored, and constitutes a larger volume than fuel droplets, thereby displacing a larger quantity of air. The flow rate at the throttle valve is therefore the sum of the atmospheric air and natural gas. The mixture shall now be termed the *charge* flow rate, requiring $\dot{m}_{at}$ in equation 2.5 to be replaced by the charge flow rate $\dot{m}_{ch}$.

The effect of throttle angle on charge flow rate can be seen in figure 3.6. It is difficult from this plot to observe the precise influence of both the throttle angle and pressure ratio on charge flow. The distinct increasing levels of mass flow rate are due to the increasing engine speed, where the maximum engine speed of 5000 rpm draws the highest charge flow rate of 63 g/s at WOT.

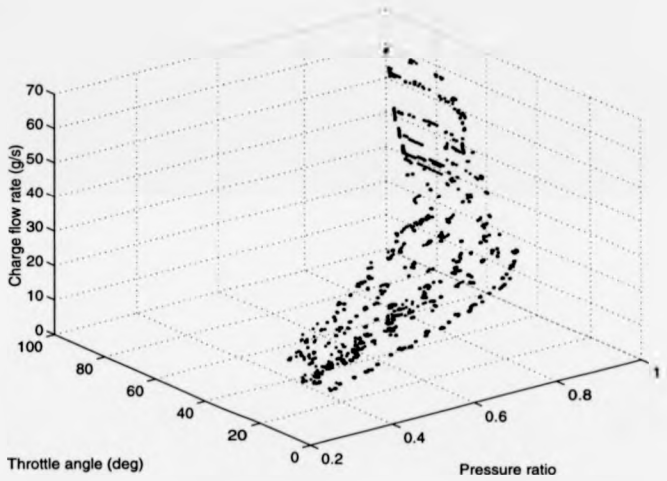

Figure 3.6: Charge flow rate dependency on throttle angle and manifold pressure ratio.

The pressure ratio influence, Φ_m, must be computed and used as the denominator of $\dot{m}_{ci}$ in the throttle model equation to isolate the throttle action. The value of the specific heats in the calculation of Φ_m must now be exchanged for that of the charge mixture and not just pure air. For a stoichiometric ratio, there exists 94.44% air to 5.56% natural gas (16.988:1 A/F ratio). Assuming homogeneity, and approximating the natural gas to consist of pure methane, the specific heat ratio for the charge mixture is computed to be $\gamma_c = 1.394$, which is a small change from that of atmospheric air at ambient temperature, but shall replace γ_a for completeness.

The normalised function of Φ_m can be seen in figure 3.7, where the pressure ratio influence is at a maximum for pressure ratios less than P_{crit}. If Φ_m is plotted as a function of the manifold pressure and throttle angle, the resulting surface is known as the *β-wing* [55]. This map is often included in the microprocessor of engine management systems as a table describing $\dot{m}_{ao}(\theta, P_m)$, to allow an estimation of the air flow using a table look-up procedure.

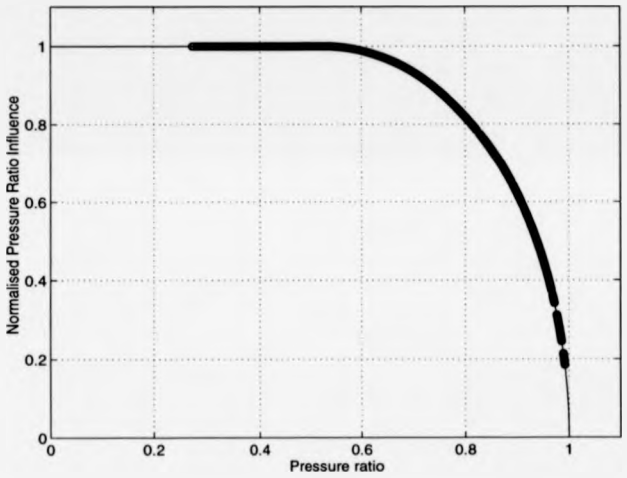

Figure 3.7: Normalised pressure ratio influence described by equation 2.6.

Upon dividing the charge flow rate by Φ_m, the effect of throttle angle is isolated and the model order can be determined using curve fitting techniques. The throttle function may be seen in figure 3.8, for which it can be observed there is rather a large spread in the data. One explanation for this large spread is the manner in which the air flow rate was derived from the pressure drop measured across the laminar deflection flow meter. The pressure was read-off by eye from a water level indicator inside a capillary tube and therefore the effect of the meniscus could naturally be expected to increase the measurement errors due to uncertainty. This effect is expected to be worsened by the fact that the water level was being read

by two individuals during engine testing.

A second explanation, is the possible variation in throttle angle during logging. The considerable vibration of the engine could well be expected to cause small vibrations in the throttle angle sensor.

An attempt at reducing the spread in data was made by incorporating the variation in relative humidity that was evident during the three weeks of testing. The effect of relative humidity on the gas constants for normal air can be seen in [74], where a 0.06 change in the moisture/air ratio causes a 2% variation in the value of the specific heat ratio. The maximum and minimum values of relative humidity were measured to be 65% and 13% respectively, but it was maintained close to a mean value of 35% due to the isolation of the test bed and dynamometer rig inside an acoustically-sealed "test-cell". The inclusion of the relative humidity variation helped to reduce the spread in data only marginally.

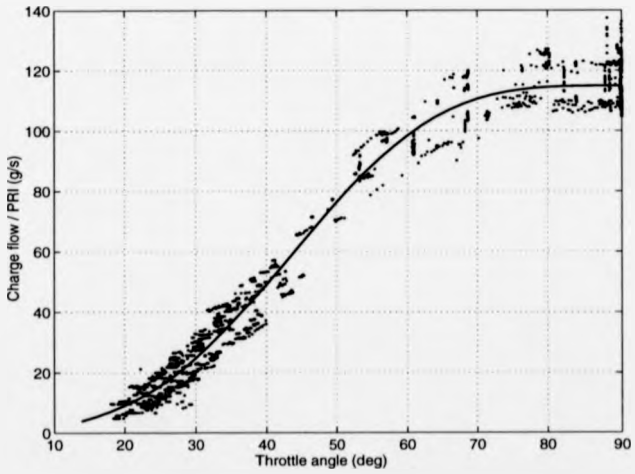

Figure 3.8: Throttle function effect on the ratio of charge flow rate and normalised pressure ratio influence factor, as described by equation 3.6.

From observation of the data of figure 3.8, a number of polynomial curve fits of

varying order were exercised using linear least squares regression techniques [90]. Of these, it was found that good fits could be produced of low order that would approximate the mean of the throttle function by running through the centre. However, due to the large spread in data at high throttle angles, the model was seen to produce a point of inflection for a 3rd order model at 80° throttle angle, indicating a reduction in the charge flow rate for increasing throttle angle above 80°. It is known, of course, that for increasing throttle angle the mass flow rate cannot decrease for a given engine speed. Therefore, in order to restrict the model fit to behave *monotonically*, a number of other model structures were attempted. These took the form of varying degrees of coefficient order involving *cos* and *sin* functions of the throttle angle. The throttle function identified by Cho and Hedrick[63] takes the form of a piecewise structure involving $cos(\theta)$ with a cut-off throttle angle at 79.46° at which maximum flow rate is achieved. By inspection of figure 3.8 it was decided that there was no justification for a similar piecewise approach and that the throttle function should be a continuous function.

The linear regression technique employed to derive the models during the model building process was that of multiple linear regression. The model is defined in terms of the measured observations (output - y_i), measured known states (input - x_i), the unknown model parameters (θ_i) and a term to denote the independent random error, or noise, ξ_i. Subscript i denotes the i^{th} measurements. Thus, in matrix notation

$$\begin{bmatrix} y_1 \\ y_2 \\ \vdots \\ y_n \end{bmatrix} = \begin{bmatrix} x_{11} & x_{12} & \cdots & x_{1p} \\ x_{21} & x_{22} & \cdots & x_{2p} \\ \vdots & & \ddots & \vdots \\ x_{n1} & x_{n2} & \cdots & x_{np} \end{bmatrix} \begin{bmatrix} \theta_1 \\ \theta_2 \\ \vdots \\ \theta_p \end{bmatrix} + \begin{bmatrix} \xi_1 \\ \xi_2 \\ \vdots \\ \xi_n \end{bmatrix} \tag{3.1}$$

which can more simply be expressed as

$$Y = X \cdot \Theta + \xi \tag{3.2}$$

where Θ is the vector of unknown parameters to be estimated. If the element of

noise is considered to be zero then the regression model reduces to

$$\hat{Y} = X \cdot \hat{\Theta} \tag{3.3}$$

where the symbol '^' denotes the model estimates.

The linear least squares estimation of Θ is then given by

$$\hat{\Theta} = (X^T X)^{-1} X^T Y, \tag{3.4}$$

which minimises the residual sum of squares. This is the approach taken in deriving all the models presented in this chapter. This calculation is easily performed in the Matlab analysis environment and can be made even more efficient by the use of the assigned Matlab backslash matrix divisional operator '\'. This allows the estimation of $\hat{\Theta}$ to be found through the equation

$$\hat{\Theta} = X \backslash Y. \tag{3.5}$$

The least squares approach was developed by considering the noise element to be zero. This approach is also acceptable when the noise is considered to be 'white', then the cross-correlation of output to input is proportional to the least squares estimation of the parameter estimates. However, if the noise is not small, then the resulting parameter estimates may be poor or significantly biased.

A third explanation for the level of noise seen in figure 3.6, is the effect of dividing the charge flow rate by the pressure ratio influence value. Any noise level on each of the two measured states is additive in the extreme.

The noise levels experienced on the throttle angle, air flow rate, fuel flow rate and manifold pressure measurements are approximately $\pm 0.25°$, $\pm 0.2 gs^{-1}$, $0.012 gs^{-1}$ and $\pm 0.05 kPa$, respectively. When considered against the maximum and minimum of each engine state, the subsequent maximum and minimum **percentage** noise levels translate to :

throttle:	max =± 2.5%	min =± 0.27%
air flow rate:	max =± 4.4%	min =± 0.33%
fuel flow rate:	max = ± 3.8%	min =± 0.33%
manifold pressure:	max =± 0.2%	min =± 0.05%

The noise level observed in figure 3.8 for Φ_m is therefore composed of the three noise levels shown above for $\dot{m}_{ai}$, $\dot{m}_{fi}$ and P_m. The noise level of Φ_m is determined to be approximately ± 9.2% on the best fit model - shown as the solid line. This is the largest noise level experienced for the captured data, and is attributed to the fact that three states ($\dot{m}_{ai}$, $\dot{m}_{fi}$ and P_m) have been combined to derive the term Φ_m.

For the states of engine speed and combustion torque, noise levels of approximately ± 5.0 *rpm* and ± 1.0 *N* where encountered due to the digital nature of the recording software.

By comparing the weighted residual sum of square values (σ^2) [91] of each model structure, the best fit model was identified to be that shown in figure 3.8 by the solid line, taking the algebraic form

$$\frac{\dot{m}_{ci}}{\Phi_m} = \hat{\alpha}_{th} + \hat{\beta}_{th} \cdot \sin^2\theta + \hat{\delta}_{th} \cdot \sin^4\theta + \hat{\epsilon}_{th} \cdot \sin^6\theta, \tag{3.6}$$

where the estimated model coefficients are shown in the table below.

Coefficient Label	Estimated Value	Unit
$\hat{\alpha}_{th}$	0.380	gs^{-1}
$\hat{\beta}_{th}$	48.51	gs^{-1}
$\hat{\delta}_{th}$	240.33	gs^{-1}
$\hat{\epsilon}_{th}$	-174.31	gs^{-1}

Table 3.1: Throttle body model coefficients.

A surface prediction of the throttle model is shown in figure 3.9, covering the full range of throttle angle and Φ_m combinations. Predictions of charge flow

rate that lay outside the range for which the engine tests were conducted, cannot be validated under steady-state, test-bed conditions. The throttle body would have to be removed from the engine and independently subjected to high pressure ratios at low throttle angles to simulate high engine speed operation at almost idle throttle angles.

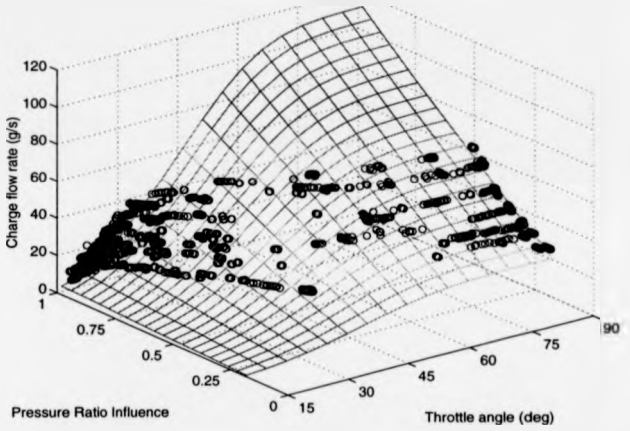

Figure 3.9: Estimation surface of throttle body model with measured engine data overlayed.

Estimates of charge flow for the identified throttle model may be seen in figure 3.10, as plotted against the actual measured charge flows. For ideal model prediction, all data points should lie on the 45° line, suggesting exact matching between the measured and estimated values.

Although the data points are seen to 'run' along this line, there is a large spread of data. This is due to the suggestions made earlier regarding the measurement techniques. However, it may be seen that the ideal model line runs through the centre of the data providing confidence in the model predictions with regard to the ability of the model to estimate trend wise agreement. For the data captured, every effort was made to reduce the spread. It was therefore regarded that the

identified model was the best achievable, as the measured values are weighted equally either side of the predictions. The weighted residual sum of squares is shown to be 2.919 for the model.

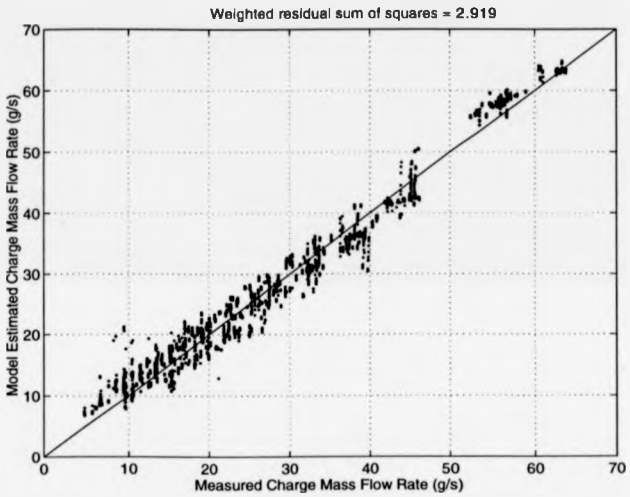

Figure 3.10: Measured throttle charge flow rates against model estimated throttle charge flow rates.

3.3.2 Inlet Port Characterisation

The port flow of air was determined in section 2.5 to be dependent upon the variables of manifold pressure and engine speed. Figure 3.11 displays the characteristic nature of the flow rate of charge through the system and it can be seen that there is an almost linear relationship between flow rate and pressure. In order to determine this relationship, linear least-squares methods were used to establish coefficient values and obtain the best fit with least residual error.

Figure 3.12 displays the linear models of charge flow and manifold pressure for speed-dependent operation. The models are shown as the solid straight lines

to the data and error bar estimations. The index 'Var' refers to the weighted residual sum of squares error, σ^2, of the models defined as [91]:

$$\sigma^2 = \frac{\sum(y - \hat{y})^2}{D_f}, \tag{3.7}$$

where y and $\hat{y}$ are the values of charge flow and estimated charge flow respectively. The term D_f is the number of degrees of freedom described by the number of data points ($ns = 4366$) less the number of model coefficients ($nm = 2$).

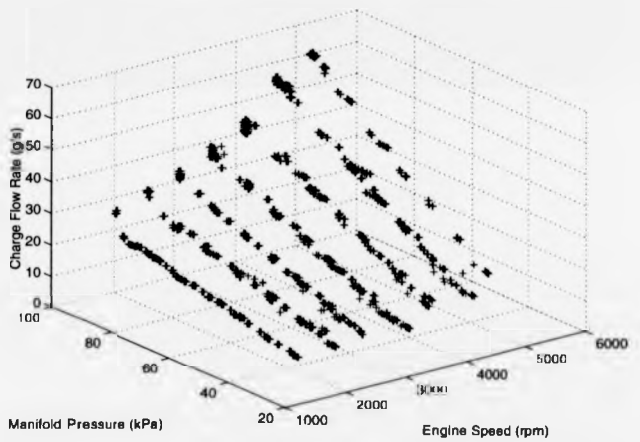

Figure 3.11: Inlet port charge flow rate map.

The models exhibit good fitting behaviour for low orders and it was found that no appreciable reduction in model error was gained for increased order models. The plots of the coefficients associated with these models, versus engine speed, are seen in figure 3.13. Least square fits are made to these coefficient values, as shown in the plot by a straight line with error bounds. It is appreciated that the 1st coefficient, which defines the gradient of the charge flow rate with changing manifold pressure, increases linearly with increasing engine speed and is acceptable considering measurement errors.

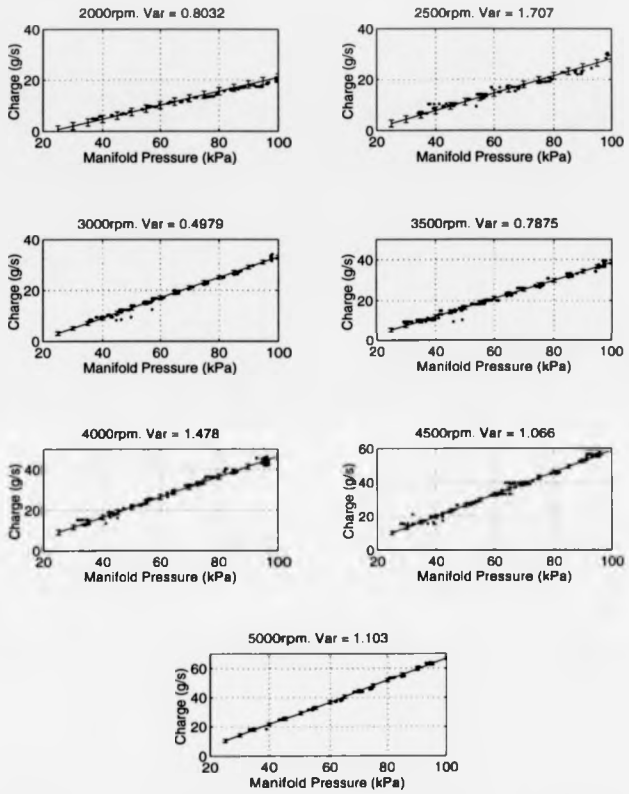

Figure 3.12: Linear charge flow rate models at given engine speeds.

The 2nd coefficient depicts the value of the origin of the charge flow for zero manifold pressure having units of gs^{-1}. This condition would occur for a completely closed throttle angle where the engine has evacuated the inlet manifold but cannot draw fresh charge through the closed intake system. The manifold pressure would theoretically drop to a vacuum for zero charge flow rate - but of course, under these circumstances the engine would stall. The model estimates for this parameter value are found to be just below zero suggesting a backflow of

charge through the inlet valves and ports. This is a phenomenon that is known to occur when to the inlet valve closure timing is set late into the compression stroke. The estimates for this parameter vary with no definite trend and it was considered that a constant value, estimated at -6 g/s, is accepted as an adequate value within the least squares estimation error and given tolerances in measurement accuracy.

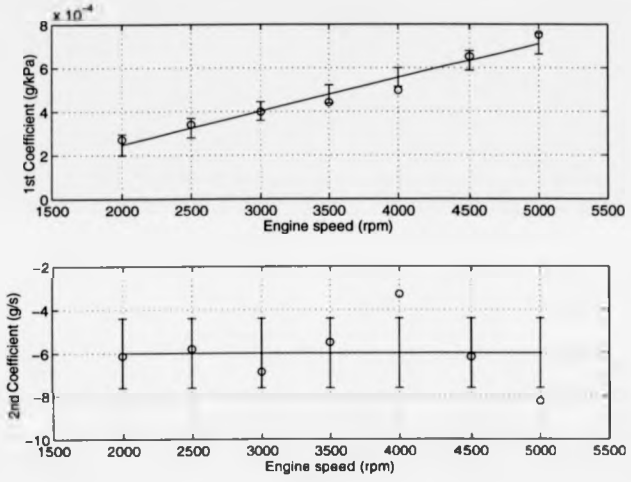

Figure 3.13: Estimated charge flow model rate coefficients dependent upon engine speed.

The port flow model is thus given by

$$\dot{\hat{m}}_{co} = \hat{\alpha}_p(N_e) \cdot P_m + \hat{\beta}_p, \tag{3.8}$$

where $\hat{\alpha}_p(N_e)$ and $\hat{\beta}_p$ are the 1st and 2nd estimated model coefficients respectively. The estimation of $\hat{\alpha}(N_e)$ is found to be linearly dependent on engine speed and $\hat{\beta}_p$ is estimated as a constant (figure 3.13), allowing equation 3.8 to take the form

$$\dot{\hat{m}}_{co} = \hat{\alpha}_{p1} P_m N_e + \hat{\alpha}_{p2} P_m + \hat{\beta}_p, \tag{3.9}$$

where the parameters $\hat{\alpha}_{p1}$ and $\hat{\alpha}_{p2}$ are the parameters of the speed-dependent $\hat{\alpha}_p(N_e)$ coefficient. The values of $\hat{\alpha}_{p1}$, $\hat{\alpha}_{p2}$ and $\hat{\beta}_p$ can then be estimated from least

squares estimation of this model to the port charge flow map. The prediction surface for the port flow model is shown in figure 3.14, where the model parameters are estimated to be :

Coefficient Label	Estimated Value	Unit
$\hat{\alpha}_{p1}$	-5.891×10^{-5}	$g \cdot kPa^{-1}$
$\hat{\alpha}_{p2}$	1.520×10^{-7}	$gs^{-1}kPa^{-1}$
$\hat{\beta}_p$	$-5.6991.$	gs^{-1}

Table 3.2: Port flow rate model coefficients.

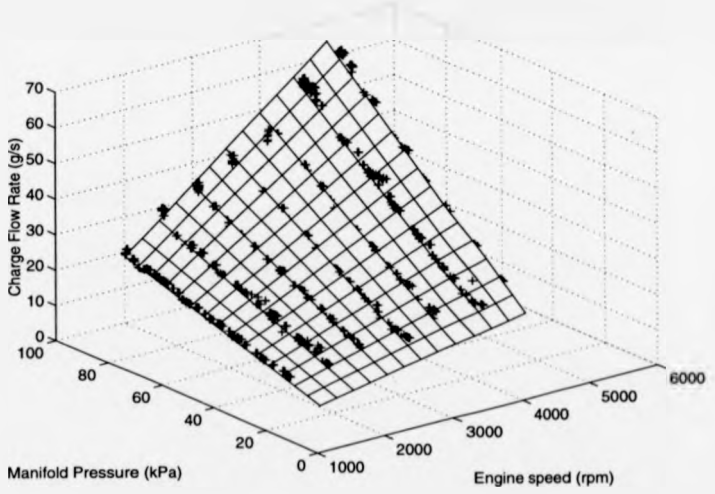

Figure 3.14: Port charge flow rate estimation surface.

The estimated values of the port flow model are seen plotted against the measured values in figure 3.15. Agreement for this model is extremely good with a total weighted residual sum of squares being 0.7796. Virtually all estimates lie on the ideal 45° line with the exception of data points at approximately 26 g/s. It is expected that these three values were not estimated accurately due to

a spurious measurement in the port model parameters - either the engine speed or the manifold pressure could have been 'corrupted' when automatically logged. They were not considered to be showing the true states of the engine as this is reflected by the dominating model prediction agreement in the remaining 4363 data points.

This demonstration of competent pressure data acquisition, therefore suggests that the spread in the throttle air flow rate, figure 3.8, is actually attributable to the throttle position measurement.

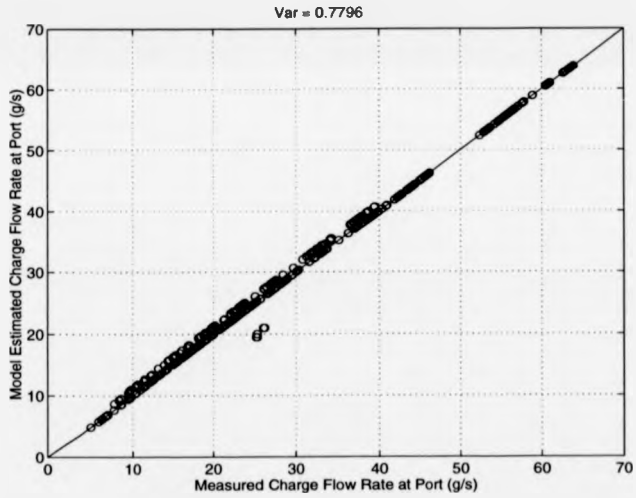

Figure 3.15: Measured port charge flow against model estimated port flow.

3.3.3 Torque Characterisation

The definition of torque in terms of meaningful physical quantities is impossible to classify explicitly and the coefficients of equation 2.49 can only be estimated by the use of regression analysis. In the absence of an established predictive torque model, many engine management systems rely on mapping exercises to

accumulate torque maps specific to an engine that allows interpolation of engine operative behaviour that was not captured during test procedures. Least squares regression is a method widely used in the estimation of such a relationship and its successful implementation can only be achieved if the quantity of data acquired is far in excess of the expected order of model. The amount of data captured during dynamometer testing numbered 4366 samples per engine variable and gave sufficient criteria for the use of least squares regression.

The order to which the regressed model should be taken is an important issue and must be chosen with care to satisfy two conditions:

- a sufficient number of terms to ensure that the data will be represented accurately, with an error of estimation and within acceptable limits without loss of detail,
- a limitation on the order of the model to eliminate overfitting and maintain the ability to filter out measurement error to reward a mean value of the dependent variable.

In order to obtain some bearing on the order to which the torque model must be raised, a similar approach to that of the port flow model was adopted to identify the independent effects of the three dependent variables. Figure 3.16 displays a series of torque models that are categorised by λ-setting and are 1st and 2nd order in N_e and $\dot{m}_{co}$, respectively. Higher order models were investigated, but no appreciable decrease in the residual sum of squares was achievable in comparison to that found for the increase from 1st to 2nd order in $\dot{m}_{co}$. An increase in order of N_e alone would raise the number of terms in the model from 5 to 9. This gave evidence for the suitability of the orders placed on $\dot{m}_{co}$ and N_e.

A similar approach to engine parameter modelling was adopted by Mencik and Blumberg [92]. Pollutant and fuel flow data from steady-state maps was modelled

using the independent variables of spark timing, A/F ratio and EGR through the use of the Taylor series expansion to determine third order models (and higher) of partial derivatives for the proposed functions. In this manner, the three variable regressed model lead to a twenty term algebraic equation of the deviations from average variable values.

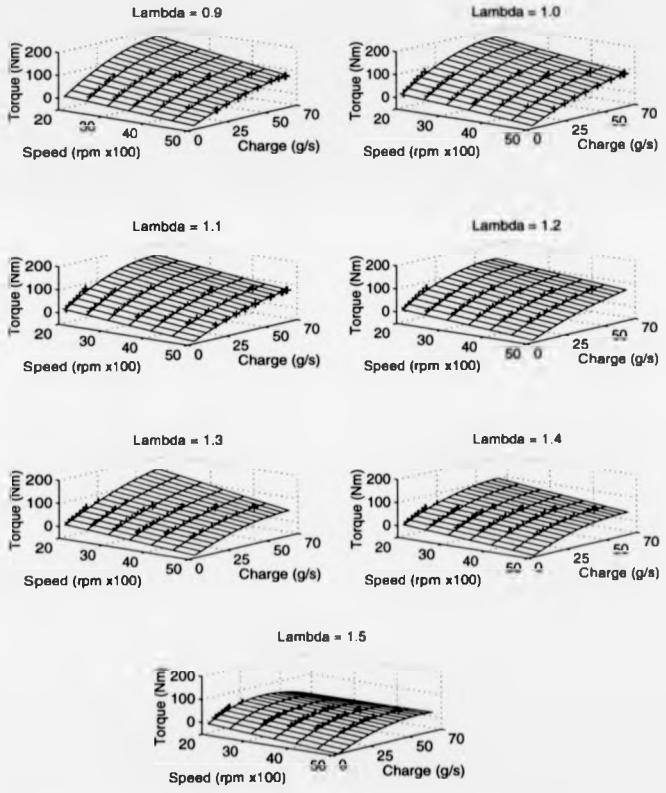

Figure 3.16: Engine torque models at given λ-settings.

With the introduction of the A/F ratio setting, it was also established that λ should be raised to 2nd order to give sufficient estimates of torque whilst being insensitive to overfitting. The resulting model involves 18 terms and a residual

sum of squares value that is comparably low to that of an extra magnitude order model that has many more coefficients. The final torque model is given by :

$$\hat{T}q_e = (\hat{\alpha}_{T1}N_e + \hat{\alpha}_{T2})\left(\hat{\beta}_{T1}\dot{m}_{co}^2 + \hat{\beta}_{T2}\dot{m}_{co} + \hat{\beta}_{T3}\right)\left(\hat{\delta}_{T1}\lambda^2 + \hat{\delta}_{T2}\lambda + \hat{\delta}_{T3}\right), \quad (3.10)$$

when expanded gives:

$$\begin{aligned}\hat{T}q_e = {} & Tq_1N_e\dot{m}_{co}^2\lambda^2 + Tq_2N_e\dot{m}_{co}^2\lambda + Tq_3N_e\dot{m}_{co}^2\lambda + Tq_4\dot{m}_{co}^2\lambda^2 + Tq_5\dot{m}_{co}^2\lambda + \\ & Tq_6\dot{m}_{co}^2 + Tq_7N_e\dot{m}_{co}\lambda^2 + Tq_8N_e\dot{m}_{co}\lambda + Tq_9N_e\dot{m}_{co} + Tq_{10}\dot{m}_{co}\lambda^2 + \\ & Tq_{11}\dot{m}_{co}\lambda + Tq_{12}\dot{m}_{co} + Tq_{13}N_e\lambda^2 + Tq_{14}N_e\lambda + Tq_{15}N_e + Tq_{16}\lambda^2 + \\ & Tq_{17}\lambda + Tq_{18}. \end{aligned} \quad (3.11)$$

The regressed model format is therefore given as

$$\mathbf{Tq_e} = \mathbf{F_{Tq}} \cdot \hat{\mathbf{P}}_{\mathbf{Tq}}. \quad (3.12)$$

where $\mathbf{Tq_e}$ is the column vector of measured torque data, $\mathbf{F_{Tq}}$ is the matrix of N_e, $\dot{m}_{co}$ and λ products and $\hat{\mathbf{P}}_{\mathbf{Tq}}$ is the column vector of estimated model coefficients.

The final value of weighted residual sum of squares is calculated as 1.695 for

the estimated parameter coefficients :

$$\hat{\mathbf{P}}_{\mathbf{Tq}} = \begin{bmatrix} Tq_1 \\ Tq_2 \\ Tq_3 \\ Tq_4 \\ Tq_5 \\ Tq_6 \\ Tq_7 \\ Tq_8 \\ Tq_9 \\ Tq_{10} \\ Tq_{11} \\ Tq_{12} \\ Tq_{13} \\ Tq_{14} \\ Tq_{15} \\ Tq_{16} \\ Tq_{17} \\ Tq_{18} \end{bmatrix} = \begin{bmatrix} -2.4245 \times 10^{-5} \\ 5.0096 \times 10^{-5} \\ -1.9569 \times 10^{-5} \\ 0.0434 \\ -0.08319 \\ -0.00930 \\ 0.0016937 \\ -0.003131 \\ 8.70495 \times 10^{-4} \\ -6.83520 \\ 11.54591 \\ 1.49873 \\ 0.0053976 \\ -0.0137866 \\ -0.004371 \\ -65.66949 \\ 145.27382 \\ -66.34686 \end{bmatrix} \tag{3.13}$$

Figure 3.17 displays the final prediction surface of model 3.12. The model exhibits a reduction in output torque for decreasing λ-value and predicts the peak value at stoichiometry.

Figure 3.18 displays the model torque estimates against the measured values. The spread of data is seen to fall equally about the 45° line without any dominance in any particular region. This demonstrates a good choice of model order and also the variability of torque on the three dependent variables. Inclusion of the spark timing may have reduced the computed residual sum of squares ($\sigma^2 = 1.695$) but, as mentioned previously, δ_s was maintained at MBT during all testing and was not logged. The torque model was therefore deemed optimal for the acquired data and for the level of model order.

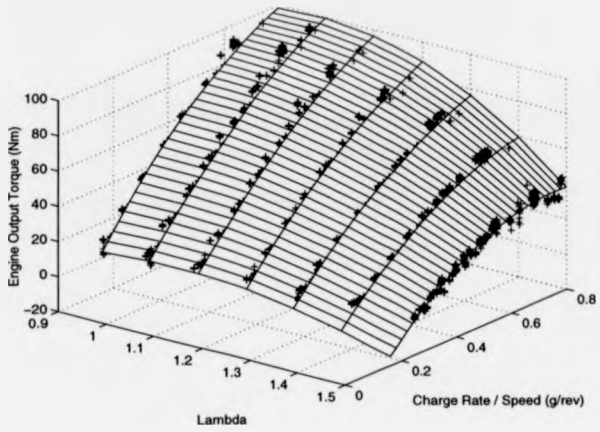

Figure 3.17: Engine torque model prediction surface.

3.4 Zirconia Sensor Characterisation

To characterise the zirconia sensor, for which the response is shown in figure 2.8, a study in the application of single-input-single-output (SISO) modelling was conducted. The approach taken was to isolate the sensor response by affecting changes in the A/F ratio whilst under static engine operation. This was completed by modulating the input voltage to the gas pressure regulator in the gas feed line, thereby affecting changes in the metered gas entering the air intake system. The regulator input and corresponding zirconia voltage output were logged to provide a set of input/output voltage pair traces that would allow identification methods to estimate the sensor dynamic characteristic.

The regulator input voltage was precisely controlled by the use of a proprietary software package known as "Plant System Identification" (PSI). The voltage sequence was predefined in the PSI environment and was sent to the regulator via an input/output board. Similarly, the sensor output voltage was acquired in the PSI environment, which itself was operating on a Toshiba T3200 laptop P.C. It

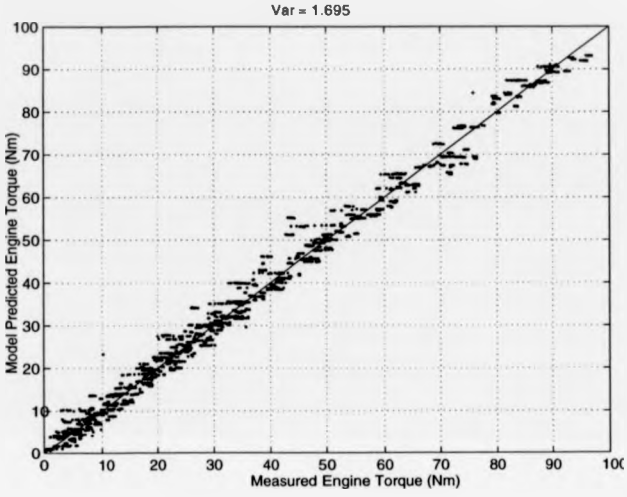

Figure 3.18: Measured engine torque versus model estimated torque.

was not the intention of the exercise to match the sensor output voltage with the exact input A/F ratio entering the combustion chamber, since the sensor output voltage varies significantly with operating temperature, as explained previously in section 1.2.3. If this was the intention, an inconsistent set of results would have been acquired throughout the period of testing, due to the operating temperature of the exhaust gases changing, which would not allow for comparisons of different operating point responses. The purpose of the modelling exercise was, therefore, to investigate the characteristics of the sensor dynamic behaviour at arbitrary operating points as the combustion A/F ratio was varied.

The SISO system model can be seen in figure 3.19; the aim of the model is to identify a transfer function relating the regulator input voltage signal $u(t)$ and the zirconia sensor output voltage signal $y(t)$. The system is described as a "Black-box" where the internal behaviour of the *plant* is not required to be known in detail as it is only the purpose of the model to relate the two known signals.

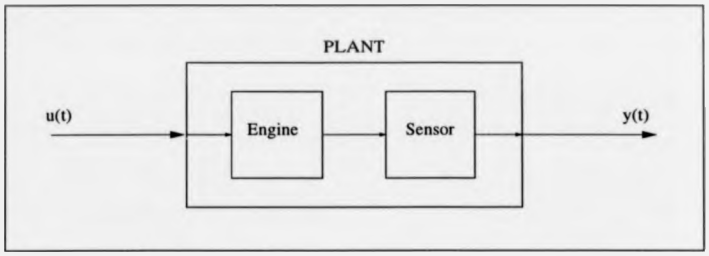

Figure 3.19: Single-Input-Single-Output engine representation.

Two examples of input/output voltage signals are shown in figures 3.20 and 3.21, where the engine operating condition is maintained at 75Nm torque and 2000 rpm for both tests. The regulator input voltage is defined as a modulation about a chosen bias voltage, with a maximum input of 5 volts. The two examples display the behaviour of the sensor to regulator signals of bias 2V and 3V with modulation amplitudes of 1V and 1.5V respectively. The corresponding output voltages display the characteristic "steps" between the rich and lean response voltages where the time spent during transition is extremely small.

Immediately obvious is the existence of a time delay between the input and output, where the input voltage step changes occur every two seconds. This is due to the gas transport delays that have been described in section 2.8. Values of time delays for the response data displayed are approximately 170 ms for step-down, and approximately 220 ms for the step-up response. These values are consistent with values detailed in section 2.8.

Also, it can be seen that there is a 'rounding' effect as the sensor begins to respond to the step change and also as the sensor output approaches its final value. This is attributable to a nonlinear sensor characteristic where the gradient outputs in the rich and lean regions are less steep than during the transition region - see figure 2.8. The sensor is therefore excellent at returning information as to whether the charge is rich or lean of the stoichiometric level - which is its primary

incentive for use as a feedback sensor in closed loop A/F ratio control.

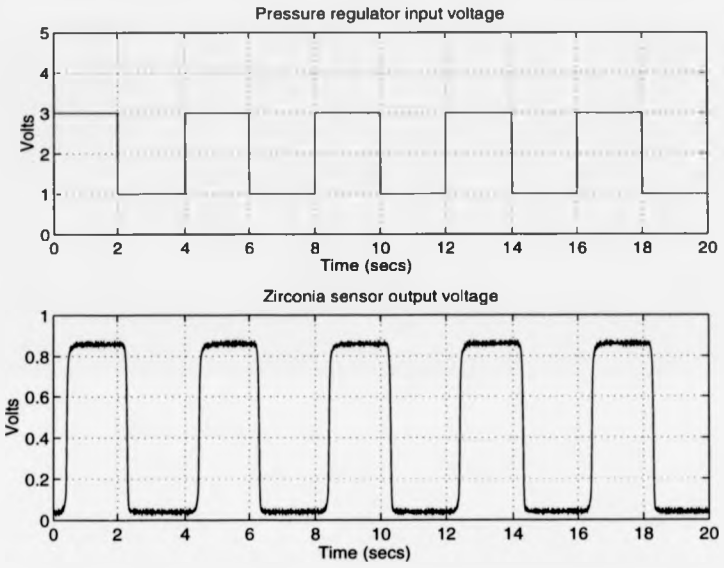

Figure 3.20: Pressure regulator pulse test for 1 volt amplitude modulation on a 2 volt bias offset.

By manipulating the output voltage trace, it is apparent that the plant, represented in figure 3.19, is a time varying system for which the time delay for the step-up response differs from the time delay for the step-down response. This is demonstrated as seen in figure 3.22 where the sensor output trace of figure 3.20 has undergone some rearrangement. A time frame of 2 seconds has been taken around one step-up response and the subsequent step-down response. The step-down trace has been inverted and then both traces are plotted on the same time axis. It can be seen that the step-down trace is much more "rapid" in its response to the input signal by the existence of a shorter time delay. In fact, it could be stated that the sensor appears to be particularly sharper overall in its response to a step-down input as the rounding effect (as mentioned previously)

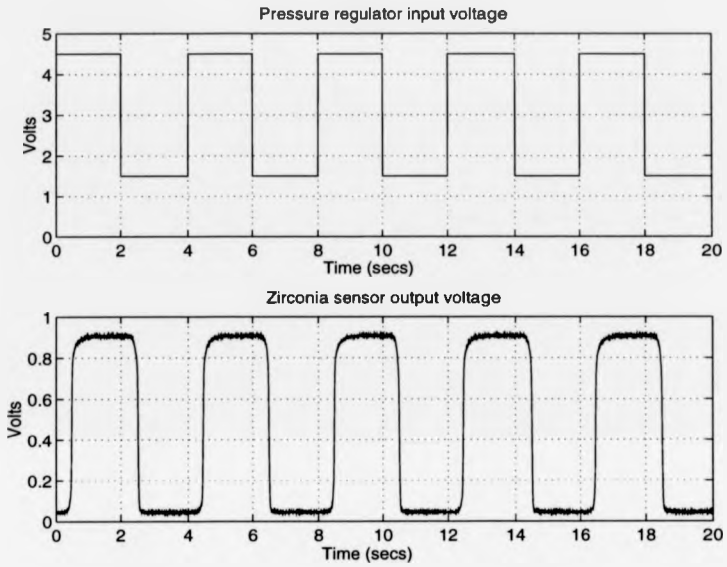

Figure 3.21: Pressure regulator pulse test for 1.5 volt amplitude modulation on a 3 volt offset.

is less obvious in comparison to the "smooth sweeping" response of the step-up response. Coupled to the fact that similar transition gradients are seen for both traces, this demonstrates the hysteresis behaviour that is typical of a zirconia sensor. The hysteresis is attributable to the chemical nature of the sensor where catalytic surface activity is dependent upon the concentration of free oxygen.

It is not expected that the variation in time delay was due to the engine behaviour as the operating point was maintained at a constant speed and load. Also, the input modulation was not produced through pulsing the air flow, which would produce significant fluctuations in both speed and combustion torque, but small modulations in the gas flow simply to bring about changes in A/F ratio.

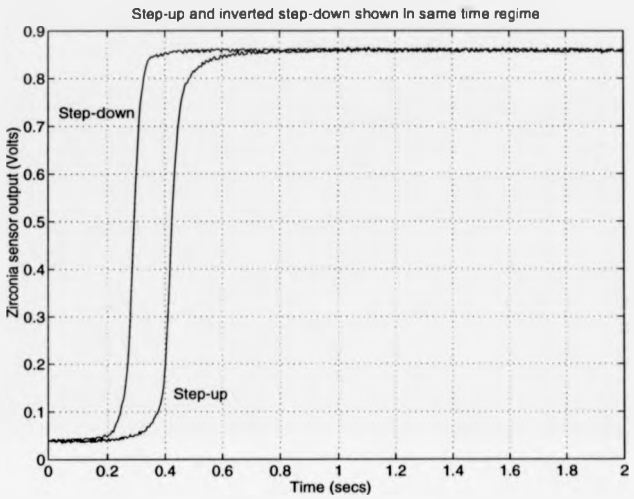

Figure 3.22: Step-up and inverted step-down sensor response traces.

ARX Model Application

A simple approach to modelling an input-output system, is in terms of the linear difference equations of the input and output signals which describe the *equation error model* [93] as:

$$y(t) + a_1 y(t-1) + a_2 y(t-2) + \cdots + a_{n_a} y(t-n_a) = \qquad (3.14)$$
$$b_1 u(t-1) + b_2 u(t-2) + \cdots + b_{n_b} u(t-n_b) + e(t),$$

which can be written in the concise form of

$$y(t) = \frac{B(q^{-1})u(t)}{A(q)^{-1}} + \frac{e(t)}{A(q^{-1})}. \qquad (3.15)$$

The term $e(t)$ defines the white-noise in the system which enters as a direct error in the difference equation. The term q^{-1} defines the short hand notation for the sum of the past values of the input-output variables, known as the *backward shift operator* described by

$$q^{-1}u(t) = u(t-1), \qquad (3.16)$$

which defines

$$A(q^{-1}) = 1 + a_1 q^{-1} + a_2 q^{-1} + \cdots + a_{n_a} q^{-n_a}, \tag{3.17}$$

$$B(q^{-1}) = b_1 q^{-1} + b_2 q^{-1} + \cdots + b_{n_b} q^{-n_b}. \tag{3.18}$$

The final model may be written in the general form as

$$y(t) = G(q^{-1}, \theta)u(t) + H(q^{-1}, \theta)e(t), \tag{3.19}$$

where the transfer functions G and H are described as

$$G(q^1, \theta) = \frac{B(q^{-1})}{A(q^{-1})}, \qquad H(q^1, \theta) = \frac{1}{A(q^{-1})}, \tag{3.20}$$

in terms of the vector of adjustable model parameters :

$$\theta = [a_1 \; a_2 \; \cdots \; a_{n_a} \; b_1 \; b_2 \; \cdots \; b_{n_b}].$$

The general black-box model equation 3.19 describes a family of transfer function models that can be defined by the particular manner in which the rational functions $G(q^1, \theta)$ and $H(q^1, \theta)$ are parameterised. The actual model of equation 3.15 is known as the *ARX* model of the present output $y(t)$ as defined by the **A**uto**R**egressive term of $A(q^{-1})$, and the e**X**ogenous (extra variable) input of the term $B(q^{-1})$ [94]. Other cases of models defined by the chosen structure of the general equation 3.19, include the models known as *ARMAX*, *ARMA*, *ARIMA* and the *ARARX* - details of which can be found in [93].

The application of the ARX model to the λ-sensor input/output data was conducted in the *Matlab* analysis environment, mentioned previously, where the parameter estimates of the chosen order of model are computed in a least squares sense. The magnitude of the delay between input and output is defined in terms of the number of previous input data increments, nk, in the model equation

$$A(q^{-1})y(t) = B(q^{-1})u(t - nk) + e(t). \tag{3.21}$$

The uppermost plot in figure 3.23, demonstrates the application of the ARX model to the input/output signals of figure 3.20. The sensor data is plotted as a dashed line, and the ARX model is represented as a solid line for clarity. The orders of the A and B parameters are low, both being chosen as 1, and it can be seen that the model over-estimates both the minimum and maximum voltage output values. The level of delay is chosen to match the step down response, of the order of approximately 51 time increments, which corresponds to a time delay of $\approx 0.2s$. The rise time of the ARX model is also seen to be much slower than the sensor, which demonstrates the essential fast switching nature of the sensor non-linearity.

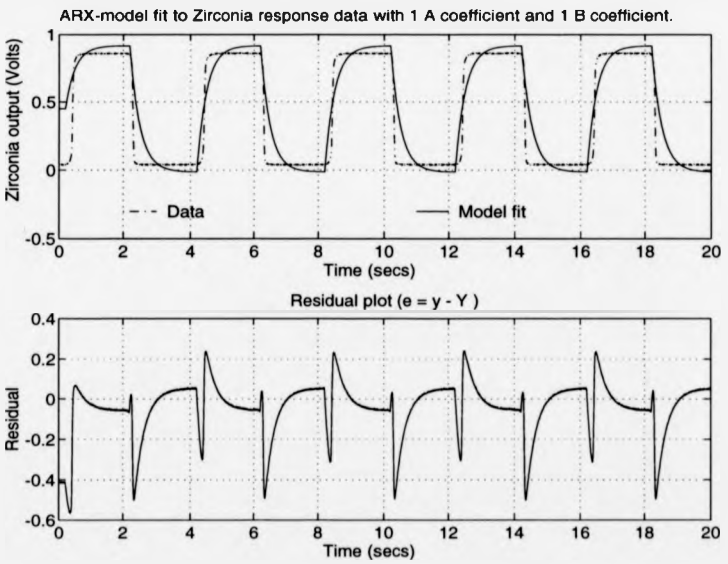

Figure 3.23: ARX model fit to zirconia sensor output. Model parameter order A=1, B=1.

The lower plot in figure 3.23, displays the error that exists between the measured sensor response and the ARX estimates to the same input signal. The error signal regularly oscillates about the zero point with large magnitudes in response

to both step-up and step-down simulations. The steady-state response settles in a position with either negative or positive bias offset revealing the model prediction inadequacy.

Upon increasing the model order to improve the model fit, the plots of figure 3.24 result. The model order of parameter $A(q^{-1})$ was increased to 3 whereas $B(q^{-1})$ remained at 1. The delay is maintained at $nk = 51$ to match the step-down time delay, which is shown in the error plot (lower) to reduce the magnitude of the step-down error in comparison to that of the step-up error.

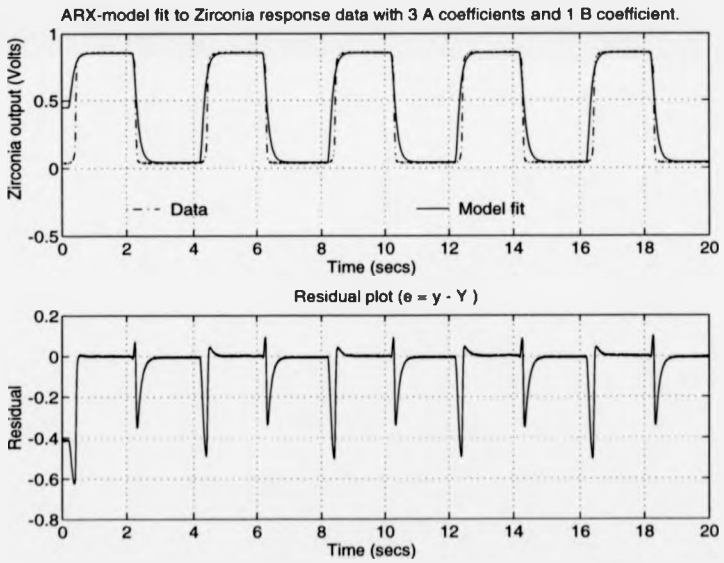

Figure 3.24: ARX model fit to zirconia sensor output. Model parameter order A=3, B=1.

The final steady-state prediction is much improved, over that shown in figure 3.23, with further improvements to the rise time of the ARX model. The error signal is seen to reside on the x-axis and with far less oscillatory behaviour than that of the error signal in figure 3.23. This second ARX model is a much closer

estimation of the system order, and defined by the parameter estimates of

$$a_1 = -1.312, \quad a_2 = -0.206, \quad a_3 = 0.522 \quad \text{and} \quad b_1 = 0.0016.$$

However, large error spikes still exist for this model (especially for the step-up response estimates) suggesting further model improvements should be sought and particularly in respect of the variation in time delay. Further investigations of varying ARX model order were applied but with no great improvement over that demonstrated in figure 3.24 for the given model order.

Much effort could be expended in the process of constructing further models that would produce better estimation and closer representation of the input-output data presented here. Indeed, from the findings of ARX model results presented above, other model structures would be required to take due consideration of the time delay variation. However, it was felt that this was not a worthy route of investigation, since a number of conclusions can be drawn from the exercise completed thus far. Further, it was regarded that it would be a fruitless task to model highly specific input/output signals for the exact engine operating points displayed, as a typical engine working under normal day-to-day conditions encounters a broad range of operating points with fluctuations in many engine states, not just gas flow. It would be impossible to characterise the sensor for all possible combinations of operating conditions.

From the results presented in this section, hysteresis is acutely evident as the A/F ratio modulates between rich and lean settings. The sensor time delay in responding to a change in A/F ratio varies, and it is postulated that the sensor responds more quickly when the A/F mixture is rich (step-down response, see figure 3.22) due to higher exhaust temperatures stimulating the active nature of the platinum electrode. The sensor displays heavy dependency on its non-linear characteristic which itself, although not demonstrated with absolute clarity here, is dependent upon the operating temperature governed by the exhaust gases. It

is concluded, therefore, that the sensor is highly sensitive to the variations in A/F ratio when crossing stoichiometry to give suitable information pertaining only to whether the charge is rich or lean. Due to the temperature effects and the variation in exhaust temperatures that could be expected under engine operation, the zirconia sensor is not deemed a suitable device for issuing information on the exact value of the A/F ratio.

3.5 Summary

The engine experimental work outlined in chapter 2 that was required to allow the completion of the model, has been presented. The approach to engine dynamometer testing and the experimental arrangement has been reported and results are seen through various engine and emission maps. The development of the non-linear submodel characteristics, and subsequent algebraic equations, have been detailed with illustrations of the accuracy of the models. A limited SISO modelling study has also concluded that the zirconia exhaust gas oxygen sensor displays highly non-linear and hysteresis behaviour. The dynamics of which can both vary over the duration of engine operation of a typical vehicle.

The key aspects of the developed model are the throttle and port air flow rates submodels. The control of the fuel flow rate must be determined from the air flow in order to achieve the desired A/F ratio. These air flow rates are determined by modelling the throttle angle effects, engine speed and subsequent manifold pressure. This approach embodies a realisation of the manifold filling and emptying effects. The manifold is considered as a volume which exerts a lag phenomena between the port flow out and the throttle air flow in. By taking full consideration of the influences of the throttle valve (at inlet) and engine speed (at outlet) the manifold air mass is modelled and the pressure derived. This state is then fed back and used as an input to both the throttle and port air flow rate

submodels.

Model validation is an important step in the process of building models of any type. Ideally, the model should be constructed from a data-set captured solely for this purpose. Validation of the model should then be verified against a second data-set captured independently from the first. In this manner, the model realism and the degree of approximation of the actual system can be ascertained.

However, after having built the engine model in this thesis, there was not sufficient resources or funding to maintain the natural gas engine under test-bed conditions to allow a second data-set to be captured. This would have allowed for a full validation process to be undertaken. The decision was therefore taken to validate the model against research papers that detail engine tests on engine systems as close as possible to that used in the thesis. The following chapter begins with some initial simulations of the coded engine model and compares them against recent published work on actual engine systems. These papers report on transient engine tests similar to those that have been conducted in the simulations. In the light of the inability to capture adequate validation data, it is believed that this approach justifies the validity of the engine model.

It has been stated that steady-state derived maps may lack the ability to control for the required conditions under fast dynamic operation. This is also true when using look-up maps to represent dynamic systems. However, the submodels of the engine model in this thesis make use of continuous differential equations to simulate the engine states. In this manner, the state estimates are not discretised would be for a look-up map which must linearly interpolate between captured data points to obtain estimates in regions that where not originally measured. The advantage of using differential equations, therefore, results from their computational efficiency as well as their ability to embody the underlying physical relationship between states. This relationship was determined during the regression analysis

step of the model building process.

When an engine state progresses outside the range of a map, the differential equation maintains the characteristic law and produces estimates which lie close to the actual state values. This is in direct contrast to map estimation techniques, which typically rely on linear extrapolation under these conditions, which may result in rather inaccurate estimates

The impetus now is to use the model to conduct A/F ratio control investigations for a range of controller structures. With the inclusion of the engine operation dependency upon A/F ratio settings, the behaviour of the engine can be simulated for transient operating conditions under numerous speed and load combinations. The following chapters are therefore concerned with the use of the model to complete these studies.

Chapter 4

Conventional GFI Control

4.1 Aims

The purpose of this chapter is to investigate the behaviour of the gas engine model under the control of the "gaseous fuel injection" controller (G.F.I.). This system is an engine conversion unit which allows the vehicle to run on either natural gas or petrol. The controller employs a closed-loop feedback strategy incorporating the λ-zirconia sensor described in the previous chapter. The feedback algorithm is that of "proportional-plus-integral" (PI) control and is simulated in the controller block of the engine model.

This chapter shall investigate the structure of conventional electronic fuel control systems, applied to internal combustion engines. The performance of closed-loop PI-control shall be investigated through the extensive use of the developed model in the previous chapters. The intention is to characterise PI-control behaviour for a variety of controller sampling rates and engine operational conditions. The aim is then to establish motivation and suggestions for possible control improvements that have been highlighted from simulation results.

The non-linear model is programmed in the continuous simulation language, ACSL, and is shown in appendix D. The integration runtime algorithm used is the Runge-Kutta fourth order algorithm, denoted by the 'IALG=5' command in the

model code. This is an efficient fixed step algorithm recommended for use with mechanical systems [95]. The Runge-Kutta fourth order routine was favoured over lower order algorithms, as it advances the state with 4 derivatives per step (one at the beginning, two at the midpoint, and one at the end) as opposed to just 1 or 2. The Runge-Kutta algorithm is also used as the system being modelled is not expected to have frequencies that differ between 3 and 4 orders of magnitude - as is the case for stiff systems.

4.2 Electronic A/F Ratio Control

Modern automotive engines use an engine management unit (EMU) to control the fuel flow rate to that of the incoming air flow. Figure 4.1 depicts a simplified structure of an electronic engine control system focusing on A/F ratio control. The EMU receives sensor signals that relate the engine conditions of speed, N_e, manifold pressure, P_m, and exhaust λ-voltage. The microprocessor controller algorithm then processes the information, and issues an output signal commanding the gas fuel injector unit.

This control unit layout is comparable to that of a conventional petrol engine - with the obvious difference being the replacement of the petrol injector with that of the gas injector. The purpose of the control unit is still the control of the air/fuel ratio at the desired set-point.

The two signals of P_m and N_e enable the controller to determine the port flow rate of air from the speed-density model of equation 2.44. The *nominal* fuel flow command is then issued, which constitutes the open-loop control action of conventional A/F ratio control structures.

The signal from the λ-sensor constitutes the closed-loop feedback controller. As discussed in sections 2.9 and 3.4, this signal will typically vary from 100 mV to 900 mV. Due to the EGO-sensor being placed in the exhaust stream, the engine

time delay is encountered and the feedback control algorithm will only receive sensor signals pertaining to the A/F ratio t_d seconds previously. It begins to emerge, therefore, that this feedback control approach *may* suffer in its designed control task, if the dynamics of the system under transient operation are comparable, or faster, than the time delay.

Further, this prompts the requirement for high controller sampling and reaction times to be faster than possible throttle transition times, to ensure that misfire is avoided.

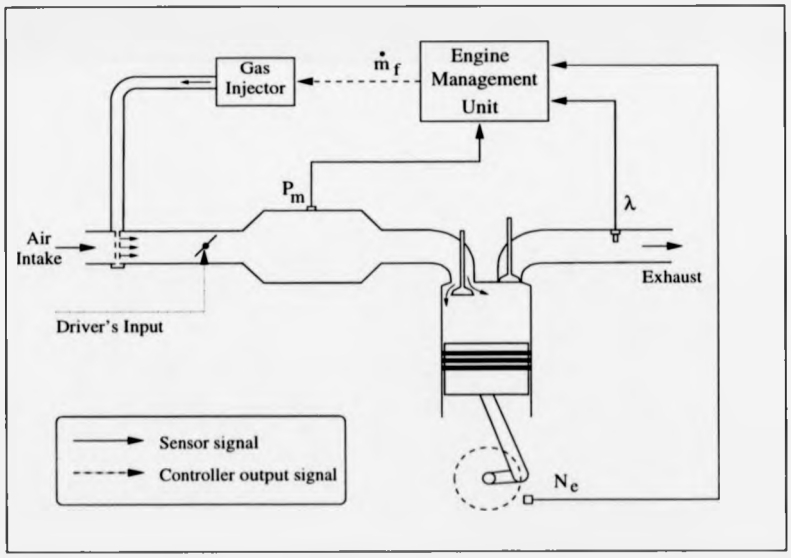

Figure 4.1: Electronic engine management A/F ratio control schematic.

4.2.1 Microprocessor Control

In an ideal situation, a controller of any physical system would have the ability to continuously monitor the input signals and subsequently issue a continuous control output signal (analogue control). However, in the practical world, a controller is

obliged to sample the input data and to issue the control signal at some discrete time interval later. This time delay is defined by the microprocessor speed and the controller can only output the control signal after one sample period has past [56].

Event-Based Sampling

For engine controllers, it is common for sampling action to be based upon events of an engine state. This is because the discrete nature of the 4-stroke reciprocating action provides a natural sampler of the engine behaviour [96, 97]. The crank angle defines the timing of the valve opening and closing events, and therefore determines the air intake duration. If the controller sample rate can be based on the crank-angle event, then the fuel can be metered to the estimated air flow for the current intake event. It was concluded by Chin and Coats [98] that, apart from the fuel dynamics, all other dynamics appear to be less variable in the crank-angle domain under varying operating conditions. This is because it is the discrete nature of the piston and valve arrangement that govern the timings of charge induction and combustion events. This is the motivation behind event-based control as opposed to fixed-rate sampling in the time domain.

But event-based sampling does have its drawbacks. For a four cylinder engine, an intake event occurs twice every crank rotation. This corresponds to a controller sample every 180° of crank angle. It can then be appreciated that sample intervals will vary significantly over a typical operating range. At idling conditions, of approximately 800 rpm, sensor samples will be taken every 37.5 ms ($\approx$ 27 Hz). However, during high speed conditions of, say, 5000 rpm, the sample rate is much faster, occurring every 6 ms ($\approx$ 167 Hz).

The principle input of the engine is the throttle angle and, as shall be demonstrated by the forthcoming simulations, has the ability to alter engine states very

rapidly. The rate at which the throttle condition varies is unpredictable and, with the exception of drive-by-wire throttles, decided upon by the driver. Hendricks [56] suggests that a minimum throttle opening time of 50 to 80 ms is achievable for a change of 30° to 60°. If this condition were to occur at idle, the suggested sample rate of 37.5 ms is deemed too slow to fully resolve the changing states. The higher speed induced sample rate, however, will allow many more samples to be taken during throttling, permitting improved control through increased status information. Clearly, the continually changing conditions of both the throttle input and engine speed will present problems for the controller in completing its task when conditions are changing significantly between samples.

Hendricks [56] also presents a good discussion on the inefficient use of microprocessors at slow engine speed. Under such conditions, long periods of microprocessor idle time are encountered, whilst at high speeds the microprocessor will suffer large computational burdens.

Fixed-Rate Sampling

Fixed-rate sampling controllers ensure that the system is sampled at constant intervals. If the microprocessor speed can be increased sufficiently, even the fastest throttle changes can be resolved. For the throttling speeds mentioned above, a sampling speed of 5 ms is deemed appropriate for capturing sufficient information of the changing conditions to enable competent transient A/F ratio control [56]. The controller will be subject to a constant computational demand due to the equidistant data samples (with respect to time). This ensures that long periods of idle time do not occur.

As the technology of semiconductor processors advances, increasing controller speeds will become both achievable and affordable. Fast controllers of this type, shall be incorporated across the range of vehicle specifications, in a continuing

effort to reduce all vehicle emissions.

The advantage of fixed-rate control over event-based sampling, therefore, is clearly the ability to detect changing conditions even at low engine speeds. The control of A/F ratio will be much improved during rapid transient operation over event-based control, which is oblivious to the rapidly changing engine states at low speeds.

4.3 Nominal Open-Loop Fuel Command

The underlying fuel flow command is controlled by the action of what is known as the *nominal fuel control.* A schematic of nominal fuel control can be seen in figure 4.2. In conventional A/F ratio control systems, the air flow is estimated from the speed-density model of equation 3.9 (or more usually by an engine map) embedded in the microprocessor. The nominal fuel flow is then computed as the product of the air flow rate and the nominal gain, K_{nom}. The value of K_{nom} is actually the inverse of the stoichiometric ratio, A/F_s, to ensure that the desired fuel flow is commanded to achieve stoichiometry for the fuel type used. The nominal fuel is thus computed as

$$\dot{m}_{f_{nom}} = \frac{\hat{\dot{m}}_{ao}}{\lambda_{des} \cdot (A/F_s)} \tag{4.1}$$

$$= K_{nom} \cdot \hat{\dot{m}}_{ao} \tag{4.2}$$

where λ_{des} is the desired λ-setting of 1 for catalytic systems.

Some manufactured engines use a dedicated air flow sensor, such as a hot wire anemometer [99], to estimate the air flow, but these tend to be found in higher specification engines.

The estimated air flow is denoted by the symbol "^" in figure 4.2, to distinguish it from the actual engine air flow, as there is expected to be some degree of estimation error. The action of nominal control is essentially open-loop and is unable

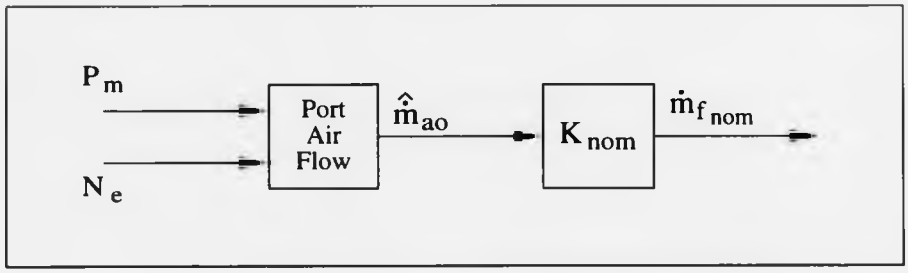

Figure 4.2: Nominal fast open-loop fuel command.

to detect errors that may occur due to inaccurate flow estimations. Nominal control does have one significant attribute - it's response to the variation in system operating conditions is considered to be fast, as it does not encounter the entire system time delay t_d. Since the port airflow is the only input to the controller, the only dynamic elements that elapse before the controller takes effect, are those of the inlet manifold.

4.3.1 Initial Simulation Results

The non-linear model developed in the previous two chapters, is programmed in the simulation language ACSL, as seen in appendix D. In order to demonstrate the successful execution of the model code, and to display the dynamic behaviour of the engine, the work carried out in this section shall be conducted solely under the nominal fuel controller, using the air flow rate equation 3.9.

It can be appreciated therefore that differences will exist between this method of air flow estimation and that derived from a map. This is due to the algebraic equation being an estimated model of the steady-state derived data. It is not the intention in this section to explore the exact differences between each approach - but to concentrate on the requirements of the control algorithm. Full investigation and discussion is given to the relative approaches in section 6.2 'Speed Density

Air Flow Mapping'. For the purposes of these early simulations, the controller is fed the exact value of the estimated are flow rate, thereby assuming perfect measurement.

The value of λ_{des} is set equal to 1, such that the desired A/F ratio is stoichiometry. Thus, any excursions away from $\lambda = 1$ will depict an incorrect fuelling command from the controller.

The first simulation is conducted for, what is considered to be, a relatively mild throttle change, and can be seen in figure 4.3. The engine is set to be in first gear operation by the selection of the corresponding flywheel inertia, as detailed in Appendix A.2. An initial steady speed is maintained under a low external torque setting. After two seconds, the throttle is increased by 5 degrees from its initial position (required to establish 2000 rpm) as a ramp over one second duration, figure 4.3(a). The throttle is maintained stable for a further 7 seconds until it is brought back to its initial position - again over a one second period.

The engine torque is seen to increase rapidly, figure 4.3(e), in response to the increasing air flow and then stabilise as the throttle motion comes to rest and engine speed increases. The load torque can be seen to increase gradually, due to modelled engine loads, allowing the engine speed to increase to a maximum of 3100 rpm, figure 4.3(c). Similarly, as the throttle angle decreases, the engine combustion torque decreases more rapidly than load torque allowing the speed to return to its initial state.

The throttle air flow rate and the port air flow rate (figures 4.3(b) and 4.3(d) respectively) are simulated using the algebraic equations 3.6 and 3.9 respectively. The port air flow map is not used to estimate port air flow at this stage.

The differences in the throttle air flow and the port air flow are due to the manifold filling dynamics. For both step up and down responses, the throttle air flow can be seen to respond rapidly to changes in the throttle input. The

port flow encounters the effects of the manifold volume dynamics, by displaying a slower response than throttle air flow. The slight overshoots observed seen in figure 4.3(d), are attributable to the abrupt throttle effects on manifold pressure.

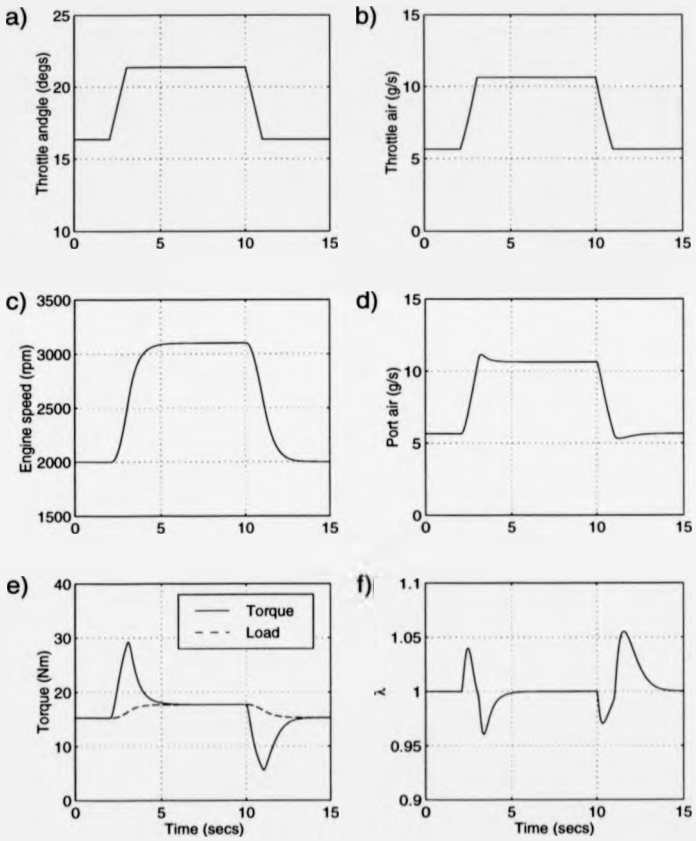

Figure 4.3: Engine simulation in first gear. Throttle ramps conducted over one second duration displaying estimated engine transient behaviour.

The λ-trace, figure 4.3(f), displaying the effects on the A/F ratio, can be seen to be maintained ideally at one during steady throttle periods. As soon the throttle varies, steady A/F ratio is lost and rich and lean excursions are

encountered. These excursions lie outside the acceptable window limits, as defined in section 1.2.3, and gives the first indication as to where the problems of A/F ratio control lie, i.e. during transient operation. Due to the fact that the throttle varies by a small amount (5°) near closure angle, the simulation displays the consequence of the torque map shown in figure 3.2. The throttle input behaviour at low angles is highly influential on the engine system as a whole, and excites large changes of state for the duration of transition.

The manifold pressure and fuel flow rate traces for the simulation are shown in figure 4.4. It can be seen the the fuel flow trace of figure 4.4b), follows that of the port air flow in figure 4.3d), since the fuel command is simply taken as the stoichiometric fraction of the air flow rate - defined by equation 4.1.

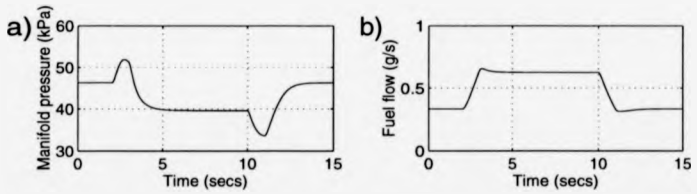

Figure 4.4: Manifold pressure and fuel flow simulation traces.

For reasons of a practical nature, it was unfortunately not possible to obtain transient experimental data from the engine. Had the engine been subjected to identical dynamic conditions, a model validation study could have been undertaken, with a direct comparison of actual engine behaviour to that of the model estimated behaviour. However, a report by Wu et. al. [70] displays results of a 1.6 litre automotive engine under similar transient conditions. The similarity between the results of figure 4.3 and the data shown by Wu, are so striking that confidence is given to the developed model. Further, communication with British Gas engineers supports at least the trend wise agreement between the simulation results, and the behaviour seen for other converted gas engines. It was concluded,

therefore, that the model was realistic enough to allow further studies to be conducted.

From the confidence developed by the initial simulation, a second simulation was conducted, to observe the engine's behaviour for throttle transients induced whilst maintaining steady-speed conditions. The aim of this investigation was to subject the engine model to what could be considered as idling conditions, where an external load (such as a power drain by an air conditioner or other electrical load) is switched on. However, as the model was built with a minimum speed of only 2000 rpm, the simulation is conducted at this setting to keep within the captured operating range, and not at typical idle speeds of 800-1000 rpm. These conditions would then correspond to vehicle motion where an ascent is encountered, and the throttle is required to open rapidly to compensate for the increase in load torque, thus maintaining constant speed. This simulation is shown in figure 4.5.

The throttle input is idealised as a step which corresponds to the compensation action to a switched in electrical load or sudden road ascent, figure 4.5(a). The engine model combustion torque can be seen, in figure 4.5(e), to rise rapidly and reach a steady state value of 60 Nm for the throttle step to 30°. The engine model speed is maintained through the action of a PI-controller generating a load torque that closely matches that of combustion. The values of the feedback gains are chosen to give acceptable speed stability for the stepped throttle inputs and it can be seen that engine speed is maintained at the desired 2000 rpm with a tolerance of ± 10 rpm, figure 4.5(c).

The traces of the air flows are much more distinct now than for the simulation of figure 4.3, and it can be seen in figure 4.5(b), that throttle air responds instantly to the rapid change in throttle angle. This difference in the flow rates is also seen in a paper by Hires and Overington [100] for a fast throttle step-up condition.

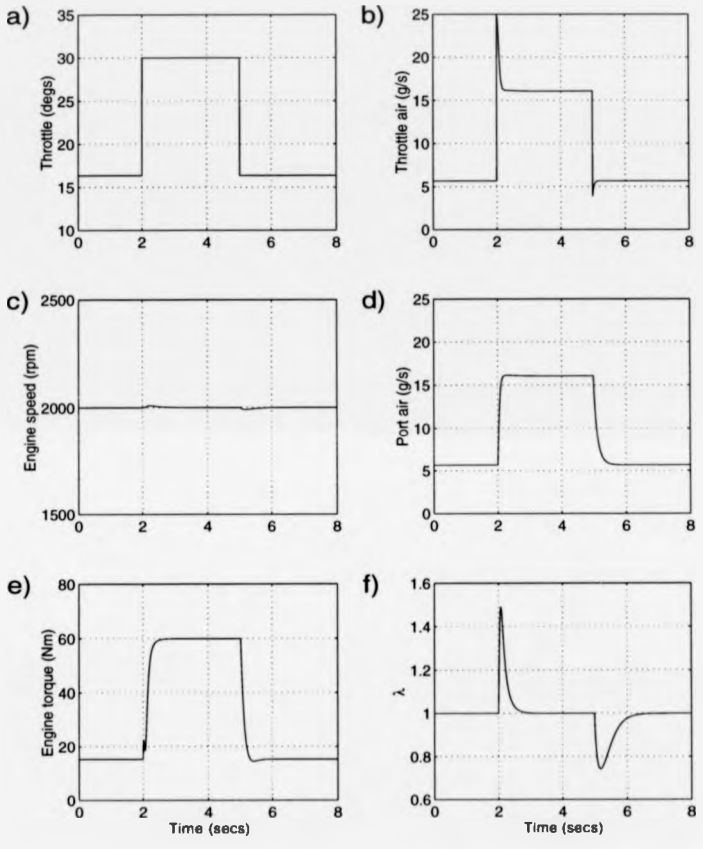

Figure 4.5: Constant speed simulation for step throttle transients depicting a controlled speed scenario under external load variations.

As the manifold pressure increases, seen in figure 4.6c), throttle air flow reduces to a level that allows stable manifold conditions and a steady flow at the port, as in figure 4.5(d). The A/F ratio can be seen to develop extremely large excursions for both step-up and step-down throttle action, figure 4.5(f). As a consequence, the combustion torque trace actually displays an undulation at the commencement of step-up throttle, and a mild undershoot during throttle step down.

The λ-trace bears extremely close resemblance to those λ-traces demonstrated by Hendricks [55], for similar throttling conditions measured from a real engine. In Hendricks' report, a 1.1 litre CFI engine is tested and subsequently modelled. A speed-density air flow model is used, similar to that characterised in this thesis. Again, confidence is given to the model in this thesis.

The nominal fuel flow rate for the simulation of figure 4.5, can be seen in figure 4.6 alongside the port air flow and manifold pressure. It is shown that the fuel flow is commanded directly from the air flow entering the combustion chambers. This is an acceptable method of determining fuel flow rate for engine systems that inject the fuel into the inlet port runners. However, due to the manifold dynamics establishing differences between the throttle and port air flows, throttle body fuel injected systems will undoubtedly suffer, resulting in A/F ratio excursions. This is also an effect recognised by Chang [67] and Hedrick [56].

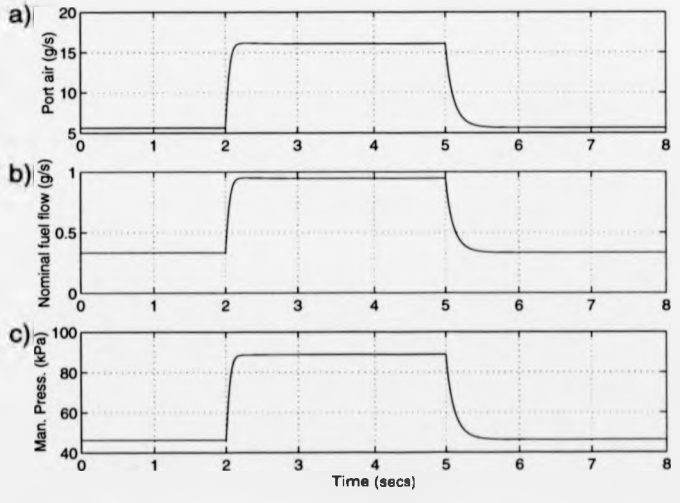

Figure 4.6: Fast open-loop nominal fuel flow rate commanded from estimated port air using speed-density model.

Investigations into air flow estimation errors are not detailed at this point, but are covered in detail in a later section, 4.3.3 "Model Estimation Accuracy" and also in Chapter 6. Here, it is assumed that the simulated air flow is measured without error, and fed directly to the air/fuel ratio controller. This is to allow an appreciation of the behaviour of the nominal controller before attempting to consider estimation and measurement errors.

The initial conclusion from these first simulations, regarding A/F ratio control, is that excursions are allowed to occur due to the fact that a speed-density model (equation 3.9) is used to estimate fuel flow. The dynamics of the manifold have been shown to slow down the port flow response in comparison to the throttle flow, and therefore the admitted gas is not entering the exact airstream from which it was commanded.

In a third simulation, it is interesting to observe the engine model's behaviour when a large external load is placed on the engine, but without compensating with an increase in the throttle angle. The results are displayed in figure 4.7.

The throttle angle is seen to be stationary at 18° and engine conditions are stable at 2500 rpm. After two seconds of operation, the external load is stepped up by 30 Nm. The engine speed rapidly drops and the air flow into the engine reduces to zero. The engine speed drops below the actual range for which the model was built (which essentially invalidates any further results) but does actually demonstrate the benefit of a continuous algebraic model, as opposed to an engine map, by allowing extrapolation of operating condition estimations.

The engine model torque also drops with the lowering air flow rate and at this point it is likely that the engine would stall. These results are comparable to the data presented in [70] for which an engine is made to stall under similar conditions, again lending further confidence to the model of engine behaviour.

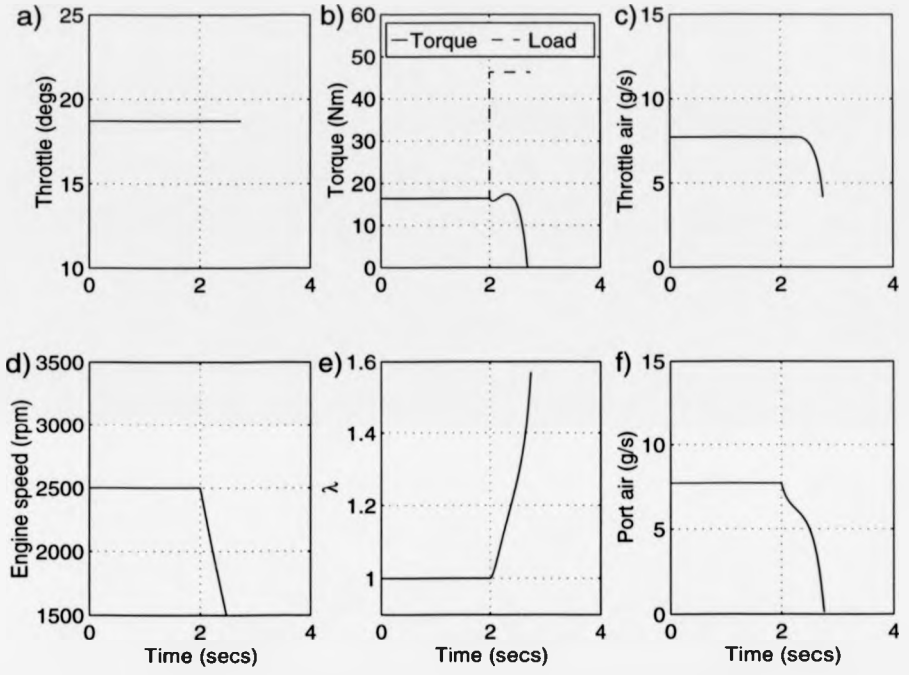

Figure 4.7: Engine stalling simulation induced by a step increase of external load whilst maintaining static throttle angle.

4.3.2 Discrete Nominal Fuelling

The fuelling control depicted in figure 4.6(b), is conducted for a continuous system with an assumed continuous controller. However, as discussed in section 4.2.1, microprocessors are required to operate in a discrete fashion.

The G.F.I. system implemented on the gas engine, employs a 12MHz processor with a controller sample-to-output time duration of 3 ms [101]. A report by Gettel et. al. [102] presents the work conducted on a duel-fuel engine, which operates on natural gas and diesel simultaneously. The frequency of the microcomputer used in their study was 5MHz, which allowed a maximum of 625,000 simple arithmetic

instructions per second (IPS). The exact value of IPS for the G.F.I controller is not known, but is expected to be somewhat larger than that of Gettel et. al. given that the G.F.I. processor speed is over double the frequency.

In order to investigate the sample rate effects of the digital nature of microcontrollers, the **DISCRETE** section in the ACSL programme was used in the model code. This enables the sampled communication behaviour between the controller and the continuous system to be replicated in the model simulations. The discrete block is executed at fixed time intervals that can be adjusted to investigate varying controller sample rates.

Figure 4.8 displays the results of three different controller sample rates in comparison to the continuous controller action. Both the fuel command and subsequent λ behaviour are displayed for each sample rate. The throttle and engine model conditions of figure 4.5 are used again in the simulations.

Sample rates chosen are: the slowest being 100 ms, figures 4.8(a,b), an intermediate at 50 ms, figures 4.8(c,d), and that of the G.F.I speed of 3 ms, figure 4.8(e,f). It can be seen that as the sample rate increases, the discrete controlled response approaches the continuously controlled response. A maximum lean excursion is encountered for the 100 ms controller of just over $\lambda = 2$. This is attributable to the significant change in air flow that develops between sample intervals. It is not until the G.F.I. microprocessor rate (3 ms) is approached, that discrete control is seen to approximate the continuously controlled response. The magnitudes of the λ-excursions are listed in table 4.1 against the corresponding microprocessor speed. This demonstrates the requirement for increasing the microprocessor sample rate to improve system control.

In conclusion from these results, it is established that the 3 ms sample time closely approximates the continuous controller action. For all of the following simulations in this chapter, discrete control shall be maintained at this sampling

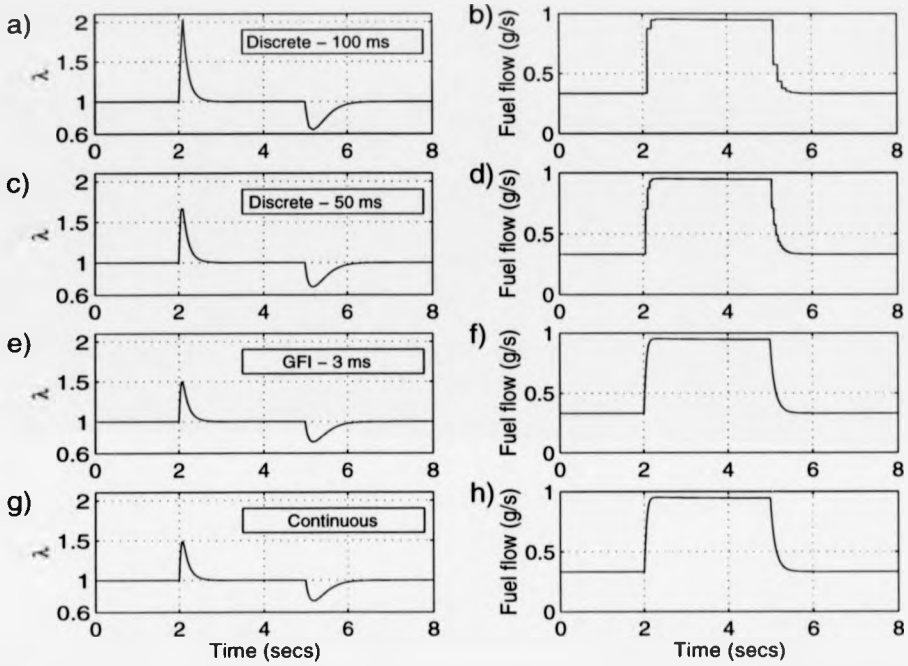

Figure 4.8: Varying controller sample rate effects on fuel flow and subsequent λ-excursions. a) 100 ms, c) 50 ms, e) 3ms (G.F.I.), g) Continuous.

interval (unless otherwise stated) to approximate the current G.F.I. control system ability.

Microprocessor Speed (ms)	Step-up λ-Excursion	Step-down λ-Excursion
100	2.0311	0.6498
50	1.6642	0.6995
3 (GFI)	1.4992	0.7403
Continuous	1.4898	0.7427

Table 4.1: Maximum and minimum λ-excursions under varying sample rates.

4.3.3 Model Estimation Accuracy

The simulation results of figure 4.8, show the effects of throttle action on λ. It is assumed that, for all four simulations, the controller estimated or measured air flow rate matches exactly that of the actual air flow rate. This is a somewhat idealistic assumption, as in all models there is some degree of inaccuracy which can lead to the wrong control decision being made. The nominal open-loop control is unable to compensate for model errors and will consequently admit an incorrect flow of fuel. This is demonstrated in figure 4.9, where a 10% error in the estimated air is introduced after two seconds of steady operation.

This simulation is conducted for first gear operation at 2000 rpm. The estimated air is seen to step to a value 10% below actual air flow. The fuel command is then reduced, as metered to the wrongly estimated flow, and the engine model performance deteriorates - as displayed by the drop in engine torque, figure 4.9(c). The value of λ rises to a lean value, just above 1.1, as the controller meters to the estimated decrease in air flow.

It is demonstrated, therefore, that A/F ratio control cannot rely solely on the estimation (or indeed direct measurement) of the air flow, as expected errors in the state being estimated will lead to further λ-excursions. These errors may also fluctuate as sensors experience noise effects, or even ageing, and could well induce unpredictable driving behaviour.

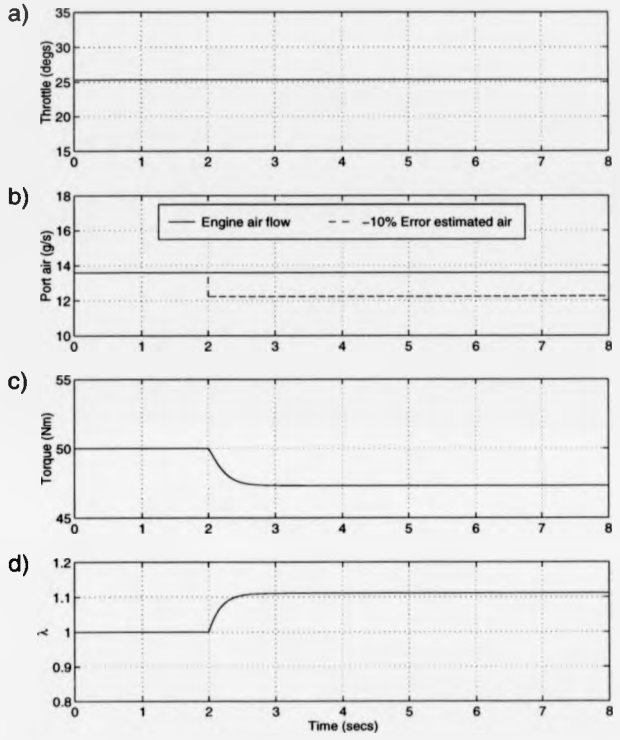

Figure 4.9: Introduction of a 10% reduction error in the port air flow estimation at 2000 rpm. The open-loop nominal controller is unable to account for modelling inaccuracies and the λ-trace is seen to drift away from set point.

4.4 PI-Closed-Loop Control

It is clear that some additional control strategy is required to ensure that A/F ratio is more strictly controlled around the desired set point by the removal of steady-state errors. Conventional A/F ratio controllers employ closed-loop techniques to perform this task and the standard approach is PI-control. A schematic for closed-loop PI-control is shown in figure 4.10.

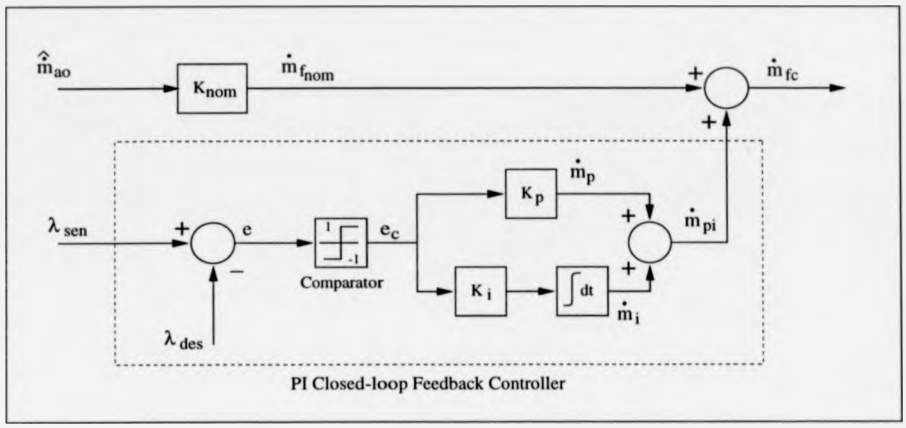

Figure 4.10: closed-loop PI-controller structure using λ-sensor feedback signal.

The nominal open-loop fuel command is shown, with the addition of the closed-loop PI-control scheme. This results in the total fuel command as the sum of the individual control efforts, as

$$\dot{m}_{fc} = \dot{m}_{f_{nom}} + \dot{m}_{pi} \tag{4.3}$$

where $\dot{m}_{pi}$ is the PI-control commanded fuel rate.

The zirconia EGO sensor feeds the voltage signal λ_{sen} (of the type presented in section 3.4) to the feedback controller. The error signal, e, is then established by the subtraction of the desired value of sensor voltage, λ_{des}, which corresponds to the desired λ-setting.

By inspection of figure 2.8, a desired set-point voltage of 650mV could well be chosen to give a λ-setting of 1. As expressed in section 3.4, this characteristic may vary considerably during vehicle operation, due to changing exhaust temperatures and ageing. The static choice of λ_{des}, therefore, will amount to a fluctuation in desired A/F ratio setting, as the sensor temperature fluctuates. The *exact* choice of λ_{des} is not of major importance, as shall explained below, as long as it resides

in the narrow window of the steep gradient between rich and lean sensor output voltage. The resulting error signal is then fed to a comparator.

The action of the comparator is to condition the error signal to give a dependable voltage output signal of either +1 (rich) or -1 (lean). It is this signal, e_c, that is then fed to the controller. This approach allows a certain amount of flexibility in the choice of λ_{des}, since the information offered is only whether the system is running rich or lean. Further, the action of the comparator goes some way to remove the hysteresis behaviour of the sensor and allows the controller to become less sensitive to the non-linear sensor dynamics.

Without the comparator, the controller would have to take action on a widely varying error signal. The selection of the feedback gains, K_p and K_i, would then be made extremely difficult as no certainty could be placed on what the error signal actually is. By the use of the comparator, the controller inputs are precisely known (± 1) and some method of gain selection can be based on the engine operating conditions.

4.4.1 Gain Selection

The choice of K_p and K_i will directly select the amount of additional fuel that is commanded from the closed-loop action. The nature of PI-closed-loop control on systems with a time delay, is that of a limit cycle [103]. The delay causes the feedback controller to maintain its current action until the output from the comparator switches in the opposite direction, where-upon the controller output changes the direction of the closed-loop fuel command. This action is maintained until the comparator output switches back to its initial state and the cycle repeats itself. The outcome of this is to set up a "modulation" of the closed-loop fuel command, $\dot{m}_{pi}$, which acts upon the baseline nominal flow, $\dot{m}_{f_{nom}}$. The subsequent A/F ratio is then also modulated about the desired λ-setting.

As discussed in section 1.2.3, the catalyst responds favourably to mild oscillations in the A/F ratio. These modulations are considered entirely tolerable if maintained within the conversion efficiency window limits. The amplitude of the fuel flow modulation must therefore be selected to ensure that the window limits are not exceeded, but provide sufficient modulation amplitude to enhance conversion.

Consider the action of the integral only controller. The controller output is computed as

$$\dot{m}_i = \int K_i \cdot e_c \, dt, \tag{4.4}$$

where the error, e_c, is defined as:

$$e_c = sgn\,(\lambda_{sen} - \lambda_{des}), \tag{4.5}$$

through the action of the comparator. The integral term mass flow, $\dot{m}_i$, will increase or decrease as a function of the time for which the input signal remains -ve or +ve respectively, (the sign of K_i is chosen as negative to reduce fuel flow when rich and increase fuel flow when lean), and K_i defines the gradient slope of the integral fuel flow. Thus, the integral fuelling action is given as

$$\dot{m}_i = K_i \cdot t_s, \tag{4.6}$$

where t_s is the time elapsed after the switching of the comparator signal. The maximum magnitude of the integral term fuel flow is defined by the maximum time, ΔT, between switches of the input signal and hence defines the amplitude of integral fuel flow, $\Delta\dot{m}_i$, as

$$\Delta\dot{m}_i = K_i \cdot \Delta T. \tag{4.7}$$

The value of ΔT is defined as the sum of system time delay, t_d (see section 2.8), and the sensor time constant, τ_s, as [87] :

$$\Delta T = t_d + \tau_s. \tag{4.8}$$

The frequency, f_i, of the fuel modulation induced solely by the action of integral control, is then defined to be

$$f_i = \frac{1}{4 \cdot \Delta T} \tag{4.9}$$

which is the expression for the limit cycle frequency for a feedback controlled system with time delay [87, 88].

The amplitude of modulation of the A/F ratio, is now considered in terms of the equivalence ratio, Φ, which is defined as the reciprocal of λ. The modulated equivalence ratio is then defined by the amplitude of the modulated fuel flow, $\Delta\dot{m}_i$, to the steady air flow, $\dot{m}_{ao}$, as

$$\Delta\Phi = \frac{\Delta\dot{m}_i \cdot (A/F_s)}{\dot{m}_{ao}}, \tag{4.10}$$

$$= \frac{K_i \cdot \Delta T \cdot (A/F_s)}{\dot{m}_{ao}}. \tag{4.11}$$

The equation for nominal fuel flow 4.1, can now be substituted to give

$$\Delta\Phi = \frac{K_i \cdot \Delta T}{\dot{m}_{f_{nom}}}, \tag{4.12}$$

which results in an expression for the integral gain as

$$K_i = \frac{\Delta\Phi \cdot \dot{m}_{f_{nom}}}{\Delta T}. \tag{4.13}$$

The value of the desired equivalence ratio amplitude, $\Delta\Phi$, is specified in the controller to maintain modulations within the catalyst conversion window limits.

The value of the integral gain is, therefore, determined by both the system time delay and mass flow rate of nominal fuel, once $\Delta\Phi$ is set. Both of these engine states are entirely dependent upon engine operating conditions, allowing the feedback integral gain to be effectively selected to maintain a constant amplitude of modulation for any given engine speed and load. The resulting action of integral-only control will slide the A/F ratio between the specified amplitude limits either side of the stoichiometric ratio.

With the addition of the proportional term, the closed-loop fuelling action shall incorporate a "jump-back" effect each time the comparator output changes direction. With correct selection of K_p, the frequency of the closed-loop PI fuelling action can be doubled, whilst the amplitude remains as that set by $\Delta\Phi$.

The proportional-plus-integral (PI) fuel command, $\dot{m}_{pi}$, is now described by

$$\dot{m}_{pi} = K_p \cdot e_c + \int K_i \cdot e_c \, dt. \tag{4.14}$$

In order to double the frequency, f_i, of the integral-only control modulation, the jump back in fuel attributable to the proportional term must be equal to the amplitude of the integral-only term. This will ensure that the fuel command jumps back to stoichiometry as soon as the comparator output changes sign.

Therefore, from the equation of the mass flow amplitude, 4.7, K_p is defined as

$$K_p = \Delta\dot{m}_i, \tag{4.15}$$

$$= K_i \cdot \Delta T, \tag{4.16}$$

and with the equation for the integral gain selection 4.13, the proportional gain becomes

$$K_p = \Delta\Phi \cdot \dot{m}_{f_{nom}}. \tag{4.17}$$

Since the comparator output changes from -1 to +1 (or vice versa), the signal entering the controller is changed by a magnitude of 2. If this value is maintained in the proportional controller, the jump back effect would be twice as much than is necessary to bring the A/F ratio back to stoichiometry, and would overshoot to the desired limit on the opposing side. For this reason, the expression for K_p is halved to ensure that overshoot is not encountered. This arrives at the final expression for the proportional feedback gain as

$$K_p = \frac{\Delta\Phi \cdot \dot{m}_{f_{nom}}}{2}. \tag{4.18}$$

The use of the comparator has been shown to allow the feedback gains to be selected purely on the operating conditions, removing the non-linear EGO-sensor characteristic that would otherwise dominate the system. Therefore, the gains can be scheduled by the controller, based on the computation of the nominal flow of fuel already computed from the nominal control algorithm.

4.4.2 PI-Control Discrete Representation

In order for a digital controller to perform closed-loop PI-control, the proportional and integral terms must be represented numerically. Numerical methods of integration can only usually give approximate solutions to the definite (continuous) integral. One such method commonly used in computers, microprocessors and some sophisticated programmable calculators, is the trapezoidal rule [104].

To evaluate the integral of a signal $e(t)$, the approach of the trapezoidal rule is to consider the signal as divided into a set of n strips. The resulting sequence of successive points, $[e(t_1), e(t_2), \ldots, e(t_{n+1})]$, are then joined by straight line segments that form a set of n trapezoidal areas (see figure 4.11). The sum of these individual areas then defines the approximate integral from a to b by geometry [105] as

$$\int_a^b e(t)\,dt \approx \frac{e(t_1)+e(t_2)}{2}\cdot(t_2-t_1)+\cdots+\frac{e(t_n)+e(t_{n+1})}{2}\cdot(t_{n+1}-t_n). \quad (4.19)$$

Since the sampling interval, T, of the G.F.I. discrete controller is set at a constant value (3 ms), the trapezoidal rule can be reduced to

$$\int_a^b e(t)\,dt \approx \frac{T}{2}\cdot\{e(a)+2e(a+T)+\cdots+2e[a+(n)\cdot T]+e(b)\}\,. \quad (4.20)$$

Trapezoidal integration is then used in *Tustin's* method [103, 106] to approximate the integrator output, $\dot{m}_i(nT)$, as

$$\dot{m}_i(nT)=\dot{m}_i(nT-T)+K_i\cdot\frac{T}{2}[e(nT-T)+e(nT)]. \quad (4.21)$$

The discrete output, $\dot{m}_p(nT)$, of the proportional block of the controller is given as the error value sampled at time nT multiplied by the proportional gain, K_p, as

$$\dot{m}_p(nT) = K_p \cdot e(nT). \tag{4.22}$$

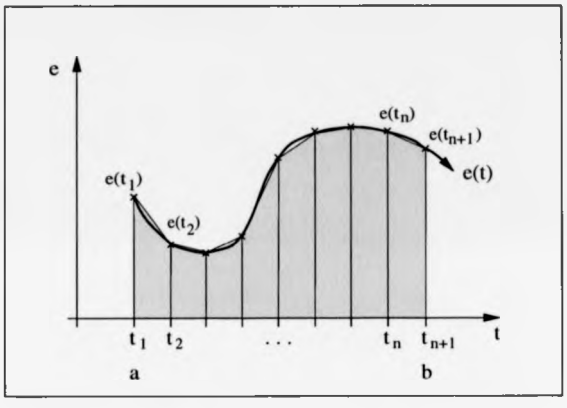

Figure 4.11: Trapezoidal rule of numerical integration.

4.4.3 Steady-state Performance

To observe the effects of closed-loop PI-control under steady-state operating conditions, two "sets" of simulations are displayed here that differ significantly in engine speed.

The first set of simulations is conducted at a steady 2000 rpm. Figure 4.12 displays the PI-control action on the fuel command trace and the resulting effect on both λ-value and engine model combustion torque. The simulation is conducted at the G.F.I. microprocessor speed of 3 ms.

The jump and slide effects on the fuel command can be seen to modulate the fuel around the baseline nominal fuel command of 0.8 gs^{-1}. The λ-trace displays the significant modulation in A/F ratio that is established, but is con-

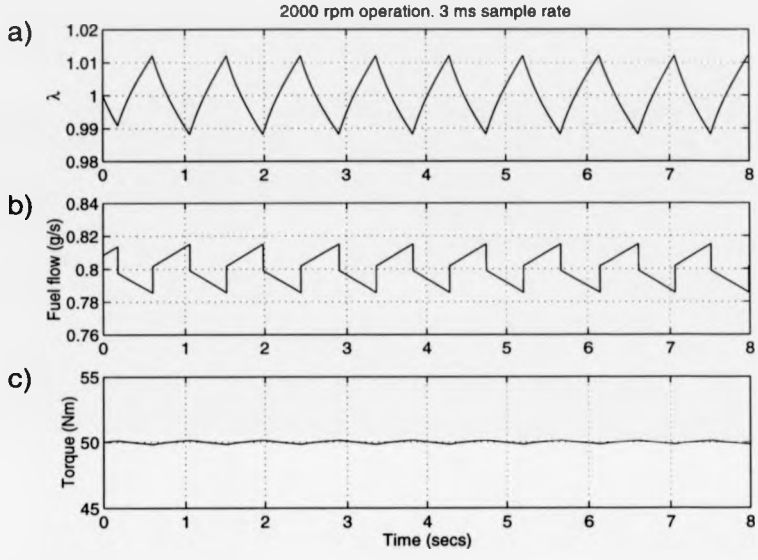

Figure 4.12: Steady-state engine operation at 2000 rpm under PI closed-loop control at the G.F.I. sample speed of 3 ms. The "jump and slide" effects in the fuel command are clearly visible, producing a modulation in the A/F ratio within the catalyst limits.

strained to remain well within the limits of the conversion window of $A/F_s \pm 0.3$ ($\lambda = 1 \pm 0.0177$), by the selection of $\Delta\Phi$. The engine model time delay was estimated to be approximately 230 ms, which defines the modulation frequency, from equation 4.9, to be approximately 1.08 Hz. This frequency is illustrated in both the fuel and λ-traces.

The effect on the combustion torque is also displayed, expressing the model prediction of the consequences of modulating A/F ratio. It is apparent that there is a slight modulation in engine model torque output at the same frequency as the A/F ratio modulation. The amplitude of torque variation is so small ($\pm$ 0.14Nm on a baseline of 50Nm), that it is not of a significant magnitude to degrade engine performance or effect driveability.

To observe the effects of varying controller sample rates, two further simulations were conducted at this 2000 rpm setting, but for 50 ms and 100 ms sample rates. These simulations are displayed in figures 4.13 and 4.14, respectively. The discrete nature of the controller sampling action is now in greater evidence, as the fuel command flow rates display a characteristic 'stepping' action from one control output to the next.

The performance of the λ is not greatly affected by the increase in sampling intervals, and only small increases in the amplitude are observed, from a maximum of $\lambda = 1.0121$ for 3 ms, to $\lambda = 1.0162$ for 100 ms. The modulation frequency reduction is, perhaps, more noticeable, dropping to approximately 1 Hz for both 50 and 100 ms. These effects are due entirely to the increased sampling intervals, where the A/F ratio is allowed to escalate to higher values between the control timings since the fuel is maintained at a constant between them.

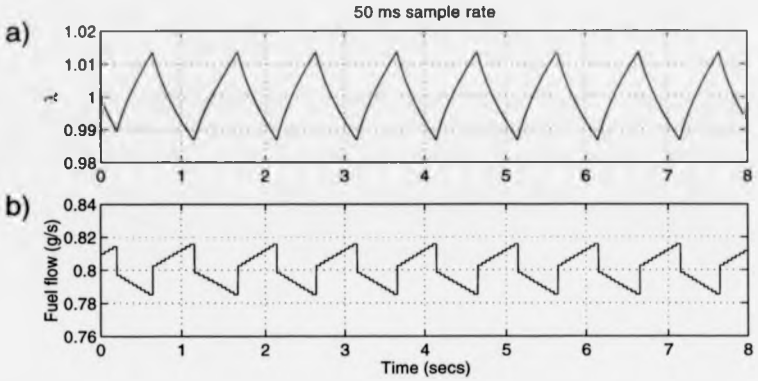

Figure 4.13: Steady-state PI-control at 50 ms sample rate, 2000 rpm engine speed.

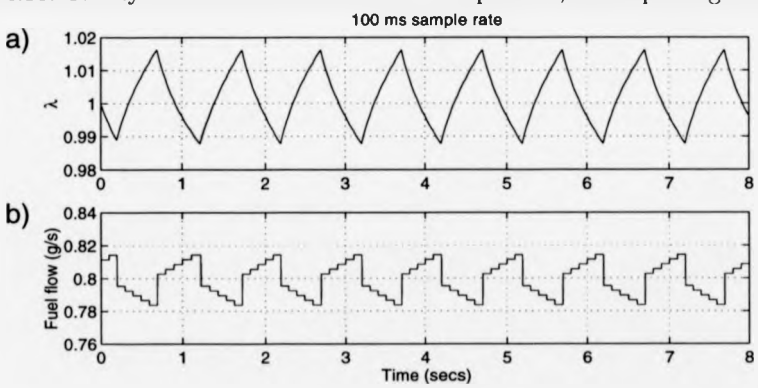

Figure 4.14: Steady-state PI-control at 100 ms sample rate, 2000 rpm engine speed.

A second set of simulations was conducted at the higher engine speed of 4000 rpm, for a baseline torque setting of 60 Nm. The first of these is shown figure 4.15 for the 3 ms sample rate. Again, the choice of $\Delta\Phi$ is selected to maintain the amplitude of λ-modulation within the catalyst conversion limits.

Due to the higher flow rate of air commanding a higher nominal fuel flow rate, the values of K_i and K_p are automatically increased (as defined by equations

4.13 and 4.18, respectively) to meet the demand for the modulation amplitude under the new operating conditions. This effect, coupled with the reduced system time delay (due to the higher engine speed and air flow rates), increases the frequency of modulation to approximately twice that of the 2000 rpm simulation. The system time delay at 4000 rpm operation is estimated to be approximately 118 ms. This results in a modulation frequency of approximately 2.12 Hz. The increase in frequency between the two G.F.I rate simulations, can quite easily be seen between the figures of 4.12 and 4.15. Again the effects on torque for the 4000 rpm simulation are not considered to significantly degrade performance.

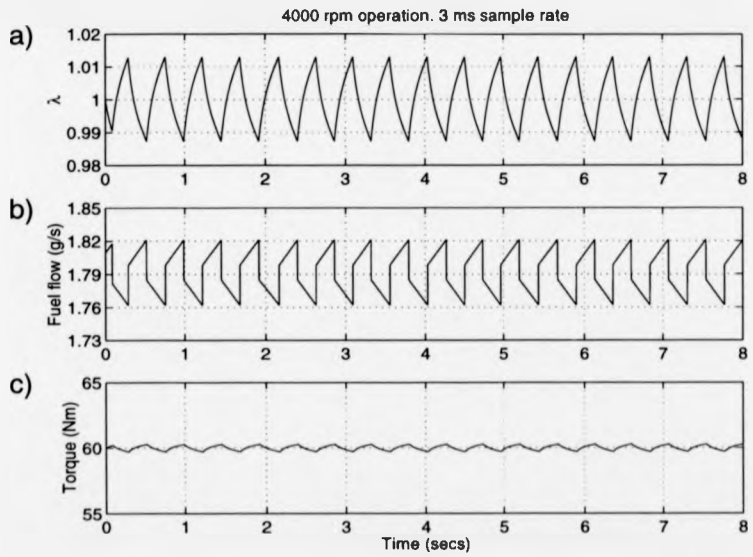

Figure 4.15: Steady-state engine operation at 4000 rpm under PI closed-loop control. The modulation frequency increases due to the increase in the feedback gains.

The effects of increased sampling intervals are perhaps more significant for the higher engine speed of 4000 rpm, than were seen for the 2000 rpm simulations.

This is borne out by the simulations depicted in figures 4.16 and 4.17, where the sample rates have, again, been increased to 50 ms and 100 ms, respectively.

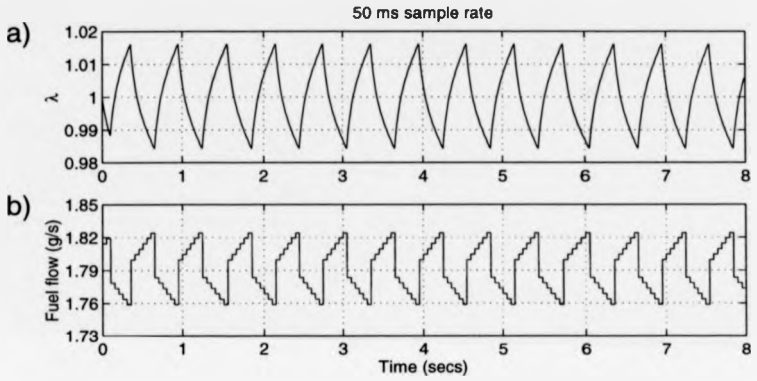

Figure 4.16: Steady-state PI-control at 50 ms sample rate, 4000 rpm engine speed.

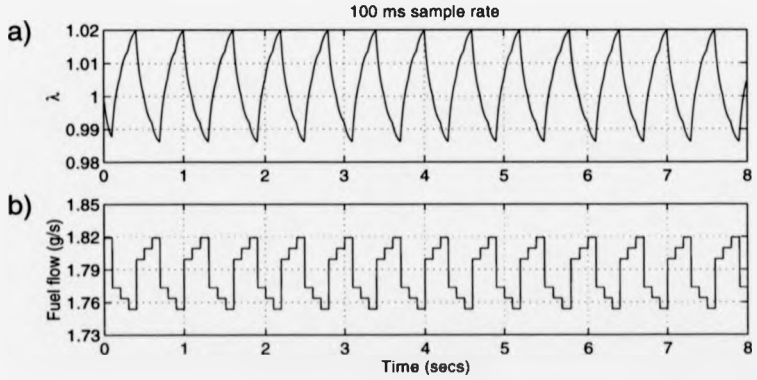

Figure 4.17: Steady-state PI-control at 100 ms sample rate, 4000 rpm engine speed.

The increased value of the feedback gains ensures that the controller action alters the fuel by a greater amount. The frequency of modulation is increased as λ is 'pushed' past the set point more often. The rate of change of the fuel flow

between switching actions is therefore increased. This induces greater changes of state between the controller samples and subsequent control actions. This means that the transient states of fuel flow and λ are being controlled on a previous control action that is rapidly becoming outdated and inappropriate for the current states that continue to change.

As a consequence, the amplitudes in the λ-traces for both the 50 ms and 100 ms simulations, increase to approximately 24% and 31% respectively, above that of the 3 ms simulation.

Interestingly enough, the amplitude of the fuel flow rate modulations remains roughly unaltered for all three simulations conducted at 4000 rpm. This is attributable to the compatibility between the sampling time and the system time delay. The sample intervals are maintained within the time delay to enable the A/F ratio to be controlled before significantly large excursions develop.

If the sample intervals lie outside the engine model time delay, the excursions become that much larger, so that more aggressive changes in fuel flow are required. This effect is depicted in figure 4.18, where the sample period is increased to a value of 250 ms, approximately twice that of the time delay of 118 ms.

It can now be seen, that 4 samples every second allows λ to drift outside the predefined modulation amplitude. Consequently, large steps in the fuel flow rate are incited by the controller, to return λ to set-point.

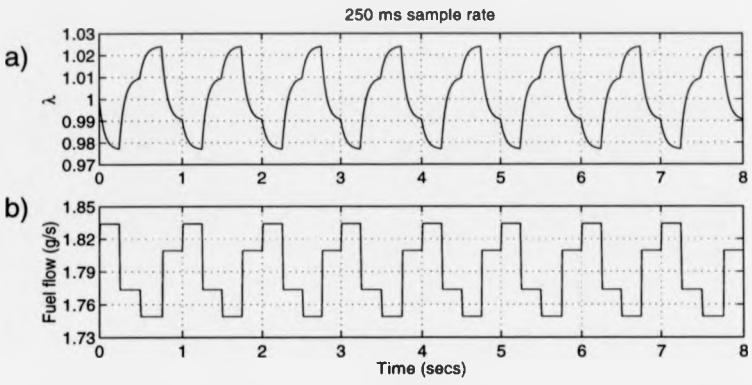

Figure 4.18: Steady-state PI-control at 250 ms sample rate, twice that of the estimated time delay at 4000 rpm engine speed.

Model Inaccuracy Correction

Aside from the beneficial effects of modulation that PI-closed-loop control affords, a correction for steady-state inaccuracies is achieved to bring the A/F ratio back to the set point. Consider the simulation of figure 4.9, where a 10% reduction error was introduced to the air estimation value. The fast open-loop controller had no method of correcting for model estimation errors and simply maintained the incorrect fuel command. Figure 4.19 now demonstrates the correction for these inaccuracies from the use of PI-feedback control.

The feedback controller receives a signal from the comparator confirming that the A/F ratio is running lean entirely due to the nominal open-loop control. The feedback controller then maintains a steadily increasing flow of gas until the comparator signals a switch back to rich operation, at which point the error is eradicated and modulation resumes. With the return of the desired A/F ratio value, the engine model torque is increased back to its initial baseline of 50 Nm .

The rate at which the A/F ratio is brought back to the set point, is governed by the magnitude of the integral gain, K_i. However, this value is limited by the

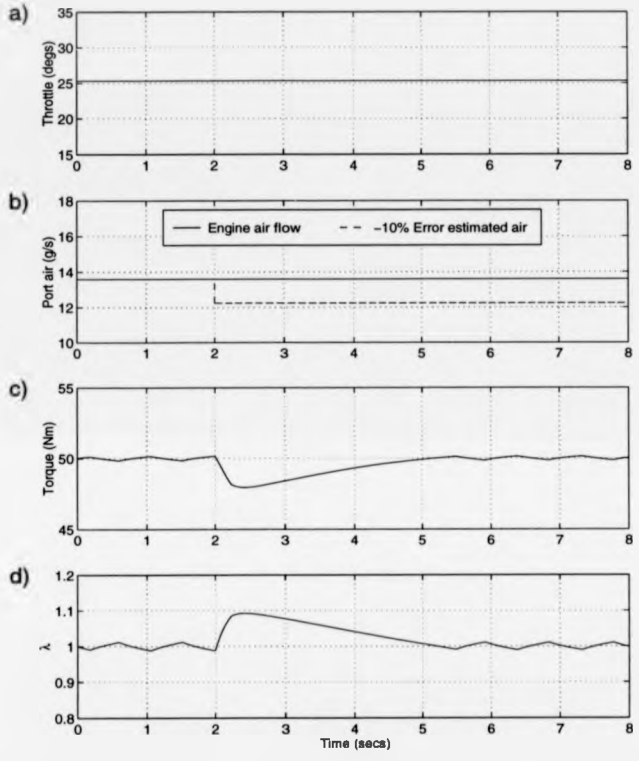

Figure 4.19: PI-control estimated air-flow error correction.

operating conditions, as defined in equation 4.13, to ensure that the A/F ratio modulation remains within the acceptable catalyst limits.

Therefore, the rate at which the error is removed cannot be increased, as the value of K_i must remain set to the value required to produce the desired A/F ratio modulation amplitude for the given operating conditions.

4.4.4 Transient Performance

PI-control has been shown to possess attractive qualities for steady-state engine operation by the removal of model estimation errors and the inducement of A/F ratio modulation. The nature of automotive engine operation under typical driving conditions, however, does not allow engine conditions to remain constant for any significant period of time. Town or urban driving requires a vehicle to make a substantial amount of "stop-start" manœuvres to negotiate heavy traffic, steep gradients, tight corners, traffic lights, etc. In order to accomplish these tasks, a driver would typically vary the throttle conditions through large angles very quickly. As shown by the simulations of figures 4.3 and 4.5, the engine model is dominated by the action of the throttle, causing major changes in physical states very rapidly. As a consequence, we can see that the A/F ratio displays large excursions away from the desired setting that is required to minimise emissions and reduce atmospheric pollution.

Referring to the λ-trace shown in figure 4.5(f), one could argue that the excursions are not particularly longlived and a return to the set point occurs fairly quickly after the throttle has come back to rest ($\approx$0.8 sec for step-up and $\approx$1.2 sec. for step-down). But considering the number of vehicles on the roads (see section 1.1.1), and a good proportion of these being situated in large built-up conurbations, the impact of these excursions is compounded. Research and development efforts should therefore be directed at methods to combat transient induced drifts.

This section is intended to demonstrate PI-control under transient performance through further simulation work, and to investigate whether sufficient action is taken by the feedback controller to maintain A/F ratio control under dynamic operation.

The conditions of the simulation shown in figure 4.5, shall be used again in a first instance, since it was demonstrated that harsh throttle variations of this

nature excite severe A/F ratio excursions. A direct comparison of A/F ratio control between nominal-only control and PI-control, is also enabled, allowing an understanding of the nature of PI-control action. Figure 4.20 displays the results of PI-control applied under the transient throttle steps and engine model conditions as shown in figure 4.5.

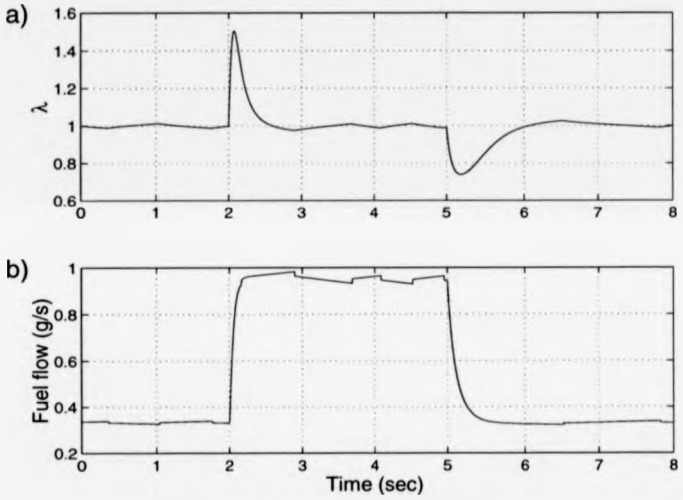

Figure 4.20: PI-closed-loop fuel control for a rapid throttle transient at 2000 rpm operation. A/F ratio excursions remain as the throttle is rapidly varied.

It can be seen that the rich and lean excursions, prevalent for nominal-only control, still persist in the PI-controlled response. The PI-fuelling command of figure 4.20(b), can be directly compared to the nominal only fuel flow of figure 4.6(b). This demonstrates that the PI-controller output maintains the modulation upon the nominal flow, but is making no attempt to reduce the error that is causing the excursions. Again, the modulation of the fuel flow manifests itself as a modulation of the λ-trace about 1. As established from the discussion in section 4.3.1, these large excursions arise from the fact that the nominal fuel is

computed from the port air flow, but is introduced into the throttle air flow further upstream. The system time delay essentially opposes the PI-control action from actually being able to alter the fuel command in response to the detection of the sharp A/F ratio excursions. It would appear then that PI-control has no effect in compensating for the fast drifts into the rich and lean λ regions, but corrects well for steady-state errors where the integral action is governed by the operating conditions.

To re-enforce this conclusion, a second simulation is illustrated (typical of many performed) where the engine model speed is not held constant but allowed to develop by varying engine model load in second gear operation. The results of this simulation can be seen in figure 4.21, where the throttle angle is initially held at a steady position of 30°. The initial engine speed is 3000 rpm until the throttle is stepped open by 20° after 2 seconds. The air flow increases - which is not shown specifically but is reflected by the increase in the fuel flow rate - and the engine model speed begins to climb to just under 5000 rpm.

The fuel flow is seen to initially respond with a step-up increase in flow rate, due to the nominal control command acting on the severe increase in port air flow. The fuel flow then rises gradually as the throttle is maintained constant and the engine model speed is allowed to increase.

The PI-control command continues to modulate the flow rate throughout the simulation. After 5 seconds, the throttle is stepped back down to its initial position allowing the engine speed to reduce gradually, back to its initial value of 3000 rpm. The simulation is allowed to continue for 15 seconds to ensure that the initial steady-state conditions are returned.

In a similar manner to the simulation of figure 4.20, the varying-speed simulation still exhibits extreme excursions at the timings of the throttle steps. When the throttle remains stationary at its maximum value of 50°, λ *does* return back to

the desired value of 1, but now with an increased frequency due to the increased feedback controller gains and reduced time delay - as explained in section 4.4.3. Conversely, when the throttle is stepped back down to its initial value, a rich mixture is encountered for a short time, sending the λ-trace to just below 0.8, before the modulation is returned with a decreasing frequency as the engine model speed returns to 3000 rpm.

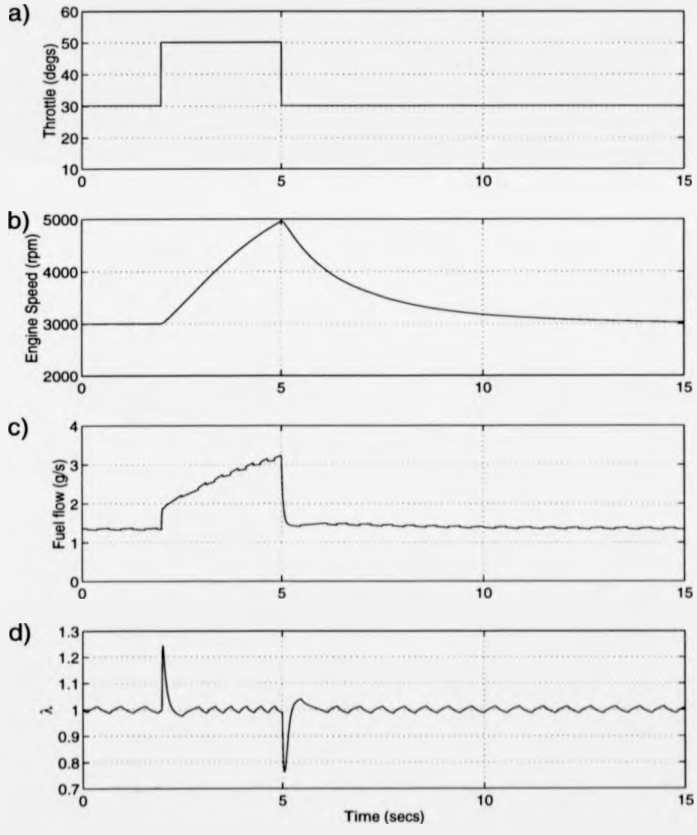

Figure 4.21: PI-closed-loop fuel control for a rapid throttle transient in 2nd gear operation. Large A/F ratio excursions develop at throttle steps inputs.

Discussion

Conclusions may be reached from the simulation results of the last two sections concerning the action and significance of PI-control. This method of fuel control, utilising an EGO sensor, certainly displays characteristics which improve the catalyst conversion ability and has been applied in production vehicles for a good number of years. PI-control has been widely adopted due to its improved performance over early production fuel metering systems, and certainly the low cost of these units, in comparison to other suggested alternatives in the mid-seventies, has aided their dominance in the practical world of mass vehicle production. An excellent report by Engh and Wallman [107] from 1977, gives a clear description of the Volvo closed-loop A/F ratio control system making use of identical hardware components described and modelled in this thesis (those of the zirconia sensor and 3-WCC). This report demonstrates the growing importance of A/F ratio almost 20 years ago and the applicability of the system in question.

Considering the length of time that PI-control systems have been in service, it is clear that they are a cost-effective, practical method of reducing pollutants. They will no doubt continue this role, becoming even more widespread as regulations force all new engines to conform to lower emission levels.

Based on the simulation results presented so far, and the presence of quite considerable λ-excursions during throttle transients, is closed-loop PI-control the answer to constant A/F ratio control?

One could certainly remark that no improvement has been demonstrated for transient simulations, which is of course correct, but it is important to understand the exact system to which the controller is being applied. It is unfair to expect the closed-loop controller (whose speed of response is inherently restricted by the engine time delay) to correct for transient fuelling errors that occur due to the fast open-loop nominal controller. It makes perfect sense to measure the air flow at the

point at which the fuel is being injected. The advantage of using a throttle air flow sensor, such as a hot wire anemometer, is to provide a fuel flow that is metered to the exact air flow into which it is injected. Hence, an air/fuel ratio would result that as close to stoichiometry as possible at the location of the injector.

For the gas engine system being modelled here, this would amount to using the estimated throttle air flow as the nominal controller input. However, the G.F.I. controller does not have access to the throttle angle condition, and, in the interests of maintaining realism and close system approximation, it is decided that the controller of the engine model shall not have a throttle angle input. Throttle air flow sensors are available [99], but of course the automotive industry is very conscious of the escalating costs and increasing complexity that arises from the incorporation of additional sensors and actuators. Further, a throttle air flow sensor was not available for testing on the engine, and thus there was no provision to complete a practical back-up for validation.

For port fuel injected systems, as described in section 1.2.1, the use of a speed-density model to decide the nominal fuel flow rate is a viable approach, as the injected fuel enters at the exact position at which air flow is being estimated. Any resulting A/F ratio excursions are then due to problems of backflow, estimation errors, controller processing rates and actuator limitations.

In answer to the posed question, PI-control in conjunction with the nominal open-loop control cannot be expected to maintain strict A/F ratio control during transient operation for the gas engine being modelled. The task, therefore, is to improve A/F ratio control above that of current PI-control with the existing sensors and systems available, i.e. manifold pressure, engine speed and λ-A/F ratio. From this point on, then, investigations shall be directed towards this goal.

4.5 PID-Closed-Loop Control

An initial investigation towards improving transient control would be to consider the inclusion of derivative action in the feedback controller. This is conducted to investigate whether a full PID feedback controller is able to 'pick out' a transient condition by monitoring the change in the exhaust A/F ratio between lean and rich conditions.

Derivative feedback control is typically used in conjunction with PI-control systems to generate a full PID feedback controller. The action of derivative control is expressed in the form

$$u = K_d \dot{e}, \tag{4.23}$$

where K_d is the feedback gain acting on the derivative of the error signal. The derivative term has the effect of removing some of the unstable behaviour arising from the integral controller action. PID control has been found to be extremely effective for process control, and can be found as the primary controller in such industries as chemical plants, petroleum refining and paper making [103].

A closed-loop PID-controller for engine A/F ratio control can be seen in figure 4.22.

The action of the derivative term in the discrete controller is approximated as the numerical derivative. Referring to figure 4.11, the gradient of the signal $e(t)$ at a given sample instant t_{n+1} can be estimated as the slope of the straight line connecting $e(t_{n+1})$ and the previous sample $e(t_n)$. This results in the finite difference approximation [108], where the derivative controller output is defined as

$$\dot{m}_d(nT) = K_d \cdot \frac{e(nT) - e(nT - T)}{T}, \tag{4.24}$$

where T remains the controller sample time of 3 ms. It is self evident that as T is reduced, closer continuous system approximation is reached for both the numerical

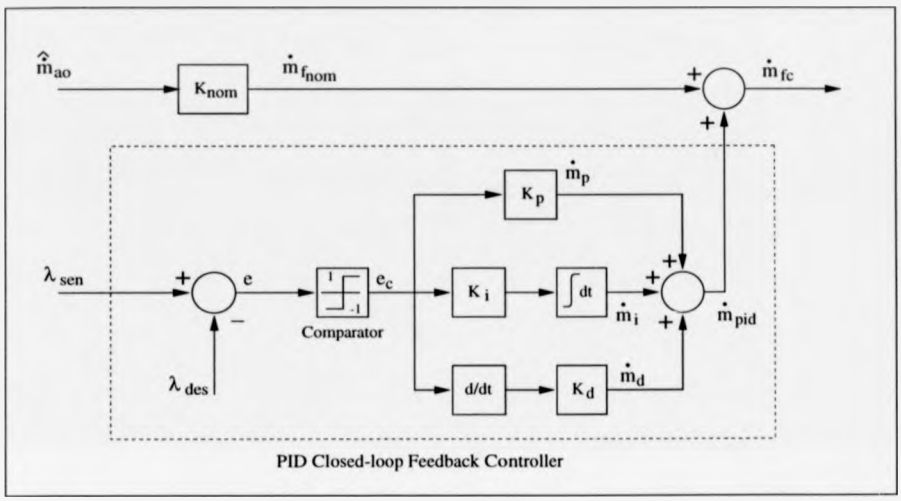

Figure 4.22: Closed-loop PID-control.

integral and differential estimates, as the sample intervals in figure 4.11 approach zero.

Consider now, the type of signal that the derivative controller will be receiving in common with the P and I terms. The comparator output is a pulse wave form, from -1 to 1, with a duty cycle dependent on vehicle operation inducement. The action of the difference equation will output zero for rich and lean periods where the comparator output is constant. When a switch is encountered, either due to the PI-controller modulation or an A/F ratio excursion, the difference equation will then be activated to give a signal of magnitude $\pm 2/T$. If the derivative gain is chosen in a similar fashion to that of K_p, where the jump back in fuel command is set to bring A/F ratio back to stoichiometry, then

$$K_d = \Delta\Phi \cdot \dot{m}_{f_{nom}}, \tag{4.25}$$

By inclusion of the comparator/difference equation effects, the gain can be speci-

fied as

$$K_d = \frac{\Delta\Phi \cdot \dot{m}_{f_{nom}}}{(2/T)} \tag{4.26}$$

$$= 0.0015 \cdot \Delta\Phi \cdot \dot{m}_{f_{nom}}, \tag{4.27}$$

for the sample rate of the G.F.I controller.

An example simulation of PID-control can be seen in figure 4.23. Identical operating conditions are maintained as shown in figure 4.21. Now, the action of the derivative fuel term is shown explicitly alongside the corresponding plots of the total fuel command, $\dot{m}_{fc}$, and the λ-trace.

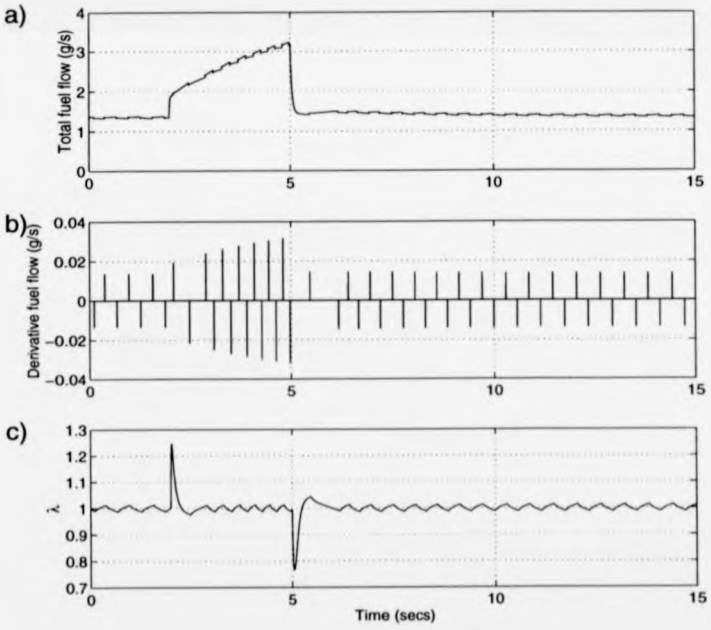

Figure 4.23: PID-control for 2000 rpm throttle steps operation. The derivative action remains zero until a switch across the stoichiometry line incites a pulse change in fuel.

The derivative term is seen to inject a fuel pulse each time there is a switch

between lean and rich. The amplitude of this pulse is governed by the value of K_d and is set to correspond to the same amplitude as the proportional term. The outcome of these pulses displays a negligible effect upon λ. This is due to the microprocessor rate initiating a fuel pulse width of only 3 ms. Further, the derivative action is not responding primarily to the excursions in A/F ratio seen at the throttle, but to the switches induced by PI-control action. Feedback derivative action, therefore, cannot be "tailored" to compensate for the transient A/F ratio excursions, as it cannot distinguish between these and normal modulation control.

4.6 Conclusions

Over the course of this chapter, it has been established that aggressive throttle operation incites severe A/F ratio drifts. Fuel flow commands from the nominal open-loop controller have demonstrated the fastest response to changing engine conditions. However, due to the 'mis-matching' of the relative positions of the estimated air flow and the injected fuel, the air/fuel ratio excursions occur because the fuel is **not** injected into the estimated air flow, but into an air flow further upstream. This is a fundamental problem that the controller cannot correct for during transient operation. This mis-matching is most obvious for rapid throttle changes, where the manifold filling and emptying dynamics accentuate the differences in flow rates.

The current G.F.I. microprocessor sample rate of 3 ms, is considered to be of sufficiently short duration that a continuous controller would provide no distinct improvements in A/F ratio control.

The application of closed-loop PI-control enhances an engine's ability to reduce emissions by:

1. the removal of steady-state estimation errors,

2. the introduction of A/F ratio modulation for improved catalyst performance.

The speed of error correction is dependent upon the choice of the feedback integral gain. Both proportional and integral gains are governed by a combination of the choice of desired A/F ratio modulation amplitude and the operating conditions. This form of control has proved to be robust in maintaining the required modulation amplitude under varying engine states.

This control algorithm is an extremely effective method of removing steady-state errors and also for establishing the air/fuel ratio modulation that enhances the conversion capability of the three way catalytic converter. The PI-closed loop control method is perfectly applicable to gas engine air/fuel ratio control, as it is for petrol operation, for exactly the same reasons. But it has been demonstrated that there exists certain operating conditions that the controller cannot compensate for (which exists for both petrol and natural gas operation). These conditions cannot be ignored. This requires a further extension to the controller algorithm, aimed at removing the transient errors.

Simulation results have demonstrated that full PID-feedback control has no beneficial effects over PI-feedback control. The derivative term cannot distinguish between A/F ratio excursions and those induced by modulation, reducing its ability to compensate for the error. In fact, due to the use of the comparator, it is not possible for the feedback controller to establish any information as to the magnitude of the error. The use of the comparator is entirely necessary, however, to enable reliable A/F ratio modulation to be commanded from a well conditioned input signal.

Furthermore, the closed-loop controller suffers from the system delay and can only begin to correct for A/F ratio errors a time t_d after they have occurred.

Based on these findings, it would appear that there are two underlying criteria that the current control system is lacking. The first is the need for a recognition of

when the system is encountering a severe transient. The second is the requirement that compensatory action must be taken with improved speed over that of current closed-loop control. These factors must be approached in the construction of a new control strategy. An extra criteria that must be remembered before proceeding, is that for a new control structure to be swiftly implemented, it cannot rely on developing new and future sensors and hardware, but must utilise current system abilities. Therefore, a new control algorithm should be restricted to only those currently-sensed engine states.

The path is now laid forward for the following chapters to demonstrate the research that has been conducted into realising these proposals.

Chapter 5

Transient A/F Ratio Control

5.1 Aims

The purpose of this chapter is to investigate methods of improving A/F ratio control based on the findings of the previous chapter. The primary target shall be to remove the transient A/F ratio excursions prevalent during harsh engine operation. The constraints of the G.F.I. processor rate and restrictions of currently available sensor inputs, shall be adhered to. This shall allow an assessment of the developed controller practicability and an evaluation of the potential benefits of its inclusion in the G.F.I system.

A recent control approach, known as SMC, shall be the subject of investigation. Through its application on the engine model, its ability to reduce transient excursions shall be assessed. Based on these findings, motivation shall then be given to the proposal of an open-loop strategy aimed at increasing the effectiveness of transient compensation.

5.2 Sliding-Mode Control (SMC)

A number of recent reports by automotive researchers, have detailed the use of sliding-mode control as applied to engine systems [109, 110, 111, 112, 113]. Of these reports, those that deal with A/F ratio control, use an EGO sensor, of the

type modelled in this thesis. The principle behind sliding-mode control is to drive an *error surface* to zero, such that the desired engine state is maintained about a desired value.

Consider the definition of the normalised A/F ratio (as defined by equation 1.7), to be given by the masses of the two constituents residing in the manifold, as

$$\lambda = \frac{1}{(A/F_s)} \cdot \frac{m_a}{m_f} \tag{5.1}$$

where (A/F_s) is the desired A/F ratio for the fuel type used. This expression is considered to define the A/F ratio entering the combustion chambers over the period for which the inlet valves are maintained open. To a first approximation, the ratio may be expressed as the flow rates of each medium entering the manifold [110] as

$$\lambda = \frac{1}{(A/F_s)} \cdot \frac{\dot{m}_{ai}}{\dot{m}_{fi}}, \tag{5.2}$$

where $\dot{m}_{ai}$ and $\dot{m}_{fi}$ are the mass flow rates of air and fuel respectively. For stoichiometric operation, λ must be maintained equal to 1, which allows the A/F ratio equation 5.2 to be rearranged as

$$0 = \dot{m}_{ai} - (A/F_s) \cdot \dot{m}_{fi}. \tag{5.3}$$

If this expression is always true, then the A/F ratio is constantly maintained at the desired setting and the control objective is achieved. In order to perform this task, Cho and Hedrick [109] suggested a surface be defined that represents the error that occurs if lean or rich excursions are encountered. The error surface, S, is then defined as

$$S = \dot{m}_{ai} - (A/F_s) \cdot \dot{m}_{fi}. \tag{5.4}$$

The control objective is one of maintaining the value of S at zero, thereby establishing stoichiometric conditions. This is typically achieved by the use of the sliding condition which imposes the Lyapunov stability criteria [87], thus ensuring

that the surface approaches zero. A Lyapunov scalar function, V, can be defined to stabilise the system asymptotically [103] if the condition $\dot{V} < 0$ is maintained. For the A/F ratio, the error-surface definition, S, the Lyapunov function derivative is defined as

$$\dot{V} = S \cdot \dot{S} < 0. \tag{5.5}$$

The Lyapunov criteria is then satisfied [110] by defining

$$\dot{S} = -\eta \cdot sgn(S), \qquad \eta > 0. \tag{5.6}$$

This equation ensures that if $S > 0$ (denoting lean A/F ratios), then the surface condition of $S = 0$ (stoichiometry) is found to be attractive by forcing the trajectory of $\dot{S}$ to be negative. Conversely, if $S < 0$, then $\dot{S}$ is forced to be positive. The trajectory of the error is always directed towards zero and, once at this minimum value, the closed-loop dynamics will slide or chatter the error along $S = 0$, in a similar fashion to PI-closed-loop control [110].

Drawing attention back to the issues raised in the conclusions of the previous chapter, there exist two areas that must be addressed if transient A/F ratio errors are to be minimised. In respect of the first point, a sliding-mode control structure (SMC) demonstrated by Kaidantzis et. al. [87], appears to tackle the problem of recognising the condition of engine transient behaviour. A full derivation of the Kaidantzis SMC approach is not intended here, but a detailed discussion of this recent approach, aimed at tackling transient effects, shall be presented.

In the SMC approach, the nominal open-loop control strategy is maintained, whilst the feedback PI-control structure is now replaced by the SMC structure. The SMC feedback control strategy, commands a fuel flow rate $\dot{m}_{smc}$, that replaces $\dot{m}_{pi}$. That total fuel command, $\dot{m}_{fc}$, is then given as the sum of each component, as

$$\dot{m}_{fc} = \dot{m}_{f_{nom}} + \dot{m}_{smc} \tag{5.7}$$

and can be directly compared to equation 4.3, where the computation of $\dot{m}_{f_{nom}}$ is exactly that defined by equation 4.1.

The SMC feedback algorithm described by Kaidantzis et. al. [87], is constructed as the integral of the product of the comparator output signal, e_c, and the SMC gain, K_{smc}, as

$$\dot{m}_{smc} = \int K_{smc} \cdot e_c \, dt. \tag{5.8}$$

The total SMC structure, therefore, amounts to the nominal open-loop control with integral-only feedback to adjust for errors. However, the fundamental difference between the I-controller seen in the previous chapter, and the SMC I-controller, enters through the selection of the SMC gain, K_{smc}.

The purpose of the SMC feedback algorithm is three-fold:

- to remove steady-state estimation inaccuracies,
- to maintain the controlled amplitude of the A/F ratio modulations,
- to distinguish between steady-state and transient operating conditions, such that corrective action may be taken to reduce large transient A/F ratio excursions.

In order to meet these objectives, Kaidantzis et. al. suggest a rather elegant method of selecting K_{smc}. The approach is to take account of the two differing conditions of steady-state (ss) and transient (tr) operation. The gain is therefore constructed as the sum of the individual components, as

$$K_{smc} = K_{ss} + K_{tr}. \tag{5.9}$$

The first term, K_{ss}, is designed to compensate for steady-state (ss) errors that occur due to measurement and metering inaccuracies - of the type seen in figures 4.9 and 4.19. The second term, K_{tr}, is directed at transient (tr) conditions which allow A/F ratio excursions to develop from rapid throttle variations.

Steady-state conditions select K_{ss} to be dominant over K_{tr}. The magnitude of K_{smc} is then defined as

$$K_{smc} = K_{ss}. \tag{5.10}$$

It can then be seen that for steady-state conditions, the SMC feedback command, $\dot{m}_{smc}$, is exactly that of the integral-only feedback command of equation 4.4. The modulation amplitude of the fuel flow will then be selected by the choice of K_{ss}. In order to maintain the same conditions of A/F ratio modulation, as was demonstrated for integral-only control, K_{ss} is selected in accordance with equation 4.13. It follows that the frequency of modulation will also be identical to that of integral-only control, as defined by the engine time delay, ΔT, in equation 4.9.

Under transient conditions, the magnitude of K_{tr} is designed to grow to a higher magnitude than K_{ss}, such that

$$K_{smc} \approx K_{tr}. \tag{5.11}$$

This will ensure that an increase in control action is provided, to compensate for rapidly changing states. In this manner, the baseline feedback gain, K_{ss}, could be considered as the *nominal feedback gain*, which operates continuously. The transient gain is provided to *trim* for rapid engine transients, which the nominal open-loop controller cannot recognise and compensate for.

A full derivation of the transient feedback gain is not to be detailed here, but is described by Kaidantzis et. al. [87] as

$$K_{tr} = \frac{\Delta_a}{\lambda_{des} \cdot (A/F_s)} \cdot \left|\dot{\hat{m}}_{ao}\right| + \Delta_f \cdot \left|\dot{\hat{m}}_{f_{nom}}\right|, \tag{5.12}$$

where $\dot{\hat{m}}_{ao}$ is the estimated port flow rate derivative out of the manifold, and $\dot{\hat{m}}_{f_{nom}}$ is the nominal fuel flow rate derivative.

The terms Δ_a and Δ_f in equation 5.12, are defined to be the upper uncertainties in the estimates of the air and fuel flow rates, respectively. An uncertainty

of 1% in the air flow will require $\Delta_a = 0.01$. It can then be seen, that if both flow rate estimates are exact (zero uncertainty), the SMC transient control gain is zero, and the controller will provide no compensation during transients. But if the estimates are inaccurate, then the additional transient control action is provided.

By using the absolute magnitudes of the flow rate derivatives, the value of K_{smc} is always maintained positive, in contrast to the negatively chosen gains of the PI-controller. If this positive gain is paired with the error, e_c, as described in equation 4.5, any steady-state errors would not converge, since the error signal takes on the values of $e_c = -1$ for lean conditions, and $e_c = 1$ for rich conditions. When these values are used as inputs to the SMC, with its positive-only gain, extra fuel will be added when running rich and fuel flow will be reduced when running lean. Therefore, the sense of the error signal must be corrected. This is completed by switching the terms at the summation junction of zirconia feedback signal and desired setting.

The comparator output signal for the SMC strategy is now given as:

$$e_c = sgn\left(\lambda_{des} - \lambda_{sen}\right). \tag{5.13}$$

The use of the flow rate derivatives allows a transient condition to be identified by the controller. A rapid throttle transient will cause both $\dot{m}_{ao}$ and $\dot{m}_{f_{nom}}$ to change rapidly. Once the estimation uncertainties are set, the transient gain is selected by the absolute magnitudes of these rates of change. The transient feedback gain is thus dictated from these operating conditions.

A block diagram for the SMC control formulation can be seen in figure 5.1. By comparison with figure 4.10, the integral feedback control gain is replaced with the equivalent steady-state gain, K_{ss}, and the transient gain is featured as a replacement to the proportional gain. Links have been established between K_{tr} and the air and fuel flow rates, to depict the stronger dependency of the feedback gain selection upon a larger number of engine states. Notice also, the changes at

the summation junction of the feedback signal and desired value.

A digital controller representation of the SMC approach, is logically achievable by following the previous descriptions of the integral and derivative numerical approximations, as detailed in sections 4.4.2 and 4.5, respectively.

An additional benefit of this SMC approach is the increased awareness of the engine state conditions. From the use of the *derivatives* of variable states, a knowledge of how the conditions are changing is afforded, but without the need for an increase in the number of sensors. This is obviously a desirable attribute, and one that follows the additional criteria set forth in the conclusions of chapter 4 - that of utilising only currently available sensors.

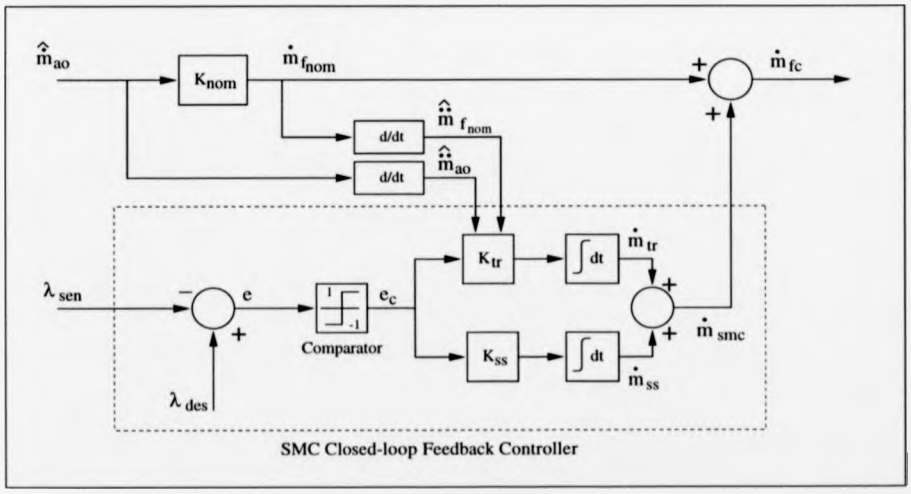

Figure 5.1: Sliding-mode control structure for transient A/F ratio control.

5.2.1 SMC Performance

The effects of this SMC approach have been investigated on the gas engine model. To stimulate the active behaviour of K_{tr}, the first category of simulations are

conducted for exactly the same engine operating conditions as the simulation in figure 4.21. However, an error of -5% in the air flow is invoked at $t = 0$, and maintained throughout the simulation, to allow the SMC transient gain to be activated at the relevant stage. The value of Δ_a is therefore assigned as 0.05, and Δ_f is set at zero by assuming that the actual injected fuel is precisely known.

The first plot, figure 5.2, is conducted for the PI-controller - to act as a comparison for the ensuing SMC simulations. It can be seen that the PI-controller successfully reduces the lean error, at commencement of simulation, due to insufficient fuel arising from the introduction of the error. The λ-trace is quickly brought back to the set-point modulation around 1. The transient induced excursions are still in evidence, and reach approximately the same magnitudes as those seen in figure 4.21 - maximum $\lambda = 1.24$ and minimum $\lambda = 0.763$.

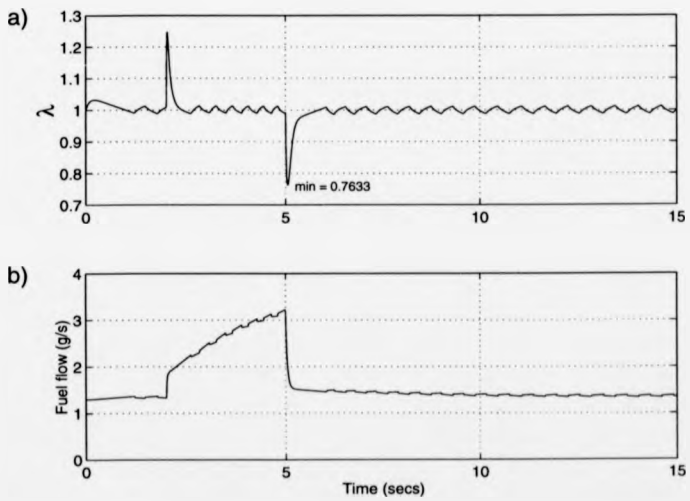

Figure 5.2: PI-controlled simulation with constant 5% error in air estimation.

A slightly prolonged rich mixture is encountered as the throttle 'step-down' excursion returns to stoichiometry. This is due to the integral action maintaining a

fuel flow modulation about a mean value *higher* than zero, since it is compensating for the -5% error in air estimation. As the nominal flow rate reduces due to reducing port air, the integral action persists in its compensating role by providing extra fuel, thereby tending to maintain a rich mixture.

The fuel flow action for PI-control is also shown and shall be used as a comparison against following SMC simulations. It should be noted that perhaps the most significant difference between the fuel flow of figures 5.2(b) and 4.21(c), is the lack of modulation that occurs at the beginning of the 5% error simulation, as the controller corrects for the error. The controller quickly removes the error and returns to its intended modulation task.

The SMC simulation can now be seen in figure 5.3, for the same driving conditions. Similar to the PI-controlled simulation, the lean condition is eradicated at the commencement of simulation. The SMC feedback gain, as depicted in figure 5.3(c), is operating, initially, in steady-state ($K_{smc} = K_{ss}$) and hence operates as an integral-only feedback controller. The most obvious difference is, therefore, the lack of 'jump-back' effect, attributable to the loss of the proportional control effort. This reduces the modulation frequency by half and promotes a smoother undulation in fuel flow command, and subsequently λ.

During the throttle motions, the SMC gain is seen to 'spike' in response to the increase in the port air flow derivative. The effect of these spikes on fuel flow is, however, very difficult to see. The port flow rate changes very quickly, coming to its steady state quite soon after the throttle has come to rest. The rise in K_{tr} consequently reaches a very high value (in comparison to K_{ss}), but is also very short lived, matching the duration time of the port flow derivative. As the feedback product, $(K_{smc} \cdot e_c)$, passes through the integrator action, the power of this gain increase to adjust the fuelling is reduced. The SMC integrator output, therefore, does not demonstrate such demanding increases in fuel flow as that

demanded by the integrator input, $K_{smc} \cdot e_c$.

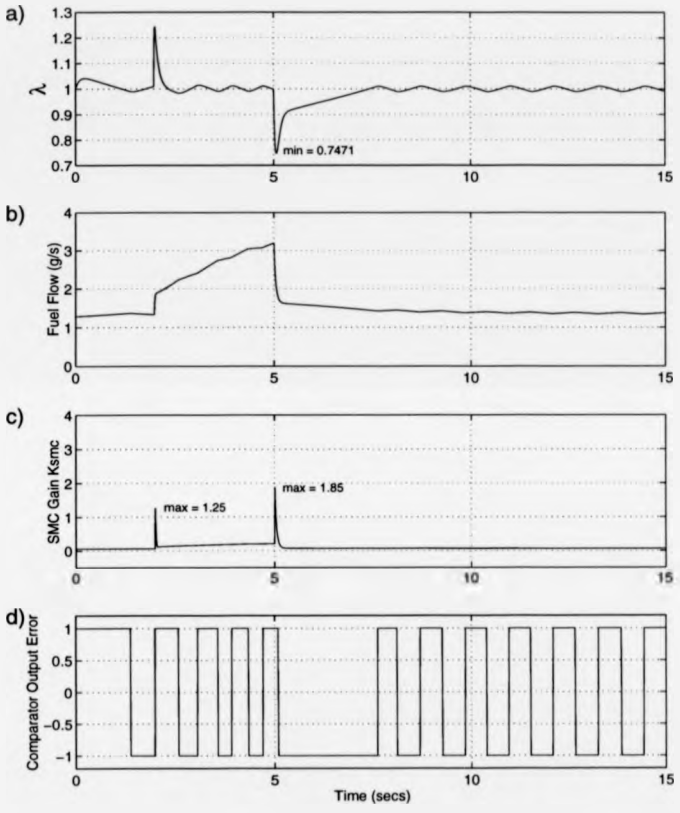

Figure 5.3: Sliding-mode controlled simulation with constant -5% error in air estimation. Air flow tolerance is set at $\Delta_a = 0.05$ to match expected estimation error.

Further to the problem of the short duration of the transient induced gain increase, a second aspect of feedback SMC is observed that presents difficulties in reducing transient excursions. It can be seen, particularly for the throttle step-down condition, that the comparator error signal remains as +1 for a short time after throttle step, which is invoked exactly on 5 seconds into the simulation

- figure 5.3(d). From equation 5.13, this error value denotes a lean A/F ratio condition, however, the system is now running rich due to the sharp throttle step-down. It is not until the engine time delay has passed, approximately 80 ms, that the comparator output signifies that a rich excursion is occurring.

The effect of the feedback SMC is, then, to *maintain* an increasing fuel flow during a *rich* excursion, when, in fact, the required adjustment is to drastically reduce the fuel. The SMC is then acting in an opposing direction to that intended by its design. This is solely attributable to the presence of system delay.

When the transient has then passed, the SMC is left to correct for the A/F ratio errors purely on integral-only feedback control. It therefore has more corrective work to complete, due to the consequence of the transient effects. This is quite clearly slower than would be for PI-control correction and manifests itself by the long track back up to stoichiometry after the throttle step-down at 5 seconds (figure 5.3,(a)).

The choice of Δ_a in this instance, is quite straight-forward, since the precise value of the imposed error is known to be set at 5%. But what should be the value of Δ_a if the estimation error is unknown?

Clearly, in a practical context, the estimate, or sensor measurement, of an engine variable is expected to have some discrepancy to that of the actual value. This is due to an inadequate model, sensor imperfection or noise, for example. A value for the difference between the actual state and estimated state, i.e. Δ_a, is extremely difficult, if not impossible, to estimate. Estimated state values are very often the only information available pertaining to the state. Also, multiple sensors are not employed on an engine to provide an average value, in an effort to improve the measurement precision!

In an attempt to try and demonstrate this hypothesis, a second simulation is illustrated, again for the same conditions as in figure 5.3, but now the upper

uncertainty in the air flow is assigned twice the known error value, i.e. $\Delta_a = 0.10$. This simulation is seen in figure 5.4.

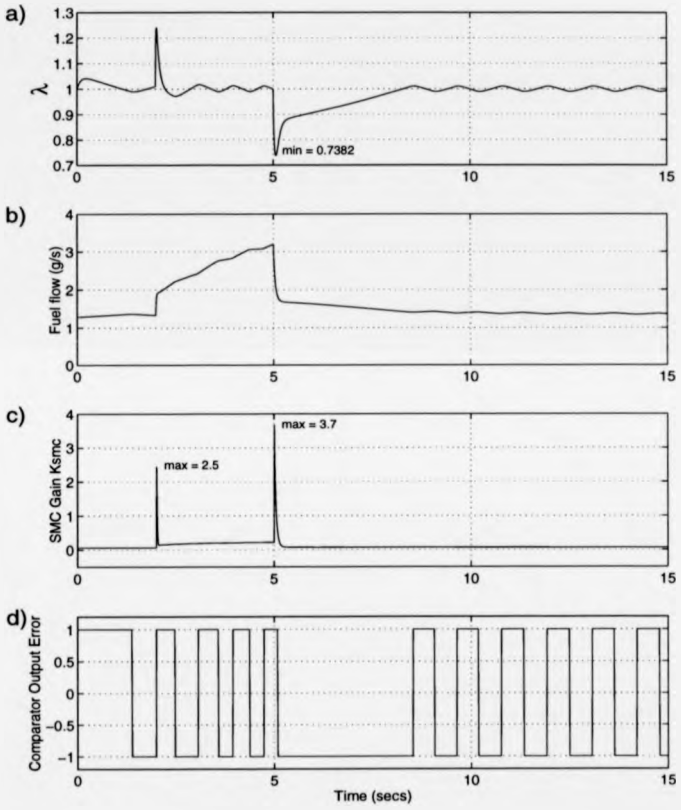

Figure 5.4: Sliding-mode controlled simulation with constant 5% error in air estimation. Air flow tolerance is incorrectly set at $\Delta_a = 0.10$, demonstrating the effects of wrongly chosen uncertainties.

Immediately obvious, is the doubling of the transient gain spikes at 2 and 5 seconds. These increases in gain produce no reduction in the λ-excursions. In fact, it can be seen, in comparison with both figures 5.2(a) and 5.3(a), that the throttle step-down excursion exhibits a greater magnitude in rich mixture

excursion reaching a minimum of 0.738 λ, in comparison to 0.7633 for the PI-control simulation. This is, again, due to the delay in the system causing the controller to receive an error signal (figure 5.4(d)) that is not reflecting current system conditions.

The increased transient gain, therefore, provides even more fuel during rich conditions. After the excursion has passed, the fuel is left at far-too-rich-a-setting that only the integral gain, K_{ss}, can correct. The error is eventually removed, as demonstrated in the λ-trace (figure 5.4(a)) and fuel trace (figure 5.4(b)), approximately 3 seconds *after* the throttle has come back to rest.

The simulations presented here are typical of many that were conducted during the investigations of this control approach. For all SMC simulations, even during throttle ramping transitions, the effect of the delayed feedback consistently promoted the problem of opposing the required fuelling action, and therefore increasing the λ-excursion.

5.2.2 Discussion

A number of conclusions may be drawn from the simulation results observed for the SMC application. But firstly, it must be remembered that severe throttle changes have been applied in the observed simulations, to subject the system to the harshest conditions that could be expected under normal operation. In respect of this, the A/F ratio controller must perform adequately well under these conditions and reduce the λ-excursions.

The manifold dynamics are considered to be much quicker than the dynamics of the crankshaft, and the air flows reach static conditions reasonably soon after a throttle step input (approximately 150 ms for the step-down response in figure 5.4). Therefore, the life of the transient gain, K_{tr}, is very short (approximately 50 ms for step-up and 150 ms for step-down), but also of very large magnitude.

If the durations of the state transients describing K_{tr}, are less than the current system time delay, t_d, then the SMC will produce an opposing fuel command to that required to reduce the A/F ratio excursion. This is because K_{smc} is always maintained as a +ve constant, relying on the sign of the error signal to govern the increase or decrease of the fuel. After the states have stabilised, the fuel flow is left either too high or too low as a result, and it is then the task of the steady-state (K_{ss}) term of the SMC to bring the A/F ratio back to the desired setting. As this is essentially integral-only control, the response is slower than for the conventional PI-controller.

The estimates of the uncertainties of Δ_a and Δ_f, are largely unknown. Essentially, this renders the transient gain selection, as described by equation 5.12, as an arbitrary figure based on an 'educated guess' as to what the uncertainties are. These values are likely to be programmed as constants in the gain selection equation in the controller algorithm, but it is highly unlikely that the actual uncertainty will be constant.

Consider then, the case for an exact measure of air and fuel flow, the values chosen of Δ_a and Δ_f will be defined as zero. Thus, the transient gain will always remain zero and no attempt will be made at all to reduce the transient excursion. However, it has already been established that these excursions do not arise solely from measurement errors, but from the the use of a speed-density derived fuel command being implemented on a throttle body injection system. Therefore, if no estimation errors exist, the SMC does nothing in way of compensation, and if they do, this SMC structure can seriously degrade transient performance.

5.3 Open-loop Transient Compensation Control (OTCC)

Although the SMC approach has difficulty in reducing the A/F excursions, for the reasons detailed above, it possesses a significant attribute that should be considered further - that of focusing the controller's attention on transient engine conditions. This is achieved through the use of the derivatives of both the fuel flow and air flow. With new thought on how to make use of these signals, the controller can be restructured to improve transient A/F ratio control.

It was concluded that one of the shortfalls behind the SMC approach was the inherent system time delay. The SMC feedback action is governed by the comparator signal, which effectively increases or decreases fuel by its action on the positive feedback gain. Therefore, the feedback controller cannot take corrective action until the feedback signal provides information about the excursion away from set point. This is not a failing particular to the SMC structure, but to the feedback control of systems with a time delay. The feedback control algorithm begins corrective action the instant a transient condition is detected, but will always be operating on the *out-of-date* error signal. To increase the speed of response of the controller to an encountered transient, the use of the flow derivative information must be applied by more effective means. This section describes the use of this signal in a new open-loop strategy developed by this work.

It was demonstrated in figure 4.6, that the nominal open-loop fuelling command is the **fast**-fuel command, reacting to system changes faster than the corrective nature of the feedback loop. If the increase in the transient gain can be applied in an open-loop sense, then the controller is not reliant upon the sensor signal to correct for throttle induced A/F ratio excursions.

The SMC structure maintains an integral term to remove steady-state errors, and simply replaces the proportional term with the transient uncertainty error

correction. This demonstrates the importance that some form of feedback control must remain in the overall A/F ratio control algorithm.

A new control approach is described here; an extension of the PI-controller demonstrated in the previous chapter. This will ensure that steady-state errors can be reliably and swiftly removed by the feedback action, already demonstrated. Also, it has already been established that PI-controllers have been in use for many years and will not present any problems in respect of applicability. This new control strategy shall be known as *open-loop transient compensation control* (OTCC), through the action of the additional control element.

A block diagram for the proposed control structure can be seen in figure 5.5. The conventional PI-feedback control architecture remains preserved. The additional open-loop control block can be seen in the upper portion of the diagram and has only one input signal. This demonstrates the requirement for **no** additional sensors to be located on the engine; only status information that is already available is utilised.

In order to obtain the air flow derivatives, the difference equation, seen in equation 4.24, is used to obtain the air flow rate derivative estimation as

$$\dot{\hat{m}}_{ao}(nT) = \frac{\hat{\dot{m}}_{ao}(nT) - \hat{\dot{m}}_{ao}(nT - T)}{T}, \tag{5.14}$$

where T remains as the controller sample rate. Note also, that $\hat{\dot{m}}_{ao}$ is assumed to be the measured, or estimated, port air flow rate.

Within the open-loop control block, the discrete differencing approximation requires the previous air flow estimate to be held. This is encompassed in the block denoted by d/dt. The derivative air flow value is then used as the input to the open-loop transient gain block, $K_{tr_{op}}$.

The total commanded fuel, $\dot{m}_{fc}$, from this control structure is therefore defined

as the sum of open-loop and feedback commanded fuel, as:

$$\dot{m}_{fc} = \underbrace{\dot{m}_{f_{nom}} + \dot{m}_{tr}}_{\text{open-loop}} + \underbrace{\dot{m}_p + \dot{m}_i}_{\text{feedback}}, \tag{5.15}$$

where $\dot{m}_{f_{nom}}$, $\dot{m}_p$ and $\dot{m}_i$ are unchanged from the conventional PI-controller.

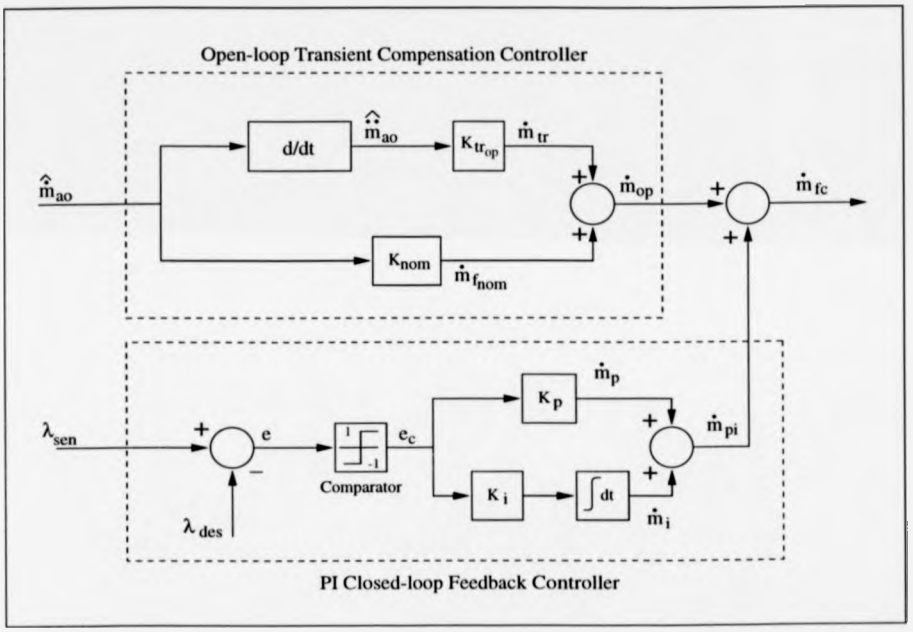

Figure 5.5: Transient compensation controller structure. The additional open-loop architecture requires no feedback signal input, allowing it to respond rapidly to changes in state. No further sensory devices are required as the single air flow rate input is utilised to give state and state-change information.

The controller of figure 5.5, is an extension to the conventional PI-closed loop air/fuel ratio controller. The PI-closed loop algorithm is maintained to ensure that the steady-state errors are removed and the desired modulation is in force. The 'extension' is embodied in the 'open-loop' algorithm approach, where the air flow derivative is coupled to the standard absolute air flow signal. This approach is

aimed at recognising a transient condition and altering the fuel accordingly to the changing engine conditions. The open-loop derivative control is much faster than any feedback approach since the engine time delay is not encountered. This is the advantage that the open-loop transient control approach has over the Kaidantzis control approach reported earlier.

5.3.1 Gain Selection

In a similar manner to the SMC approach, it was proposed that the open-loop transient gain, $K_{tr_{op}}$, be maintained as a positive value. However, with the absence of the feedback error signal, the sign of the air flow *derivative* must be used to decide on whether to increase or decrease the open-loop fuel command. Thus, for an increasing air flow ($\ddot{\dot{m}}_{ao} > 0$), $\dot{m}_{tr}$ remains positive to meet the demand of an increasing flow rate. Therefore, it is the actual value of $\ddot{\dot{m}}_{ao}$ that is used in the open-loop algorithm, as opposed to the *absolute* value in the SMC algorithm. As the derivative state changes occur immediately, as a consequence of transient behaviour, the system time delay is not encountered, upon waiting for a feedback signal to relate A/F ratio swings. Transient compensation can begin the instant a major excursion begins to occur.

The open-loop compensation fuel command is structured as the product of $\ddot{\dot{m}}_{ao}$ and the transient gain, $K_{tr_{op}}$, as

$$\dot{m}_{tr} = K_{tr_{op}} \cdot \ddot{\dot{m}}_{ao}. \tag{5.16}$$

It is considered that the transient open-loop gain must vary to account for varying engine conditions. It can be appreciated that engine behaviour differs significantly, for the same throttling conditions but at differing engine speeds and load. It is desired then, that $K_{tr_{op}}$ adapt itself to accommodate varying flow rate changes throughout the speed and load range of the engine model applicability. A method for scheduling $K_{tr_{op}}$ to the engine conditions must then be found.

Selecting suitable criteria that should be used in the scheduling process of $K_{tr_{op}}$, lead to the approach of using dimensional analysis. By considering the states that construct the open-loop gain and the state being controlled, $\dot{m}_{tr}$ (measured in unit mass per unit time - gs^{-1}), a basis for the magnitude of $K_{tr_{op}}$ could be found that would not rely upon an intuitive input, but would be selected based on the air flow change of state and operating speed.

From equation 5.16, it can be seen that the port flow rate derivative and commanded fuel flow rate define the gain in dimensions of time (s). To accommodate changing engine conditions, it is proposed that $K_{tr_{op}}$ is dependent upon the reciprocal of engine speed $[(rpm/60)^{-1}]$, thereby maintaining unit consistency and correct dimensions. Therefore, the transient open-loop gain is defined as

$$K_{tr_{op}} = \frac{C_{tr}}{N_e}, \tag{5.17}$$

where C_{tr} is the open-loop gain coefficient and N_e is the engine speed.

In order to establish the value of C_{tr}, the engine model was subjected to a series of simulations, at steady engine speeds, covering the engine operating range for which the model was constructed. For each simulation, the throttle was stepped from near closure angle (that giving only a low torque output) to wide open throttle (WOT) after 2 seconds, and back down again after 5 seconds simulation time. This approach was adopted to excite the most severe A/F ratio excursions under PI-control, over a full sweep of the throttle angle range. The value of $K_{tr_{op}}$ was adjusted at 'run-time' to increase/decrease the open-loop compensation fuel command. It was then possible to select the optimal value of $K_{tr_{op}}$ that displayed significant improvements in the A/F ratio about $\lambda = 1$ during transients.

Figures 5.6 through 5.9, display the speed dependent simulations for adjustments in $K_{tr_{op}}$. The λ-traces for PI-only control are also displayed above the corresponding improved λ-traces of the open-loop transient controller. This allows a direct comparison of the A/F ratio control approaches. The fuel flow rate

under the compensation scheme is also displayed for each simulation.

It should be stressed that for all simulations shown within this chapter are for 'clean' signals where it is assumed that there is no noise or error terms. This approach is taken to allow the OTCC gains to be selected and to demonstrate the ability of the new algorithm. In Chapter 6, the effects of noise, error and map-estimated air flow are investigated to uncover any practical problems that might be met upon transferring the algorithm to the real engine environment.

The substantial reduction in the λ-excursion is clearly visible for each simulation. However, for the compensated simulations, a lean spike is observable on the commencement of throttle step-up. This is due to the microprocessor sample rate allowing the severe throttle transient to promote significant state variations between sampling actions. These spikes are extremely short lived (3ms), and the open-loop compensation returns the A/F ratio back to stoichiometry at the next sample instance as the controller issues the command to adjust the fuelling. To confirm this explanation, the compensation control algorithm was also coded in the continuous block of the model controller. The simulations were performed again, and an example of the continuous control effect can be seen for the 2000 rpm case in figure 5.10. As there is no discrete sampling action, a continuous monitoring of the changing states, and hence continuous control, allows any excursions to be compensated for immediately. Therefore, the λ-trace does not display the large lean spike, seen in figure 5.6(b), but has been eliminated to remain within the catalyst boundary limits. Any subsequent λ-error under this control approach would be attributable to the delay in the gas transportation delay from the injector unit to the spray bar position in the air intake pipe.

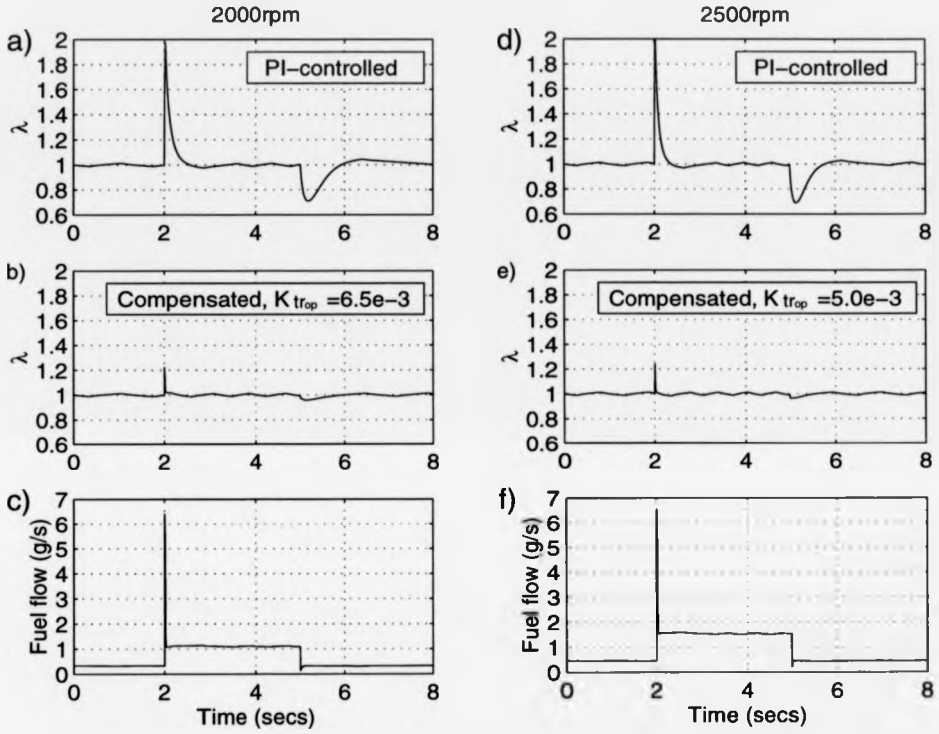

Figure 5.6: Speed-dependent optimal selection of $K_{tr_{op}}$ (2000rpm and 2500rpm).

For each simulation, the fuel flow traces display sharp "spikes" of fuel increase and decrease, in response to the rapid changes in the flow rate changes. Although the controller receives signals pertaining to the port flow rate (i.e. speed-density derived estimation), the compensation algorithm effectively feeds the controller an air flow estimation that matches more closely the throttle air flow rate. In this manner, the fuel injected into the throttle intake area, encourages an A/F ratio closer to stoichiometry further upstream. Consequently, through mixing in the manifold, the A/F ratio of the charge entering the chambers will further be improved.

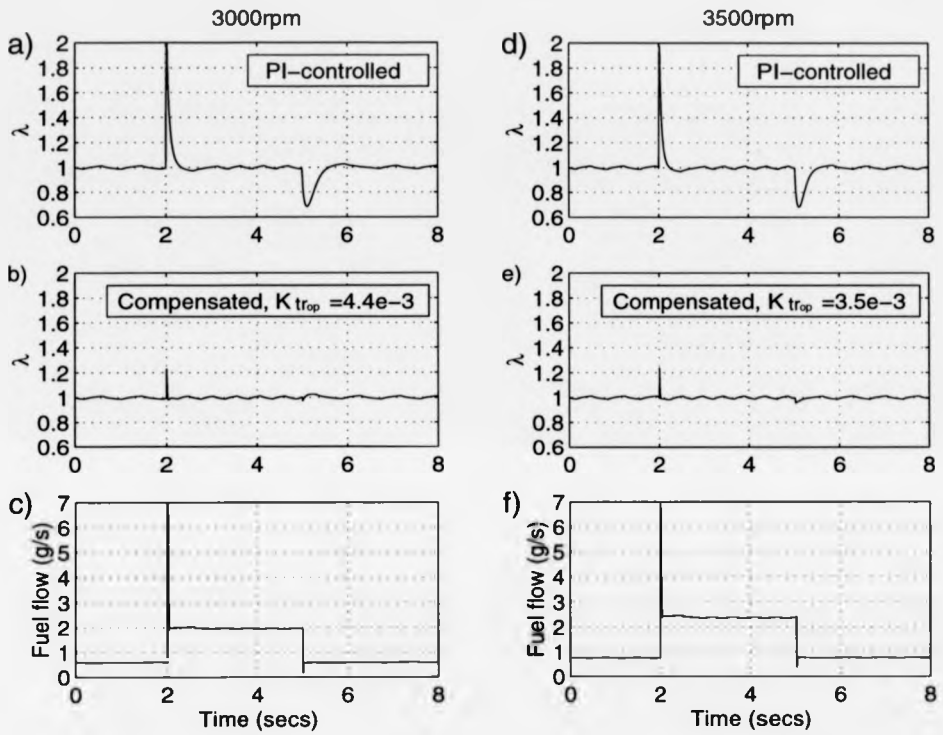

Figure 5.7: Speed-dependent optimal selection of $K_{tr_{op}}$ (3000rpm and 3500rpm).

As the engine speed increases, it is found that the optimum value of $K_{tr_{op}}$ reduces, as summarised in table 5.1. This is because, proportionally, the required alteration of the fuel, demanded from the open-loop compensation algorithm, reduces in comparison to the magnitude of nominal open-loop fuel flow, for increasingly higher speeds. This is highlighted by the fact that the maximum value for each fuel enrichment only ranges between 6.4 and 6.99 for the entire speed range, also displayed in table 5.1. Whereas, it can be seen from the simulation results, that the nominal fuel flow rate increase from a minimum of 0.33 gs^{-1} for minimum speed and throttle angle (2000 rpm and 16.5° - figure 5.6(c)) to a

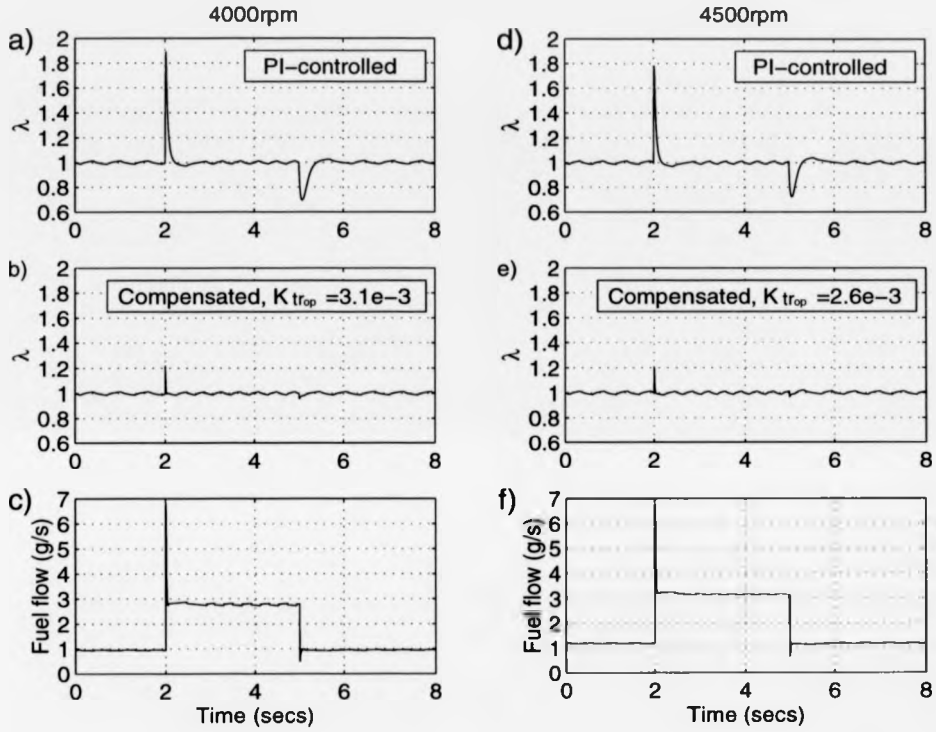

Figure 5.8: Speed-dependent optimal selection of $K_{tr_{op}}$ (4000rpm and 4500rpm).

maximum fuel flow rate of 3.5 gs^{-1} for maximum speed and throttle angle (5000 rpm and 90° - figure 5.9(c)).

The gain coefficient, C_{tr}, of equation 5.17, can now be found by regression analysis. This will allow the embedded controller algorithm to continually schedule the value of $K_{tr_{op}}$ to the changing engine operating speed. Figure 5.11 displays the least-squares regression fit for equation 5.17, and the value of C_{tr} is found to be 12.64.

The open-loop controller now has a method of selecting the transient compensation gain based on operating conditions, in contrast to the SMC approach.

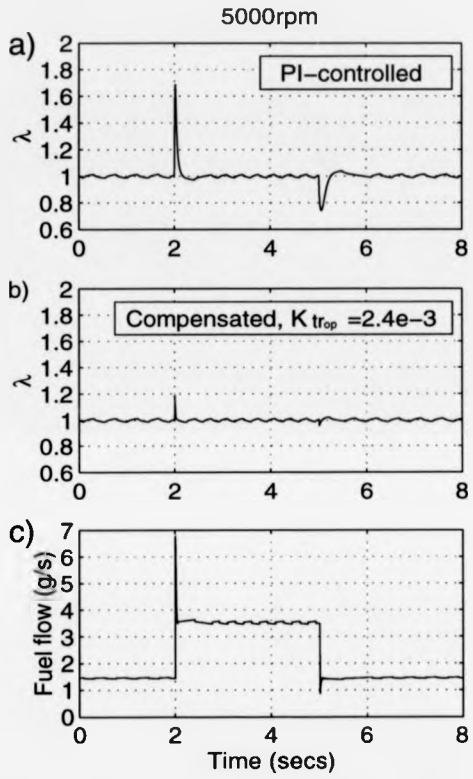

Figure 5.9: Speed-dependent optimal selection of $K_{tr_{op}}$ (5000rpm).

Therefore, the controller now requires the engine speed sensor signal as an input. This signal is available on virtually all engines, and is already being used as an input for the nominal open-loop controller, see figure 4.2. Hence, there exists no increase in cost or complexity due to increased hardware.

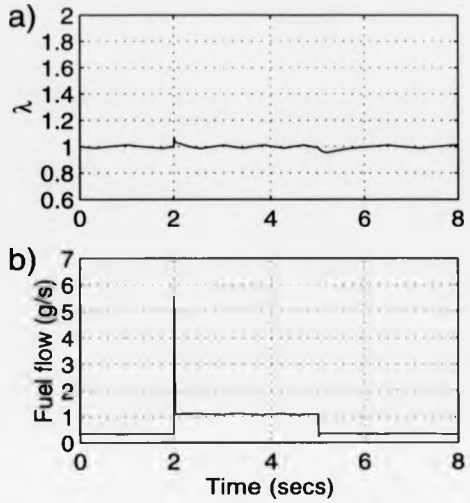

Figure 5.10: Example of transient compensation under continuous control, conducted at 2000 rpm and comparable to figure 5.6 b) & c).

Engine Speed (rpm)	$K_{tr_{op}}$	Maximum Required Fuel Flow (g/s)
2000	0.0065	6.4078
2500	0.0050	6.5482
3000	0.0044	6.9985
3500	0.0035	6.8260
4000	0.0031	6.8575
4500	0.0026	6.7847
5000	0.0024	6.7847

Table 5.1: Optimal values of $K_{tr_{op}}$, as seen in figures 5.6 through 5.9

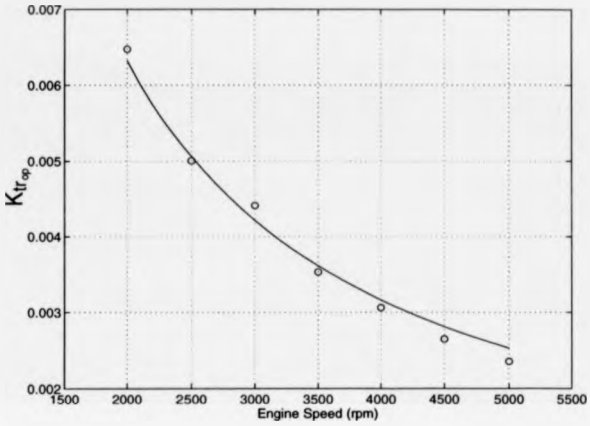

Figure 5.11: Regression of optimal open-loop gain values.

5.3.2 OTCC Performance

A number of simulations have been performed to investigate the behaviour of the developed open-loop compensation algorithm under dynamically varying conditions.

The first of these to be shown here, is chosen to demonstrate improved A/F ratio control upon that already seen in figure 4.21, under conventional PI-control. The compensation control simulation is displayed in figure 5.12.

The stepped throttle conditions were seen to induce large A/F ratio excursions in figure 4.21(d), but it can now be seen, in figure 5.12(c), that the open-loop compensation algorithm is providing a sharp increase in fuel flow during throttle-up, and a faster reduction in fuel flow during throttle-down. These rapid alterations in the fuel flow are short lived due to the nature of the port flow rate of change. The quick throttle action incites large flow rate changes. The variation between the throttle and port flows, during throttle transition, grows significantly during the throttling period, but quickly recedes when the throttle is at rest.

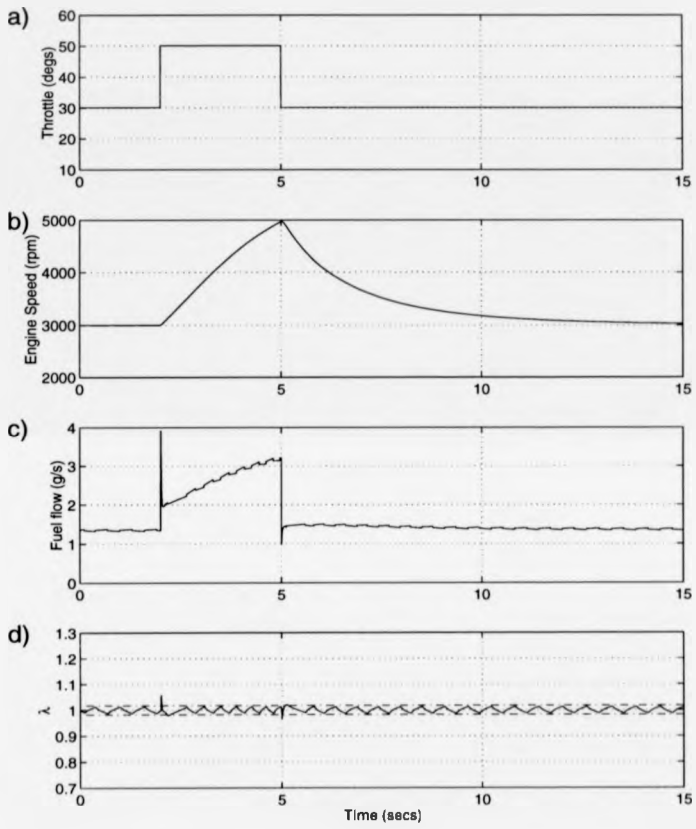

Figure 5.12: Transient A/F ratio compensation control under severe throttle conditions for 2nd gear operation.

The resulting λ-trace, figure 5.12(d), displays excellent behaviour about the desired value of 1. The modulation is maintained through the PI-control action, and can be seen to remain within the λ-window limits (denoted by the two dashed lines) required for catalyst systems. There exist extremely small 'spikes' in λ at the instance of throttle steps, which just manage to exit the window limits. These are due to the fast throttle action exciting large changes of states between the

controller sampling times. These spikes are rapidly brought back into the limits at the subsequent sampling and control action, demonstrating the requirement for fast microprocessor sampling rates. The larger the duration between samples, the larger the A/F ratio excursions will be allowed to develop.

A second illustrated simulation, for stepped throttling action, can be seen in figure 5.13. The simulation commences at 2000rpm and the throttle undergoes two step sequences after 2 seconds and 6 seconds. The torque is maintained at a low enough value to allow the engine to reach 4000 rpm.

The fuel flow action is shown in figure 5.13(c), where the fast compensation action is clearly visible upon the usual PI-commanded fuel. The fuel flow is commanded to alter rapidly to the changing conditions producing the characteristic fuel 'spikes', whilst the 'step and slide' action of the PI-controller persists in addition to the nominal fuel command.

The resulting compensation λ-control, figure 5.13(d), can be directly compared to the PI-control ability, figure 5.13(e), for the same simulation conditions. It is clear that transient compensation is completing the task of reducing the transient excursions.

There is a slight visible lean period under compensation control, after the throttle step down at 7.5 seconds - figure 5.13(d). This is attributable to the choice of compensation gain. During the reduction in port flow rate, the gain K_{tr} is selected at a slightly higher value than is required to produce stoichiometry. Consequently, the fuel is reduced at a greater rate than is necessary. As the port flow rate of change stabilises, the feedback action returns A/F ratio back to stoichiometry, displayed by the characteristic negative gradient.

This effect is due to the rapidly changing flow rates induced by the fast throttle action. Whereas the rotational dynamics are comparably slower, the gain reduces inversely proportional to the decreasing engine speed. It should be remembered,

that the gain selection criteria was based on steady engine speeds, and therefore is expected to display some deviation under dynamic operation.

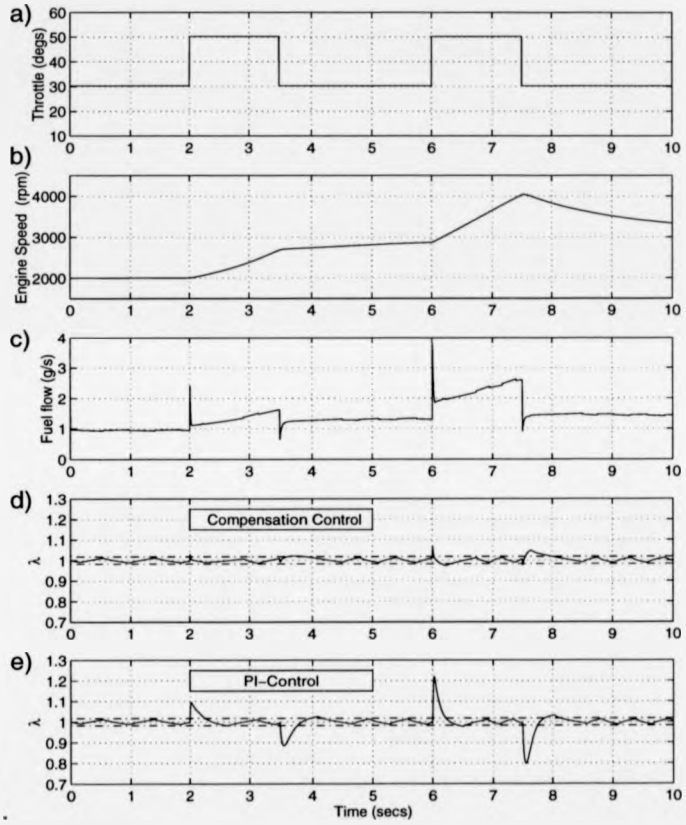

Figure 5.13: Transient A/F ratio compensation control with two throttle steps under 2nd gear operation.

Both OTCC simulations have involved stepped throttle changes. It is true that these conditions excite the most rapid changes in state and produce the most severe A/F ratio excursions. However, realistic throttle transitions occur over some finite time governed by the driver action. For a more slowly varying

throttle, the throttle air flow still leads the port air flow, due to the manifold dynamics, but the magnitude of the difference between the flow rates is not as great as those induced by throttle steps. Conversely, the variation in flow rates is prolonged for as long as the throttle action persists. The effect on A/F ratio control using port air flow to command the nominal fuel, is a more prolonged excursion of lower magnitude.

Figure 5.14 demonstrates this effect, as the engine's responds to a throttle input that varies over half a second. The fuel flow command shown in plot 5.14(c), is commanded from the full compensation control algorithm. The moderate changes in port flow rate do not now induce the large fuel spikes seen for the step simulations, and a more continuous fuel trace is depicted.

The λ-trace remains strictly inside the window limits, figure 5.14(d), even though the port air flow lags behind the throttle air flow - into which the gas is being injected. The PI-controller on the other hand, figure 5.14(e), suffers the initial A/F ratio excursion during the throttle action. After the throttle down sequence, the gradual engine speed reduction from 4700rpm, reduces the port air flow before the throttle air flow whilst the throttle remains stationary. Hence, the fuel flow commanded from the port flow will be reduced, but is actually entering the higher throttle air flow rate. This incites a lean condition ($\lambda > 1$) in the PI-controlled system which is slowly removed by the feedback controller.

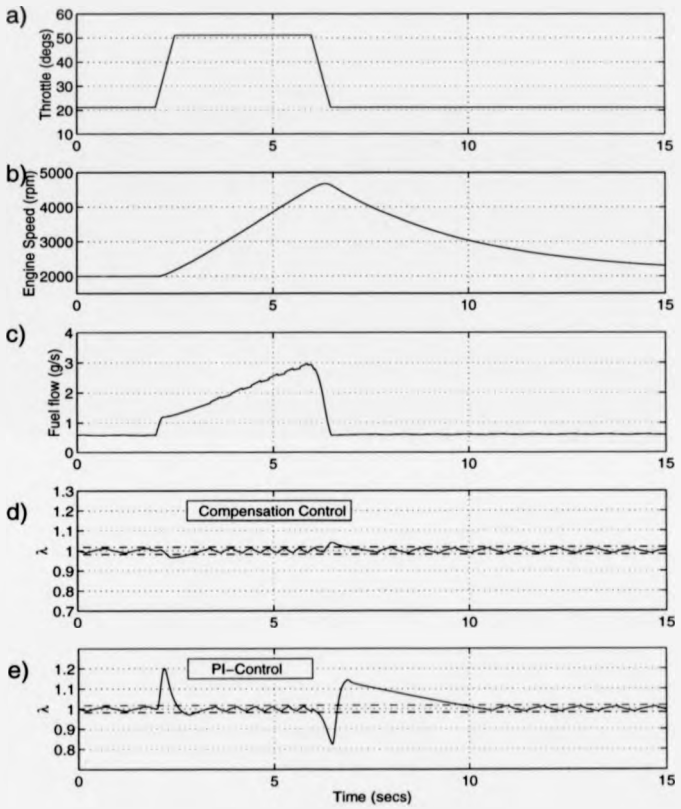

Figure 5.14: Transient A/F ratio compensation control under throttle ramping action. 3rd gear operation.

A rather typical simulation, involving throttle 'ramping' inputs, is shown in figure 5.15.

The engine initially operates at a steady 4000rpm in 3rd gear, and the throttle is varied by 10° with a constant gradient over 0.75 seconds. These conditions could be construed as releasing the throttle whilst the vehicle is cruising at a moderate speed. Again, the compensation controller maintains much improved

A/F ratio control over that of the PI-controller. Whilst the engine is increasing or decreasing in speed, the compensation algorithm continues to be active even though the throttle remains static. This is due to the engine speed being the primary governing factor of the port air flow. Whereas the comparable PI-controlled λ, seen in figure 5.15(e), has no open-loop control and is left to correct for lean conditions solely under feedback action.

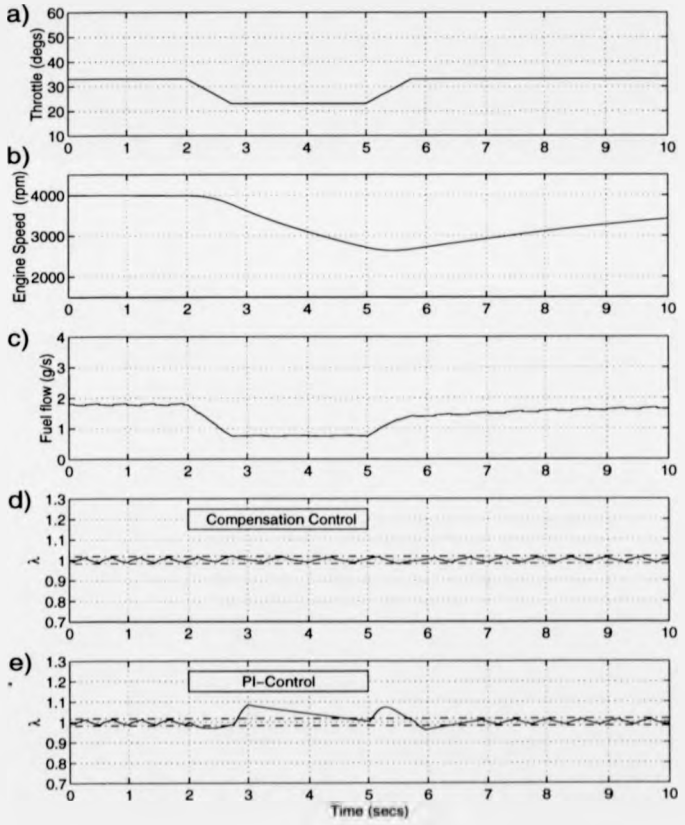

Figure 5.15: Transient A/F ratio compensation control under throttle ramping action, 3rd gear operation.

After the throttle is ramped back up to its initial position, and is then held stationary, the port air flow increases before the throttle air flow due to the increasing speed. Under PI-control, the tendency is for the mixture to drift into the rich region ($\lambda < 1$) as the fuel flow, injected into the throttle air, is commanded from the greater port air flow. Under compensation control, the A/F ratio is maintained inside the window limits as the compensation action remains active due to the port flow rate increase.

5.4 Conclusions

At the outset of this chapter, the aim was to improve the control of the A/F ratio during transient driving conditions. A feedback strategy, known as SMC, was investigated, that differed significantly from the conventional PI-feedback algorithm. Although this control approach provided a significant step forward, in allowing a transient condition to be recognised, its application was shown to be hindered by the use of the delayed feedback EGO-sensor signal. Through the results of simulations, making extensive use of the natural gas engine model, it was demonstrated that this controller could actually accentuate transient A/F ratio excursions.

The salient point of utilising the air flow rate derivative, was duly appreciated, leading to its adoption in an open-loop control algorithm. Motivation for this was taken from the speed of response of the nominal open-loop controller, that was highlighted in chapter 4. By using this approach, the open-loop compensation controller has demonstrated independency from the delayed feedback signals.

The method of finding the optimal OTCC gains made full use of the benefits of modelling. By subjecting the engine (model) to the most extreme throttle conditions, it was possible to alter the gains at run-time in the computer simulation environment and thereby alter the amount of compensatory fuel action. This

approach could be extremely difficult to achieve in practice, if the resulting engine output torque is not matched quickly enough by the load torque to maintain a constant speed. Transient λ-excursions were then shown to be removed by the OTCC approach, for a number of typical simulations, with the λ-value remaining within the catalyst window limits.

The question now raised is 'how applicable is this control approach to an actual engine environment?'. The subject of the next chapter shall be to investigate how the OTCC approach could be expected to perform and possible difficulties that might reduce its effectiveness.

Chapter 6

Practical Considerations

6.1 Aims

The purpose of this chapter is to consider the aspects of an actual engine environment that might present difficulties to the OTCC approach. The use of an embedded speed-density air flow map, to increase simulation realism, shall be investigated, which is the typical approach for conventional A/F ratio controllers. Input signal noise effects are to be considered, with an investigation into how the derivative nature of the open-loop controller reacts to significant levels of injected noise.

A control approach using throttle air flow estimation is considered, to investigate an alternative method to the speed-density approach. The effects of using a statically derived map in a dynamic environment shall then be assessed.

Engine phenomena that have not been encompassed in the non-linear model are to be highlighted, and shall present possibilities for future work. In turn, this will allow an expansion of the model to becoming a more comprehensive representation of the natural gas engine. A more rigorous testing of the OTCC performance would then be possible.

This entire chapter is devoted to dealing with the likely issues that would arise when applying the control OTCC algorithm to a real engine, and those

which would cause difficulties in maintaining effective control. This is one of the advantages of using models for research, since the resources were not available at the sponsoring company to encode the algorithm in an actual ECU. Thus, the approach adopted in this chapter is aimed at investigating the potential problems that would be found in practice, and goes some way to being aware of the implications.

6.2 Speed-Density Air Flow Mapping

A strong motivation for controlling the A/F ratio using feedback strategies is the removal of steady-state errors that arise from measurement or estimation inaccuracies of the engine states. In the simulations of figures 4.9 and 4.19, a specifically known error is introduced to the air flow estimation signal being sent to the controller. However, it is more probable that the microprocessor will suffer from a continual and varying estimation error that almost certainly cannot be evaluated. These errors are due to a number of factors including sensor noise and drift, changing atmospheric conditions and sensor hardware ageing. Another, more immediate factor, is that of using steady-state derived engine maps to perform in a dynamic system environment.

Almost all engine A/F ratio controllers use an engine air map to look-up the estimated air flow, given a number of engine states. The controller algorithm interpolates between the mapped data points to compute estimates of air flow rates that have not been explicitly measured. These maps are conventionally derived from steady-state, test-bed data of the sort used in this thesis, and therefore suffer from the lack of accounting for the dynamic conditions.

In the interest of increasing simulation realism and thereby subjecting the control algorithm to more probable conditions, it is now suggested that the controller encompass an air map to estimate air flow. In this approach, the algebraic equa-

tions of the throttle and port air flow models, equations 3.6 and 3.9 respectively, are to be considered as the *actual* engine flow rates. An embedded air map in the controller block shall then estimate the engine air flow rate from the engine input states. This signal is then used as the input to the controller algorithm.

The speed-density air flow map for the natural gas engine, is that shown in figure 6.1. This is comparable to the flow prediction surface of figure 3.14. The difference between the two plots is that the prediction surface is derived from the algebraic equation 3.9, whereas the displayed map is established directly from the measured data. Linear interpolation and extrapolation is utilised to populate the map over the entire speed-pressure matrix. This is a valid method for display purposes, since the controller algorithm in the EMU, will use this method to estimate the air flow. Hence, there is expected to be some disagreement between the air flow map estimate and the algebraic estimate.

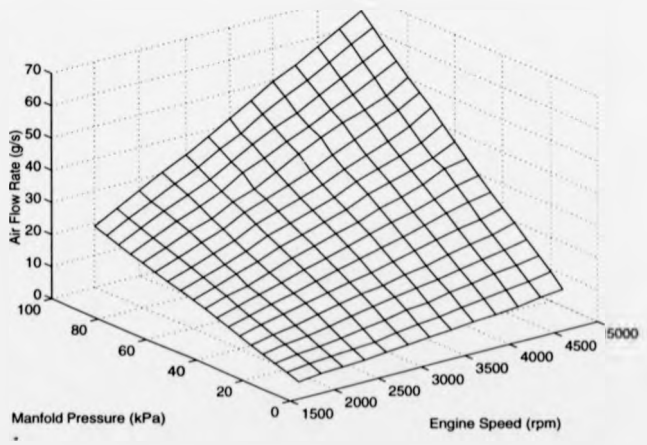

Figure 6.1: Speed-density air flow map for the 1.4 litre natural gas engine.

The independent inputs of manifold pressure, (P_m), and engine speed, (N_e), are the states required to be fed to the A/F ratio controller to fulfill the open-

loop control requirements of both the nominal and compensation schemes. This system modelling approach can be visualised in figure 6.2. The A/F ratio control unit consists of the embedded map and controller algorithm. The λ-sensor voltage signal remains as the feedback signal to adjust for the expected drifts.

From the control block diagram of figure 6.2, it is seen that the engine inputs and controller inputs are different. This reinforces the assertion that this control structure approach will always suffer from the dynamics of the manifold and rotational elements in the open-loop algorithm, and the time delay in the feedback algorithm. The EMU will receive signals pertaining to the system states which encounter large dynamic elements, whereas the fuel is being injected further upstream at the throttle, where it has already been established that throttle air flow response is instantaneous to changes in throttle input angle and manifold pressure.

If the EMU can be given a control input in common with the engine, i.e. throttle angle (θ_{th}), then it may be possible to estimate the air flow much more quickly in response to the changing states. This would inherently improve the open-loop algorithm, allowing more effective control decisions to be made in response to the changing conditions. This idea is dealt with in a later section, 6.6.1.

Figures 6.3 and 6.5 display two simulations under the control of the air map estimator approach. The operating conditions and throttle angle inputs differ significantly for both, but the gear setting remains the same, chosen to be in 2^{nd} gear.

The actual air flow, described by the algebraic port flow equation is plotted against the map estimation. It is seen that there is a continually varying discrepancy between the two, and the difference is highlighted by the percentage error traces. Due to the map being derived from steady-state testing techniques, the estimation error displays unpredictable behaviour during transient operation, and

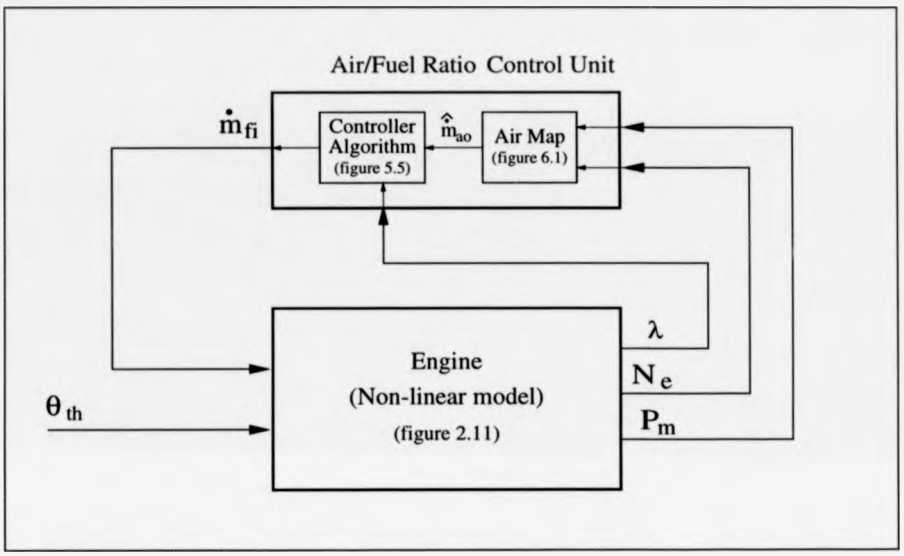

Figure 6.2: A/F ratio controller structure incorporating speed-density air map estimator.

certainly one that would be difficult to incorporate in the SMC approach. Under steady-state operation, the error assumes a constant bias value, for which the feedback algorithm must constantly correct.

The transient compensation algorithm, in conjunction with conventional PI-control, maintains effective A/F ratio control, restricting the mixture closely within the defined window limits, as displayed by the λ-traces.

Even though the absolute value of the air flow rate is wrongly estimated under steady-state conditions, the air flow derivative will actually be correctly estimated as zero, since there is no change in the state conditions of P_m and N_e. When a transient operation ensues, the estimation of the derivative is again very close to the actual derivative, whilst there remains an error in the absolute estimation of the air flow rate. This is because the direction of the changing air flow will always

be estimated in the correct manner, in response to the changing engine states. This effect is illustrated in figures 6.4 and 6.6, which display the flow derivatives of actual and map estimated air flow rates, for figures 6.3 and 6.5, respectively.

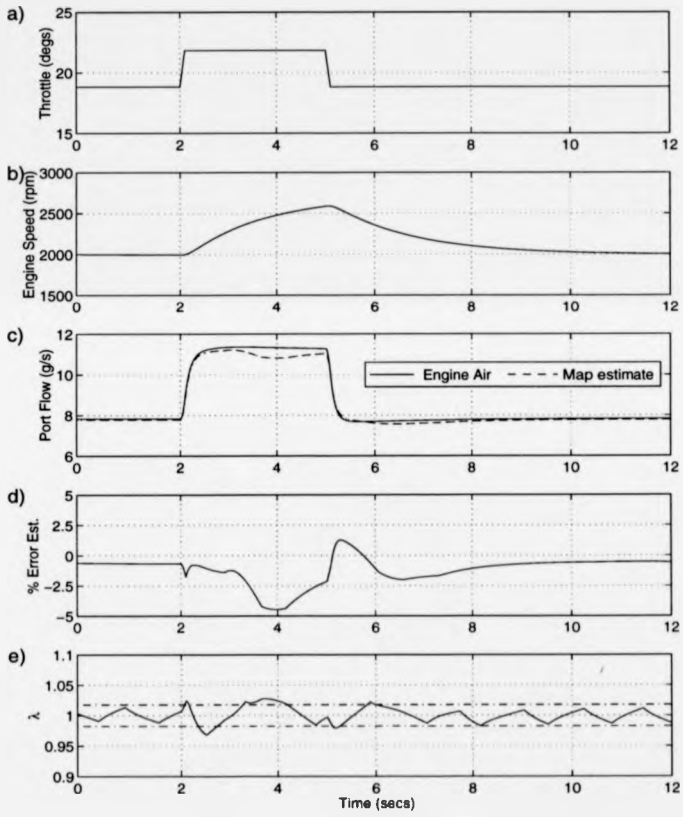

Figure 6.3: Simulation of engine transient under air map control. (2^{nd} gear operation)

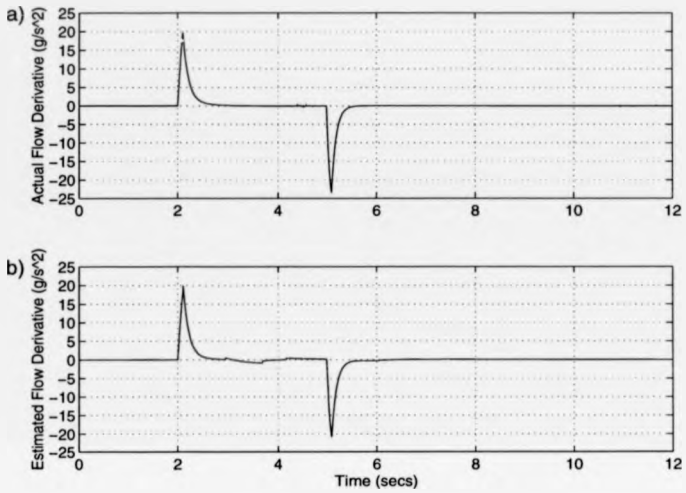

Figure 6.4: Actual and map estimated air flow derivatives for the simulation of figure 6.3.

Thus, it appears that the compensation controller is robust to estimation errors of a bias nature, as the input signal required is not the magnitude of the air flow rate, but its derivative. This is an attractive feature, since, as the engine components and sensors age, the inaccuracy of state estimation may tend to increase.

This will inevitably present a problem for the nominal open-loop controller, relying more and more on the feedback algorithm to correct for wrongly-commanded fuel flows. Whereas, for the open-loop compensation controller, so long as the error remains a bias in the short term (i.e. between sampling times), there will be very little effect on the computed state derivative estimations. The gradient change in states will still be accurately estimated between sampling intervals, ensuring a close estimation of the rate of change of the air flow.

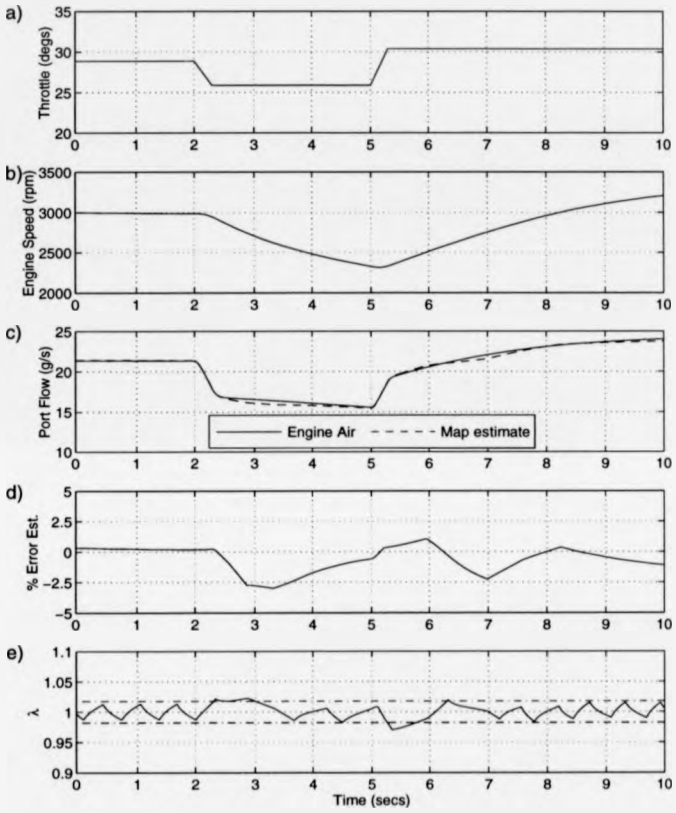

Figure 6.5: Second transient simulation under the control of the map air flow estimation.

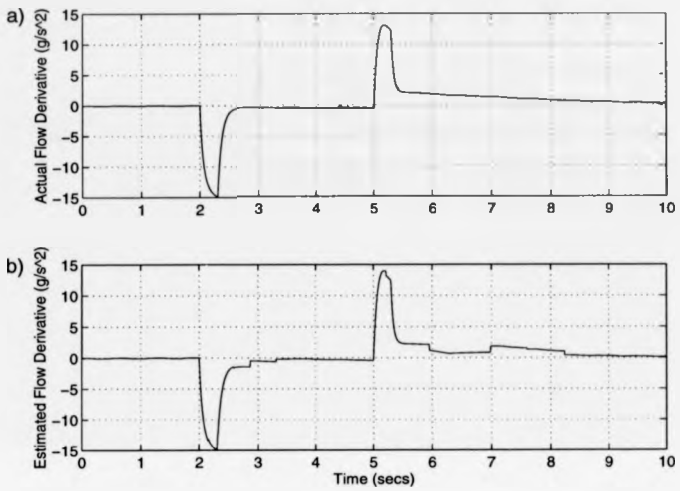

Figure 6.6: Actual and map estimated air flow derivatives for the simulation of figure 6.5.

6.3 Injector Rate Limitations

From the simulations of figures 5.6 through 5.9, and 5.12 and 5.13, the question of fuel injector rate limitation is raised. Can the demanded rapid increases in fuel be met by the current injector unit?

Two chief areas of concern are :

1. maximum flow rate achievable,

2. injector response time.

6.3.1 Maximum G.F.I. Flow Rate

In respect of the first, it has been seen that throttle step-up simulations induce large spikes of fuel increase under transient compensation control. From the con-

trol structure, the magnitude of the mass flow derivative, $\dot{m}_{ao}$, governs the transient compensation open-loop fuel command. The requirement to rapidly increase the fuel to a larger flow rate, for a short period, is then defined by this derivative. For all the simulations conducted in selecting the optimal values of $K_{tr_{op}}$ (figures 5.6 through 5.9), throttle steps covering a full step of the throttle range were used to incite the largest possible transition of states, thereby inciting a high demand from the compensation algorithm. In all the simulations, the average value of the fuel spikes was 6.7439 gs^{-1}, the maximum being $\dot{m}_{f_{max}} = 6.99\ gs^{-1}$ for figure 5.7(c) - see also table 5.1.

The G.F.I. injector unit is rated to have a maximum flow rate capacity of 2650 scfh ($20.86 \times 10^{-3}\ m^3s^{-1}$), at a working pressure of 100 psi ($689.5\ kPa$) [101]. Using the state equation 2.11, the maximum flow rate of the injector unit, $\dot{m}_{i_{max}}$, can be obtained. The molar mass of the fuel is taken as that of pure methane (CH_4), $\bar{M} = 16\ g \cdot mol^{-1}$. Thus,

$$\dot{m}_{i_{max}} = \frac{689.5(kPa) \cdot 20.86 \times 10^{-3}(m^3s^{-1}) \cdot 16(g \cdot mol^{-1})}{8.31441(J \cdot mol^{-1} \cdot K^{-1}) \cdot 298(K)}, \tag{6.1}$$

$$\approx 92.9gs^{-1}, \tag{6.2}$$

therefore

$$\dot{m}_{i_{max}} \gg \dot{m}_{f_{max}}. \tag{6.3}$$

Thus, the injector unit can more than adequately provide the required fuel flow rate. In fact, the injector unit is a very accommodating device, and is actually designed to be used on a wide variety of vehicles ranging from small capacity engine, as used in this thesis, up to a maximum of 8 litre for use in heavy duty vehicles. The controller algorithm, therefore, is not envisaged to push the injector system beyond its capacity limits, and the required compensation fuel command is deemed fully achievable.

6.3.2 Injector Actuation Duration

The second criteria of concern, the response time, governs the rate at which any increase or decrease in fuelling can be made. If the rate of injector actuation is significantly slow, then compensation control shall be severely affected, as its fuelling demand cannot be met with sufficient urgency during severe transients.

To investigate injector actuation limitation, it is considered that the most severe consequences of injector rate limitation, are a pure time delay between when the controller has made its command decision, and when the injector has moved to the appropriate position to implement this fuel command. Thus, the actual fuel flow rate would not meet the controller demand until some time, t_{inj}, after the controller decision is made. The value t_{inj}, is the transient time for the injectors to actuate from the current position to the required position. The opening and closing times of the G.F.I. injector valves, from fully closed to fully open, are stated to be in the region of one to two milliseconds [101].

By following this approach, the flow rate is not considered to rise or fall on a continuous basis, as the injector solenoid moves from its initial to final position. Instead, the flow rate is assumed to alter instantly to the binary nature of the solenoid action, where the injector solenoid has a time delay for actuation. This effect is implemented in the model code by the use of the SCHEDULE command. The commanded fuel flow rate, from the controller algorithm in the initial discrete block, is issued to a second discrete block scheduled t_{inj} seconds after the command fuel has been made. This second discrete block effectively delays the fuel command being sent to the continuous engine model.

Figure 6.7 presents some simulation results for throttle step conditions, where t_{inj} has been adjusted from 0 ms up to the microprocessor sample rate in steps of 1 ms. The speed has been maintained at a constant value of 3000 rpm and the open-loop compensation controller is maintaining strict control of A/F ratio. The

air flow rate estimation is taken to be that of the algebraic equation, to focus on rate limitation effects by the removal of estimation errors.

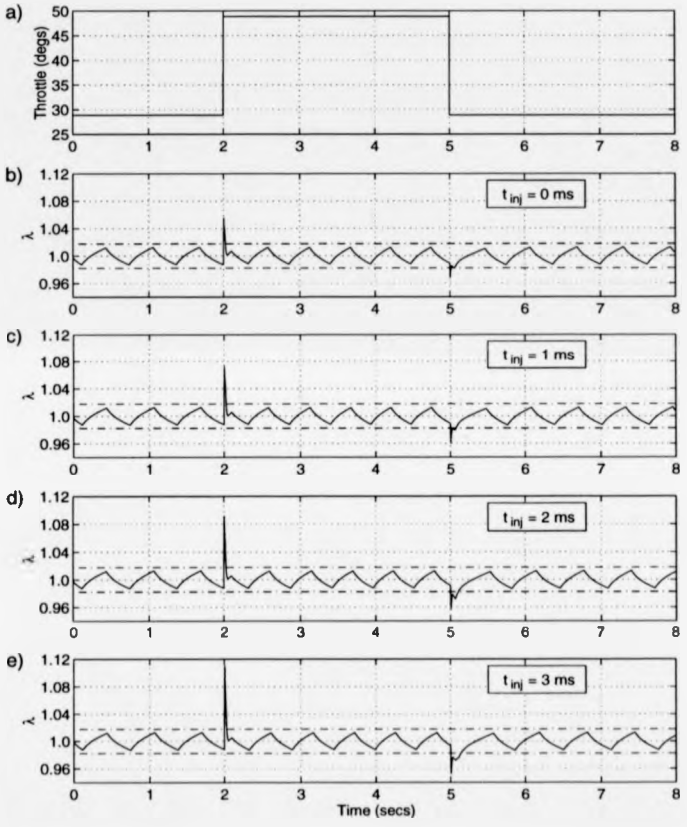

Figure 6.7: Effects of injector-actuation time variations on λ-control, for throttle step inputs.

It can be seen that, as the injector-opening time increases, both peak minimum and maximum λ-excursions increase, as a consequence of the growing fuel flow retardation. Table 6.1 summarises the percentage change in λ from the ideal injector actuation duration of 0 ms. It is seen that for each increase of $t_{inj} = 1$ ms,

there is approximately 1.8% growth in lean λ for the throttle step-up condition, and a maximum decrease of 1.46% in rich λ for the throttle step-down condition.

It should be remembered, however, that the largest demand in the compensated fuel flow rate comes as a consequence of throttle step inputs. The throttle inputs of figure 6.7 are implemented as ideal steps, changing from one position to another without a time period for the transition. But in a practical context, when these fast throttle changes are encountered, there will always be some time duration associated with the change. Therefore, these 'step' inputs are somewhat theoretical, but do demonstrate the controller's ability to operate under the most aggressive driving conditions possible. If the controller maintains the desired A/F ratio for the theoretical steps, then the lesser demanding, but still extremely taxing, driver requirements are well within the ability of the controller.

As highlighted by Hendricks [56] in section 4.2.1, typical times associated with throttle actuation can be as fast as 50 ms. Thus, realistic operating conditions will not change as quickly as suggested by the theoretical steps, and the commanded fuel spike is not expected to be as large in magnitude. It is considered then, that the effect of injector rate limitation shall not be as much in evidence for conditions where there is a finite actuation time defined by a driver's control of the accelerator pedal. This was demonstrated in figures 5.14 and 5.15, that under more typical throttle ramping action no fuel 'spikes' exist, but the compensation algorithm continues to be active.

To further illustrate this assumption, the simulation of figure 6.7 was repeated for the same throttle bounds, but over a duration of 50 ms for both throttle up and down. The results of this simulation can be seen in figure 6.8.

As expected, the rich and lean excursions are not as great in magnitude as was seen in figure 6.7. The percentage increase in λ-excursion, has also been computed for the increasing t_{inj} value, and can be seen in table 6.1 against those of throttle

steps. The table allows for a comparison between the consequences of the throttle step and fast ramp simulations.

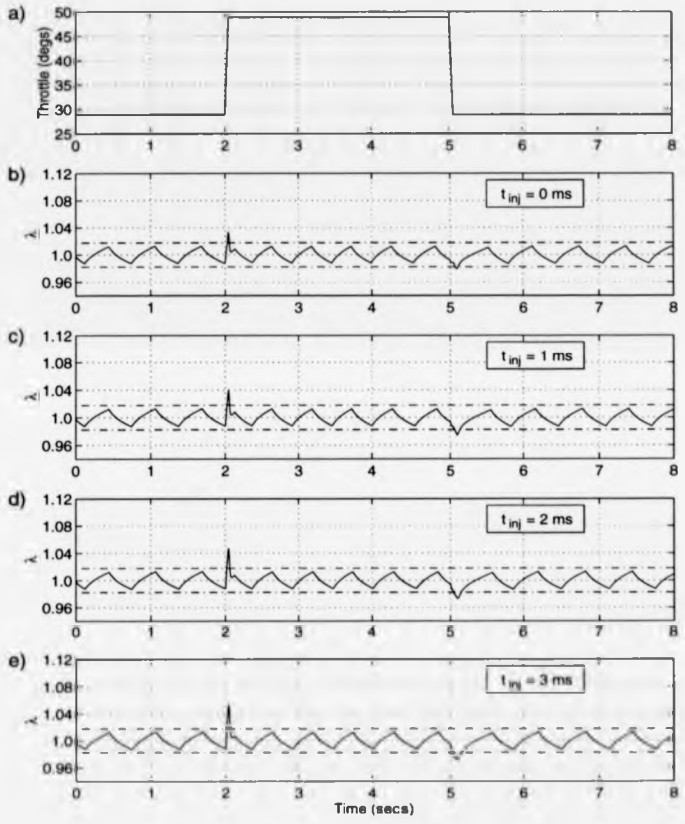

Figure 6.8: Effects of injector actuation time variations on λ-control, for fast throttle ramp inputs of 50 ms duration.

It can be seen that the incremental increases of t_{inj}, raises the throttle ramp % deviations by approximately 0.7% for throttle-up, and approximately 0.13% for throttle-down. In comparison, the step conditions incite much larger excursions rates due to the greater amount of air flow rate change, before the controller flow

rate command is realised at the injector unit. Conversely, although the throttle ramp induces large state changes, the injector actuation duration is more tolerable since the controller demand is not as severe as it was for the step condition.

t_{inj} (ms)	% Deviation from peak λ-excursion			
	Throttle-up		Throttle-down	
	Step	Ramp	Step	Ramp
1	+1.65	+0.57	-0.70	-0.52
2	+3.47	+1.29	-1.15	-0.64
3	+5.25	+1.92	-2.61	-0.79

Table 6.1: Percentage deviations from peak λ-excursions for throttle step and fast ramp conditions. As the injector actuation time increases, greater variance from the ideal ($t_{inj} = 0$) is seen for the theoretical throttle step inputs, than for typical throttle ramps.

To conclude the concerns of the injector limitation bounds, the current G.F.I. injector unit is considered to be able to meet the requirements of the compensation algorithm demand. Firstly, the absolute flow is entirely achievable, with a maximum flow rate well in excess of that required for the 1.4 litre engine studied in this thesis. The maximum flow rate of fuel demanded during step transient conditions, is in fact only slightly above that demanded from the nominal controller for high load and speed conditions (see figure 5.12(c)).

Secondly, the speed of injector actuation is not considered to inhibit A/F ratio control adversely. This has been demonstrated through simulations, where a pure time delay between when the controller command decision is made, and the injector actuation time has elapsed. For what are considered to be typical fast throttle conditions in a realistic driving scenario, the A/F ratio does not display major detrimental increases in the excursions for even the slowest injector time of 3 ms.

6.4 Input-Signal Noise

The A/F ratio controller module of figure 6.2, is seen to have three input signals [λ, N_e and P_m]. In the computer simulation environment, these signals are said to be "clean" and free from noise. But in the engine bay of a vehicle, the situation is one where sensor outputs will contain noise. One such source is electromagnetic radio-frequency interference (RFI). This could sufficiently corrupt the sensor signals to degrade the quality of the air flow rate estimation and hence control.

RFI is typically carried by the power supply connections and can also radiate from the high-voltage ignition system [114]. The best solution conventionally adopted to tackle this problem, is to shield the source of the electromagnetic field. If this is not possible, the next approach is to screen any, or all, of the sensor transducers by enclosing them in electrically conductive containers.

Typical feedback signals from the zirconia EGO sensor, have already been seen in figures 3.20 and 3.21. The signal-to-noise ratio (STN) for these traces are approximately 45% for lean conditions, and 2% for rich conditions. The STN is expressed as the noise *amplitude* as a percentage of the mean value. The difference in ratios is attributable to an essentially constant noise level (or amplitude) on two distinct and differing output voltages. The STN varies considerably for the two operating conditions. Zirconia sensor noise is not deemed a problem, however, as the controller algorithm passes the signal through a comparator, for the reasons discussed in section 4.4. Therefore, EGO sensor noise shall not be considered any further.

The engine speed signal is generated from the use of a Hall effect sensor. This requires a toothed wheel, made from a permanent magnet or ferrous material, to be placed on the crankshaft flywheel. A Hall probe (or sensor pick-up) is located at a fixed position close to the toothed wheel edge. As the engine crank rotates, the approaching ferrous teeth alter the reluctance of the internal magnetic

circuit controlling the Hall probe output [114]. The processing of this raw signal is sometimes done in the main EMU, or sometimes in a separate ignition module. The engine speed information is calculated by measuring the time between pulses. This gives a very robust system which can reject high levels of noise, because any noise pulses would occur outside the window for a real pulse based on many previous pulses [115].

The manifold absolute pressure (MAP) sensor used during testing, was a capacitive type. These sensors are less prone to error than the more common piezoresistive sensor, due the lack of hysteresis and non-linearity [114]. Such sensors consist of a pair of conductive silicon electrodes - one rigid, the other a diaphragm. Pressure changes cause the diaphragm to deform, which in turn changes the capacitance of the pair arrangement. The sensor is robust to side stress, due to the total change in capacitance arising from the integral deformation of each part of the diaphragm. This makes it particularly tolerable to the harsh vibratory conditions of the engine bay.

Whilst every realistic effort is made to screen RFI, and use the best available sensors, controller input signal noise still can exist in practice. If this signal noise is of sufficient magnitude, air flow and air derivative estimations may well deviate from the actual values to such an extent as to cause unacceptable λ-excursions. In order to investigate noise effects on the full controller using the air map estimator, it was decided to artificially introduce random noise. In view of the above discussion, it was further decided that the signals of λ and N_e shall remain untouched, since they can generally be regarded as clean signals. Therefore, noise shall only be added to the manifold pressure signal.

Data on typical levels of input noise is not generally a well-collated area, and is entirely dependent on the system in question. Knowing what magnitude of noise to inject therefore, proved rather difficult. The approach taken was to raise

the level of noise to establish what conditions could be tolerated before the A/F ratio's lay significantly outside the catalyst window limits.

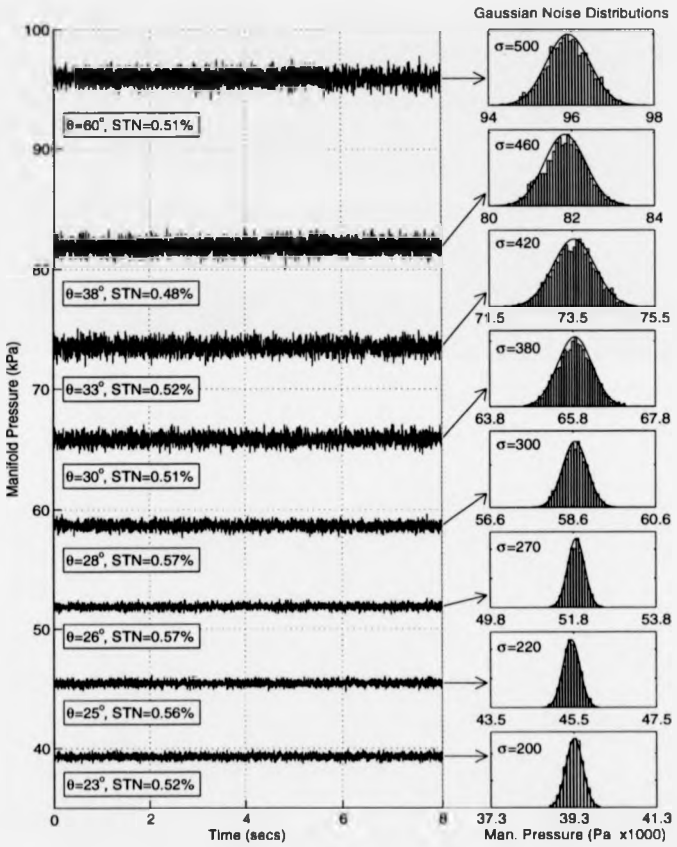

Figure 6.9: Variation of tolerable noise levels dependent on operating conditions.

Figure 6.9 presents the results of eight, steady speed simulations. The engine speed is 3000 rpm and the eight static throttle positions are arbitrarily selected, through a full sweep of the model range, to induce significant changes in combustion torque and hence manifold pressure. Throttle angles, θ, are detailed in the

"boxes" of the pressure traces.

A noise signal, of a Gaussian nature, has been injected onto each manifold pressure trace before entering the A/F ratio controller. This type of signal was favoured since its properties describe random errors, symmetric about the computed manifold pressure [116, 117].

The standard deviation, σ, of each noise level has been adjusted for each operating condition. The final values of σ are selected as those maximum values which can be tolerated by the controller. The fear is that, under steady-state conditions, the open-loop compensation controller will be activated due to its derivative algorithm. The corresponding Gaussian distributions are shown to the right of the pressure traces, and it can be seen that, as the manifold pressure increases, higher levels of σ can be tolerated. (Note: the displayed Gaussian distributions are in kPa). However, the actual signal-to-noise ratio (STN), displayed alongside the throttle angle condition, denoted by the **STN** value, is seen to remain approximately constant at an average of 0.53%.

Figure 6.10 displays the actual λ-traces for each corresponding throttle-dependent simulation, for which it is considered that the window limits (denoted by the dashed lines) are not breached to any significant level, and thus the noise level is deemed tolerable.

Based on these simulations (and others conducted at varying speeds, but not shown), the minimum tolerable level of noise is found to be dependent upon the operating condition of manifold pressure. This is because the pressure is used as one of the air estimator input signals, and at low air flow conditions, large noise levels will cause proportionally large errors in the estimation. Conversely, for greater air flow rate conditions (i.e. for the high pressure simulation), seemingly larger noise levels can be tolerated that give comparably similar estimation errors.

This presents a situation where the controller can only perform adequately

if the noise level is limited to a specified magnitude as the operating conditions vary. However, it seems more sensible to attempt to continually screen any noise to the absolute possible minimum. For the simulations conducted, this value is estimated to have an STN ratio of approximately 0.5%.

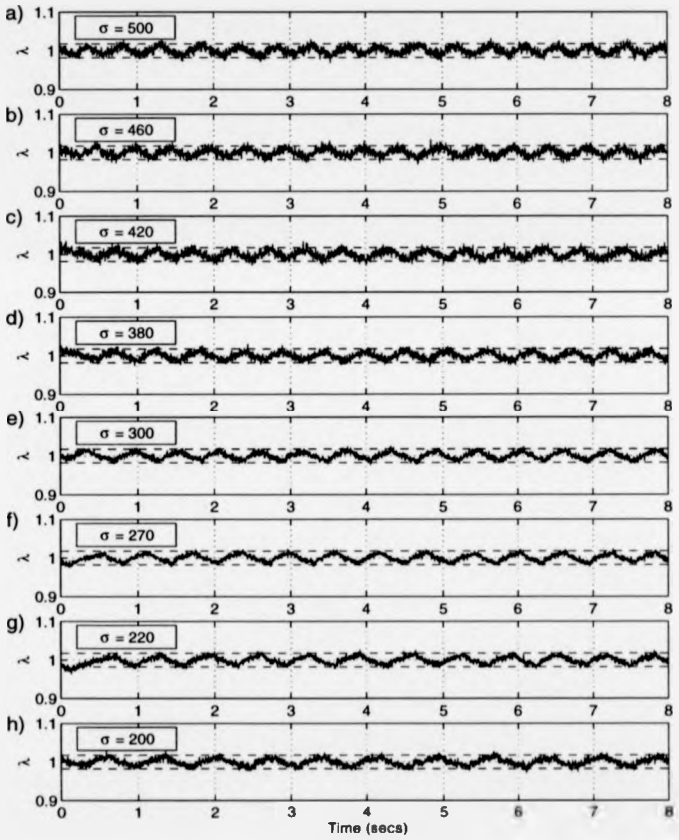

Figure 6.10: λ-trace responses for the varying levels of Gaussian noise.

To demonstrate the consequence of too-high a noise level, a simulation, conducted at a steady-speed of 2000 rpm, is shown in figure 6.11 where a constant

$\sigma = 500$ is injected. It is then obvious, for changing conditions, the STN ratio will vary. The manifold pressure commences at approximately 46 kPa, for which the injected noise level is considered over twice that tolerable, as seen in figure 6.9. Therefore, the controller has difficulty in maintaining the correct fuel flow rate and the λ-trace, figure 6.11(c), is not bound within the window limits.

When a step throttle input induces an increased air flow rate and manifold pressure, λ is controlled as the STN ratio falls into the tolerable bounds. After 5 seconds simulation time, the throttle returns back to its initial position of 16°, the controller suffers difficulty again and λ begins to drift. The PI-control action can be seen to be making an attempt at returning λ into the desired window limits, but a considerable time period is required.

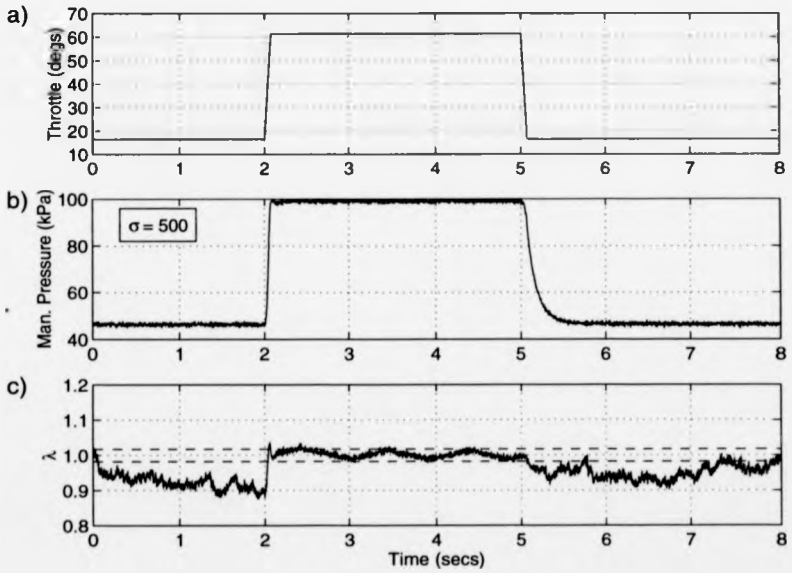

Figure 6.11: Simulation of a high constant noise level ($\sigma = 500$) that causes control difficulties for significantly changing operating conditions.

If the noise level is now reduced to a constant value of $\sigma = 200$, the controller

is expected to adequately maintain λ for all operating conditions, as the STN ratio will not be breached. This is now demonstrated in figure 6.12, where the same operating conditions apply as for figure 6.11. It is seen that the A/F ratio is strictly controlled during steady state, and the open-loop compensation controller performs acceptably well for the transient conditions. It should also be remembered that the speed-density air map is being used in the A/F ratio controller block to estimate the air flow rate.

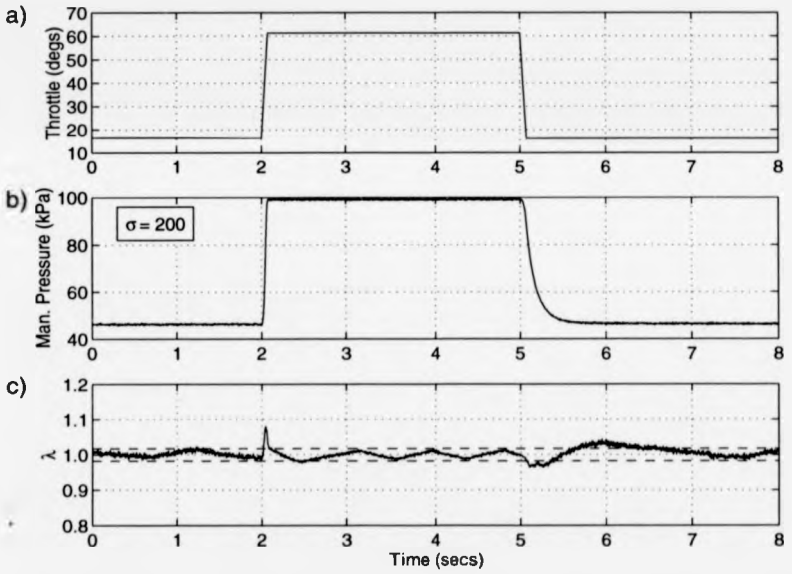

Figure 6.12: Simulation of injected noise that can be tolerated during all possible operating conditions.

The importance of reducing system noise to as low a value as possible, has therefore been demonstrated through a process of simulations. The use of a Gaussian distribution signal, injected onto the controller input signal, was used to allow a statistical comparison of the spread (σ) of noise levels, and the corresponding STN ratio, which were deemed to push the controller to its bearable limits. Of

course, it is not expected that real manifold pressure would always display this characteristic, but this approach is intended to provide some insight to the practical effects encountered by engine controllers.

6.5 Manifold Pressure Pulsing

The air flow into the combustion chambers requires the inlet valves to open and close once per engine cycle, per cylinder. The effect of the inlet valve is to close off the air passage for each cylinder for a considerable duration of the engine cycle: for the engine modelled in this thesis, each inlet valve is **closed** for 240° of crank rotation (one third of the 4-stroke cycle). Thus, air flow is not continuous through each inlet port runner.

The resulting pulsing induction action, and possible backflow effects, cause large pulsations in the mass flow rate in comparison to the mean mass flow rate. Consequently, the manifold pressure will display cyclical pulsations with a frequency in relation to the crank shaft speed. An excellent example of this is shown in the two illustrations of figure 6.13, [56]. These figures are reproduced with the kind permission of Professor Elbert Hendricks and associated authors, at the Technical University of Denmark.

These figures show that, for a fast throttle step from 17° to 53°, an untuned intake manifold may promote the development of mass flow rate fluctuations. The amplitude of these can increase to more than twice the mean flow rate. The subsequent manifold pressure is then seen to respond with equal frequency but with a reduced amplitude.

As a similar consequence to that of the electrical noise, investigated in section 6.4, the derivative open-loop algorithm will suffer the effects of pressure pulses. What is clear is that, even if all electrical signal noise can be screened, pressure pulsations will still exist, and shall vary in magnitude according to the manifold

design and operation condition. Again, the compensation controller will become activated under steady-state conditions, the derivative action accentuating the pressure pulsation effects, and inevitably supply fluctuations in fuel not matched for the conditions of a true throttle transient.

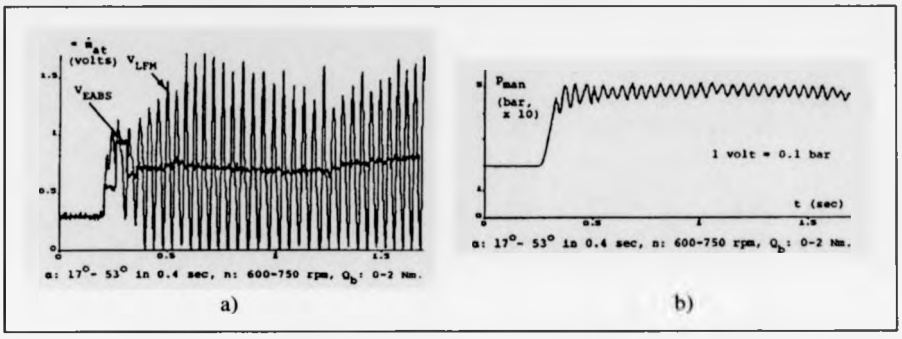

Figure 6.13: Examples of manifold pumping effects during a fast throttle step-up for a 4-cylinder engine. Both the mass flow rate (a) and the manifold pressure (b) exhibit large fluctuations at a frequency defined by the engine speed, but whose amplitude can vary according to the operating conditions. Courtesy of Elbert Hendricks [56].

This effect is not encountered in the simulations displayed, as the manifold model is only designed to estimate the mean value of the air flow rate entering the combustion chambers. In steady-state, the model estimates a mean value of the pressure without any pulsing effects. In order to increase the manifold model realism, the model would require further restructuring and engine testing, to a more comprehensive level - possibly to allow each port runner air flow rate to be estimated. Only then can a closer approximation of the pulsing effect be derived.

Further manifold modelling has not been been encompassed in this thesis. Methods of dealing with manifold pulsing have also not been fully researched, as this topic is considered to constitute a substantial research effort, which lies out of the scope this thesis. However, some thought has been given to this area of

research, as presented in the "Future Work" section, 6.7.

6.6 Improved Air Estimation

For all simulations conducted thus far, computation of the required fuel has been made utilising the *speed-density* approach in estimating the air flow rate. This has been realised through either the empirically derived algebraic equation, or by the steady-state, air flow map. The motivation for this approach has been to investigate and develop a method of improving A/F ratio control of the **current** system in operation. Thus, since the speed-density approach is used in the actual G.F.I. controller structure, an improved control algorithm has been devised that compensates for the inadequate transient control of this system.

A major consequence of the speed-density approach, is the fact the air flow being estimated is not the air flow where the natural gas is being injected. Ideally, the air flow should be estimated as close to the fuel admittance point as possible. The question now raised is: can A/F ratio control be improved through the estimation of the throttle air flow?

6.6.1 Modified Speed-Density Estimation

To answer this question, thought is returned to a point raised in section 6.2. It was seen that, for the speed-density approach, the controller block receives different input signals than the engine itself. In this manner, the actual input signals used, allow the manifold and rotational dynamics to be encountered in the air flow rate estimation. This presents the controller with an air flow rate estimation that differs significantly to that into which the fuel is introduced. This is an inherent problem with the speed-density approach.

If the *throttle* air flow rate can be estimated, the problems of the dynamic elements are removed and the fuel is metered to the air flow into which it is injected.

One approach to estimating the throttle air flow rate requires the introduction of a throttle angle sensor, and is known as the *modified speed-density* model - so called because only the manifold pressure is replaced by the throttle position signal. It can now be appreciated, that the controller and the engine share a common input.

Another approach is to measure the air flow directly with a hot wire anemometer. This would be advantageous, for both gas and petrol, as it would render the actual air flow rate that the gas is being injected into - as opposed to an estimation using other states. The feedback controller would still be required, as the calibration of the device would still drift with age, giving rise to air/fuel ratio errors. However, a hot wire anemometer was not available for testing, and the natural progression towards throttle air flow estimation is the 'modified' speed-density approach. This is because the throttle angle sensor measurements have been previously measured and therefore readily at hand.

In order to implement the modified speed-density strategy, the relevant map must be encoded in the controller. The modified speed-density map for the natural gas engine, as obtained from the steady-state tests, is now that seen in figure 6.14.

Estimating the throttle air flow rate in this way, was first introduced by Hendricks and Sorenson in 1991 [55]. Since then, this approach has been extensively used by other researchers in recent years [67, 56, 118, 119, 50]. Reasons for its popularity are obviously for stricter A/F ratio control, but also due, in part, to the lowering cost and increased reliability of throttle position sensors.

These devices are frequently potentiometer based, utilising conductive polymer tracks over which the throttle contact slides. The multifingered contact design ensures good contact even under severe shock and vibration. They are sealed to a high standard to withstand possible fuel, water and battery acid leakage [114]. It is recognised by Hendricks [56], that the requirement for a throttle position sensor will increase production costs and present calibration disadvantages. However,

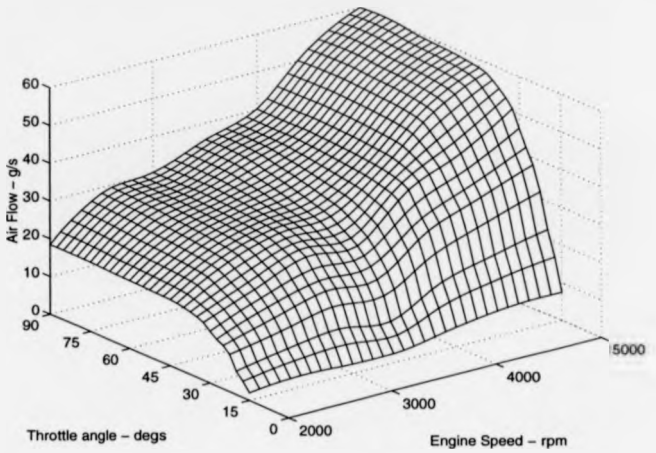

Figure 6.14: Modified speed-density air flow map for the 1.4 litre natural gas engine.

given the high accuracy of these devices, it is generally not a large disadvantage and the improvement in A/F ratio control can be quickly realised.

The control arrangement for the modified speed-density strategy can now be seen in figure 6.15. This can be compared to figure 6.2, where it shall be realised that the same number of controller input signals exist, but where the modified system approach requires a new sensor to supply the throttle input signal to the controller.

The modified speed-density map of figure 6.14, is now embedded in the discrete model block control unit. The transient compensation control algorithm must be "turned-off", since the controller is receiving different input signals than were used to select the transient compensation gains. This is because the air map is now estimating system conditions for a different engine location than was previously estimated. Thus, the control approach reverts back to the conventional PI-controller of figure 4.10, but where the input signal to the nominal open-loop

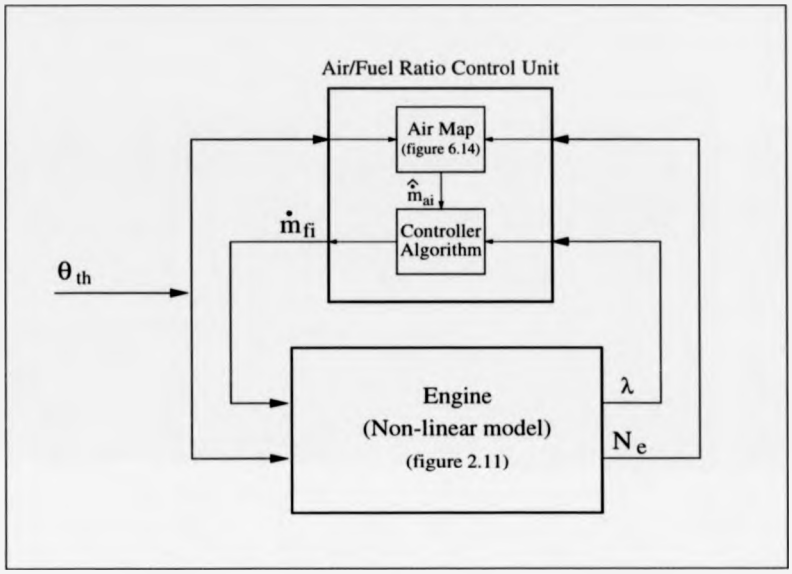

Figure 6.15: A/F ratio controller arrangement for modified speed-density air map. The engine and the controller share a common input signal - that of the throttle angle θ_{th}.

block changes from the port flow rate, $\hat{\dot{m}}_{ao}$, to the throttle air flow rate, $\hat{\dot{m}}_{ai}$.

An example of A/F ratio control under this scheme is now demonstrated in figure 6.16. The simulation is conducted in 2nd gear, and the throttle angle ramps quickly over a period of 75 ms. The λ-plot for the modified speed-density control map is shown in figure 6.16(c). There exist excursions for the throttle changes that lay outside the window limits. These occur due to the nature of a statically derived map used for dynamic control.

However, the excursions are shorter lived and lower in magnitude than the comparable speed-density map control without any compensation, figure 6.16(d). The modified control approach estimates changes in air flow rate at the throttle allowing it to alter the fuel command more quickly to changing conditions than

can the standard unmodified approach.

For comparison, the compensated control approach λ-plot is displayed in figure 6.16(e). It can be seen then, that the open-loop compensation controller provides much better control over that of the modified controller.

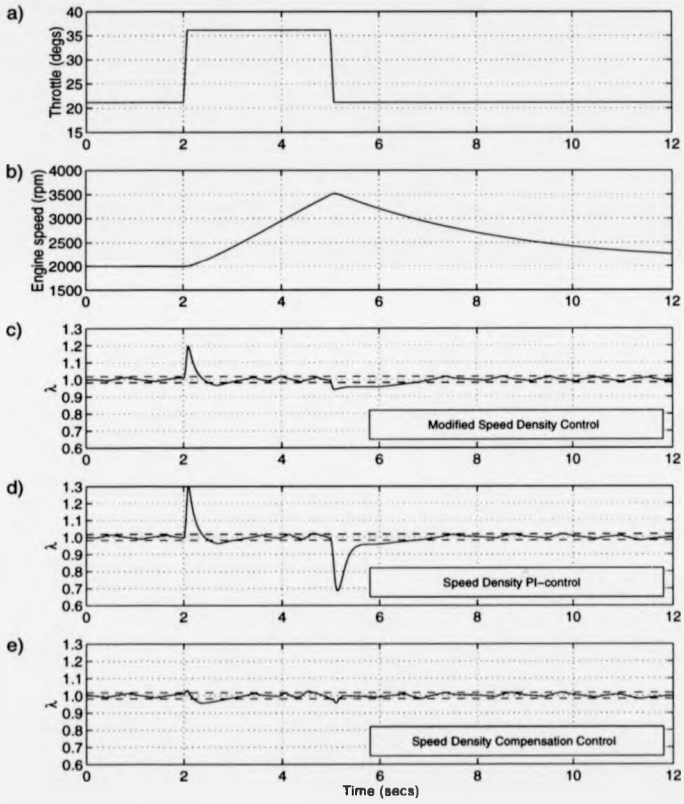

Figure 6.16: Comparison of modified speed-density control to that of the standard approach and the compensated open-loop approach.

The actual throttle air flow rate is displayed in figure 6.17(a), alongside the modified speed-density estimation, (b), and the standard speed-density estimation, (c).

It is clear, from these simulation results, that the modified approach is estimating much more closely the throttle air flow rate - into which the fuel is injected. This is due to the use of the throttle angle input signal, which removes the dynamic element that persisted with the manifold pressure input signal. However, there remains a large error at 2 seconds, which is attributable to the manifold map lacking the requirement to be able to estimate transient operative flow rate changes.

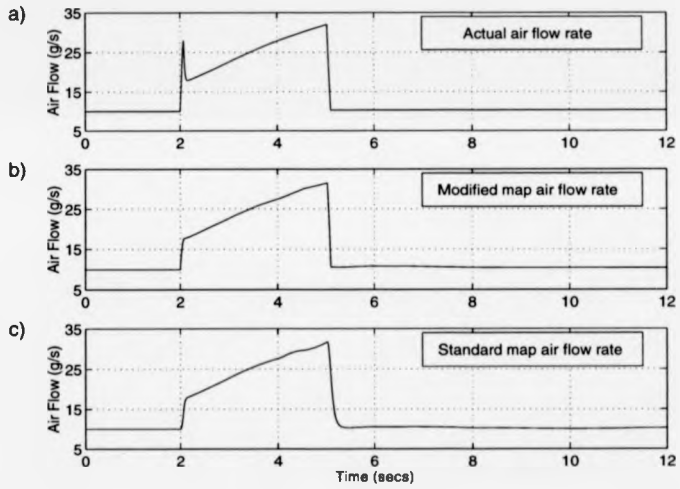

Figure 6.17: Comparison of actual throttle air flow rate to throttle estimation and port estimation.

The modified speed-density approach does not have the potential to improve upon the OTCC approach, as it too is based upon a map. It has been established that map control has limitations in its ability, unless compensated in some way. This is where the OTCC algorithm steps in. If the modified speed-density approach was to better the usual speed-density approach, it would require some further compensation control to counteract the inadequacy of a statically derived map being used in the dynamic environment. Again, the gains for this compen-

sation controller would have to be selected to suit the operating conditions.

One further point about this modified speed-density approach is that it removes the need for a pressure sensor and hence avoids the need to account for manifold pressure pulsation, as discussed in the next section.

6.7 Future Work

From the conclusions drawn over the modelling and control work reported, some scope for further research can be discussed.

6.7.1 Improved Manifold Model

In order to fully evaluate the consequences of implementing the OTCC algorithm, it would be necessary to construct a more comprehensive model that affords an estimation of the pressure pulsations. Sensor noise from electrical sources has been investigated in section 6.4. However, noise from interference is considered less of a problem, as screening techniques can be implemented to such degrees, as to virtually eliminate this problem.

It is envisaged, that a model that can estimate the individual air port flow rates, could be adopted to simulate the pulsing of the manifold pressure fluctuations. As the conservation of mass equation is used to estimate the manifold mass, the discontinuous flow rates at the ports, as opposed to the mean estimate which is the sum of all ports, would thereby exert a pulsating behaviour of the manifold pressure.

6.7.2 Cancellation of Steady-state Derivatives

The derivative action of the designed controller, digitally computes $\dot{\bar{m}}_{ao}$ based on estimates separated by one microprocessor sample time, 3 ms (G.F.I.). This is the fundamental problem of the algorithm, as any small change in the flow rate

is amplified. A suggestion for further research is made here, that is aimed at "desensitising" the discrete derivative whilst operating in the steady-state.

From observation of figure 6.13, it is seen that the pulsation frequency is dependent upon the engine speed. The four-cylinder engine is operating at 600-750 rpm, establishing an intake-event frequency of $F_{iv} = 20 - 25$ Hz. This frequency is reflected in both the mass flow rate and pressure traces. If the derivative computation is now made based on the samples that occur at each intake event (eg at the peak of each pulsation), the variation in measured (or map-estimated) flow rate is less variable. This reduced variation of states in the 'crank-angle domain' was highlighted in section 4.2.1. This approach is visualised in figure 6.18.

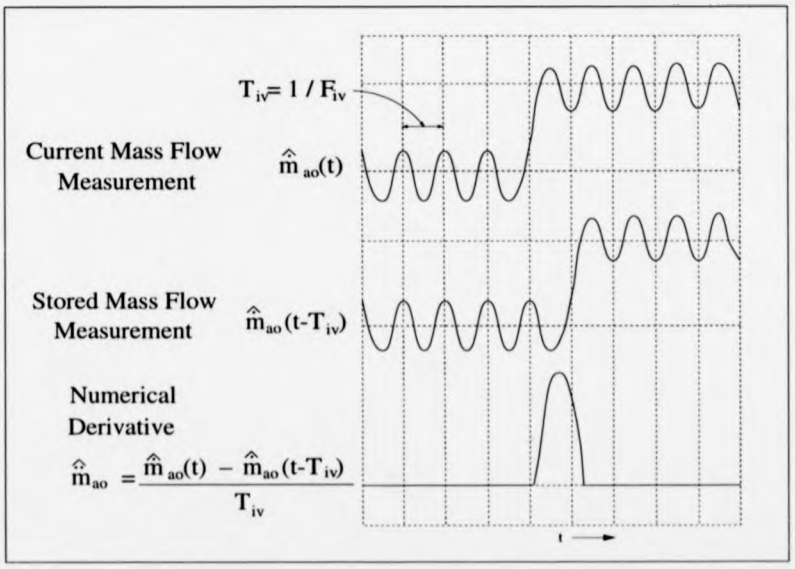

Figure 6.18: Numerical derivative of mass flow rate using event-based sample rate.

The mass flow pulsation trace is not expected to be perfectly sinusoidal, but it does in fact demonstrate definite cyclical nature; figure 6.18 depicts a prospective mass flow measurement trace. The pressure is still sampled at the microprocessor

speed, but the mass flow sample which is now held (stored), is that which is one whole cycle, one intake event T_{iv}, behind the current value. Therefore, the derivative computation (or, moreover, differencing) uses samples which are much closer in estimation during steady-state conditions, in comparison to samples that are taken at the much faster fixed sample rate.

This approach is basically that of a nonrecursive digital filter, the output of which is a finite unitary weighted sum of the present input and a finite number of previous input samples. This is known as a finite impulse response (FIR) filter [120]. For this application, the actual sample held is identified by the intake event duration. Hence, the numerical derivative is defined by

$$\hat{\dot{m}}_{ao}(t) = \frac{\dot{m}_{ao}(t) - \dot{m}_{ao}(t - T_{iv})}{T_{iv}}. \tag{6.4}$$

The resulting derivative will display a cancellation of the current and stored mass flow rates. However, a transient condition will still be recognised. The fast air flow dynamics are expected to promote significant differences in the two state samples, enabling transient operation to alter the value of $\hat{\dot{m}}_{ao}(t)$ and shall be 'picked-out' by this new filtering approach. Note, a new set of gains would probably have to be mapped to get optimal control with the event-based derivative.

6.8 Conclusions

The designed OTCC algorithm has been the subject of investigative procedures, to assess its practicability. It was found that the compensatory action is not adversely affected if the state estimation of the air flow rate is inaccurate, due to either sensor measurement error or the use of an air flow map. This is because the fundamental derivative nature of the controller maintains a recognition of the magnitude of changing conditions. The compensatory action remains inactive during steady-state conditions, even with the existence of estimation errors, and

the derivative estimation remains close to the actual derivative.

Simulations were conducted, with the artificial injection of signal noise, in an attempt to characterise the effects of a realistic engine environment. It was concluded that the magnitude of the signal-to-noise ratio, has a major consequence on the quality of state estimation. Through simulations, it was discovered that noise levels should be minimised, at least to the maximum tolerable for low load operation (i.e. low throttle conditions), to maintain A/F ratio levels within the catalyst window limits. This limit was found to be a constant 0.5% signal-to-noise ratio for the entire operating range.

The aim of the designed controller was to improve the performance of current system abilities, without an increase in the demand for extra hardware. A situation was then envisaged, where it was possible to access information pertaining to the throttle angle condition, in order to estimate the throttle air flow rate. It was displayed that this approach improves A/F ratio control, over that of the conventional speed-density approach, since the correct air flow rate is being estimated. The consequences of steady-state mapping techniques were still prevalent, allowing the compensation algorithm to demonstrate improved λ-control. This approach is also not susceptible to excitation from the manifold pressure pulsations discussed in section 6.7.

Chapter 7

Conclusions

The combination of natural gas as an S.I.-engine fuel and a 3-way catalytic converter allows large reductions in exhaust pollutants. For the 3-way catalytic converter to be effective, strict A/F ratio control is needed. The ratio must be maintained within defined window limits to increase conversion efficiency and reduce catalyst poisoning.

Modelling and simulation has become an extremely useful tool in almost all fields of engineering design. The benefits of this approach are numerous, but perhaps two of the main incentives worth mentioning are: 1) the reduction in cost and time in comparison to "real-world" investigations, and 2) the ability to conduct investigations otherwise intolerable to the physical system, sometimes referred to as *"what if?"* type studies, where the model is subject to a variety of simulation conditions. These benefits were appreciated throughout the modelling exercise conducted in this thesis.

A non-linear dynamic model was constructed of a 1.4 litre S.I. engine, which is currently in production. A design approach based on a mathematical representation of the engine processes, afforded a compact model, described by a set of empirical functions and non-linear differential equations, which have been fully described in chapter 2. In order to complete the model, a steady-state dynamome-

ter testing programme was identified, that would afford the relevant engine state measurements.

It was possible to collect a wide range of steady-state operating results from the testing programme. These allowed the submodels to be characterised and, using least-squares regression analysis, model orders and coefficients to be defined. Test results and final submodel definitions were presented in chapter 3.

A full model validation process was not possible, but the results demonstrate dynamic engine behaviour in common with other reported models. The model is deemed to represent good trend-wise agreement with the converted engine, and is considered suitable for further investigative studies. The model provides the mean values of the engine states required to investigate methods of A/F ratio control, by controlling the fuel flow rate entering the throttle intake air-stream.

The non-linear model was found to be an extremely versatile tool for conducting A/F ratio control studies. The action of conventional closed-loop PI-control was investigated, and, for steady-state operating conditions, is adequate for maintaining A/F ratios within the catalyst boundaries with a modulation around the set-point. The modulation frequency is effectively determined by the engine system time delay. It is not possible to increase the rate of estimation error correction, since the integral feedback gain, governing this control aspect, is required to be a specific value to meet the desired A/F ratio modulation amplitude. The structure of PI-control has been fully discussed in section 4.4.

The limitations of PI-control are encountered during transient engine conditions, where rapid throttle angle variations cause fast changes in the air flow rates. The resulting A/F ratio excursions cannot be controlled by the closed PI-control action. An investigation into the effects of microprocessor rates, identified a need to use a sampling frequency, as fast as practicably possible, to restrict even greater A/F ratio excursions. The current G.F.I. sample rate of 3 ms (333.3 Hz)

is sufficient to achieve this, as discussed in section 4.3.2.

The speed-density control approach is not an appropriate air flow rate estimation approach for the throttle body G.F.I. system. Under transient conditions, the large differences in throttle air flow and port air flow, necessitate compensatory action. Closed-loop control algorithms, such as sliding-mode-control (SMC), cannot be used to fulfill this task, as the delayed feedback signal inhibits the speed of increased controller action. Under circumstances where the engine time delay is greater than the air flow transient duration, feedback compensation can actually worsen the A/F ratio excursion. The SMC approach has been fully detailed in section 5.2.

By removing the dependency upon any delayed input signals, it was possible to develop an open-loop transient compensation control algorithm (OTCC), using the air flow rate derivative, that began corrective action the instant a transient condition was encountered. A method of selecting the gains for the OTCC, made full use of the advantages found in system modelling. It was possible to subject the engine to severe throttle conditions otherwise unachievable in practice, and thereby select the optimal compensatory gains. The optimal gain selection procedure was presented in section 5.3.1. The gains were found to be dependent upon the engine speed, allowing an algebraic regression model to be utilised in the control algorithm.

The OTCC algorithm can be confidently used in conjunction with a speed-density air-flow map, typically embedded on conventional A/F control systems, without the danger of the derivative action accentuating estimation errors. The map estimated air flow rate may, or may not, contain an error. Under steady-state conditions, this error will remain constant. The resulting air flow *derivative* estimate will remain zero, and thus, the OTCC will remain inactive during the time when it is not required. Under transient conditions, the air estimation error

may indeed vary, but the derivative estimation will closely approximate the actual derivative, dependent upon the accuracy of the speed-density map. This has been demonstrated in section 6.2.

The G.F.I. system injector limitations do not present major consequences for the OTCC algorithm. The maximum demanded fuel flow rate for the 1.4 litre engine, modelled in this thesis, does not exceed the capacity of the G.F.I. capabilities. An increase in the injector actuation duration inhibits the speed at which the demanded fuel flow rate can be met, with a reduction in the quality of A/F ratio excursion elimination. The G.F.I. actuation times, of approximately 1 - 3 ms, are fast enough to enable OTCC action to be utilised, as was seen in section 6.3.

Controller input signal corruption can be tolerated up to a maximum level, dependent upon the signal-to-noise ratio of the input signal in question. Ideally, the amplitude of the noise should be constantly screened to at least the maximum levels tolerated at the lowest input signal magnitude (i.e. low manifold pressure operating conditions). This shall reduce the variability in the state being estimated, or measured, and provide a higher quality control input. The effects of noise on controller input signals has been investigated in section 6.4.

The air flow rate measured or estimated in the controller, should, ideally, be the air flow into which the fuel is being injected. An immediate improvement in the G.F.I. nominal control algorithm, can be realised if the controller and the engine share a common input signal. If a throttle position sensor signal is accessible, the use of a throttle air flow map (modified speed-density map) removes the dynamics associated with the manifold pressure input signal. This approach estimates the *throttle* air flow, where the G.F.I. spray bar is located. However, the statically-derived map does not encompass the dynamics of the throttle air flow in operation, and cannot totally remove A/F ratio excursions during severe throttle transients.

The throttle air flow control approach was demonstrated in section 6.6.1.

An important phenomenon, that of the manifold pressure pulsing effects, has been identified as having significant implications for the OTCC algorithm. Large variations in the air flow rate estimates, due to the large fluctuations in the manifold pressure, will cause large fluctuations in the air mass derivative estimation at the sample rate of the G.F.I. system. Although this concern is somewhat similar to the effect of signal noise, it was not possible to investigate manifold pressure pulsations, due to the limitations of the model.

The initial aim of the model was to afford a mean value estimate of the manifold pressure, by considering the port air flow rate as the sum of the individual port flows. The pressure pulsation was not identified as an influential engine state to be estimated, during the early stages of defining the model requirements, and therefore has not been modelled.

The modified speed-density approach does not suffer from the manifold pulsation phenomenon, since it does not rely on the manifold pressure measurement. This is one way around the problem, and is becoming a more common approach, but the need for a further sensor increases both the cost and calibration requirements.

The requirement for a comprehensive investigation of the effects of manifold pressure pulsation, lead to the identification of a number of further work aspects. The model should be adapted to encompass the individual port flow rates, and thereby estimate the discrete induction process effects on the manifold emptying process. This would increase the complexity of the model, but would afford an increase in system representation, required to complete a full investigation of the implications of the OTCC algorithm. The need for further testing, where data acquisition takes place over a period of time during steady-state operation, as opposed to static measurements, is necessary to validate the extended model.

The approach to using a non-recursive digital filter paired with the frequency of the air induction events, could then be investigated. It is expected that the manifold pressure pulsations can be filtered using this approach (a 'blend' of fixed-rate and event-based sampling) to provide an estimation of the 'mean' air flow rate derivative. These areas of further work have been discussed in section 6.7.

Bibliography

[1] L. H. Watkins. *Air pollution from road vehicles.* HMSO, 1991.

[2] N. A Henein and D. J. Patterson. *Emissions From Combustion Engines And Their Control.* Ann Arbor Science Publ. Inc., 1972.

[3] *Energy and Cleaner Air: Costs for Reducing Emissions.* OECD, 1987.

[4] T. Y. Chang and D. P. Chock. Urban and regional ozone air quality: Issues relevant to the automobile industry. *Critical Rev. Env. Control*, Vol. 22 no. 1:27–66, 1992.

[5] J. M. Dunne and P. J. Greening. Longer term development of emission regulations. *The Future For Worldwide Vehicle Emissions*, September 1994.

[6] S. A. C. Shillington. The greenhouse challenge. *I. Mech. E Tribology Group*, 1993.

[7] O. Hadded, J. Stokes, and D. W. Grigg. Low emissions vehicle technology for ULEV and European Stage 3 Emissions Standards. *I. Mech. E. "Autotech Seminar 18: Emissions - Update and Developments"*, 1993. C462/18/126.

[8] A. L. Waddams. *Chemicals From Petroleum.* John Murray Publishers, 1963.

[9] J. B. Heywood. *Internal Combustion Engine Fundamentals.* McGraw-Hill, Inc., 1988.

[10] J. B. Heywood. Pollutant formation and control in spark-ignition engines. *Prog. Energy Combust. Sci.*, Vol. 1:135–164, 1976.

[11] Science Research Council. *Combustion-Generated Pollution.* Science Research Council, 1976.

[12] W. E. Bernhardt. Kinetics of nitric oxide formation in internal-combustion engines. *Instn. Mech. Engrs.*, pages 279–285, 1971. C149/71.

[13] U. Adler, editor. *Automotive Handbook.* Bosch, 2nd edition, 1986.

[14] M. Dürnholz, G. Eifler, and H. Endres. Exhaust gas recirculation - a measure to reduce exhaust emissions of DI Diesel engines. 1992.

[15] L. Mikulic, M. Kuhn, J. Schommers, and E. Willig. Exhaust emission optimisation of DI-Diesel passenger car engine with high pressure fuel injection and EGR. *SAE Transactions - 931035*, 1993.

[16] J. H. Weaving, editor. *Internal Combustion Engineering - Science And Technology.* Elsevier Science Publishing Co., Inc., 1990.

[17] M. Kano, I. Tanimoto, K Nakamura, and A. Fujiki. Effect of the EGR system on valve train wear in diesel engine. *Journal of Japanese Society of Lubrication Engineers (JSLE)*, pages 133 – 138, 1988. No. 9.

[18] A. Amstutz and L. R. Del Re. EGO sensor based robust output control of EGR in diesel engines. *IEEE Transactions On Control Systems Technology*, Vol. 3:39 – 48, March 1995.

[19] C. Arcoumanis and J. H. Whitelaw. Fluid mechanics of internal combustion engines - a review. *Proc. Instn. Mech. Engrs.*, Vol. 201. No. C1:57–74, 1987.

[20] R. Stone. *Introduction To Internal Combustion Engines.* Macmillan Education Ltd., 1985.

[21] J. Chapman, A. C. Cole, S. Wallace, and J. H. Weaving. Meeting vehicle pollution regulations by combustion technology. *Proceedings of I. Mech. E. Eurotech Direct 91*, 1991. C413/059.

[22] R. W. Hurn, editor. *Approaches To Automotive Control.* American Chemical Society, 1974.

[23] J. Hartley. Reducing NOx emissions. *Automotive Engineer*, pages 68 – 70, August/September 1978. ImechE.

[24] G. E. Andrews and F. M. Salih. Ignition timing and mixture strength influences on emissions for a gasoline/30% ethanol fuel. *I. Mech. E. "Autotech Seminar 18: Emissions - Update and Developments"*, 1993. C462/18/020.

[25] I-Y. Ohm, H-S. Ahn, W-J Lee, W-T. Kim, S-S. Park, and D-U Lee. Development of HMC axially stratified lean combustion engine. *SAE Transaction - 930879*, 1993.

[26] T. Sakurai, M. Iko, K. Okamoto, and F. Sholi. Basic research on combustion chambers for lean burn gas engines. *SAE Transactions - 932710*, 1993.

[27] J-P. Pirault and G Fraidl. Controlled burnrate combustion system for 4 valve cylnder engines. *I. Mech. E. "Autotech Seminar 12: Understanding Combustion-Gasoline Engines"*, 1993. C462/12/232.

[28] P. D. Ronney, M. Shoda, S. T. Walda, C. Westbrook, and W. Pitz. Knock characteristics of liquid and gaseous fuels in lean mixtures. *SAE Transactions - 912311*, 1991.

[29] C. K. Westbrook and W. Pitz. The chemical kinetics of engine knock. *E & TR*, February/March 1991.

[30] C. D. Falk and Mooney. J. J. Three-way conversion catalysts: Effect of closed-loop feed-back control and other parameters on catalyst efficiency. *SAE Transactions - 800462*, pages 1822 – 1832, 1980.

[31] R. P. Canale, S. R. Winegarden, C. R. Carlson, and D. L. Miles. General motors phase II catalyst system. *SAE Transaction - 780205*, pages 843 – 852, 1978.

[32] B. Cooper. The future of catalytic systems. *Automotive Engineer*, Vol. 100:9 – 12, April 1992.

[33] W. Gõpel, J. Hesse, and J. N. Zemel, editors. *Sensors: A Comprehensive Survey. Chemical and Biochemical Sensors*, volume Vol. 2. VCH, 1991. Part 1.

[34] W. J. Fleming. Zirconia oxygen sensor - an equivalent circuit model. *SAE Transactions - 800020*, 1980.

[35] W. J. Fleming. Sensitivity of the zirconia sensor to temperature and flow rate of exhaust gas. *SAE Transactions - 760020*, 1976.

[36] H-M. Wiedenmann, L. Raff, and R. Noack. Heated zirconia oxygen sensor for stoichiometric and lean air-fuel ratios. *SAE Transactions - 840141*, 1984.

[37] Q. Wang, D. Sperling, and J. Olmstead. Emission control cost-effectiveness of alternative fuels. *SAE Transactions - 931841*, 1993.

[38] U Cantoni. Alternative fuels utilization in fuel cells for transportation. *SAE Transactions - 931816*, 1993.

[39] M. P. Walsh. global warming: The implications for alternative fuels. *SAE Transactions - 891114*, 1989.

[40] E. M. Goodger. *Petroleum And Performance.* Butterworth Scientific Publications, 1953.

[41] S. R. Bell. Natural gas as a transportation fuel. *SAE Transactions - 931829*, pages 29 – 35, 1993. Special Publication.

[42] British Gas: Internal. The environmental benefits of natural gas vehicle operation. *Doc. No. P0077*, June 1994.

[43] W. Wang, M. Gautam, X. Sun, R. Bata, N. Clark, G. Palmer, and D Lyons. Emissions comparisons of twenty-six heavy-duty vehicles operated on conventional and alternative fuels. *SAE Transactions - 932952*, 1993.

[44] R. Moreno and D. Fallen Bailey. Alternative transport fuels from natural gas. *World Bank Technical Paper Number 98.*

[45] Fiona Navesey. A clear alternative. *Relay: Gas in Industry and Commerce*, pages 15 – 17, February 1992. British Gas Research and Technology.

[46] N. Nuttal and K Eason. Step on the gas for a cleaner country. *The Times*, 3rd June 1995.

[47] Department of Transport. Government research department, 1995.

[48] A. Unich, R. M. Bata, and D. W. Lyons. Natural gas: A promising fuel for I.C. engines. *SAE Transactions - 930929*, 1993.

[49] C. S. Weaver. Natural gas vehicles - a review of the state of the art. *Journal of Fuels and Lubricants*, Vol. 98:1190 – 1210, 1989. (SAE Transactions).

[50] S. Farrall. *A Study in the use of fuzzy logic in the management of an automotive heat engine/electric hybrid vehicle powertrain.* PhD thesis, University of Warwick, 1993.

[51] A. S. Cherry, A. Costa, and Jones. R. P. MBS modelling, non-linear simulation and linear analysis techniques for integrated vehicle control. 1995. Proceedings of IFAC Workshop on Advances in Automotive Control, Monte-Verita.

[52] R. J. Tabaczynski. Effects of inlet and exhaust system design on engine performance. *SAE Transactions - 821577*, 1985.

[53] A. D. Gosman. Computer modelling of flow and heat transfer in engines, progress and prospects. *Proceedings of the International Symposium on Diagnostics and Modelling of Combustion in Reciprocating Engines*, September 1985. CODIA 85.

[54] A. D. Gosman. Modelling of cold flows and turbulence in reciprocating engines. *SAE Transaction - 850344*, 1985.

[55] E. Hendricks and S. Sorenson. SI engine controls and mean value engine modelling. *SAE Transaction - 910258*, 1991.

[56] E. Hendricks, M. Jensen, P. Kaidantzis, P. Rasmussen, and T. Vesterholm. Transient A/F ratio errors in conventional SI engine controllers. *SAE Technical Paper - 930856*, 1993. Special Publication SP - 955.

[57] J. J. Moskwa and J. K. Hedrick. Automotive engine modeling for real time control application. *Proc. American Control Conference*, pages 341 - 346, June 1987. WA10 - 11:00.

[58] B. K. Powell and J. A. Cook. Nonlinear low frequency phenomenological engine modeling and analysis. *Proc. American Control Conference*, pages 332 – 340, June 1987. WA10 - 10:30.

[59] B. S. Massey. *Mechanics of Fluids.* Chapman and Hall, 6th edition, 1989.

[60] N. F. Benninger and G Plapp. Requirements and performance of engine management systems under transient conditions. *SAE Transactions - 910083*, pages 118 – 127, 1991.

[61] G. R. Purdy, C. Gong, R. J. Douglas, and S. Thompson. The development of a phenomenological model of a single cylinder four-stroke spark ignition engine: Testing and validation. *I. Mech. E.*

[62] D. L. Harrington and J. A. Bolt. Analysis and digital simulation of carburetor metering. *SAE Transactions - 700082*, 1970.

[63] D. Cho and J. K. Hedrick. Automotive powertrain modeling for control. *Journal of Dynamic Systems, Measurement and Control*, 111:568 – 576, 1989. Transactions of the ASME.

[64] D. J. Dobner. A mathematical engine model for development of dynamic engine control. *SAE Transactions - 800054*, Section 1:373 – 381, 1980.

[65] S. Thompson and S. Y. Duan. Modelling, parameter selection and simulation of a single-cylinder four-cycle engine. *Proc Instn Mech Engrs*, 205:49 – 57, 1991.

[66] G. Rogers and Y. Mayhew. *Engineering Thermodynamics : Work and Heat Transfer.* Longman Scientific and Technical, 4th edition, 1992.

[67] C-F. Chang, N. P. Fekete, and J. D. Powell. Engine air-fuel ratio control using an event-based observer. *SAE Transactions - 930766*, pages 1002 – 1017, 1993.

[68] A. Amstutz, N. P. Fekete, and J. D. Powell. Model-based air-fuel ratio control in SI engines with a switch-type EGO sensor. *SAE Transactions - 940972*, 1994.

[69] V. K. Jones, B. A. Ault, G. F. Franklin, and J. D. Powell. Identification and air-fuel ratio control of a spark ignition engine. *IEEE Transactions On Control Systems Technology*, Vol. 3:14 – 21, March 1995.

[70] H. Wu, C. F. Aquino, and G. L. Chou. A 1.6 liter engine and intake manifold dynamic model. *AMSE*, Vol. 106, 1984. 83-WA/DSC-39.

[71] C. F. Aquino. Transient A/F control characteristics of the 5 liter central fuel injection engine. *SAE Transactions - 810494*, 1981.

[72] H. D. Jander H-E. Endres and W. Göttler. A test system for gas sensors. *Sensors and Actuators B (Chemical)*, pages 163 – 172, 1995.

[73] P. W. Atkins. *Physical Chemistry.* Oxford University Press, 5th edition, 1994.

[74] C. F. Taylor. *The Internal Combustion Engine in Theory and Practice*, volume Vol. 1. The M.I.T. Press, 1966.

[75] D. Z. Wang and K. P. Oh. Development of an engine modelling capability for a broad range of problems. *ASME*, DE-Vol. 40:537 – 549, 1991. Advanced Automotive Technologies.

[76] W. E. Snyder, M. R. Wright, and S. G. Dexter. A natural gas engine combustion rig with high-speed photography. *Journal of Engineering for*

Gas Turbines and Power, Vol. 110:334 – 342, July 1988. (Transactions of the ASME).

[77] C. A. Amann. Cylinder-pressure measurement and its use in engine research. *SAE Transactions - 852067*, 1985.

[78] R. J. Alfredson. First and second derivatives of internal combustion engine cylinder pressure diagrams. *Journal of Sound and Vibration*, pages 287 – 291, 1982. Letters To The Editor.

[79] D. J. Dobner. Dynamic engine models for control development - part 1: Non-linear and linear model formulation. *Int. J. of Vehicle Design*, pages 54 – 74, 1983. Special Publication - SP4.

[80] D. J. Boam, I. C. Finlay, and J. J. G. Martins. A model for predicting engine torque response during rapid throttle transients in port-injected spark ignition engines. *SAE Transactions - 890565*, 1989.

[81] B. K. Powell. A dynamic model for automotive engine control analysis. *I.E.E.E.*, pages 120 – 126, 1979. Conference on Decision and Control.

[82] J. A. Cook and B. K. Powell. Modeling of an internal combustion engine for control analysis. *I.E.E.E. - Control System Magasine*, Vol. 8:20 – 26, August 1988. No:4.

[83] W. W. Yuen and H. Servati. A mathematical engine model including the effect of engine emissions. *SAE Transactions - 840036*, pages 225 – 241, 1984.

[84] L. A. M. van Dongen. The efficiency characteristics of manual and automatic passenger car transaxles. *SAE Transactions - 820741*, 1982.

[85] E. Hendricks, T. Vesterholm, and S.C. Sorenson. Nonlinear, closed loop, SI engine control observers. *SAE Technical Paper - 920237*, 1992.

[86] E. Hendricks and T. Vesterholm. The analysis of mean value SI engine models. *SAE Technical Paper - 920682*, 1992.

[87] P. Kaidantzis, P. Rasmussen, M. Jensen, T. Vesterholm, and E. Hendricks. Robust, self-calibrating lambda feedback for SI engines. *SAE Technical paper - 930860*, 1993. Special Publication - SP955.

[88] D. R. Hamburg and M. A. Shulman. A closed-loop A/F control model for internal combustion engines. *SAE Transactions - 800826*, 1980.

[89] Y. A. Çengel and M. A. Boles. *Thermodynamics: An engineering approach.* McGraw-Hill, 1989.

[90] M. S. Younger. *A Handbook for Linear Regression.* Duxbury Press., 1979.

[91] Sanford Weisberg. *Applied Linear Regression.* Wiley Series in Probibilty and Mathematical Statistics, 1980.

[92] Z. Mencik and P. N. Blumberg. Representation of engine data by multivariate least-squares regression. *SAE Technical Paper - 780288*, 1978.

[93] L. Ljung. *System Identification Theory For The User.* prentice-Hall, Inc., 1987.

[94] J. P. Norton. *An Introduction To Identification.* Academic Press, 1986.

[95] Mitchell and Gauthier Associates. *ACSL - User Guide/Reference Manual.* 3rd edition, 1981.

[96] P. A. Hazell and J. O. Flower. Sampled-data theory applied to the modelling and control analysis of compression ignition engine - part 1. *Int. J. Control*, 13, No. 3:549 – 562, 1971.

[97] W. L. Fehr and J. V. Medanic. Using an angle-based, sampled data approach to modeling a diesel engine. pages 239 – 244, 1989. Caterpillar Inc., and University of Illinois.

[98] Y-K. Chin and F. E. Coats. Engine dynamics: Time-based versus crank angle based. *SAE Transaction - 860412*, 1986.

[99] C. O. Nwagboso, editor. *Automotive Sensory Systems.* Chapman & Hall, 1st edition, 1993.

[100] S. D. Hires and M. T. Overington. Transient mixture strength excursions - an investigation of their causes and the development of a constant mixture strength fueling strategy. *SAE Transactions - 810495*, pages 1834 – 1850, 1981.

[101] Stewart & Stevenson. G.F.I. instruction manual.

[102] L. E. Gettel, G. C. Perry, J. Boisvert, and P. J. O'Sullivan. Microprocessor dual-fuel diesel engine control system. *SAE Transactions - 861577*, 1986.

[103] G. F. Franklin, J. D. Powell, and A. Emami-Naeini. *Feedback Control of Dynamic Systems.* Addison-Wesley, 2nd edition, 1991.

[104] M. Attenborough. *Engineering Mathematics Exposed.* McGraw Hill, 1st edition, 1994.

[105] W. Kaplan. *Advanced Mathematics for Engineers.* Addison-Wesley, 1981.

[106] C. L. Phillips and H. T. Nagle. *Digital Control System Analysis and Design.* Prentice Hall International Editions, 1st edition, 1995.

[107] G. T. Engh and S. Wallman. Development of the volvo lambda-sond system. *SAE Transactions - 770295*, pages 1393 – 1407, 1977.

[108] D. K. Anand and R. B. Zmood. *Introduction to Control Systems.* Butterworth Heinemann, 3rd edition, 1995.

[109] D. Cho and J. K. Hedrick. A nonlinear controller design method for fuel-injected automotive engines. *Transaction of ASME*, 110:313 – 320, July 1988.

[110] D. Cho and J. K. Hedrick. Sliding mode fuel-injection controller: Its advantages. *Journal of Dynamic Systems, Measurement and Control*, 113:537 – 541, 1991. Transactions of the ASME.

[111] J. J. Moskwa. Sliding mode control of automotive engines. *Journal of Dynamic Systems, Measurement, and Control*, Vol. 115:687 – 693, December 1993. Transaction of ASME.

[112] S-K. Nam, M-H. Lee, and W-S Yoo. Predictive sliding control with fuzzy logic for fuel-injected automotive engines. *I. Mech. E.*, 206:237 – 244, 1992.

[113] S-K. Nam, J-S. Kim, and W-S. Yoo. Fuzzy sliding-mode control of gasoline fuel-injection system with oxygen sensor. *JSME International Journal*, Vol. 37, 1994. Series C, No. 1.

[114] M. H. Westbrook and J. D. Turner. *Automotive Sensors.* Institute of Physics Publishing, 1st edition, 1994.

[115] Personal communication with British Gas engineers.

[116] F. Daly, D. J. Hand, M. C. Jones, A. D. Lunn, and K. J. McConway. *Elements of Statistics.* Addison Wesley, 1st edition, 1995.

[117] G. L. Squires. *Practical Physics.* Cambridge University Press, 1st edition, 1985.

[118] N. P. Fekete and J. D. Powell. Observer based air-fuel ratio control. *Advances in Automotive Control*, pages 12 – 19, March 1995. IFAC Workshop (Switzerland).

[119] C-F. Chang, N. P. Fekete, A. Amstutz, and J. D. Powell. Air-fuel ratio control in spark-ignition engines using estimation theory. *IEEE Transactions On Control Systems Technology*, Vol. 3:22 – 31, March 1995.

[120] S. M. Bozic. *Digital and Kalman Filtering.* Edward Arnold, 1st edition, 1979.

Appendix A

Data Used In Engine Model

A.1 Rover K16 Engine Specification

The engine used in the modeling study was a Rover K16 1.4 litre, of the type discussed in section 1.2.2. Details are shown below.

Engine Type	Rover K16
Cylinders	4 In-line
Capacity	1397 cm^3
Manifold Volume	2500 cm^3
Stroke	79.0mm
Cylinder Bore Liner	75.0mm
Compression Ratio	10.0:1
Ignition Timing	Best Torque (MBT)
Ignition Timing @ Idle	10 ± 5^o B.T.D.C
Idle Speed	875 ± 50 rpm
Valve Mechanism	16 valve Hydraulic Actuation
Valve Timings : Inlet Open at	15^o B.T.D.C
Inlet Close at	45^o A.B.D.C
Exhaust Open at	55^o B.B.D.C
Exhaust Close at	5^o A.T.D.C
Camshaft	Double Over Head Camshaft (DOHC)
Exhaust System	3-Way CC

Table A.1: Natural gas engine specification.

A.2 Gear Ratios and Inertias

Gear	Gear Ratio	Overall Gear Ratio. (Final Drive 3.938:1)	Equivalent Flywheel Inertia (kg m^2)
Neutral			0.1
First	3.417:1	13.456:1	0.8
Second	1.947:1	7.667:1	2.1
Third	1.333:1	5.249:1	4.4
Fourth	1.054:1	4.150:1	6.9
Fifth	0.854:1	3.363:1	10.0
Reverse	-3.583:1	-13.225:1	0.7

Table A.2: Engine inertias, gear-box and final drive ratios.

Appendix B

Dynamometer and Test-bed Specifications

B.1 Dynamometer and Exhaust Analyser

Dynamometer	Borghi & Saveri Eddy current water cooled
Exhaust analyser:	Horiba MEXA 9100H:
CO/CO_2	Infrared
THC	Flame Ionisation
O_2	Magneto-pneumatic
NOx	Chemi-luminescent
EGO sensor	Bosch Zirconia
EGO sensor placement	37cm after exhaust valves
Exhaust sample tap	103cm after exhaust valves
Exhaust temperature sensor	111cm after exhaust valves

Table B.1: Dynamometer and exhaust analyser specification.

B.2 Test and Dynamometer Architecture

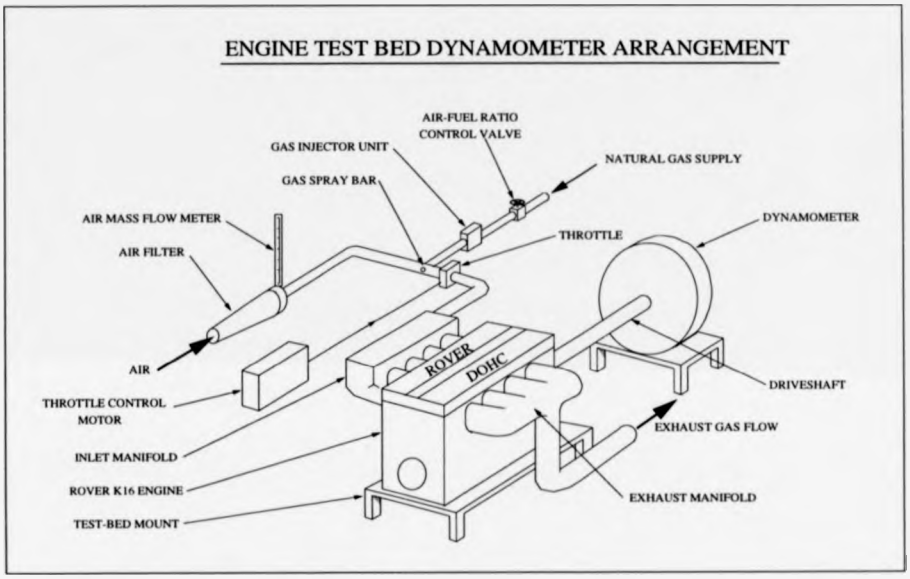

Figure B.1: Engine test bed arrangement and dynamometer arrangement.

B.3 Engine Sensors

Data Acquisition and Sensor Type	
Engine speed	60 tooth flywheel magnetic pickup (rpm)
Combustion torque	Dynamometer resistance (Nm)
Throttle angle	Potentiometer (%)
Lambda	Horiba Sensor (λ)
Air inlet temperature	Thermocouple (°C)
Gas temperature at meter	Thermocouple (°C)
Gas pressure at meter	Transducer (mbar)
Barometric pressure	Transducer (mbar)
Manifold depression	Transducer (mbar)
Gas pressure at spray bar	Transducer (mbar)
Engine power	Calculated (kW)
ISO standard power	Calculated (kW)
Fuel flow rate	Meter device (m^3/h)
Air flow rate	Pressure drop across laminar (mmH_2O)
Relative humidity	%
Gas calorific value	Gas chromatograph (MJ/m^3)

Table B.2: Engine measurement sensors.

Appendix C

Engine Steady State Test Bed Data

C.1 Speed Density Air Flow Map data

Port air flow rate for speed density map in g/s									
Engine Speed	Manifold pressure in kPa								
(rpm)	15	20	25	30	35	40	45	50	55
2000	-2.32	-0.96	0.22	1.45	2.66	3.92	5.23	6.44	7.74
2250	-1.45	0.00	1.35	2.81	4.11	5.71	6.87	8.32	9.92
2500	-1.21	0.48	1.94	3.68	5.32	7.26	8.76	10.16	11.27
2750	-0.85	0.96	2.81	4.84	7.02	8.95	10.45	12.10	13.69
3000	-0.15	1.39	3.87	6.29	8.47	10.45	12.44	14.42	16.35
3250	0.39	2.52	4.89	7.55	9.82	11.90	14.18	16.21	18.39
3500	0.97	3.38	6.29	8.71	10.74	13.11	15.87	18.15	20.47
3750	1.45	3.97	6.77	9.77	12.34	14.81	17.52	20.18	22.26
4000	2.27	5.08	8.23	10.65	13.31	16.45	19.11	22.02	24.82
4250	2.71	6.05	9.19	12.02	15.00	18.05	20.90	23.56	26.52
4500	3.38	7.02	10.55	13.31	16.45	19.60	22.94	25.65	28.65
4750	4.60	7.89	11.37	14.52	17.66	20.81	24.68	28.06	31.84
5000	5.32	9.19	12.60	15.97	19.60	22.65	25.89	29.52	33.15
	60	65	70	75	80	85	90	95	100
2000	8.85	10.16	11.37	12.68	14.03	15.10	16.35	17.66	18.97
2250	11.13	12.58	14.03	15.48	16.94	18.39	19.84	21.30	22.74
2500	13.43	14.76	16.55	18.39	20.23	21.77	23.35	24.68	26.52
2750	15.48	17.08	18.87	20.81	22.45	24.68	26.61	28.45	30.39
3000	18.29	20.20	22.16	24.19	25.89	27.58	29.64	31.94	34.11
3250	20.32	22.26	24.43	26.59	27.05	31.60	33.39	35.81	37.98
3500	22.50	24.58	26.76	29.18	31.65	34.35	37.02	38.83	41.85
3750	24.60	26.81	29.15	31.84	35.56	37.74	40.40	43.06	45.53
4000	27.58	29.93	32.18	35.03	37.84	40.65	43.21	46.69	49.74
4250	29.52	32.18	34.75	37.98	41.61	44.03	46.94	49.96	52.98
4500	31.45	34.26	37.26	40.89	43.79	46.94	50.32	53.71	56.98
4750	33.58	36.68	40.16	43.55	46.35	50.32	53.71	57.58	60.73
5000	36.77	40.52	44.13	47.18	50.32	53.71	57.10	61.00	64.60

Table C.1: Interpolated port air flow rate data.

C.2 Modified Speed Density Air flow Map Data

Throttle air flow for modified speed density map in g/s							
Throttle Angle	Engine Speed in rpm						
(degrees)	2000	2250	2500	2750	3000	3250	3500
15.0	4.5614	4.7656	4.4498	4.3062	4.2424	4.2105	4.1627
17.5	6.5008	6.4860	6.6986	6.7464	6.8660	6.8900	6.9617
20.0	8.8485	9.1675	9.0909	9.2823	9.3222	9.3780	9.3301
22.5	11.2217	11.7193	11.8182	11.8182	12.3923	12.3764	11.8421
25.0	13.4928	14.2711	14.8804	15.1675	15.9649	15.9490	15.9330
27.5	14.8708	16.5359	17.7990	18.3732	19.3142	19.7129	20.0957
30.0	15.9681	18.0989	20.2392	21.1483	22.7193	23.2855	23.8278
32.5	16.9378	19.4386	21.9139	23.1579	25.2313	26.3477	27.2727
35.0	17.4737	20.4274	23.0622	25.1675	27.0175	28.9633	30.3589
37.5	17.6778	21.0016	23.8278	26.5550	28.4689	31.3876	32.7273
40.0	17.9841	21.2887	24.2584	27.4641	29.8086	32.4083	34.7368
42.5	18.2137	21.4801	24.6890	27.8947	30.5901	33.6204	36.5311
45.0	18.3158	21.7671	25.0718	28.4211	31.1483	34.5774	37.1053
47.5	18.4434	21.9904	25.3110	28.7560	31.7624	35.2153	37.7512
50.0	18.4944	22.0861	25.5502	29.0909	32.3206	35.5981	38.2536
55.0	18.5965	22.2137	25.6938	29.3301	32.7671	36.0447	38.8278
60.0	18.6220	22.3094	25.8373	29.4258	33.0463	36.3636	39.4737
65.0	18.6220	22.3732	25.9809	29.4737	33.1579	36.6826	39.8325
70.0	18.6730	22.3413	26.0766	29.5694	33.2137	36.8102	40.1196
75.0	18.6730	22.3732	26.0766	29.4258	33.2695	37.0016	40.3349
80.0	18.7241	22.4370	26.1244	29.5694	33.2695	36.9378	40.3349
90.0	18.7496	22.4051	26.0766	29.7608	33.4370	36.9378	40.4067
	3750	4000	4250	4500	4750	5000	
15.0	4.3062	5.0239	4.2982	4.6491	4.9761	4.9761	
17.5	6.3876	6.8581	6.8421	6.8421	7.0813	7.2727	
20.0	9.2584	9.4896	9.2982	9.6491	9.6651	9.6651	
22.5	12.3445	11.7225	12.1053	12.5439	12.5359	12.7273	
25.0	15.9330	15.8692	16.0526	16.0526	16.1722	16.1722	
27.5	20.3828	20.1754	20.3509	20.5263	19.7129	20.4785	
30.0	24.3301	25.1994	24.5614	25.3509	25.2632	24.4976	
32.5	28.2057	29.5056	29.9123	29.9123	30.7177	30.4306	
35.0	31.0766	32.7751	33.6842	34.2982	34.7368	36.1722	
37.5	35.3828	36.1244	37.2807	38.4211	39.5215	41.2440	
40.0	37.3923	39.2344	41.1404	42.1053	43.1579	45.6459	
42.5	38.3971	40.7496	42.7193	44.3860	45.9330	47.8469	
45.0	39.9761	41.9458	44.3860	46.4912	49.4737	50.7177	
47.5	41.1962	43.1419	45.7895	48.1579	50.3349	52.5359	
50.0	41.9856	44.5774	46.8421	49.2105	52.4402	54.3541	
55.0	42.6316	45.2153	48.0702	50.8772	53.8756	56.3636	
60.0	43.1340	46.1722	48.8596	52.2807	55.4067	57.8947	
65.0	43.2775	46.6507	49.2982	52.8070	55.7895	59.0431	
70.0	43.4211	46.9697	49.8246	53.1579	56.4593	59.6172	
75.0	43.5646	46.9697	50.2632	53.2456	56.6507	59.6172	
80.0	43.5646	47.2089	50.2632	53.4211	56.6507	59.7129	
90.0	43.7081	47.2089	50.4386	53.4211	56.8421	59.9043	

Table C.2: Interpolated throttle air flow rate data.

Appendix D

Engine Model Code

```
PROGRAM Engine model with choice of controllers
  !
INITIAL
  MINTERVAL mint = 1.0e-10
  MAXTERVAL maxt = 1.0e-3
  NSTEPS    nstp = 1
  CINTERVAL cint = 1.0e-3
  ALGORITHM ialg = 5
  CONSTANT tstop = 1.5
  !
  !*****************************************************************
  !
  ! " INITIAL CONDITIONS SETTINGS OF ENGINE SPEED AND TORQUE "
  !  ------------------------------------------------------
  !
  CONSTANT Neic=33.333
  Speedic=Neic*60
  Tfmepic=(0.97+(0.15*Speedic/1000)+(0.05*Speedic/1000))*100
  CONSTANT Tlind=10
  Tloadic=(Tfmepic*Vd)/(4*pi) + Tlind
  !
  !*****************************************************************
  !
  ! " INITIAL CONDITIONS COMPUTATION "
  ! ---------------------------------
  !
  ! Compute initial conditions to set up combustion,
  ! torque = load torque and corresponding manifold
  ! pressure, air flows and engine speed
  !
```

```
! " TORQUE MODEL CONSTANTS "
!
CONSTANT a=-2.4245e-5 , b=5.0096e-5   , c=-1.9569e-5
CONSTANT d=0.0434     , e=-0.08319    , f=-0.00930
CONSTANT g=0.0016937  , h=-0.003131   , i=8.70495e-4
CONSTANT j=-6.83520   , k=11.54591    , l=1.49873
CONSTANT m=0.0053976  , n=-0.0137866 , o=-0.004371
CONSTANT p=-65.66949  , q=145.27382   , r=-66.34686
CONSTANT Lambdaic=1
!
! " INITIAL TORQUE MODEL TERMS "
!
Tq1icA =a*speedic*Lambdaic**2
Tq2icA =b*speedic*Lambdaic
Tq3icA =c*speedic
Tq4icA =d*Lambdaic**2
Tq5icA =e*Lambdaic
Tq6icA =f
Tq7icA =g*speedic*Lambdaic**2
Tq8icA =h*speedic*Lambdaic
Tq9icA =i*speedic
Tq10icA=j*Lambdaic**2
Tq11icA=k*Lambdaic
Tq12icA=l
Tq13icA=m*speedic*Lambdaic**2
Tq14icA=n*speedic*Lambdaic
Tq15icA=o*speedic
Tq16icA=p*Lambdaic**2
Tq17icA=q*Lambdaic
Tq18icA=r
!
X1ic=(Tq1icA+Tq2icA+Tq3icA+Tq4icA+Tq5icA+Tq6icA)
X2ic=(Tq7icA+Tq8icA+Tq9icA+Tq10icA+Tq11icA+Tq12icA)
X3ic=(Tq13icA+Tq14icA+Tq15icA+Tq16icA+Tq17icA+Tq18icA)
!
!*****************************************************************
!
!             " PORT MASS FLOW I.C. COMPUTATION "
!             ----------------------------------
!
! Initial port mass flow rate required to give the desired
! combustion torque at the desired engine speed
!
```

```
Portic=(-X2ic+sqrt((X2ic**2)-(4*X1ic*(X3ic-Tloadic))))/(2*X1ic)
!
! " PORT FLOW MODEL CONSTANTS "
!
CONSTANT Porta=-5.891e-5
CONSTANT Portb=1.5202e-7
CONSTANT Portc=-5.6991
!
!*****************************************************************
!
! " MANIFOLD PRESSURE I.C. COMPUTATION "
! -------------------------------------
!
! Compute inital manifold pressure for steady-state at the
! given mass flow of port air.
!
Pmic=(Portic-PortC)/(PortA+(PortB*speedic))
!
! " AIR FLOW RELATED CONSTANTS "
!
CONSTANT Gam=1.4        !--Specific Heat Ratio
CONSTANT Pamb=100000.0  !--Ambient Pressure (Pascals)
CONSTANT Pcrit=0.528    !--Critical Pressure Ratio
!
!*****************************************************************
!
! " PRESSURE RATIO INFLUENCE (PRI) I.C. COMPUTATION "
! --------------------------------------------------
!
PRic=Pmic/Pamb
PRIicabove=sqrt((2/(Gam-1))*((Pric**(2/Gam)) &
           -(Pric**((Gam+1)/Gam))))
PRIicbelow=sqrt((2/(Gam+1))**((Gam+1)/(Gam-1)))
PRIic=RSW(Pric.le.Pcrit,PRIicbelow,PRIicabove)
PRIicnorm=PRIic/PRIicbelow
MOPRIic=Portic/PRIicnorm
!
!*****************************************************************
!
! " THROTTLE ANGLE I.C. COMPUTATION "
! ----------------------------------
!
! The structure of the 'throttle angle' model does not allow the
```

```
! throttle angle to expressed explicitly in terms of the model
! parameters. The IMPLICIT command is used to obtain the initial
! condition of the throttle angle given the throttle mass flow
! and the pressure ratio influence.
!
! " THROTTLE BODY MODEL CONSTANTS  "
!
CONSTANT Tha=0.380     ,  Thb=48.5148
CONSTANT Thc=240.3269 ,  Thd=-174.3109
CONSTANT yic=0.178606   !--sin(THETA)^2 in radians
CONSTANT erry=0.0001
CONSTANT Niy=10
CONSTANT ydl=0.01
CONSTANT radcon=0.017453293 !-- Radians-to-degrees consatnt
!
y=yic
impl(y=yic,erry,Niy,efly, &
       (MOPRIic-THa-(THc*y**2)-(THd*y**3))/THb,ydl)
!
thric=asin(sqrt(y))
thic=thric/RADCON    !--Initial throttle angle (degrees)
!
!*************************************************************
!
! " GAS DELIVERY DELAY DUE TO FEED PIPE"
! -------------------------------------
!
! The fuel delivery pipe is included as a volume producing a
! fuel hold up. The pressure within the pipe is required
! to be computed in a similar appraoch as the manifold
! pressure and pressure ratio influence term.
!
! " FUEL DELIVERY PIPE CONSTANTS "
!
CONSTANT flowC=3.1952e+5  !--Pipe flow constant
CONSTANT pradius=6.35e-3  !--Pipe radius in metres (0.25in)
CONSTANT plength=0.5      !--Pipe length (m)
CONSTANT Gamgas=1.299     !--Specific heat ratio for methane
CONSTANT mmf = 16.0       !--Molar Mass of gas
CONSTANT xic=0.8          !--Initial estimate of pri
CONSTANT errx=0.0001      !--Implicit error
CONSTANT Nix=10           !--Number of Implicit iterations
CONSTANT xdl=0.01
```

```
CONSTANT pi=3.142
!
PVol=pi*(pradius**2)*plength  !--Fuel pipe volume (m^3)
pipecon=(Rm*Temp)/(PVol*mmf)  !--Pipe constant
Gasinic=Portic/Stoich
Gasoutic=Gasinic
PRIpipeic=Gasoutic/(flowC*Area)
x=xic
impl(x=xic,errx,Nix,eflx,(((PRIpipeic**2)*(GamGas-1)/2) + &
(X**((GamGas+1)/GamGas)))**(GamGas/2),xdl)
Ppipeic=Pamb/X                !--Initial pipe pressure condition
!
!*****************************************************************
!
! " DEFINE THE THROTTLE ANGLE TIME INPUTS"
! ---------------------------------------
!
! Time constants to affect change in throttle angle.
!
CONSTANT Tup   = 3.0
CONSTANT Tdown = 1.0
CONSTANT THmin=15
CONSTANT THmax=90
!
!*****************************************************************
!
! " Pseudo state vector for initialising feedback fuel signal "
!
! Constant Time Sample Variables
!
PmD=Pmic              !--Manifold Pressure
SpeedD=Speedic        !--Engine Speed
Unom=portic/STOICH    !--Nominal Fuel
Up=0.0                !--Proportional Fuel
Ui=0.0                !--Integral Fuel
Uip=0.0               !--Integral Fuel (Previous time step)
Ud=0.0                !--Derivative Fuel
Upi=0.0               !--P+I Fuel
Aird=0.0              !--Gradient Air Flow
Map=portic            !--Previous Air Flow Rate at Throttle
Ktrd=0.0              !--Transient Control Gain
Utr=0.0               !--Transient Fuel
Upitr=0.0             !--Compensation fuel
```

```
  !
  !  Controller Block Schedule
  !
  Ucont = 0.0
  Ucontc= 0.0
  !
  mfin = portic/STOICH
  !
END   ! of Initial
  !
  !*************************************************************
  !
DYNAMIC      !--Begin Dynamic Block
  !
DERIVATIVE   !--Begin Derivative Block
  !
  ! " DEFINE THE THROTTLE ANGLE INPUT "
  ! ----------------------------------
  !
  CONSTANT Tdur = 0.5 !--Duration time of RAMP
  !
  CONSTANT Mag1 = 10  !--Magnitude of RAMP
  CONSTANT Mag2 = 15
  !
  ThetaRub=Thic - mag1*RAMP(Tdown) + mag1*RAMP(Tdown+Tdur) &
         + mag2*RAMP(Tup) - mag2*RAMP(Tup+Tdur)
  !
  ThetaR = BOUND(THmin, Thmax, ThetaRub)
  !
  ! --Pulse throttle action
  !
  CONSTANT period=2, width=1, tz=1, PUmag=20
  Thps = THic + PUMAG*Pulse(tz, period, width) ! Pulse steps
  !
  ! --Choose between pulse or ramp
  !
  !
  LOGICAL THpulse
  CONSTANT Thpulse=.true.
  THub = RSW(THpulse, Thps, ThetaR)
  !
  Th=BOUND(THmin, Thmax, THub)
  !
```

```
! --Convert throttle angle from degrees to radians.
!
thr=th*radcon
!
!*************************************************************
!
! " THROTTLE BODY MODEL "
! ----------------------
!
! Compute throttle angle function (THfunc) in
! throttle body model
!
THfunc=THa+(THb*(sin(thr)**2))+(THc*(sin(thr)**4)) &
       +(THd*(sin(thr)**6))
!
! Pressure ratio influence computation
!
Pr=Pm/Pamb
PRIabove=sqrt((2/(Gam-1))*((Pr**(2/Gam))-(Pr**((Gam+1)/Gam))))
PRIbelow=sqrt((2/(Gam+1))**((Gam+1)/(Gam-1)))
PRI=RSW(Pr.le.Pcrit,PRIbelow,PRIabove)
PRInorm=PRI/PRIbelow
!
! " Throttle Air Mass Flow Computation "
!
THair=THfunc*PRInorm
!
!*************************************************************
!
! "  THROTTLE AIR FLOW MAPS "
! ---------------------------
!
! **" Speed density air flow map "**
!
! Independent variable inputs are
! engine speed and manifold pressure.
! Speed-density map is called in with
! the 'INCLUDE' command
!
INCLUDE 'S_D_MAP.inc'
!
spdair = airmap1(pm,speed) !--Speed-density air estimation (g/s)
!
```

```
!*****************************************
!
! **" Modified speed density air flow map " **
!
! Independent inputs are engine speed and throttle angle
! Modified Speed-density map is called in with
! the 'INCLUDE' command
!
INCLUDE 'MOD_SD_MAP.inc'
!
thdair = airmap2(speed,th) !--Modified speed-density air
                           !--estimation (g/s)
!
!--Choose either speed-desity or modified approach
!
LOGICAL spdensity
CONSTANT spdensity = .true.
mapair=RSW(spdensity, spdair, thdair)
!
!*************************************************************
!
! " MANIFOLD PRESSURE COMPUTATION "
! --------------------------------
!
! " Manifold and gas constants "
!
CONSTANT rm=8.31441  !--Molar gas constant
CONSTANT temp=298.0  !--Ambient Temperature (K)
CONSTANT Vm=0.0025   !--Manifold Volume (m^3)
CONSTANT mma=28.84   !--Air molar mass
CONSTANT Vaccum=0.0  !--Vacuum pressure (Pa)
!
ManCon=(Rm*Temp)/(Vm*Mma)   !--Manifold Constant
Flowdiff=THair-Pair         !--Mass equivalence
!
! " Manifold pressure computation "
!
Pman=ManCon*integ(Flowdiff,Pmic) !--Manifold pressure (Pascals)
!
Pmn = BOUND(Vaccum, Pamb, Pman)  !--Manifold pressure (Pascals)
!
! Define noise on manifold pressure reading
!
```

```
CONSTANT  STDpm = 1.0          !--Noise standard deviation
Pmub = pmn + GAUSS(0.0, STDpm)
!
Pm = BOUND(Vaccum, Pamb, Pmub)
!
!*************************************************************
!
!             " PORT AIR MASS FLOW COMPUTATION "
!             ---------------------------------
!
Pair=(PortA*Pm)+(PortB*Pm*speed)+PortC
!
CONSTANT Emag=10
CONSTANT Et1=2
Perr=0.0 + Emag * step(Et1)   !--Port flow rate (g/s)
!
PairE  = Pair+(Pair*Perr/100) !--Error injection
!
!*************************************************************
!
!             " GAS DELIVERY COMPUTATION "
!             ---------------------------
! " Delivery pipe constants "
!
CONSTANT Stoich=16.988  !--AFR stoichiometric
CONSTANT Area=2.064e-5  !--Area of spray disc opening (m^2)
CONSTANT Pipe=0.5       !--Delivery pipe length (m)
!
CONSTANT Lamdeslic = 1.0 !--Initial Lambda
CONSTANT Tl=2.0
CONSTANT MagL = 0.1
LamDesL= Lamdeslic + MagL*step(Tl) !--Desired Lambda value
!
! **" Feedback Error Signal "**
!
Error=sign(1.0,LamDesV-LamV)
!
!*************************************************************
!
!   " CONTROL OPTIONS "
!
! *************** " NOMINAL open loop gas command " ****
!
```

```
!
LOGICAL  usemap
CONSTANT usemap=.false.
Airin = RSW(usemap, mapair, PairE)
!
mfnom = Airin/(STOICH*LamdesL)   !--Continuous nominal fuel
!
! *************** " P + I CONTROL " ********************
!
! " Closed loop control "
!
CONSTANT Lampi=0.01  !--Integral modulation amplitude
CONSTANT Lampp=0.01  !--Proportional modulation amplitude
CONSTANT Lampd=0.01  !--Derivative modulation amplitude
!
DelT=Tdelz+Tsen      !--Delay Time
!
KI =  Lampi*mfnom/DelT      !--Integral     Gain
KP =  Lampp*mfnom/2         !--Proportional Gain
Kd =  Lampd*mfnom*(Tsamp/2) !--Derivative   Gain
!
!
mfp = (KP * Error)   !--Proportional Fuel Command (continuous)
!
CONSTANT mfiic=0
mfi= integ(KI * Error,mfiic) !--Integral Fuel Command
!
CONSTANT DivE = 0.0
diverror=derivt(DivE, error)
mfd=Kd*diverror              !--Derivative Fuel Command
!
mfpi = mfnom+mfp+mfi+mfd     !---Continuous total gas flow
!
! ************* " TRANSIENT COMPENSATION " ************
!
CONSTANT Gconst=0.004  !--Test for constant gain
CONSTANT TrCoef=12.64  ! Transient gain coefficient
Gvar=TrCoef/Speed      ! Variable Tolerance
!
LOGICAL VGain           !--Constant gain or variable
CONSTANT VGain=.true.
Ktr=RSW(VGain,Gvar,Gconst) !--Transient gain
!
```

```
pairdiv=derivt(madic,pair)
madiv=derivt(madic,airin) !--Derivative of port flow rate rate
!
mfdiv=derivt(mfdic,mfin)  !--Derivative of fuel flow rate
!
mftr=Ktr * madiv          !--Transient Fuel compensation
!
mfpitr = mfpi + mftr      !--Totoal transient fuel command
!
! *************** " Sliding Mode Control " ************
!
! " See the reference papers by Kaidantizs (1993) "
! " for theory on Sliding mode control             "
!
CONSTANT DelA=0.10      ! Upper uncertainty in air flow
CONSTANT DelF=0.00      ! Upper uncertainty in fuel flow
!
CONSTANT madic=0        ! Initial condition of air derivative
CONSTANT mfdic=0        ! Initial condition of fuel derivative
!
!----------------------KIADANTZIS SMC METHOD
!
Kss  =  Lampi*mfnom/DelT
KtrA =  DelA*abs(madiv)/STOICH
KtrF =  DelF*abs(mfdiv)
Ksmc =  Kss + KtrA + KtrF
!
CONSTANT mfsmic=0.0
mfsmcdiv = Ksmc * Error
mfsmcin  = integ(mfsmcdiv, mfsmic)
mfsmc = mfnom + mfsmcin
!
!*************************************************************
!
! This section gives control on which algorithm to choose,
! ie, discrete - continuous, sample nature, SMC - P+I etc.
!
!--Choose between transient compensation
!                  control algorithm or ordinary P+I control
!
LOGICAL PIcont
CONSTANT PIcont=.true.
mfincpi=RSW(PIcont, mfpi, mfpitr)
```

```
!
!--Choose between PI or SMC gas control "
!
LOGICAL  smc
CONSTANT smc=.false.
mfinc = RSW(smc, mfsmc, mfincpi)
!
!------------------Choose between discrete or continuous
!                  control
!
LOGICAL  cont
CONSTANT cont = .true.
mfinub = RSW(cont, mfinc, mfdpi) !--Unbounded
CONSTANT bb=0 , tb=10
mfin=BOUND(bb, tb, mfinub)       !--Bounded
!
!*************************************************************
!
! " FUEL DELIVERY HOSE MODEL "
! ---------------------------
!
! " Pipe pressure ratio influence computation for fuel pipe"
!
PRpipe=Pamb/Ppipe
PRIPabove=sqrt((2/(GamGas-1))*((Prpipe**(2/GamGas)) - &
          (Prpipe**((GamGas+1)/GamGas))))
PRIPbelow=sqrt((2/(GamGas+1))**((GamGas+1)/(GamGas-1)))
PRIpipe=RSW(PRpipe.le.Pcrit,PRIPbelow,PRIPabove)
mfo=flowC*area*PRIpipe
Pmassdiff=mfin-mfo
Ppipe=integ(pipecon*Pmassdiff,Ppipeic)
!
! " Choose between continuous or discrete PI gas control "
!
!*************************************************************
!
! " AIR FUEL RATIO (AFR) COMPUTATION "
! -----------------------------------
!
! " Manifold air-fuel ratio"
!
AFR=integ((AFR*mancon/Pm)*(Thair-(AFR*mfo)),STOICH)
!
```

```
Lambda=AFR/STOICH
!
!*************************************************************
!
!  " SYSTEM DELAY COMPUTATION "
!  ---------------------------
!
! " Zirconia lambda output - delayed by time Tdel dependent upon  "
! " engine speed and air-flow rates. TdelZ takes into account the "
! " transportation delays due to the engine combustion            "
! " stroke and exhaust flow down to the ZrO2 sensor.              "
!
CONSTANT RHOair = 1205.0     !--Air Density (g/m^3)
CONSTANT ManAx  = 3.6637e-3  !--Manifold X-sect Area (68mm Diameter)
CONSTANT Aexh   = 1.2566e-3  !--2.0cm radius * PI (m^2)
CONSTANT Lexh   = 0.32       !--Sensor placement (m)
!
! ******** " CRANK ROTATION DELAY " ******************
!
Constant Cranks = 123.3 !--(2 revs + 20degs) * 60 (s/rev)
Tdel1 = Cranks/Speed    !--Time delay 2 due to engine strokes (s)
!
! ******** " EXHAUST MANIFOLD DELAY " ***************
!
Tdel2 = (RHOair*Aexh*Lexh)/(2*Pair)  ! Time delay (s)
!
! ******** " TOTAL TIME DELAY "  ********************
!
TdelZ = Tdel1 + Tdel2 !--Total delay to reach lambda sensor (s)
!
! ******** " DELAYED LAMBDA SIGNAL " ***************
!
delminZ=0.01
PARAMETER(nmxZ=10000)
LambdaZ = delay(Lambda,Lambdaic,TdelZ,nmxZ,delminZ)
!
! ******** " TIME LAG CONTSANT OF SENSOR " **********
!
! " Zirconia sensor time LAG effect. The time constant associated "
! " with the sensor is defined by the coefficient of the transfer "
! " function denominator - Tsen                                   "
!
CONSTANT numZ=0
```

```
CONSTANT Tsen=100e-3 !--100 ms
!
LamZ = ledlag(numZ,Tsen,LambdaZ,Lambdaic)
!
! ******** " CONVERSION OF LAMBDA TO VOLTAGE SIGNAL " *********
!
! " TABLE OF ZIRCONIA SENSOR CHARACTERISTIC "
! ------------------------------------------
!
table Lam2V, 1, 10                          &
      /0.8335, 0.8751, 0.9247, 0.9697, 0.9999 &
      ,1.0001, 1.0667, 1.1326, 1.1949, 1.2861 &
      ,0.9062, 0.8886, 0.8622, 0.8299, 0.8006 &
      ,0.0733, 0.0469, 0.0352, 0.0264, 0.0205 /
!
LamV=Lam2V(LamZ)        !--Sensor voltage signal
LamDesV= Lam2v(LamDesL) !--Desired Lambda voltage (from table)
!
!************************************************************
!
!             " COMBUSTION TORQUE COMPUTATION "
!             --------------------------------
!
Tq1 =a*speed*(Pair**2)*Lambda**2
Tq2 =b*speed*(Pair**2)*Lambda
Tq3 =c*speed*(Pair**2)
Tq4 =d*(Pair**2)*Lambda**2
Tq5 =e*(Pair**2)*Lambda
Tq6 =f*(Pair**2)
Tq7 =g*speed*Pair*Lambda**2
Tq8 =h*speed*Pair*Lambda
Tq9 =i*speed*Pair
Tq10=j*Pair*Lambda**2
Tq11=k*Pair*Lambda
Tq12=l*Pair
Tq13=m*speed*Lambda**2
Tq14=n*speed*Lambda
Tq15=o*speed
Tq16=p*Lambda**2
Tq17=q*Lambda
Tq18=r
Torque1=Tq1+Tq2+Tq3+Tq4+Tq5+Tq6+Tq7+Tq8+Tq9
Torque2=Tq10+Tq11+Tq12+Tq13+Tq14+Tq15+Tq16+Tq17+Tq18
```

```
Torqu=Torque1+Torque2
!
CONSTANT zero=0.0
!
if (Torqu .lt. zero) then
   Torque1=0
else
   Torque1=Torqu
end if
!
LOGICAL overun
CONSTANT overun=.false.
Torque = RSW(overun, Torqu, Torque1) !--Torque (Nm)
!
!************************************************************
!
! " ROTATIONAL DYNAMICS "
! ----------------------
!
CONSTANT jin=0.8  ! First gear engine inertia
!
! " Speed control."
! " For constant speed simulations, PI control on the load torque "
! " applied is governed from the feedback of engine speed "
!
! *** " P+I Control on speed setting " *******
!
SpeedREF=Speedic             !--Reference speed
SPerror = SpeedREF - Speed   !--Speed error
CONSTANT KItq=-3             !--Integral gain
CONSTANT KPtq=-3             !--Proportional gain
!
CONSTANT TQintic=0.0
TQint=KItq*integ(SPerror,TQintic)
TQprop=KPtq*SPerror
Tloadss=Tloadic + TQint+TQprop  !--PI Controlled Load torque
!
! *** " Independently adjusted load " ******
!
CONSTANT periodl=10
CONSTANT widthl=3
CONSTANT tlmag=10
CONSTANT tzl=20
```

```
!
!--Friction MEP
!
tfmep = (0.97+(0.15*Speed/1000)+(0.05*Speed/1000))*100
!
CONSTANT Varea=1.78   ! Vehicle frontal area m^2
CONSTANT Cdrag = 0.36 ! Coeff of drag
!
!--Aero dynamic drag
!
Faero = 0.5*(Rhoair/1000)*Varea*Cdrag*(Vspeed*1000/(3600))**2
Laero = Faero*Wheel/GearR
!
CONSTANT Vd=1.4  !--Engine displacement
Tlic=(Tfmep*Vd)/(4*pi) + Tlind
!
Tloadv = tlic + Laero
!
! *** " Choose between constant speed or constant load " **
!
LOGICAL steady
CONSTANT steady=.true.
Tload = RSW(steady, Tloadss, Tloadv)
!
Torqdiff=Torque-TLoad
!
rotaccel=(1/Jin)*(Torqdiff) ! Engine acceleration
!
Ne=integ(rotaccel,Neic)   !--Engine speed (r/s)
Speedn=Ne*60              !--Engine speed (r/m)
!
! *** " VEHICLE SPEED " *********************************
!
CONSTANT GearR=12.54568  !--First Gear ratio
CONSTANT Wheel=0.25      !--Wheel Radius (metres)
vspeed=((speed*60)/(GearR))*(2*pi*Wheel/1000) !--km/Hour
!
!************************************************************
!
!             " TERMINATION CONDITION "
!             ------------------------
!
TERMT(t .ge. tstop, 'TSTOP HAS BEEN REACHED')
```

```
  !
END   ! of Derivative Block
  !
  !*************************************************************
  !
  ! " DISRETE SAMPLING OF STATE VARIABLES FOR DISCRETE CONTROL "
  ! -----------------------------------------------------------
  !
DISCRETE   ! Begin Discrete Block
  !
  INTERVAL tsamp=0.003 !--Sample time (GFI=0.003 s)
  !
  ! " Terms with 'D' extension refer to discretised values "
  !
  Errordiff=error - errorp
  Errorp = Error
  !
  PmD=Pm        !--Manifold pressure
  !
  SpeedD=Speed !--Engine speed
  !
  PairD = PortA*PmD + PortB*PmD*SpeedD + PortC !--Port air
  !
  !
  PairDe=PairD + (PairD*Perr/100)  !--Injected error
  !
  !--Fast open-loop nominal gas flow
  !
  AirEst= RSW(usemap, mapair, PairDe) !--Map estimation
  !
  Unom  = AirEst/(STOICH*LamdesL)     !---Nominal Fuel Command
  !
  !--Slow outer loop P+I control
  !
  Up = KP*error                 !---Proportional Fuel Command
  !
  Uip= Ui
  Ui = Uip + KI*Error*TSAMP     !---Integral Fuel Command
  !
  Ud = Kd * Errordiff/Tsamp     !---Derivative Fuel Command
  !
  Upi=Unom+Ui+Up+Ud             !---Discrete Total Fuel command
  !
```

```
  !
  !--Fast Transient Compensation
  !
  Aird  = (AirEst - map)/Tsamp !--Derivative estimate
  Map   = AirEst               !--Mass flow rate (t-1)
  Ktrd  = TRcoef/Speed         !--Transient gain
  Utr   = Ktrd * Aird          !--transient fuel command
  !
  Upitr = Upi + Utr            !--Total transient fuel
  !
  !--Choose between transient command on or off.
  !
  LOGICAL Comp
  CONSTANT Comp=.false.
  !
  mfdcom = RSW(Comp, Upitr, Upi) !--Discrete fuel injection command
  !
  !
  ! " Schedule the "dac" block for output after a "
  ! " simulated injector actuation time           "
  !
  CONSTANT delaytime = 0.0        !--Tinj (actuation duration)
  SCHEDULE dac .AT. t + delaytime
  !
  !
  CALL LOGD(.false.)
  !
END   ! of Discrete Block
  !
  !*****************************************************************
  !
DISCRETE dac  ! Begin DAC Block (digital to analogue)
  !
  CALL LOGD(.false.)
  !
  ! " Make control value available to continuous engine system"
  !
  mfdpi = mfdcom
  !
  CALL LOGD(.false.)
  !
END   ! of DAC block
  !
```

```
  !*************************************************************
  !
END   ! of dynamic
  !
END   ! of program
```

Appendix E

I. Mech. E. Seminar Paper

Published
Papers
Not filmed
for Copyright
reasons

7